SERRI Report 70015-009

PHYSICAL TESTING AND HYDRAULIC SIMULATION OF WAVE OVERTOPPING OF EARTHEN LEVEES

SERRI Project: *Increasing Community Disaster Resilience Through Targeted Strengthening of Critical Infrastructure*

Project Principal Investigator:
Isaac L. Howard, PhD

Report Written and Performed By:

Steven A. Hughes – US Army Corps of Engineers

Jeremy A. Sharp – US Army Corps of Engineers

Justin M. Shaw – Mississippi State University

Isaac L. Howard – Mississippi State University

William H. McAnally – Mississippi State University

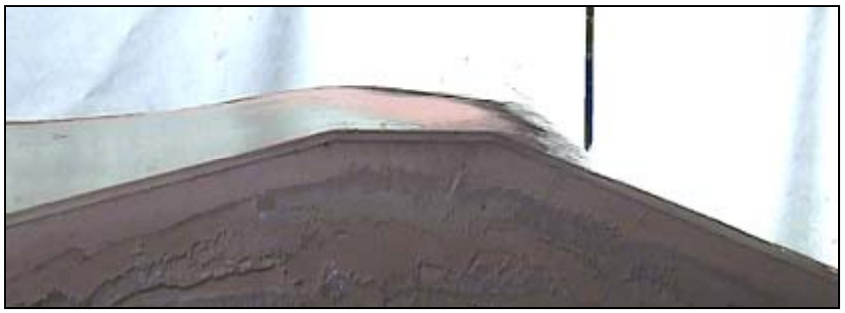

This material is based upon work supported by the U.S. Department of Homeland Security under U.S. Department of Energy Interagency Agreement 43WT10301. The views and conclusions contained in this document are those of the authors and should not be interpreted as necessarily representing the official policies, either expressed or implied, of the U.S. Department of Homeland Security.

SERRI Project: Increasing Community Disaster Resilience
Through Targeted Strengthening of Critical Infrastructure

PHYSICAL TESTING AND HYDRAULIC SIMULATION OF WAVE OVERTOPPING OF EARTHEN LEVEES

Performing Organization Report No. CMRC-10-06

Written By:

***Steven A. Hughes**, PhD, PE, Senior Research Engineer, US Army Engineer Research and Development Center (ERDC)*
***Jeremy A. Sharp**, Research Hydraulic Engineer, US Army Engineer Research and Development Center (ERDC)*
***Justin M. Shaw**, Former Graduate Student, Mississippi State University*
***Isaac L. Howard**, PhD, Assistant Professor, Mississippi State University*
***William H. McAnally**, PhD, PE, Research Professor, Mississippi State University*

Date Published:

June 2011

Prepared for
U.S. Department of Homeland Security
Under U.S. Department of Energy Interagency Agreement 43WT10301

Prepared by
OAK RIDGE NATIONAL LABORATORY
Oak Ridge, Tennessee 37831-6283
managed by
UT-BATTELLE, LLC
for the
U.S DEPARTMENT OF ENERGY
under contract DE-AC05-00OR22725

This page was intentionally left blank.

TABLE OF CONTENTS

LIST OF FIGURES

LIST OF TABLES

ACKNOWLEDGEMENTS

Thanks are due to many for the successful completion of this project. The authors are especially grateful for the financial support provided by the *Southeast Region Research Initiative* (*SERRI*) program. In addition, due gratitude is extended to everyone employed at the *Department of Homeland Security* (*DHS*) and *Oak Ridge National Laboratory* (*ORNL*) who worked diligently with the authors to make this project a success. A great deal of the success of this research can be attributed to the efforts of *DHS* and *ORNL* personnel.

Special thanks are extended to Dr. Charlie Berger and Dr. Gaurav Savant (International Contractor) with the US Army Corps of Engineers (USACE) Coastal and Hydraulics Laboratory (CHL) at the Engineer Research and Development Center (ERDC) in Vicksburg, MS. Without their expertise and feedback in Adaptive Hydraulics (AdH) and modifications to the code the simulations performed in this report would not be possible. The authors are particularly grateful to Mr. Hugh Acuff and Ms. Julie Cohen for their excellent support of the physical model experiments and data collection. The success of the entire physical model study can be largely attributed to their knowledge and dedication.

LIST OF SYMBOLS

A	Channel cross section area [m^2]
B	Dike crest width [m]
b	Weibull distribution shape factor for overtopping discharge [-]
C	Chezy coefficient [-]
C_2	Slope-dependent empirical coefficient [-]
C_3	Crest empirical coefficient [-]
$C_{Ah2\%}$	Empirical flow thickness coefficient determined from test data for 2% runup [-]
$C_{Ah50\%}$	Empirical flow thickness coefficient determined from test data for 50% runup [-]
$C_{Au2\%}$	Empirical velocity coefficient determined from test data for 2% runup [-]
$C_{Au50\%}$	Empirical velocity coefficient determined from test data for 50% runup [-]
C_f	Friction factor [-]
c	Weibull distribution scale factor for overtopping discharge [$m^3/s/m$]
D_{50}	Median grain size [mm]
D_{75}	Grain size at which 75% of the grains are smaller [mm]
F_r	Froude number [-]
f_D	Darcy Friction Factor [-]
f_F	Fanning Friction Factor [-]
g	Gravitational acceleration [m/s^2]
$H_{1/3}$	Average of highest 1/3 waves (significant wave height = H_s) [m]
H_{m0}	Energy-based significant wave height [m]
H_{rms}	Root-mean-square slope-perpendicular wave height on landward-side slope [m]
H_s	Significant wave height [m]
h	Instantaneous flow thickness [m]
h_0	Flow thickness of steady, uniform flow at terminal velocity [m]
h_1	Upstream head (difference between surge elevation and levee crest elevation) [m]
h_1	Instantaneous flow thickness at up-stream location [m]
h_2	Instantaneous flow thickness at down-stream location [m]
h_A	Flow thickness at the levee crest seaward edge [m]
$h_{A2\%}$	Flow thickness at the levee crest seaward edge exceeded by 2% of the waves [m]
h_B	Flow thickness at the levee crest landward edge [m]
$h_{B2\%}$	Flow thickness at the levee crest landward edge exceeded by 2% of the waves [m]
h_c	Steady flow critical depth [m]
h_m	Mean flow thickness [m]
h_{rms}	Root-mean-square of the peak flow thickness on the landward-side slope [m]
h_{sb}	Flow thickness on the levee landward slope [m]
$h_{sb2\%}$	Flow thickness on the levee landward slope exceeded by 2% of the waves [m]
K_2	Slope parameter [$m^{1/3}s^{2/3}$]
K_3	Discharge parameter [$s^{1/3}m^{2/3}$]
K_4	Velocity parameter [m/s]
L	Characteristic length [m]
$L_{m-1,0}$	Wave length associated with mean wave energy [m]
m	Subscript denoting model scale [-]
N_g	Prototype-to-model gravity scale [-]
N_L	Prototype-to-model length scale [-]

N_Q	Prototype-to-model scale discharge scale [-]
N_T	Prototype-to-model wave period scale [-]
N_t	Prototype-to-model time scale [-]
N_V	Prototype-to-model velocity scale [-]
N_X	Prototype-to-model scale ratio of parameter X [-]
N_μ	Prototype-to-model dynamic viscosity scale [-]
N_ρ	Prototype-to-model density scale [-]
n	Manning's roughness coefficient [-]
P	Channel wetted perimeter [m]
$P1$	Pressure gauge number 1 [-]
$P2$	Pressure gauge number 2 [-]
$P3$	Pressure gauge number 3 [-]
$P4$	Pressure gauge number 4 [-]
$P5$	Pressure gauge number 5 [-]
$P6$	Pressure gauge number 6 [-]
$P7$	Pressure gauge number 7 [-]
PI	Plasticity index [-]
P_s	Stream power per unit area of levee [kN-m/s/m^2]
$P_{\%}$	Percent exceedance probability of overtopping waves [%]
p	Pressure [kPa]
p	Subscript denoting prototype scale [-]
p_d	Probability density function [-]
Q_m	Total model-scale flume discharge [m^3/s]
$Q_{p,mean}$	Mean of discharge peaks per unit length [m^3/s/m]
Q_p	Total prototype-scale flume discharge [m^3/s]
Q_p	Peak discharge per unit length [m^3/s/m]
$Q_{p,rms}$	Root-mean-square of discharge peaks per unit length [m^3/s/m]
$Q_{p,1/3}$	Average of the highest 1/3 discharge peaks per unit length [m^3/s/m]
$Q_{p,1/10}$	Average of the highest 1/10 discharge peaks per unit length [m^3/s/m]
$Q_{p,1/100}$	Average of the highest 1/100 discharge peaks per unit length [m^3/s/m]
Q_{p*}	Reference peak discharge level per unit length [m^3/s/m]
q	Instantaneous overtopping discharge per unit length [m^3/s/m]
q	Steady overflow discharge per unit length [m^3/s/m]
q_0	Steady overflow discharge per unit length at terminal velocity [m^3/s/m]
q_c	Steady flow critical discharge per unit length [m^3/s/m]
$q_{combined}$	Average combined wave-surge overtopping discharge per unit length [m^3/s/m]
$q_{m,P2}$	Average overtopping discharge per unit length at location P2 [m^3/s/m]
$q_{m,P6}$	Average overtopping discharge per unit length at location P6 [m^3/s/m]
q_p	Prototype-scale pump discharge per unit length [m^3/s/m]
q_{rms}	Root-mean-square of the instantaneous discharge per unit length [m^3/s/m]
q_{surge}	Steady overflow discharge per unit length due to surge [m^3/s/m]
q_w	Average wave-only overtopping discharge per unit length [m^3/s/m]
q_{wave}	Average wave-only overtopping discharge per unit length [m^3/s/m]
q_{ws}	Average combined wave-surge overtopping discharge per unit length [m^3/s/m]
q_*	Reference discharge level per unit length [m^3/s/m]
R	Hydraulic radius [m]

R	Dimensionless freeboard (= R_c/H_{m0}) [m]
R_c	Crest freeboard = $-h_1$ [m]
$R_{u2\%}$	Runup elevation exceeded by 2% of the waves [m]
S_f	Friction slope (slope of the energy-grade line) [-]
S_0	Friction slope at steady flow terminal velocity = $\sin\theta$ [-]
s	Coordinate parallel to the landward-side levee slope [m]
$s_{2,1}$	Distance along slope between up-stream and down-stream locations [m]
s_b	Distance along landward-side slope from edge of crest [m]
$T_{1/3}$	Average of highest 1/3 wave periods [s]
T_m	Mean wave period [s]
$T_{m\text{-}1,0}$	Mean spectral energy wave period [s]
T_p	Peak spectral wave period [s]
t	Time [s]
$t(i)$	Time at interval i [s]
$t(i+1)$	Time at interval $i+1$ [s]
u_A	Velocity at the levee crest seaward edge [m/s]
$u_{A2\%}$	Velocity at the levee crest seaward edge exceeded by 2% of the waves [m/s]
u_B	Velocity at the levee crest landward edge [m/s]
$u_{B2\%}$	Velocity at the levee crest landward edge exceeded by 2% of the waves [m/s]
u_{sb}	Velocity on the levee landward slope [m/s]
$u_{sb2\%}$	Velocity on the levee landward slope exceeded by 2% of the waves [m/s]
V	Characteristic velocity [m/s]
v	Instantaneous velocity parallel to levee surface [m/s]
v_0	Steady, uniform flow terminal velocity [m/s]
$v_1(i)$	Instantaneous velocity at up-stream location [m/s]
$v_2(i)$	Instantaneous velocity at down-stream location [m/s]
$v_1(i+1)$	Instantaneous velocity at up-stream location , one time increment later [m/s]
$v_2(i+1)$	Instantaneous velocity at down-stream location, one time increment later [m/s]
v_c	Steady flow critical velocity [m/s]
v_m	Mean velocity on the landward-side slope [m/s]
v_{mean}	Mean velocity on the landward-side slope [m/s]
W	Levee crest width [m]
X_m	Value of parameter X in model [units of X]
X_p	Value of parameter X in prototype [units of X]
x	horizontal length coordinate [m]
x_C	Distance along levee crest from seaward edge [m]
y	vertical length coordinate [m]
z_b	Bed elevation [m]
α	Seaward levee slope angle (this report) [-]
α	Landward levee slope angle (some previous literature) [-]
Γ	Mathematical gamma function [-]
γ_b	Reduction factor for influence of berm [-]
γ_h	Reduction factor for influence of shallow foreshore [-]
γ_r	Reduction factor for influence of roughness [-]
γ_v	Reduction factor for influence of vertical wall [-]
γ_w	Specific weight of water [N/m^3]

γ_β	Reduction factor for influence of angle of wave attack [-]
Δ	Mathematical discrete increment [-]
θ	Landward-side levee slope angle (this report) [-]
θ	Seaward-side dike slope angle (some previous literature) [-]
μ	Dynamic viscosity [N-s/m^2]
υ_l	Kinematic viscosity [m^2/s]
$\xi_{m-1,0}$	Iribarren number based on deepwater wave length and mean energy period [-]
ξ_p	Iribarren number based on deepwater wave length and peak spectral [-]
ρ	Density of water [kg/m^3]
σ	Reynolds stress [N/m^2]
τ	Time lag [s]
τ_0	Instantaneous shear stress [N/m^2]
$\tau_{0,mean}$	Mean shear stress [N/m^2]
$(\tau_{0,mean})_{max}$	Maximum mean shear stress at terminal velocity [N/m^2]
$\tau_{p,1/3}$	Average of highest 1/3 shear stress peaks [N/m^2]
$\tau_{p,1/10}$	Average of highest 1/10 shear stress peaks [N/m^2]
$\tau_{p,1/100}$	Average of highest 1/100 shear stress peaks [N/m^2]

LIST OF ACRONYMS

CHEN3D	Numerical model developed at Texas A&M University
DHS	Department of Homeland Security
SERRI	Southeast Region Research Initiative
CEE	Civil and Environmental Engineering
MSU	Mississippi State University
ORNL	Oak Ridge National Laboratory
AdH	Adaptive Hydraulics
NRF	National Response Framework
HLT	Hurricane Liaison Team
NICC	National Infrastructure Coordinating Center
ASCE	American Society of Civil Engineers
MRGO	Mississippi River Gulf Outlet
USACE	United States Army Corps of Engineers
ERDC	Engineer Research and Development Center
CHL	Coastal and Hydraulics Laboratory at ERDC
PG	Pressure Gage (Druck PDCR-200)
LDV	Laser Doppler Velocimeter
RANS	Reynolds Averaged Navier-Stokes
TMA	Texel, Marsen, and Arsole
RMS	Root-mean-squared
FHWA	Federal Highway Administration
BSA	Burst Spectrum Analyzer
EurOtop	European overtopping manual
TAW	Technical advisory committee on flood defense (The Netherlands)

EXECUTIVE SUMMARY

This report summarizes small-scale physical model experiments that simulated combined wave overtopping and storm surge overflow of an earthen levee having a trapezoidal cross section. Included in this report are results from numerical model simulations of steady overflow for a trapezoidal levee. In the physical model, time series of irregular and unsteady instantaneous flow thickness were obtained at two locations on the levee crest and at five locations on the levee landward-side 1V:3H slope. Time series of unsteady overtopping flow velocity were obtained at two locations coincident with flow thickness measurements. The data acquisition and instrumentation program used in this research is a defining characteristic not common to previous research efforts attempting to characterize overtopping of earthen levees.

Data acquired during 9 experiments were used to prove that the time series of instantaneous overtopping discharge is conserved between locations on the levee landward-side slope with the only difference being a small time lag. Data measured during an additional 27 experiments were used to calculate the time series of instantaneous shear stress representing the average behavior over a 4.8-m-length of levee slope. Empirical relationships are presented for estimating the mean shear stress for steady overflow and for combined wave and surge overtopping. For the latter case, additional formulas are given to estimate representative parameters of the irregular shear stress peaks. While not directly measured, conservative estimates were developed of the shear stress conditions that could occur at portions a considerable distance down the levee face where the overtopping flow has reached terminal velocity.

Numerical model simulations successfully reproduced the hydrodynamics measured in the physical model for steady overflow. The model was then used to examine variations in shear stress due to levee surface roughness and the effect of slope transition between the steep levee slope and mild-sloped berm. Numerical hydraulic models calibrated with physical measurements can be valuable and used to perform parametric investigations of conditions beyond the scope or means of physical testing.

The data presented in this report can be used to evaluate erosion rates during overtopping, in design of levee armoring systems, or for other applications where shear stress profiles under a variety of surge and combined overtopping might occur and could be useful design inputs. The data presented in this paper was collected for use in SERRI Report 70015-010, where a rapidly deployable armoring system (RDAS) is being designed. Design inputs for a RDAS will have many uses for flooding, and especially for hurricane events.

CHAPTER 1 – INTRODUCTION

1.1 General Background Information

The work presented in this report was developed in partial fulfillment of the requirements of Task Order 4000064719 sponsored by the *Department of Homeland Security (DHS)* through its *Southeast Region Research Initiative (SERRI)* program administered by *UT-Battelle* at the *Oak Ridge National Laboratory (ORNL)* in Oak Ridge, Tennessee. The research was proposed by members of the *Department of Civil and Environmental Engineering (CEE)* at *Mississippi State University (MSU)* to *SERRI* in a document dated 1 June 2007. The proposed research was authorized by *UT-Battelle* in its task order dated 10 December 2007. This task order included a scope of work defined through joint discussions between *MSU* and *SERRI*. Work on the project was initiated on 1 January 2008. A modification of Task Order 4000064719 was proposed on 9 September 2008 and agreed upon on 29 September 2008. A second Task Order modification dated 22 June 2010 was also performed, which is the Task Order used to generate this report.

The scope of work associated with Task Order 4000064719 included several related components. The general objectives of the project were to investigate means for rapidly using on-site materials and methods in ways that would most effectively enable local communities to rebuild in the wake of a flooding disaster. Within this general framework, several key work components were associated with Task Order 4000064719. Specifically, the scope of work dated 22 June 2010 includes research efforts in the following six task groups:

Task 1: Erosion Control-Erosion Protection for Earthen Levees.

Task 2: Bridge Stability-Lateral & Uplift Stability of Gravity-Supported Bridge Decks.

Task 3: Levee Breach Repair-Closure of Breaches in Flood Protection Systems.

Task 4: Pavement Characterization and Repair.

Task 5: Emergency Construction Material Development-Staging Platform Construction.

Task 6: Fresh Water Reservoir-Restoration of Fresh Water Supplies.

The research described in this report was associated with Task 1. The report of this work was the 9th deliverable of the research project, hence the designation of the report as *SERRI Report 70015-009* of Task Order 4000064719. Work related to Task 1 was also delivered in *SERRI Report 70015-010*. The research contract was delivered in a series of reports to allow users to more efficiently obtain the information of interest.

1.2 Task Order Objectives

A key component of this research was to develop solutions which may be rapidly deployed to achieve maximum benefit to the community, typically through the use of on-site

materials, pre-engineered components, and innovative construction materials and techniques. This research aimed to develop solutions for protecting and/or expeditiously reconstituting critical civil infrastructure components. In this context, the specific objective of the total effort of Task Order 4000064719 was to develop specialty materials and design and construction procedures which may be rapidly deployed to protect and restore selected key civil infrastructure components.

The primary objective of the research presented in this report was to perform physical model testing and numerical simulations of combined wave overtopping and surge overflow of earthen levees to characterize shear stresses experienced by the landward side of the levee. These shear stresses are intended for use in investigating means of rapidly armoring the landward side of the levee to prevent failure prior to sustained overtopping from events such as a hurricane. A secondary objective was to improve numerical simulation techniques related to levee overtopping and to provide unique physical model test results for use by future researchers.

1.3 Scope of Report

The revised Task 1 scope of work dated 22 June 2010 includes eight items. These eight items are the full deliverable of Task 1; this report partially addresses item a) and fully addresses items b) through e). *SERRI Report 70015-010* addresses the remainder of item a) and fully addresses items f) through h).

a) Conduct a literature review to investigate key parameters related to levee overtopping. Items of interest could include erosion, anchoring, geosynthetics, storm surge, mechanical connection, adhesive connections, and/or a range of appropriate field conditions.

b) Produce a scale model representing a typical flood protection levee. The model shall be constructed within an existing modeling flume outfitted with a controlled wave generator.

c) Use the scale model from b) to conduct instrumented testing to characterize parameters associated with wave and surge overtopping under a range of conditions associated with hurricane events. Instrumentation will be used to measure pressure and velocity profiles on the protected side of earthen levees.

d) Perform adaptive hydraulics (AdH) simulations to compliment the data from c).

e) Use information from c) and d) to develop shear stress profiles along key portions of an earthen levee.

f) Investigate anchoring geosynthetics to a levee face. The investigation could include physical testing, practice review coupled with fundamental design principles using adaptations of existing technology, and/or numerical modeling as appropriate to investigate anchoring a geotextile system to the protected side of an earthen levee. Testing options include large scale investigations using a portal frame system and

evaluation of the connection mechanism between the anchor and the geosynthetic. The connection could also be evaluated with a number of other approaches; the research team will select an approach or approaches. Connection schemes could vary from pinned/bolted to cables to adhesive depending on the information obtained. Numerical modeling will be considered to investigate anchor/geosynthetic/soil interaction in conjunction with or in place of physical testing.

g) Conduct parametric numerical modeling of levees and their protection mechanisms to establish parameters such as required anchor depth, required anchor spacing, and similar. The intent is to use information from a) to f) within the model as inputs for calibration.

h) Provide construction guidance for using geotextiles as a rapidly deployable temporary armoring for earthen levees.

1.4 Incorporation into the *National Response Framework*

The *National Response Framework* (*NRF*) is a document that guides the United States when conducting all-hazards response (response refers to immediate actions to save lives, protect property and the environment, and meet basic human needs). This framework is entailed in NRF (2008), which has complimentary material found in print and online. The *NRF* is a continuation of previous federal level planning documents (e.g. Federal Response Plan of 1992), and serves as the state of the art in responding to disaster events. The following paragraphs summarize how the research within Task 1 could be applicable to the *NRF* and in what manner. The tone of the paragraphs assumes the reader is at least casually familiar with the *NRF* and supporting documentation.

According to NRF (2008), "Resilient communities begin with prepared individuals and depend on the leadership and engagement of local government, nongovernmental organizations, and the private sector." The word "prepared" in the previous sentence is very powerful and could refer to numerous components. The current state of practice in emergency strengthening prior to a water-based catastrophe is an area where the authors feel the United States is not fully "prepared". To approach a state of readiness where the United States is "prepared" for these events, concepts need to be developed that are studied to reasonable resolution where design methods and materials are developed (primarily laboratory scale and analytical studies). These methods and materials then need to be demonstrated at full scale, and thereafter training needs to be performed to ensure construction responders can perform the needed tasks. In present day, this level of preparedness does not exist.

The *NRF* is primarily oriented toward implementing nationwide response policy and operational coordination for any domestic event. NRF (2008) focuses on responding to and recovering from incidents that do occur, which is one of four major parts of a larger *National Strategy for Homeland Security*. NRF (2008) states that although some risk may be unavoidable, first responders can effectively anticipate and manage risk through proper training and planning. An entire chapter of NRF (2008) addresses planning. One of the three

principal benefits that is listed for planning is "it contributes to unity of effort by providing a common blueprint for activity in the event of an emergency. Planning is a foundational element of both preparedness and response and thus is an essential homeland security activity.

Neither training nor planning appears to be performed to any significant extent related to emergency design and construction for the purpose of rapidly strengthening and/or repairing civil infrastructure. Training programs that result in certifications to perform certain activities would expedite selection of qualified groups in the highly time sensitive environment of a disaster. Having known quantities of certified contractors in place would also be valuable during planning exercises. The end products of the work within Task 1 would need to be further developed into full scale demonstrations. Contractors and design firms could then be certified to perform the tasks.

The goals of the research conducted in this report possibly align with the needs of the *Hurricane Liaison Team (HLT)*, whose goal is to enhance hurricane disaster response. Response was stated earlier to refer to immediate actions to save lives, protect property and the environment, and meet basic human needs. The *NRF* is not specific as to whether response refers to actions immediately prior to an event that temporarily strengthen key infrastructure (i.e. work presented in this report). Task 1 does align with *Scenario 10: National Disaster-Major Hurricane* of the National Planning Scenarios that have been established in NRF (2008).

"**National Infrastructure Coordinating Center (NICC)**. The *NICC* monitors the Nation's critical infrastructure and key resources on an ongoing basis. During an incident, the NICC provides a coordinating forum to share information across infrastructure and key resources sectors through appropriate information-sharing entities such as the Information Sharing and Analysis Centers and the Sector Coordinating Councils." Selection of which levees to temporarily strengthen were outside of the scope of the research, but in future activities this selection process could be coordinated with the *NICC*.

Repeatedly preparedness is stated (directly or indirectly) as an essential precursor to response. The *RESPONSE ACTIONS* chapter of NRF (2008) shows a circular preparedness cycle consisting of the following four categories: 1) plan; 2) organize, train, and equip; 3) exercise; and 4) evaluate and improve. Under the organize category, assembling well-qualified teams of paid and volunteer staff for essential response and recovery tasks is listed. Also under the organize category is discussion of *Pre-Scripted Mission Assignments*. They are used to assist in planning for and reduction in time necessary to deploy resources that can be tailored for training, development, and to exercise rosters of deployable resources. These assignments would need to be developed for Task 1.

Advanced Readiness Contracting is used to ensure contracts are in place before an incident for often needed commodities (a list is provided that does not include construction materials). Geosynthetics and anchors are construction items that would need to be included in *Advanced Readiness Contracting*. This could be an essential step for successful construction of a rapid levee armoring system.

1.5 Problem Introduction

Earthen levees are used throughout the world to protect communities and resources from elevated water levels in coastal and inland areas. These flood protection systems are at risk of failure due to several mechanisms including erosion of levee soil, seepage and piping through the earthen structure, and settlement due to weak foundation soils. Ideally, all levees would have a crest elevation with ample freeboard to prevent wave and/or surge overtopping for any conceivable storm scenario. However, economics dictate more practical levee designs having lower crest elevations, but with the risk that some wave/surge overtopping will occur during extreme events. Rapid erosion of levee soil can occur during overtopping flood events; and if unchecked, there is a risk of a catastrophic levee breach with massive flooding of the protected region. Earthen levees constructed without slope protection or armoring must rely on the erosion resistance of the outer soil layer during episodes of wave and/or storm surge overtopping.

Hurricane Katrina made landfall in August 2005 with storm surge elevations that reached 7.6 m in some locations. Post-Katrina investigations concluded that erosion of the landward levee slope (protected side slope) due to storm surge overflow and wave overtopping was the primary contributor to the failure of 272 km of levees in Louisiana (ASCE 2007, Irish et al. 2003). Figure 1.1 illustrates typical minor damage from overtopping where weaker, unprotected soil was eroded on the levee backside slope (right side of photograph). In this case, overtopping was probably not severe or the duration of overtopping was relatively short.

Figure 1.1. Minor erosion due to overtopping on the Citrus Back levee

If the surge level continues to rise, and greater volumes of water overtop the levee for an extended period, the initial erosion areas will expand until eventually the levee crest and portions of the flood side are eroded as shown for the Mississippi River Gulf Outlet (MRGO) levee in Figure 1.2. Once the levee crown or grass covering on the protected side is lost, there is a higher risk of levee breaching and catastrophic flooding.

Figure 1.2. Crown erosion along MRGO levee in St. Bernard Parish

Common terms and definitions related to levee geometry and storm surge conditions are shown in Figure 1.3. The vertical difference between the surge elevation and levee crest elevation is the "freeboard" represented by the notation R_c. When the storm surge elevation is lower than the levee crest elevation, the freeboard is positive. When the surge elevation is higher than the levee, freeboard is negative.

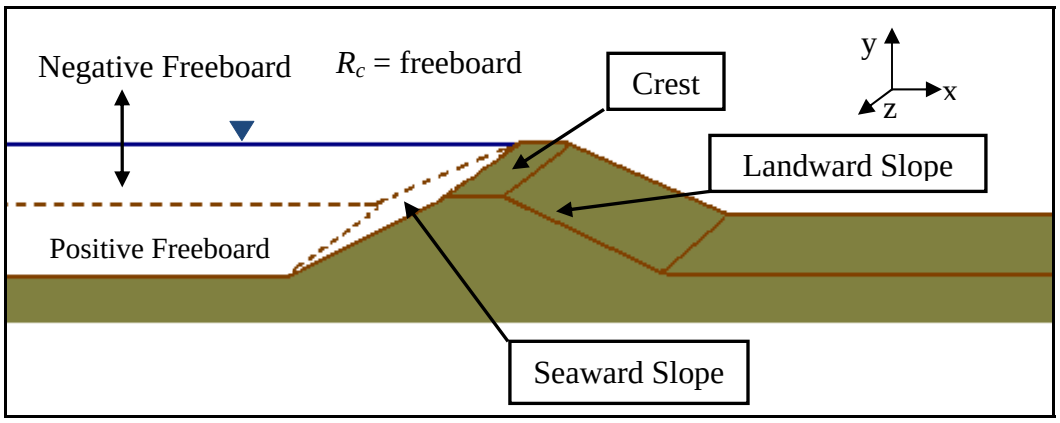

Figure 1.3. Levee terminology

Figure 1.4 illustrates the three levee overtopping cases that might occur for positive and negative freeboards. Wind generated waves will overtop levees facing larger bodies of water before the still water level reaches the elevation of the crest as shown in Figure 1.4(a). Waves will periodically spill over the levee crest, but the crest and landward slope are not constantly under a sheet of water. Levees not exposed to wave activity (e.g., river levees) will not be overtopped until the still water level exceeds the levee crest elevation as illustrated by Figure 1.4(b). In this case there is a relatively steady flow of water over the crest and down the landward-side slope. The overflowing water level may vary slowly in time due to tide, a time-varying surge hydrograph, or long-period seiching of a lake or basin. The third, and most problematic overtopping, is shown in Figure 1.4(c). The still water level exceeds the levee crest elevation, and hurricane waves provide a pulsing, unsteady

component to the overtopping flow. This is a destructive overtopping condition characterized by large peaks in water depth and flow velocity (ASCE 2007, Hughes 2008, Hughes and Nadal, 2009, Nadal and Hughes 2009).

Figure 1.4 shows common erosion progression on a levee's landward slope during surge overflow; note erosion appearing on the landward slope. Usually erosion resistance for wave or surge overtopping is most needed on the levee crown and down the rear slope on the protected side of the levee as evidenced in Figures 1.1 and 1.2. Levees constructed with a top layer of good clay and well-established vegetation with a healthy root system have much better erosion resistance than top layers of sandy soil with sparse or unhealthy vegetation. Where expected overtopping rates are within permissible ranges, the crown and protected-side slope clay layer can be adequately protected with good quality grass having a well-established root system, but continual maintenance is needed to assure the grass covering remains in top condition. At locations where the levee crest elevation cannot be raised to the elevation associated with permissible overtopping for grass-covered slopes, it will be necessary to protect the levee soil with some type of armoring system that can withstand the forces of the anticipated hydrodynamic loading.

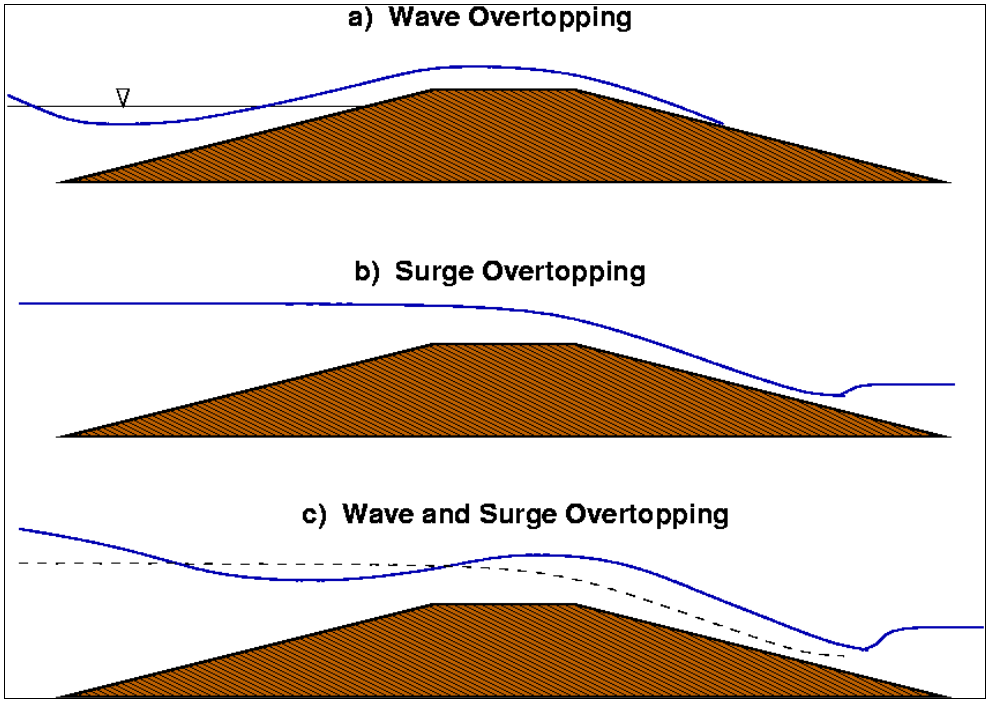

Figure 1.4. Overtopping of earthen levees

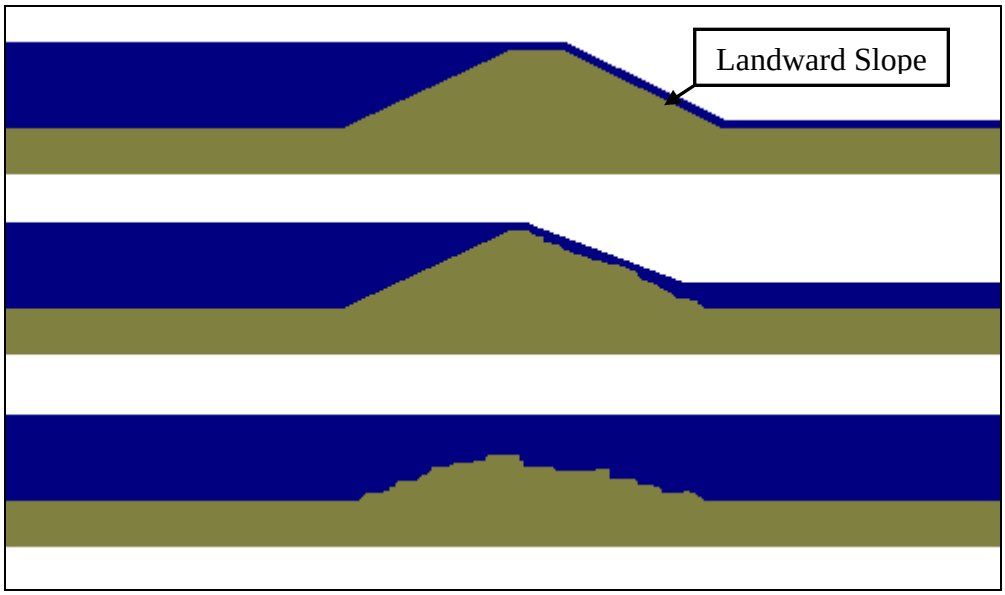

Figure 1.5. Erosion of a levee due to surge overflow causing failure

1.6 Overview of Physical Model

A small-scale physical model of a typical levee cross section adjacent to the Mississippi River Gulf Outlet (MRGO) was previously constructed and installed in a 0.9-m-wide wave flume at the U.S. Army Engineer Research and Development Center (ERDC), Coastal and Hydraulics Laboratory (CHL) in Vicksburg, MS. Funding for original model construction was provided to CHL by the U. S. Army Engineer District, New Orleans. This model was activated and utilized for the studies described in this report.

The physical model featured fixed-bed bathymetry seaward of the levee, and the levee cross-section was fabricated out of high-density foam. Because of scaling effects, no attempt was made to construct the levee using erodible soil. Thus, aspects related to erodibility of the underlying soil were not simulated in these tests. In addition to the wave generation capacity, a recirculation system was installed to simulate steady surge overflow of the levee combined with wave propagation and overtopping. Thus, the physical model was capable of simulating steady storm surge overflow, wave overtopping when the surge level was lower than the levee crest elevation, and wave overtopping when the surge elevation exceeded the levee crest elevation (see Figure 1.4).

The objectives of the physical model portion of the study were: (1) quantify flow hydrodynamics associated with combined wave overtopping and surge overflow, (2) develop estimates of average and peak shear stresses acting on the landward-side levee slope during combined wave and surge overtopping associated with a broad range of combined wave and surge overtopping parameters, and (3) verify that the time series of irregular and unsteady instantaneous overtopping discharge is the same everywhere on the landward slope with only a time shift difference.

1.7 Overview of the Numerical Adaptive Hydraulics Model (AdH)

The Adaptive Hydraulics Numerical Model (AdH) is an unstructured finite element code developed by the U.S. Army Engineer Research and Development Center (ERDC). The 2-dimensional form of the AdH model was applied to a typical levee section in a numerical flume. Funding for the model development was provided by the *Department of Homeland Security* and sponsored by the *Southeast Region Research Initiative* (*SERRI*) at the Department of Energy's Oak Ridge National Laboratory. The numerical modeling tasks described in this report were conducted at Mississippi State University.

The numerical flume was a 12,600-node mesh with the first third of the flume domain containing the levee section and seaward side. The remainder of the flume was designed to prevent back water effects so that a steady-state flow over the levee cross section could be maintained. The model was run in fixed-bed mode because no attempt was made to evaluate levee erosion with the model. The numerical model simulated a series of steady-state surge-only events to estimate the shear stress on the landward side slope.

The objective of this work was twofold: (1) validation of numerical model with respect to physical modeling of surge overtopping, and (2) exploration of changes in landward-side levee face shear stresses due to levee berm effects and variations in slope roughness.

1.8 Study Tasks

The testing program conducted in the small-scale physical model, and the complementary numerical simulations using the Advanced Hydraulics model, were designed to provide necessary information relevant to the following study tasks.

a) Quantify the unsteady hydrodynamic flow parameters associated with combined wave and storm surge overtopping of the MRGO levees, and develop appropriate shear stress estimation techniques in terms of the incident wave and surge parameters.
b) Examine the mass continuity assumption that instantaneous overtopping discharge at one location is the same at other locations when a small time shift is applied.
c) Validate numerical model by reproducing physical model results for steady overflow.

1.9 Report Organization and Content

This report focuses on results and analyses obtained from the small-scale levee physical model and from the Advanced Hydraulics numerical model. The chapters of this report are organized in typical order beginning with a review of literature and ending with conclusions based on measured and computed final results.

Chapter 2 reviews numerical modeling literature and existing empirical methodologies for estimating hydrodynamic parameters associated with wave-only and surge-only levee overtopping. Chapter 3 overviews the principles of physical modeling, discusses known scale and laboratory effects, presents the design of the physical model, and

discusses the model experimental setup and target test condition. The chapter also reviews initial and final data processing steps used to analyze the measurements. Chapter 4 presents results from physical model tests, and analyzes flow hydrodynamics and shear stresses associated with combined storm surge overflow and wave overtopping. Engineering methods for estimating hydrodynamic parameters and shear stress are given based on the physical model measurements. Chapter 5 overviews the numerical model used to simulate steady overflow of a trapezoidal levee and compares results to physical model measurements. Finally, Chapter 6 presents the summary and conclusions from this study. References are included at the end of the main text, and additional numerical modeling results are presented in Appendix A.

CHAPTER 2 – LITERATURE REVIEW

This chapter discusses previous literature related to overtopping processes with a focus on theoretical formulations and empirical relationships developed from small-scale and large-scale physical model studies. Some literature related to numerical simulation of wave overtopping is included in this chapter, but the abundant literature pertaining to steady overflow is not reviewed in this report.

The purpose of this literature review is to examine methods of estimating overtopping discharge, flow thickness, velocity, and shear stress on the levee landward-side slope. Flow thickness in the context of overtopping is defined as the thickness of the flowing water perpendicular to the levee surface. On the horizontal levee crest, flow thickness is the same as water depth, but on slopes water depth and flow thickness are not the same.

2.1 Storm Surge Overflow

Surge overflow occurring at a levee can be well approximated as two-dimensional steady overflow of a broad-crested weir provided the levee crest is at a uniform elevation for a considerable distance along the crest, and the time variation of the surge elevation is relatively slow compared to wave overtopping. For the case of water overflowing a levee as illustrated in Figure 2.1, subcritical flow exists on the high-water side of the levee (left side in Figure 2.1), critical flow occurs somewhere on the levee crest, and the flow down the backside slope is supercritical unless the landward-side slope is very small. At the toe of the levee, or when the downward flowing water joins with the tailwater (i.e., ponding flood water), a hydraulic jump is formed as the flow returns to subcritical. Erosive turbulence occurs at the location of the hydraulic jump. For the flow situation depicted in Figure 2.1 discharge is determined by the upstream head, h_1. (Note that the upstream head is the same as negative freeboard, i.e., $h_1 = -R_c$.)

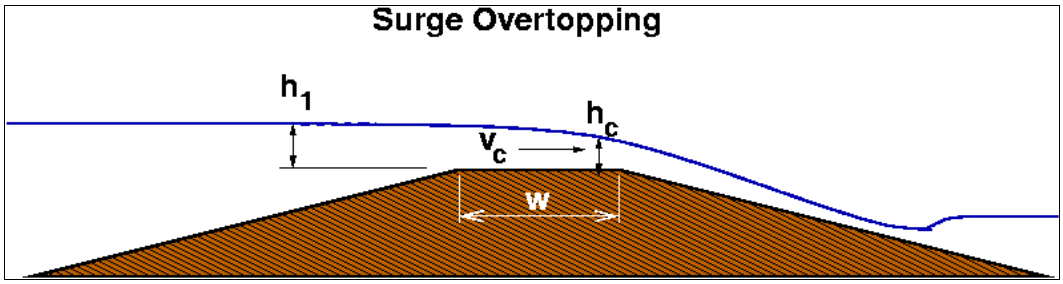

Figure 2.1. Surge overtopping design parameters.

As the tailwater continues to rise in the flooded area, the hydraulic jump moves up the slope. Eventually, the tailwater reaches an elevation above the levee crest and near that of the upstream flow, and discharge is controlled by upstream head and the tailwater. This flow condition has importance for roadway embankments, but it is not relevant for levees because tailwater at this elevation indicates complete inundation on the protected area (polder) behind the levee system.

2.1.1 Discharge and Critical Velocity

If the levee crest for the surge overtopping case shown in Figure 2.1 is sufficiently long to maintain a hydrostatic pressure distribution, critical flow (transition between subcritical and supercritical flow) will occur somewhere along the levee crest. Assuming minimal frictional energy losses along the crest, the discharge per unit width of levee is computed by the generally accepted equation for flow over a broad-crested weir given by open channel flow texts (e.g., Henderson 1966, Chaudhry 1993) as:

$$q = \left(\frac{2}{3}\right)^{3/2} \sqrt{g}\; h_1^{3/2} = 0.5443 \sqrt{g}\; h_1^{3/2} \tag{2.1}$$

where:

q = discharge per unit levee length
g = gravitational acceleration
h_1 = upstream head (difference between surge elevation and levee crest elevation)

Note that surge elevation can include effects of slowly varying tides. Equation 2.1 is dimensionally homogeneous, and it can be applied using any consistent set of units because the numerical coefficient is dimensionless.

Discharge per unit levee length can also be represented in terms of the flow Froude number (F_R) by the expression:

$$q = \sqrt{g h^3}\; F_R \tag{2.2}$$

where h is flow depth. Froude number is the dimensionless ratio of stream velocity to wave velocity and indicates if the flow regime has reached critical or supercritical conditions (Henderson 1966); see Table 2.1. Flow is critical if a small amplitude shallow water gravity wave has the same velocity as the flow. Subcritical flow occurs when a small amplitude gravity wave velocity is greater than flow velocity, and in subcritical flow water surface disturbances can move upstream. Supercritical flow is characterized by small depths and large velocities. Flow disturbances cannot move upstream in supercritical flow because the stream velocity is greater than the wave velocity.

Table 2.1. Froude Flow Regime Classification.

Froude Number	Flow Classification
$F_r < 1$	Subcritical
$F_r = 1$	Critical
$F_r > 1$	Supercritical

For critical flow, $F_R = 1$, and critical discharge is calculated using Eqn. 2.3

$$q_c = \sqrt{g\, h_c^3} \tag{2.3}$$

where q_c is the critical discharge and h_c is the critical depth (see Figure 2.1). For steady flow, mass continuity yields constant discharge at every location so Eqns. 2.1 and 2.3 are equivalent, and the critical depth is found by equating the two equations as

$$h_c = \frac{2}{3} h_1 \tag{2.4}$$

When the Froude number is unity, the critical velocity v_c is given by

$$v_c = \sqrt{g\, h_c} \tag{2.5}$$

or

$$v_c = \sqrt{\frac{2}{3} g\, h_1} \tag{2.6}$$

when Eqn. 2.4 is substituted for h_c.

2.1.2 Supercritical Flow on Landward-Side Levee Slope

Storm surge overflowing a levee transitions from critical to supercritical flow across the levee crest, and the water accelerates as it flows down the landward-side slope. If the slope were frictionless, water would continue to accelerate under the force of gravity. However, slope surface roughness resists the flow by forming a turbulent boundary layer, and a balanced steady flow condition is established. Flows of this type can then be analyzed using a flow resistance equation.

The mean velocity for a fully-developed resistance flow where the boundary layer is turbulent in the fully-rough range (independent of Reynolds number) is often given by the Chezy equation

$$v = C \sqrt{R\, S_f} \tag{2.7}$$

where:

v = velocity
C = Chezy coefficient (determined empirically)
R = hydraulic radius [$R = A/P$]
A = channel cross section area
P = channel wetted perimeter
S_f = slope of the total energy line (friction slope)

Chezy's equation may be used to calculate velocity assuming steady flow and small slopes (Chaudhry 1993). The typical landward levee slope, including the model levee examined in this report, is not considered small and the Chezy equations may not be applicable (Hughes 2008). The Chezy flow resistance equation is dimensionally non-homogeneous because the Chezy coefficient has dimensions of square root of length divided by time. Thus, care must be exercised when applying this equation.

The Chezy coefficient can be estimated through empirical relationships, field observations, or by Equation 2.8 (Hughes 2008, Chaudhry 1993, Henderson 1966).

$$C = \frac{R^{1/6}}{n} = \sqrt{\frac{8g}{f_D}} = \sqrt{\frac{2g}{f_F}} \tag{2.8}$$

where:

n = Manning's roughness coefficient
f_D = Darcy friction factor
f_F = Fanning friction factor

For very wide channels (e.g., flow over a levee having constant crest elevation), the hydraulic radius, R, is equal to the flowing water thickness h_o taken perpendicular to the slope. If the landward-side slope is linear with nearly similar roughness along its length, the flow becomes uniform with a terminal velocity at some down-slope location, and the water free surface is parallel to the levee slope. For this condition of steady, uniform flow the slope of the total energy line is the same as the levee slope so $S_f = S_o = \sin\theta$ where θ is the angle of the landward-side slope relative to the horizontal. Substituting $R = h_o$ and $S_f = \sin\theta$ into Eqn. 2.7, and representing the Chezy coefficient by Eqn. 2.8 yields Eqn. 2.9

$$v_o = \sqrt{\frac{8g}{f_D}}\ \sqrt{h_o \sin\theta} = \sqrt{\frac{2g}{f_F}}\ \sqrt{h_o \sin\theta} \tag{2.9}$$

where v_o represents the slope-parallel mean velocity for fully-developed, steady, uniform flow on the landward-side slope.

Perhaps the most popular flow resistance equation is the Manning formula. Substituting Eqn. 2.8 into Eqn. 2.7 gives the SI version of the Manning equation:

$$v = \frac{R^{2/3}\, S_f^{1/2}}{n} \tag{2.10}$$

with v in units of m/s and R in units of meters. Converting Eqn. 2.10 to the English system of units gives the usual form of the Manning equation

$$v = \frac{1.49\, R^{2/3}\, S_f^{1/2}}{n} \tag{2.11}$$

with v having units of ft/s and R given in units of feet.

For steady, uniform flow $R = h_o$, $S_f = \sin\theta$, and $h_o = q_o / v_o$. Making these substitutions into Eqns. 2.10 and 2.11, and solving for v_o gives the following equation for the mean terminal flow velocity in SI and English units.

$$v_o = \left[\frac{\sqrt{\sin\theta}}{n}\right]^{3/5} q_o^{2/5} \qquad \text{SI units} \tag{2.12}$$

$$v_o = \left[\frac{1.49\sqrt{\sin\theta}}{n}\right]^{3/5} q_o^{2/5} \qquad \text{English units} \tag{2.13}$$

The discharge q_o has units of m^3/s per m in the SI system and units of ft^3/s per ft in the English system. Manning's n is always given in metric units, so care must be taken when applying the Manning equation. Because of mass continuity, the discharge q_o equals the critical discharge q_c which can be estimated using Eqn. 2.1. Typical values for Manning's n are 0.025 for earth with some rocks and weeds up to 0.150 for very weedy, winding, and overgrown natural rivers.

2.2 Wave-Only Overtopping

Wave overtopping has similar physical characteristics to surge overtopping in that the landward slope velocity increases while flow thickness decreases down the slope with velocity eventually reaching terminal velocity. The main difference between wave overtopping and surge overtopping (see Figure 1.4) is the periodic nature of the unsteady wave overtopping. Although average wave overtopping discharge rates may be similar to that of steady overflow, the intermittent nature of wave overtopping produces large depth and velocity peaks which can be more destructive than surge overtopping. As each wave overtops, it has a forward velocity across the levee crest and down the landward-side slope that is larger than the steady velocity of comparable surge steady overflow. Thus, unprotected soil on the levee that is stable for low levels of surge overflow may erode if waves overtop. However, the wave overtopping flow condition is unsteady and peak velocities are sustained for only a brief time. Consequently, any erosion on the backside slope due to wave overtopping is intermittent, and the erosion rate will vary with overtopping intensity. This subsection presents available empirical equations for estimating average discharge and flow parameters associated with wave-only overtopping when the surge still water elevation is lower than the levee crest elevation.

2.2.1 Average Wave Overtopping Discharge

Multiple studies have been performed examining overtopping discharge of flood protection structures. The studies included tests of several shoreline protection systems including those with smooth, rough, steep, and/or mild slopes, long or short crests widths, and with or without a vertical wall. Overtopping discharges ranging from 0.1 to 100 liter/second per meter were included in the analyses.

The most widely used empirical equations for estimating the average wave-only overtopping discharge in terms of hydrodynamic parameters and levee geometry are given in TAW (2002) and reproduced with additional guidance in the European overtopping or EurOtop Manual (Pullen, et al. 2007). These equations modify the original equations proposed by van der Meer and Janssen (1995), and represent the average of all observations. Thus, the following equations are considered appropriate for probabilistic applications.

$$\frac{q}{\sqrt{g\,H_{m0}^3}} = 0.067 \cdot \frac{\xi_{m-1,0} \cdot \gamma_b}{\sqrt{\tan\alpha}} \cdot \exp\left(-4.75 \cdot \frac{R_c}{H_{m0}} \cdot \frac{1}{\xi_{m-1,0}} \cdot \frac{1}{\gamma_f \gamma_b \gamma_v \gamma_\beta} \right) \quad \text{for } \xi_{m\text{-}1,0} < 5 \qquad (2.14)$$

with a maximum of

$$\frac{q}{\sqrt{g\,H_{m0}^3}} = 0.2 \cdot \exp\left(-2.6 \cdot \frac{R_c}{H_{m0}} \cdot \frac{1}{\gamma_f\ \gamma_\beta} \right) \qquad (2.15)$$

In Eqn. 2.14 the Iribarren number, based on deepwater wave length and mean energy wave period, is defined as

$$\xi_{om-1,0} = \frac{\tan\alpha}{\sqrt{H_{m0} / L_{om-1,0}}} \qquad (2.16)$$

with

$$L_{om-1,0} = \frac{g}{2\pi} T_{m-1,0}^2 \qquad (2.17)$$

and the variables in Eqns. 2.14 - 2.17 are defined as:

q	=	wave overtopping discharge
H_{m0}	=	significant wave height
α	=	seaward-side slope angle
$\xi_{m-1,0}$	=	Iribarren number (also referred to as the *Surf Similarity Parameter*)
R_c	=	levee freeboard (positive for wave-only overtopping)
γ_b	=	berm influence factor
γ_f	=	roughness influence factor
γ_β	=	wave approach angle influence factor
γ_v	=	vertical wall on slope influence factor
$L_{m-1,0}$	=	mean energy wave length
$T_{m-1,0}$	=	mean energy wave period

In the EurOtop Manual (Pullen, et al. 2007) a slightly more conservative set of equations is recommended for deterministic design or safety assessment. Those equations increase the estimate of average wave overtopping discharge by one standard deviation. The deterministic equations are given below.

$$\frac{q}{\sqrt{g\,H_{m0}^3}} = 0.067 \cdot \frac{\xi_{m-1,0} \cdot \gamma_b}{\sqrt{\tan\alpha}} \cdot \exp\left(-4.3 \cdot \frac{R_c}{H_{m0}} \cdot \frac{1}{\xi_{m-1,0}} \cdot \frac{1}{\gamma_f \gamma_b \gamma_v \gamma_\beta} \right) \quad \text{for } \xi_{m\text{-}1,0} < 5 \qquad (2.18)$$

with a maximum of

$$\frac{q}{\sqrt{g\,H_{m0}^3}} = 0.2 \cdot \exp\left(-2.3 \cdot \frac{R_c}{H_{m0}} \cdot \frac{1}{\gamma_f\ \gamma_\beta} \right) \qquad (2.19)$$

Okayasu, et al. (2005) measured wave overtopping depth and velocity using smooth and stepped seawalls. Laser Doppler velocimeters (LDVs) measured overtopping velocity, and a catch basin was used to determine overtopping volume. Significant wave heights ($H_{1/3}$) and wave periods ($T_{1/3}$) were generated by an absorption-type wave generator (Okayasu, et al. 2005). Table 2.2 provides wave conditions of Okayasu, et al. (2005).

Table 2.2. Okayasu, et al. (2005) Wave Conditions

Case		$H_{1/3}$ (cm)	$T_{1/3}$ (s)	Case		$H_{1/3}$ (cm)	$T_{1/3}$ (s)	Case		$H_{1/3}$ (cm)	$T_{1/3}$ (s)
A	1	9.6	1.40	B	1	6.7	1.37	C	1	8.4	1.40
	2	9.8	1.59		2	8.4	1.40		2	8.4	1.61
	3	10.9	1.42		3	8.4	1.61		3	10.1	1.42
	4	11.4	1.59		4	10.1	1.42		4	10.1	1.61

Overtopping volume captured in the basin was comparable to estimates of wave overtopping discharge determined from depth and velocity. A three-dimension *Large Eddy Simulation* numerical model was developed and compared to physical model data. The numerical and physical wave overtopping depths and velocities were not in agreement, and wave overtopping volume in the numerical model was half the volume measured in the physical model. According to Okayasu et al. (2005) the discrepancy was possibly due to a bottom non-slip condition with velocity and wave reflection altered depth readings.

In recent years many researchers, (Causon, et al. 2000; Hu, et al. 2000; Hubbard and Dodd 2002; and Shiach, et al. 2004) have implemented numerical models to simulate wave overtopping. Work conducted by Reeve, et al. (2008) explored the effects of combined wave and surge overtopping discharge in a numerical flume by applying the 3-dimensional

Reynolds Averaged Navier-Stokes, RANS, equations with a finite difference scheme. The model used was a modified version of RIPPLE and a turbulence model that had been expanded to solve complex free surfaces (Lin and Xu 2006), since the model originally was developed in two dimensional form by Lin and Liu (1998). In the 3-dimensional form, Reeve, et al. (2008) found that the "majority of the numerical model results were slightly larger than the corresponding predictions from empirical equations" (Reeve, et al. 2008, pg 161). Reeve, et al. (2008) accounted for this discrepancy by the fact that flow acceleration might be underestimated with the use of the simple linear superposition (Reeve, et al. 2008). Further validation of the numerical model was done using experimental data results from Soliman (2003) and Soliman and Reeve (2004). Although the work included the simulation of several slopes, and surge and wave overtopping events, Reeve, et al. (2008) expressed the need for further experiments that would include determination of the velocities experienced on the structure.

Reeve, et al. (2008) simulated irregular wave overtopping of a seawall with conditions listed in Table 2.3 where R is dimensionless freeboard defined as freeboard divided by significant wave height (R_c/H_{m0}). About 200 waves were run for each simulation.

Table 2.3. Reeve, et al. (2008) Wave Overtopping Conditions.

Run	R_c (m)	R	Slope
1	0.900	0.39	1V:3H
2	1.125	0.49	1V:3H
3	1.350	0.59	1V:3H
4	1.575	0.68	1V:3H
5	1.800	0.78	1V:3H
6	2.250	0.98	1V:3H
7	0.5625	0.33	1V:4H
8	0.675	0.39	1V:4H
9	0.900	0.52	1V:4H
10	1.125	0.65	1V:4H
11	1.350	0.78	1V:4H
12	1.575	0.91	1V:4H
13	1.800	1.04	1V:4H

The significant wave height (H_s) for each simulation was 1.22 m with a mean wave period (T_m) of 3.8 s and a peak wave period (T_p) of 5.0 s. A numerical analysis of irregular wave overtopping at 1V:3H and 1V:4H sloped seawalls with positive freeboard between 0.1 and 0.3 meters produced Eqn. 2.20. The model results were larger than previous empirical studies performed by Van der Meer and Janssen (1995).

$$\frac{q}{\sqrt{g H_s^3}} \frac{\sqrt{\tan\alpha}}{\xi_p} = 0.09 \exp\left(-4.12 R\right) \qquad \text{for} \quad 0.3 < R < 1.0 \tag{2.20}$$

where ξ_p is the Iribarren number associated with the peak spectral wave period, T_p.

2.2.2 Wave Overtopping Velocity and Flow Thickness

Typically wave overtopping flow thickness decreases along the crest and down the landward slope similar to surge flow. Experiments were conducted in Europe at small and large scale with the aim of quantifying the wave overtopping flow parameters on the inner slope of dike and levees (Schüttrumpf, et al., 2002; van Gent, 2002; Schüttrumpf and van Gent, 2003; and Schüttrumpf and Oumeraci, 2005). The researchers studied the variation in wave overtopping parameters at typical seadikes. Physical processes included wave shoaling and breaking on the seaward slope, wave run-up and run-down on the seaward slope, and wave overtopping of the dike crest with unsteady supercritical flow down the landward-side slope of the smooth seadike. Independent laboratory experiments were conducted in The Netherlands (van Gent 2002) and in Germany (Schüttrumpf, et al. 2002). These two studies produced very similar estimation analysis techniques with only minor differences in the details. A joint paper (Schüttrumpf and van Gent 2003) reconciled the differences to the extent possible.

Van Gent's (2002) small-scale experiments had a 1V:100H foreshore slope with a 1V:4H slope on the seaward side of the dike. Two levee crest widths (0.2 and 1.1 m) were combined with two landward-side slopes (1V:2.5H and 1V:4H) to give four different dike geometries using a smooth dike surface. A fifth test series was conducted with a rough surface. Velocity and flow thickness were measured at the edges of the crest and at three locations spaced down the landward-side slope. Micro-impellers were used to measure velocity. Eighteen irregular wave tests were performed for the different dike geometries, ten with single-peaked spectra and 8 with double-peaked spectra. Incident wave conditions were determined by measuring the generated waves without the structure in place, and applying the Mansard and Funke (1980) frequency-domain method to remove reflection caused by the dissipating beach profile. Van Gent (2002) used the wave parameter $H_{1/3}$ in the analysis, but did not indicate how this time-domain parameter was determined from the frequency-domain value of H_{m0} found from the reflection analysis. Wave period was specified as mean period $T_{m-1.0}$, and it was estimated from the moments of the incident wave frequency spectra. The mean period was reported to better represent double-peaked spectra.

Schüttrumpf, et al.'s (2002) experiments included both small-scale and large-scale tests. The small-scale tests utilized three seaward-side slopes (1V:3H, 1V:4H, and 1V:6H), a crest width of 0.3 m, and five different landward-side slopes (1V:2H, 1V:3H, 1V:4H, 1V:5H, and 1V:6H). A total of 270 tests were run using regular waves and irregular waves conforming to the JONSWAP spectrum. Wave overtopping discharge was collected in a container and weighed using load cells. This provided the cumulative overtopping water volume necessary to calculate the average wave overtopping discharge. Flow thickness at

various locations on the dike surface was measured by resistance wave gauges. Data were sampled at a 40-Hz rate, and flow thickness measurements were confirmed using video recordings. Flow thickness measurements less than eight millimeters were discarded. Velocity measurements were recorded at a 20-Hz rate using micro propellers mounted on the dike surface. For the large-scale tests the seaward-side slope was 1V:6H, the crest width was 2 m, and the landward-side slope was 1V:3H. A total of 250 model tests were run using some regular waves, but mostly irregular waves. Flow depth and velocity were measured using wave gauges and micro-impellers.

Wave data from Schüttrumpf, et al.'s (2002) tests were analyzed in the frequency domain using the reflection method of Mansard and Funke (1980). The time-domain wave height parameter $H_{1/3}$ was used in their overtopping analysis with the conversion from the frequency domain wave height given as $H_{1/3} = 0.94\ H_{m0}$ (Schüttrumpf 2006, personal communication). This conversion may have been a typographical error because $H_{1/3}$ is expected to be greater than H_{m0} for shallow water waves. Also, the conversion is strictly only valid for these tests and not in general because it was determined for wave flume data with a constant water depth for all tests. The wave period was specified as the mean wave period, and it was determined from the calculated incident wave spectra by the simple relationship $T_m = 0.88\ T_p$ (Schüttrumpf 2006, personal communication).

Schüttrumpf and Oumeraci (2005) developed analytical expressions to represent the velocity and flow thickness at the edge of the crest on the seaward side, at the edge of the crest on the landward side, and down the landward-side slope as illustrated in Figure 2.2.

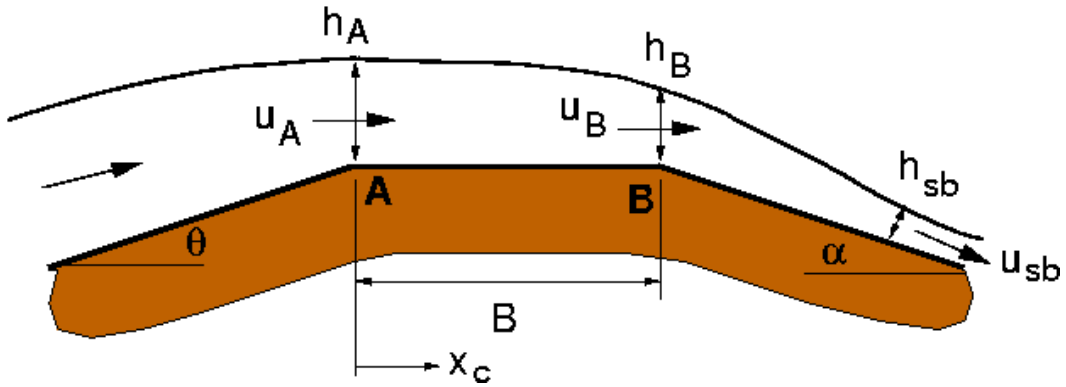

Figure 2.2. Wave overtopping definition sketch (after Schüttrumpf and Oumeraci 2005).

The key parameters necessary for estimating the flow velocities and depths are the levee freeboard, R_c, the runup elevation exceeded by 2% of the waves, $R_{u2\%}$, and the Fanning friction factor, f_F, that accounts for frictional energy loss as the overtopping wave travels across the crest and down the landward-side slope.

2.2.2.1 Flow Parameters at the Seaward-Side Levee Crest Edge

At the seaward-side edge of the levee crest (denoted by the subscript letter A in Figure 2.2) the flow parameters are given by the following equations

$$\frac{h_{A2\%}}{H_s} = C_{Ah2\%}\left[\frac{R_{u2\%} - R_c}{H_s}\right] \tag{2.21}$$

and

$$\frac{u_{A2\%}}{\sqrt{gH_s}} = C_{Au2\%}\sqrt{\frac{R_{u2\%} - R_c}{H_s}} \tag{2.22}$$

where

$h_{A2\%}$	=	peak flow thickness exceeded by 2% of the waves
$u_{A2\%}$	=	flow depth-averaged peak velocity exceeded by 2% of the waves
H_s	=	significant wave height [=H_{m0}]
$R_{u2\%}$	=	runup elevation exceeded by 2% of the waves
R_c	=	crest freeboard [= crest elevation minus still water elevation]
g	=	acceleration of gravity
$C_{Ah2\%}$	=	empirical flow thickness coefficient determined from test data
$C_{Au2\%}$	=	empirical velocity coefficient determined from test data

The values of $h_{A2\%}$ and $u_{A2\%}$ were determined from the peaks of the overtopping wave time series, and these parameters represent the levels exceeded by only 2% of the total waves during the tests. For example, if a test had 1000 waves, perhaps only 200 waves overtopped the crest. The 2% exceedance level would be the level exceeded by 20 of the 1000 waves (0.02 x 1000), but this is 10% of the overtopping waves. Schüttrumpf, et al. (2002) also provided coefficients for the average overtopping parameters $h_{A50\%}$ and $u_{A50\%}$. All of the equations pertain to the maximum velocity at the leading front of the overtopping wave. Flow velocities and thicknesses of a single wave decrease after passage of the wave front.

Note in Eqns. 2.21 and 2.22 that significant wave height H_s in the denominator cancels on both sides of the equations. Thus, the flow thickness is directly proportional to the difference between the 2%-runup and levee freeboard, and the depth-averaged flow velocity is proportional to the square root of this difference. Wave parameters enter into the estimation of flow depth and velocity at the seaward-side crest edge through the estimation of the 2%-runup parameter, $R_{u2\%}$. As noted by van Gent (2002), the calculated $R_{u2\%}$ is a fictitious value in cases where runup exceeds the structure freeboard. It is the level that would be exceeded by 2% of the waves if the seaward-side slope was continued upwards indefinitely. The values of the empirical coefficients determined for the two studies are given in Table 2.4. The superscripts behind each number refer to the references given in the list below Table 2.4.

Table 2.4. Empirical Coefficients for Seaward-Side Crest Edge Flow Parameters.

Coefficient	Schüttrumpf	van Gent
$C_{Ah2\%}$	0.33 [2,3] and 0.22 [4]	0.15 [1,3]
$C_{Au2\%}$	1.55 [2] and 1.37 [3]	1.30 [1,3]
$C_{Ah50\%}$	0.17 [2,4]	––
$C_{Au50\%}$	0.94 [2, 4]	––

[1] van Gent (2002)
[2] Schüttrumpf, et al. (2002)
[3] Schüttrumpf and van Gent (2003)
[4] Schüttrumpf and Oumeraci (2005)

The coefficient $C_{Ah2\%}$ is a constant that is equal to a slope-dependent constant, C_2, divided by tan θ, where θ is the seaward-side structure slope. Values of C_2 given in the various papers are used in an equation slightly different than Eqn. 2.21. The value for $C_{Ah2\%}$ given by Schüttrumpf was revised from 0.33 to 0.22 in the most recent paper (Schüttrumpf and Oumeraci 2005), and this probably represents a better value as shown by the data plot given in their paper and by the fact it is closer to the value obtained by van Gent. The value of $C_{Au2\%}$ = 1.55 is derived from a table in Schüttrumpf, et al. (2002) that associated this coefficient with large-scale tests. A coefficient associated with the 10%-exceedance level can also be derived from the same table as $C_{Au10\%}$ = 1.37 for large-scale tests. In Schüttrumpf and van Gent (2003) the value of $C_{Au2\%}$ = 1.37 was reported, and this is thought to be a typographical error. The correct value should have been $C_{Au2\%}$ = 1.55.

Schüttrumpf and van Gent (2003) attribute differences in empirical coefficients to different dike geometries and instruments, but noted the differences are not too great. Van der Meer, et al. (2006) suggested an error in measurement or analysis might have caused the factor-of-two difference seen for the coefficient $C_{Au2\%}$, but the revised value of 0.22 brings the results closer. A more probable cause for variation might be in the method each investigator used to estimate the value of 2%-runup, $R_{u2\%}$. Van Gent (2002) estimated $R_{u2\%}$ using a formula developed earlier (van Gent 2001) that uses $H_{1/3}$ and $T_{m-0.1}$ as the wave parameters. Schüttrumpf estimated $R_{u2\%}$ using the equations of de Waal and van der Meer (1992) with wave height $H_{1/3}$ and wave period T_m instead of spectral peak period T_p. Both formulas give reasonable estimates that fall within the scatter of the 2%-runup data, so whichever formula is selected for calculating $R_{u2\%}$ the estimates for overtopping flow parameters should be reasonable.

Until further clarification becomes available, it is recommended that values of $C_{Ah2\%}$ = 0.22 and $C_{Ah2\%}$ = 1.55 be used to estimate the overtopping flow parameters associated with the flow depth and velocity exceeded by 2% of the incoming waves.

2.2.2.2 Flow Parameters at the Landward-Side Levee Crest Edge

Overtopping waves flowing across the dike or levee crest decrease in height, and the velocity decreases as a function of the surface friction factor, f_F. The flow depth (or thickness) can be estimated at any location on the crest with the equation

$$h_{B2\%} = h_{A2\%} \exp\left(- C_3 \frac{x_C}{B} \right) \tag{2.23}$$

where B is the crest width, x_c is distance along the crest from the seaward-side edge, and C_3 is an empirical coefficient. The flow thickness at the landward-side crest edge (denoted by the subscript letter B in Figure 2.2) is given when $x_c = B$. Different values of the coefficient were given in the various publications, i.e., based on the 2%-exceedence levels $C_3 = 0.89$ for Texel, Marsen, and Arsole (TMA) spectra and $C_3 = 1.11$ for natural spectra (Schüttrumpf, et al. 2002); $C_3 = 0.40$ and 0.89 (Schüttrumpf and van Gent 2003); and $C_3 = 0.75$ for irregular and regular waves (Schüttrumpf and Oumeraci 2005). The factor-of-two difference between van Gent and Schüttrumpf was attributed to the difference in estimating wave runup.

For levee calculations it is recommended that a value of $C_3 = 0.75$ be used on the assumption that earlier values had been corrected by publication of the 2005 journal article. The 2%-runup elevation should be estimated using the runup formulas of de Waal and van der Meer (1992). Note that Eqn. 2.23 is applicable for estimating $h_{B50\%}$ if the flow depth $h_{A50\%}$ is used instead of $h_{A2\%}$. In fact, Schüttrumpf and Oumeraci (2005) presented only the 50% exceedance values.

Flow velocity along the dike crest exceeded by 2% of the waves is given by a similar equation

$$u_{B2\%} = u_{A2\%} \exp\left(- \frac{x_C \, f_F}{2 \, h_{B2\%}} \right) \tag{2.24}$$

where f_F is the Fanning friction factor appropriate for the levee crest surface and $h_{B2\%}$ is the flow thickness at that location on the crest obtained via Eqn. 2.23. At the landward-side crest edge, evaluate Eqn. 2.23 with $x_c = B$. Van Gent (2002) had a different expression for $u_{B2\%}$; but in Schüttrumpf and van Gent (2003) both authors agreed on Eqn. 2.24. A theoretical derivation for Eqn. 2.24 is given in Schüttrumpf and Oumeraci (2005).

2.2.2.3 Estimation of Friction Factor

The Fanning friction factor has a significant influence on flow velocity across the crest and down the landward-side slope. The small-scale experiments of Schüttrumpf, et al. (2002) had a structure surface constructed of wood fiberboard, and the friction factor was determined experimentally to be $f_F = 0.0058$ (Schüttrumpf and Oumeraci 2005). The structure in the companion large-scale experiments was constructed with a bare, compacted clay surface; and experimental results gave the friction factor as $f_F = 0.01$ (Schüttrumpf, et

al. 2002). Schüttrumpf and Oumeraci (2005) also list the following representative values for friction factor on the landward-side slope: f_F = 0.02 (smooth slopes), and from Cornett and Mansard (1994) f_F = 0.1 to 0.6 (rough revetments and rubble-mound slopes). Grass-covered slopes would probably have a friction coefficient above f_F = 0.01.

Determination of an appropriate value of friction factor for various slope surfaces may be difficult because of the lack of published values. As a first approximation an estimate can be made if a representative value of Manning's n is known for a particular surface slope or armoring product. Manning's n is related to the Chezy coefficient, C_z, by the expression shown as Eqn. 2.8. Solving Eqn. 2.8 for f_F, and recognizing for wide channels the hydraulic radius, R, is essentially the same as the depth, h, yields Eqn. 2.25 (in metric units) for f_F in terms of Manning's coefficient and flow depth h in meters.

$$f_F = \frac{2\,g\,n^2}{h^{1/3}} \tag{2.25}$$

The validity of Eqn. 2.25 has not been proven, and it is based on the assumption that friction factors and Manning's n associated with steady supercritical overflow that has reached equilibrium (e.g., Chezy or Manning equation) will be the same for unsteady, rapidly varying flows due to wave overtopping. Therefore, caution must be exercised when applying Eqn. 2.25.

2.2.2.4 Flow Parameters on the Landward-Side Levee Slope

Both groups of European investigators derived theoretical expressions for the wave front depth-averaged, slope-parallel flow velocity down the landward-side slope based on simplification of the momentum equation. Schüttrumpf and Oumeraci (2005) presented an iterative solution, whereas van Gent (2002) derived an explicit formula. A comparison between the two solutions revealed only small differences in the result, and both formulations approached the same equation in the limit as distance down the slope becomes large (Schüttrumpf and van Gent 2003). For ease of application, van Gent's formula is preferred, and it was given as

$$u_{sb2\%} = \frac{K_2}{K_3} + K_4 \exp\left(-3\,K_2 \cdot K_3^2 \cdot s_b\right) \tag{2.26}$$

with

$$K_2 = \left(g \sin\alpha\right)^{1/3} \tag{2.27}$$

$$K_3 = \left[\frac{f_F}{2}\,\frac{1}{h_{B2\%} \cdot u_{B2\%}}\right]^{1/3} \tag{2.28}$$

$$K_4 = u_{B2\%} - \frac{K_2}{K_3} \tag{2.29}$$

where α is the angle of the landward-side slope, s_b is the distance down the slope from the crest edge, and $h_{B2\%}$ and $u_{B2\%}$ are the flow thickness and flow velocity, respectively, at the landward-side crest edge. For long distances down the slope, the exponential term in Eqn. 2.25 vanishes, and the velocity equation reduces to Eqn. 2.30.

$$u_{sb2\%} = \frac{K_2}{K_3} = \left[\frac{2\, g \cdot h_{B2\%} \cdot u_{B2\%} \cdot \sin \alpha}{f_F} \right]^{1/3} \tag{2.30}$$

Flow thickness perpendicular to the slope at any point down the landward-side slope is found from the continuity equation as

$$h_{sb2\%} = \left[\frac{h_{B2\%} \cdot u_{B2\%}}{u_{sb2\%}} \right] \tag{2.31}$$

Equations 2.23 through 2.31 can be used to estimate the wave overtopping peak velocity and associated flow depth that is exceeded by only 2% of the incoming waves.

2.3 Wave Overtopping at Zero Freeboard

Schüttrumpf (2001) and Schüttrumpf, et al. (2001) gave equations for dimensionless average wave overtopping discharge based on laboratory experiments with zero freeboard. The equations shown below (Eqns. 2.32 and 2.33) from the Overtopping Manual (Pullen, et al. 2007) are a slightly revised version of Schüttrumpf's equations.

$$\frac{q_w}{\sqrt{g\, H_{m0}^3}} = 0.0537 \cdot \xi_{m-1,0} \qquad \text{for} \quad \xi_{\text{m-1,0}} < 2 \quad \text{(breaking waves)} \tag{2.32}$$

$$\frac{q_w}{\sqrt{g\, H_{m0}^3}} = \left(0.136 - \frac{0.226}{\xi_{m-1,0}^3} \right) \qquad \text{for} \quad \xi_{\text{m-1,0}} \geq 2 \quad \text{(nonbreaking waves)} \tag{2.33}$$

The Iribarren number $\xi_{\text{m-1,0}}$ in Eqns. 2.32 and 2.33 is the same as given by Eqn. 2.16.

Reeve, et al. (2008) also applied the RANS model described in the wave-only overtopping section to the case of zero freeboard. They used a surf similarity parameter (ξ_p) of 1.715, and they applied the model for the conditions listed in Table 2.5.

Table 2.5. Reeve, et al. (2008) Zero Freeboard Irregular Wave Characteristics.

Run	H_s	T_m	T_p
	(m)	(s)	(s)
1	0.56	3.5	5.06
2	0.81	4.1	5.73
3	0.82	3.6	5.00
4	0.83	3.6	5.00
5	0.83	3.7	5.00
6	1.22	3.8	5.00
7	1.23	3.9	5.00
8	1.24	3.9	5.00
9	1.39	4.0	5.00
10	1.48	4.6	6.02

The results of the numerical model were compared to Schüttrumpf, et al.'s (2001) results; and the agreement was favorable, thus validating the Reeve, et al. (2008) numerical model for wave overtopping with zero freeboard.

2.4 Combined Wave Overtopping and Storm Surge Overflow

Combined wave overtopping and storm surge overflow produces a nearly continuous unsteady discharge over the levee with flow thickness and velocity peaks related to the irregular incident waves. Pullen, et al. (2007) proposed calculating combined overtopping discharge by superposition of surge discharge (Eqn. 2.1) and wave discharge at zero freeboard (Eqn. 2.32 or 2.33). For example, the combined discharge for breaking waves with $\xi_{m-1,0} < 2$ would be the following:

$$q_{combined} = q_{surge} + q_{wave} = 0.6\sqrt{g}\left|-R_c\right|^{3/2} + 0.0537 \cdot \xi_{m-1,0}\sqrt{g\,H_{m0}^3} \tag{2.34}$$

The freeboard, R_c, will be negative for this case, and it must be entered as a negative number to avoid producing a complex number for the result. In the EurOtop Manual (Pullen, et al. 2007) a coefficient of 0.6 is used in Eqn. 2.1 rather than 0.5443. Equation 2.34 was acknowledged as being tentative until such time that supporting experimental data could be collected.

Reeve et al. (2008) performed a numerical analysis of combined overtopping on 1V:3H, 1V:4H, and 1V:6H sloped seawalls using conditions shown in Table 2.6. The wave characteristics in Table 2.6 provided surf similarity parameters less than two. Reeve, et al. gave the following equations for dimensionless average discharge corresponding to

combined wave and surge overtopping discharge as a function of wave height, surf similarity, freeboard, levee slope, and gravity. The equations are for small values of relative freeboard.

$$\frac{q_{ws}}{\sqrt{g\,H_{m0}^3}} = 0.051 \cdot \frac{\xi_p}{\sqrt{\tan\alpha}} \cdot \exp\left(-1.98 \cdot \frac{R_c}{H_{m0}\,\xi_p}\right) \qquad \text{for} \quad \xi_p < 2 \tag{2.35}$$

$$\frac{q_{ws}}{\sqrt{g\,H_{m0}^3}} = 0.233 \cdot \exp\left(-1.29 \cdot \frac{R_c}{H_{m0}}\right) \qquad \text{for} \quad \xi_p \geq 2 \tag{2.36}$$

where ξ_p is the Iribarren number based on peak spectral wave period, T_p, and the value of freeboard, R_c, should be entered as a negative number.

Hughes and Nadal (2009) developed a discharge relationship for combined wave overtopping and surge overflow under a variety of flow conditions using a small-scale levee physical model. The test facility and levee model was the same physical model set-up used for the study described in this report, and complete details of the physical model are presented in Chapter 3. Testing took place in a 45-m flume with the levee crest roughly 32 m from the wave board. Overtopping water was re-circulated to an input manifold seaward of the levee allowing for long duration testing that includes overflow. Flow thickness was recorded by pressure cells inlaid on the model levee crest and landward-side slope, and velocity parallel to the levee crest was measured with a laser Doppler velocimeter (LDV) at a location near the landward-side edge of the levee crest directly above a pressure gauge. Data were collected at 50-Hz during 27 runs, each lasting five minutes. Each run was a variation of the following prototype conditions which can be scaled to model size using a prototype-to-model length scale of 25-to-1.

- Freeboard, R_c: -0.3, -0.9, and -1.5 m
- Significant Wave Height, H_{m0}: 0.9, 1.8, and 2.7 m
- Peak Wave Period, T_p: 6, 10, and 14 s

Hughes and Nadal (2009) measured flow depth and velocity at on the levee crest at the co-located pressure gauge and LDV, and they calculated discharge as the product of depth and velocity. Figure 2.3 plots the dimensionless combined wave and surge average overtopping discharge versus the relative (negative) freeboard for all 27 experiments. The indicated surge levels in the plot legend are the average of the negative freeboards determined for all nine experiments at each nominal surge level. The measurements gave a trend with increasing relative freeboard, and the solid line is a best-fit empirical equation given by the formula

$$\frac{q_{ws}}{\sqrt{g\,H_{m0}^3}} = 0.034 + 0.53\left(\frac{-R_c}{H_{m0}}\right)^{1.58} \qquad ; \quad R_c < 0 \tag{2.37}$$

Table 2.6. Reeve, et al. (2008) Combined Overtopping Wave Characteristics.

Run	H_s	T_m	T_p	R_c	R	Slope
	(m)	(s)	(s)	(m)		
1	1.22	3.8	5.00	−0.061	−0.027	1V:3H
2	1.22	3.8	5.00	−0.122	−0.053	1V:3H
3	1.22	3.8	5.00	−0.244	−0.106	1V:3H
4	1.39	4.0	5.00	−0.278	−0.113	1V:3H
5	1.22	3.8	5.00	−0.366	−0.159	1V:3H
6	1.22	3.8	5.00	−0.488	−0.212	1V:3H
7	1.39	4.0	5.00	−0.556	−0.226	1V:3H
8	1.22	3.8	5.00	−0.610	−0.265	1V:3H
9	1.24	3.9	5.00	−0.620	−0.267	1V:3H
10	1.22	3.8	5.00	−0.732	−0.318	1V:3H
11	1.22	3.8	5.00	−0.854	−0.371	1V:3H
12	1.24	3.9	5.00	−0.868	−0.374	1V:3H
13	1.22	3.8	5.00	−0.976	−0.424	1V:3H
14	1.22	3.8	5.00	−1.098	−0.477	1V:3H
15	1.22	3.8	5.00	−1.220	−0.530	1V:3H
16	1.22	3.8	5.00	−0.061	−0.035	1V:4H
17	1.22	3.8	5.00	−0.122	−0.071	1V:4H
18	1.48	4.6	6.02	−0.296	−0.129	1V:4H
19	1.22	3.8	5.00	−0.244	−0.141	1V:4H
20	0.83	3.7	5.00	−0.249	−0.175	1V:4H
21	1.22	3.8	5.00	−0.366	−0.212	1V:4H
22	1.22	3.8	5.00	−0.488	−0.283	1V:4H
23	1.22	3.8	5.00	−0.610	−0.353	1V:4H
24	1.48	4.6	6.02	−0.888	−0.388	1V:4H
25	1.22	3.8	5.00	−0.732	−0.424	1V:4H
26	1.22	3.8	5.00	−0.854	−0.495	1V:4H
27	0.83	3.7	5.00	−0.747	−0.525	1V:4H
28	1.22	3.8	5.00	−0.976	−0.566	1V:4H
29	1.22	3.8	5.00	−1.098	−0.636	1V:4H
30	0.56	3.5	5.06	−0.056	−0.071	1V:6H
31	1.22	3.8	5.00	−0.061	−0.053	1V:6H
32	1.22	3.8	5.00	−0.122	−0.106	1V:6H
33	1.22	3.8	5.00	−0.244	−0.212	1V:6H
34	0.80	4.7	7.20	−0.320	−0.239	1V:6H
35	1.22	3.8	5.00	−0.366	−0.318	1V:6H
36	1.22	3.8	5.00	−0.488	−0.424	1V:6H
37	0.56	3.5	5.06	−0.560	−0.710	1V:6H
38	1.22	3.8	5.00	−0.610	−0.530	1V:6H
39	0.80	4.7	7.20	−0.640	−0.477	1V:6H
40	1.22	3.8	5.00	−0.732	−0.636	1V:6H
41	1.22	3.8	5.00	−0.854	−0.742	1V:6H

(Note that R_c must be entered as a negative number so the ratio in brackets will be positive.) For zero freeboard (R_c = 0), Eqn. 2.37 yields a constant dimensionless average wave overtopping rate of 0.034.

Hughes and Nadal (2009) compared their predictions for combined wave and surge average overtopping discharge with those made using the equations of Schüttrumpf (given in Pullen, et al. 2007) and the equations of Reeve, et al. (2008). Figure 2.4 plots the comparison. The solid line is Eqn. 2.37, and it is essentially the measured data for combined wave and surge average discharge. Calculations using the other two methods overestimated the measurements with the equations of Reeve, et al. showing the greatest difference. Schüttrumpf's equations were not intended for the case of negative freeboard, and the linear addition of steady surge overflow was only suggested as an interim methodology. Nevertheless, the over-prediction using Schüttrumpf's equations is not too great, and it errors on the conservative side.

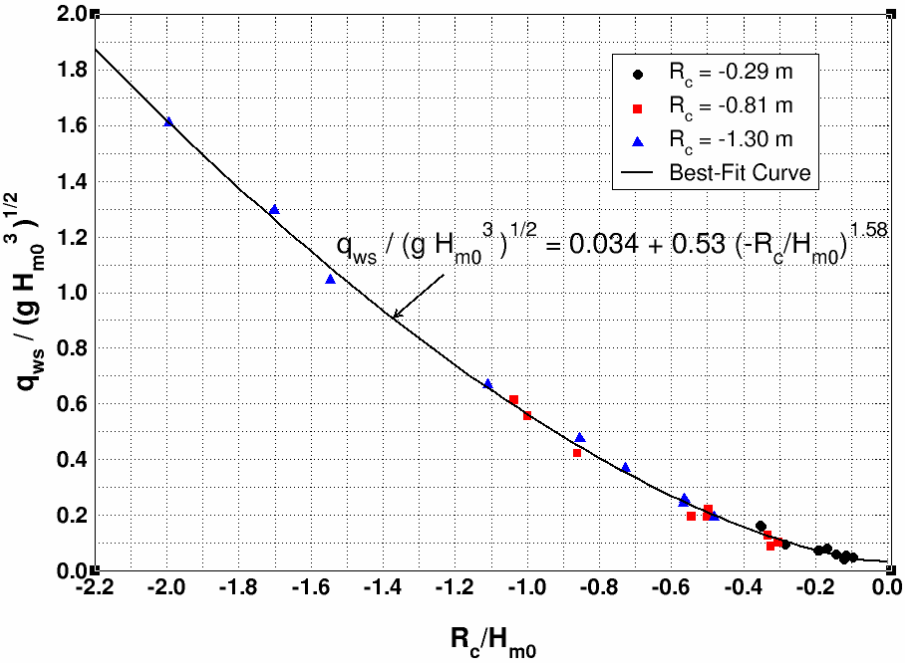

Figure 2.3. Dimensionless combined wave/surge average discharge versus relative freeboard.

Hughes and Nadal (2009) also used the experimental measurements to develop empirical equations to estimate average flow thickness and velocity on the landward slope as a function of combined average overtopping discharge, q_{ws}, and the landward-side slope angle, θ. The mean flow thickness, h_m, was given as

$$h_m = 0.4 \left[\frac{1}{g \sin\theta} \right]^{1/3} \left(q_{ws} \right)^{2/3} \tag{2.38}$$

and the mean flow velocity was given by the expression shown as Eqn. 2.39.

$$v_m = 2.5\left(q_{ws} \cdot g \cdot \sin\theta\right)^{1/3} \tag{2.39}$$

These equations are only applicable to landward slopes of 1V:3H with a small friction factor.

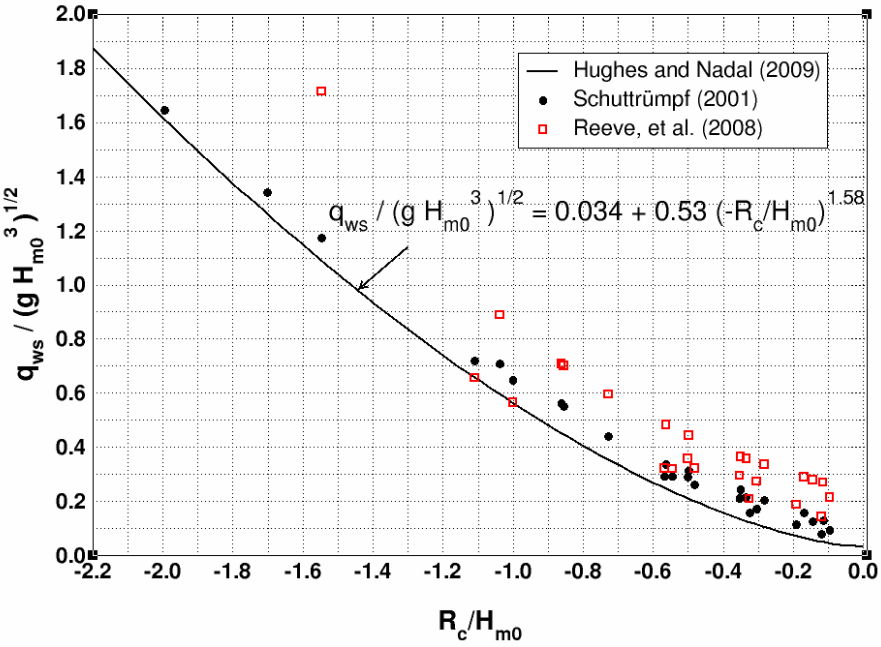

Figure 2.4. Overtopping discharge estimates by Schüttrumpf (2001) and Reeve, et al. (2008).

2.5 Overtopping Shear Stresses

For analysis of one-dimensional, unsteady flows, the unknown variables are flow thickness and velocity as functions of both spatial distance and time. The governing equations required for the solution of these unknown variables are the set of two partial differential equations known as *dynamic wave*, or *Saint-Venant*, equations (Sturm, 2001). Considering only the one-dimensional case of a very wide channel (i.e., long-crested levee) with the major axis aligned with the levee slope, the momentum equation applicable to steep slopes is given by

$$\frac{\partial v}{\partial t} + v\frac{\partial v}{\partial s} + g\frac{\partial h}{\partial s} + g\,S_f - g\sin\theta = 0 \tag{2.40}$$

where h is flow thickness perpendicular to the slope, θ is angle of levee slope to horizontal, v is flow velocity parallel to the slope, g is acceleration of gravity, s is the down-slope coordinate, t is time, and S_f is friction slope (net change in energy between two locations on the slope). The first term in Eqn. 2.40 is the temporal acceleration, the second term is the convective acceleration, the third term represents the change of pressure along the slope, the fourth term comes from the slope resistance friction, and the fifth term is due to the weight of water on the slope. Equation 2.40 can be rearranged to the form

$$\tau_0 = \gamma_w \, h \left[\sin\theta - \frac{\partial h}{\partial s} - \frac{\partial}{\partial s}\left(\frac{v^2}{2g} \right) - \frac{1}{g}\frac{\partial v}{\partial t} \right] \tag{2.41}$$

with the bottom shear stress defined as

$$\tau_0 = \gamma_w \, h \, S_f \tag{2.42}$$

where τ_0 is shear stress and γ_w is the specific weight of water. Thus, it is seen that the friction slope (the terms in the square brackets in Eqn. 2.41) is the sine of the bed slope minus the spatial change in depth and the spatial and temporal change in velocity.

The forms of the momentum equation given by Eqns. 2.40 and 2.41 are valid for unsteady, non-uniform one-dimensional flows, and they should be suitable for analyzing unsteady flows due to wave overtopping or combined wave and surge overtopping. However, the equations are intended for mild bed slopes. Typical levee landward-side slopes are considered steep because sin θ is greater than 0.01 (Henderson 1966). Because of the steep landward-side slopes, shear stresses estimated using Eqn. 2.41 may not correctly account for spatial and temporal changes in depth and velocity (Hughes and Nadal 2010).

Estimation of shear stress on the landward-side levee slope due to unsteady, non-uniform overtopping flow requires synoptic time series of slope-perpendicular flow depth and slope-parallel flow velocity at two down-slope locations to evaluate a discrete version of Eqn. 2.41. Nadal and Hughes (2009) and Hughes and Nadal (2010) estimated overtopping shear stresses for combined wave overtopping and surge overflow based on measurements reported in Hughes and Nadal (2009). They had synoptic measurements of flow thickness at two locations on the levee slope, but they only had velocity measurements at one of the locations. The velocity time series at the second location was synthesized based on the hypothesis that the time series of instantaneous discharge was the same at both locations with the only difference being a short time lag. They shifted the discharge time series from the first location to the second location, and then calculated the corresponding velocity time series at the second location as the discharge divided by the flow thickness, i.e., $v(t) = q_{ws}(t) / h(t)$. Additional details of this procedure are given in Nadal and Hughes (2009). The hypothesis that the discharge time series is conserved along the levee landward-side slope was proven during the present research as reported in Chapter 4 and in a journal publication (Hughes and Shaw 2011).

Hughes and Nadal calculated the shear stress time series using Eqn. 2.41 for each of the 27 experiments, and they presented an empirical relationship between the hydrodynamic parameters and the corresponding mean shear stresses estimated from the synthesized shear stress time series. The best best-fit of the data was a simple expression (Eqn. 2.43) relating the mean shear stress to the specific weight of (fresh) water, γ_w, and the root-mean-square of the flow thickness perpendicular to the levee slope, h_{rms}, i.e.,

$$\tau_{0,mean} = 0.235 \, \gamma_w \, h_{rms} \tag{2.43}$$

Figure 2.5 shows a plot of the mean shear stress correlation with Eqn. 2.43 represented by the solid line.

Estimation of mean shear stress using Eqn. 2.43 requires an expression for the root-mean-squared flow thickness, h_{rms}, in terms of the forcing hydrodynamic parameters. Hughes and Nadal (2010) gave the following expression

$$\frac{h_{rms}}{h_m} = 1 + 0.0077 \left(\frac{g H_{m0} T_p}{q_{ws}} \right)^{2/3} \tag{2.44}$$

where h_{m} is the mean flow thickness (see Eqn. 2.38), H_{m0} is the incident energy-based significant wave height, T_p is the spectrum peak wave period, and q_{ws} is average combined wave and surge overtopping discharge (see Eqn. 2.37). It is important to note that Eqn. 2.43 applies only to smooth slopes having similar frictional resistance as the levee model used in the tests, and the equation may only apply for the same 1V:3H landward-side slope. However, slope is included in the parameter h_{rms} through the mean depth, h_{m}.

The mean shear stress values estimated by Eqn. 2.43 provide an overall average that occurs during a combined wave and surge overtopping event. However, in the time series of instantaneous shear stress acting on the landward-side slope, the peak stresses associated with the overtopping wave crests can be several times the magnitude of the mean shear stress. The peak shear stress acts for a short duration as the wave passes down the slope, but the peak shear stress may well be the defining parameter with respect to stability of armoring alternatives or for determining rates of soil erosion.

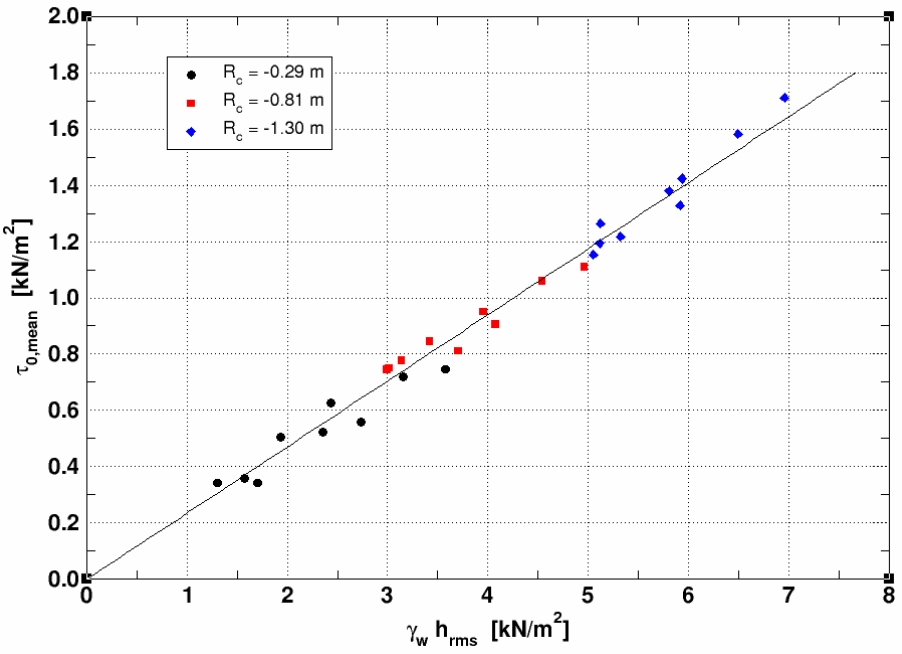

Figure 2.5. Mean shear stress as a function of h_{rms}.

Nadal and Hughes (2009) analyzed the calculated time series of instantaneous shear stress in the time domain using standard up-crossing analysis. The maximum shear stress values for each identified wave were rank-ordered, and representative values were determined for the average of the highest 1/3, highest 1/10, and highest 1/100 of the peak shear stresses. These values were denoted as $\tau_{p,1/3}$, $\tau_{p,1/10}$, and $\tau_{p,1/100}$, respectively. Good correlations were found between the representative peak shear stresses and the product of specific weight of water, γ_w, and a representative measure of flow depth given by the root-mean-square overtopping wave height on the landward-side levee slope, H_{rms}.

$$\tau_{p,1/3} = 0.53\,\gamma_w H_{rms} \tag{2.45}$$

$$\tau_{p,1/10} = 0.69\,\gamma_w H_{rms} \tag{2.46}$$

$$\tau_{p,1/100} = 0.93\,\gamma_w H_{rms} \tag{2.47}$$

Application of Eqns. 2.45 through 2.47 requires an estimate of H_{rms} perpendicular to the landward-side slope. Hughes (2008) provided the following empirical equation for estimating H_{rms} as a function of freeboard (R_c), incident significant wave height (H_{m0}), and mean flow thickness (h_m).

$$\frac{H_{rms}}{h_m} = 3.43 \cdot \exp\left(\frac{R_c}{H_{m0}}\right) \tag{2.48}$$

Freeboard must be entered as a negative number for the case of combined wave and surge overtopping, and the appropriate value for h_m is determined using Equation 2.38. Based on the relatively good fit of the data, Nadal and Hughes (2009) concluded that Eqns. 2.45 – 2.47 provide a reasonable estimate for the more extreme shear stresses that can occur on levee slopes having relatively smooth surfaces.

Briaud, et al. (2008) examined soil erodibility caused by steady overflow during Hurricane Katrina. This study focused on soil type and construction methods and the relationship between flow velocity and erosion. A Reynolds-averaged Navier-Stokes (CHEN3D) numerical model was used to estimate steady overflow on a levee with a 5-m crest and 1V:5H landward-side and seaward-side slopes. The water free surface had an elevation 1 m above the levee crest. Model forcing was by a 3-m/s horizontal current imposed on the upstream boundary in addition to gravity flow down the landward-side slope. Shear stress values from CHEN3D were compared to soil samples to determine erosion rates.

The numerical model estimated a maximum velocity of 11.8 m/s near the landward-side levee toe, and maximum shear stresses at the toe was stated to be between 50 and 60 N/m^2. These computed shear stresses are an order of magnitude smaller than calculated by Nadal and Hughes (2009) for similar flows using measured data from small-scale experiments. The validity of Briaud, et al.'s shear stress estimates can be examined using the widely-accepted equations presented in this chapter for steady overflow.

First, the steady overflow discharge corresponding to a negative freeboard of R_c = -1.0 m (i.e., h_1 = 1.0 m) is estimated using Eqn. 2.1 as follows.

$$q = 0.5443\sqrt{g}\ h_1^{3/2} = 0.5443\sqrt{9.816\ \text{m/s}^2}\ (1.0\ \text{m})^{3/2} = 1.7\ \text{m}^3/\text{s per m}$$

Next, at the landward-side toe of the levee with a computed velocity of 11.8 m/s, the estimated flow thickness is found from mass continuity simply as

$$h = \frac{q}{v} = \frac{1.7\ \text{m}^3/\text{s/m}}{11.8\ \text{m/s}} = 0.14\ \text{m}$$

Finally, the shear stress on the slope created by the flowing water is estimated from Eqn. 2.42 with the friction slope S_f replaced with sin θ, i.e.,

$$\tau_0 = \gamma_w\ h\ S_f = \left(10\ \text{kN/m}^3\right)\left(0.14\ \text{m}\right)\sin\left(11.3^o\right) = 0.275\ \text{kN/m}^2 = 275\ \text{N/m}^2$$

Thus, the simple approximation of shear stress using established empirical equations produces shear stress estimates that are between 4 and 5 times greater than computed by Briaud, et al.'s numerical model simulation. Substitution of the maximum velocity and the overflow discharge into Manning's equation (Eqn. 2.12) gives a calculated value for Manning's n of n = 0.01, which is the same value given by Munson, et al. (2002) for glass surfaces.

The Federal Highway Administration (FHWA 2005) developed Table 2.7 as a reference for designing flexible drainage channel linings. Values listed in Table 2.7 are given as an example of permissible shear stresses for typical erosive materials that may be present in open channel flow. The plasticity index (*PI*) is a range of water content (in percent) over which a soil will exhibit plastic behaviors (Budhu 2008). The parameters D_{75} and D_{50} represent average grain size of sand, gravel, and riprap. For example, D_{75} is the 75% largest grain size, and D_{50} is the median grain size.

Table 2.7. Permissible Shear Stress for Typical Natural Materials.

Material		Permissible Shear Stress (N/m^2)
Bare Soil Cohesive ($PI = 10$)	Clayey Sands	1.8 to 4.5
	Inorganic Silts	1.1 to 4.0
	Silty Sands	1.1 to 3.4
Bare Soil Cohesive ($PI \geq 20$)	Clayey Sands	4.5
	Inorganic Silts	4.0
	Silty Sands	3.5
	Inorganic Clays	6.6
Bare Soil Non-Cohesive ($PI < 10$)	Finer than Coarse Sand, $D_{75} < 1.3$ mm	1.0
	Finer Gravel, $D_{75} = 7.5$ mm	5.6
	Gravel, $D_{75} = 15$ mm	11
Gravel Mulch	Coarse Gravel, $D_{50} = 25$ mm	19
	Very Coarse Gravel, $D_{50} = 50$ mm	38
Rock Riprap	$D_{50} = 0.15$ m	113
	$D_{50} = 0.30$ m	227

2.6 Numerical Modeling

Many researchers, (Causon et al. (2002), Hu et al. (2000), Hubbard and Dodd (2002), and Shiach et al. (2004)) have implemented numerical models to simulate wave overtopping. Reeve et al. (2008) explored the effects of combined wave and surge overtopping discharge in a numerical flume by applying the 3-dimensional Reynolds Averaged Navier-Stokes, RANS, equations with a finite difference scheme. The model used was a modified model of RIPPLE and a turbulence model that had been expanded to solve complex free surfaces (Lin and Xu 2006), since the model originally was developed in two dimensional form by Lin and Liu (1998). In the 3-dimensional form, Reeve et al. (2008) found that the "majority of the numerical model results were slightly larger than the corresponding predictions from empirical equations" (Reeve et al. (2008), pg 161). Reeve et al. (2008) accounted for this discrepancy by the fact that flow acceleration might be underestimated with the use of the simple linear superposition (Reeve et al. 2008). Further validation of the numerical model was done using experimental data results from Soliman et al. (2003) and Soliman and Reeve (2004). Although the work included the simulation of several slopes, and surge and wave overtopping events, Reeve et al. (2008) expressed the need for further experiments that would include determination of the velocities experienced on the structure.

CHAPTER 3 – EXPERIMENTAL PROGRAM

This chapter overviews the physical model experimental program conducted at the U.S. Army Engineer Research and Development Center (ERDC) Coastal and Hydraulics Laboratory (CHL). Included in the chapter is a discussion of the appropriate scaling to attain correct similitude between the model and the full-scale conditions being replicated, a short review of the physical model design, a description of the experiment setup and target test conditions, details of the testing procedures, and a description of the data collection and data analysis techniques.

3.1 Physical Model Appropriateness

In many cases, a coastal problem can be examined by several different methods including numerical models, physical models, analytical techniques, statistical analyses, and desktop studies. Selecting which techniques are most suited to a particular problem requires the following: (a) knowledge of the primary forcing and responses that shape the coastal processes in the problem area, and (b) an understanding of how well the forcing and response are replicated by the alternative technologies. Often multiple technologies are employed with each technology providing part of the problem solution.

Physical models are appropriate where the hydrodynamic physical processes are complex (wave nonlinearities, wave/current interactions, complex bathymetry, numerous boundaries), and where the response to the hydrodynamics is not well understood or quantified. In addition, the similitude relationships for the dominant processes must be known, and the potential scale and laboratory effects must be thought to be surmountable.

Combined wave and storm surge overtopping of earthen levees qualifies as a complicated hydrodynamic physical process. The hydrodynamic regime for this situation is complicated by a number of physical processes. When the surge level exceeds the levee crest elevation, water flows across the levee crown, passes through the critical flow threshold, and flows down the protected-side slope as super-critical flow. If waves also propagate on an overtopping storm surge, the flow processes become unsteady with sudden increases of overtopping water as the wave crests propagate over the levee crown. This causes rapid changes in pressure on the protected-side slope, and flow accelerations will be important. Depending on the surge water elevation relative to the levee crest, some waves may break directly on the levee crown, or propagate across the crown as broken waves.

3.2 Physical Model Similitude

The basis of all physical modeling is the idea that the model behaves in a manner similar to the prototype it is intended to emulate. Thus, a properly validated physical model can be used to predict the prototype (real world) under a specified set of conditions. However, there is a possibility that physical model results may not be indicative of prototype behavior due to scale effects or laboratory effects. The role of the physical modeler is to minimize scale effects by understanding and applying proper similitude relationships, and to minimize laboratory effects through careful model construction and operation.

Similarity between the real world (prototype) and a small-scale replica (model) of a coastal project area is achieved when all major factors influencing reactions are in proportion between prototype and model while those factors that are not in proportion throughout the modeled domain are so small as to be insignificant to the process. For coastal levee physical models featuring steady surge overflow combined with overtopping by short waves, three general conditions must be met to achieve model similitude: geometry similarity, kinematic similarity, and dynamic similarity.

1) Geometric similarity exists between two objects or systems if the ratios of all corresponding linear dimensions are equal. This relationship is independent of motion of any kind and involves only similarity in form (Warnock 1950). Geometrically similar models are also known as geometrically undistorted models because the horizontal and vertical length scales are the same. Departure from geometric similarity is restricted to hydrodynamics of long waves and unidirectional flows.

2) Kinematic similarity indicates a similarity of motion between particles in model and prototype. Kinematic similarity is achieved when the ratio between the components of all vectorial motions for the prototype and model is the same for all particles at all times (Hudson et al. 1979). In a geometrically similar model, kinematic similarity gives particles paths that are geometrically similar to the prototype. Kinematic similarity assures the flow velocities, accelerations, and pressures associated with water overtopping the levees are correctly replicated in the physical model.

3) Dynamic similarity between two geometrically and kinematically similar systems requires that the ratios of all vectorial forces in the two systems be the same (Warnock 1950). This means that there must be constant prototype-to-model ratios of all masses and forces acting on the system. The requirement for dynamic similarity arises from Newton's second law that equates the vector sum of the external forces acting on an element to the element's mass reaction to those forces. Dynamic similitude is required when the model is used to estimate shear stress forces exerted on the levee slope by the overtopping water velocities and accelerations.

Perfect similitude requires that the prototype-to-model ratios of the inertial, gravitational, viscous, surface tension, elastic, and pressure forces be identical. In practice, perfect similitude is impossible at reduced model scale. Fortunately, many coastal problems and free-surface flow regimes are adequately modeled by an imperfect similitude where inertia and gravity forces dominate while all other forces are small in comparison.

For convenience, physical modeling similitude requirements are expressed in terms of scale ratios, defined as the ratio of a parameter in the prototype to the value of the same parameter in the model. The scale ratio is represented by the notation:

$$N_X = \frac{X_p}{X_m} = \frac{\text{value of X in prototype}}{\text{value of X in model}} \tag{3.1}$$

where N_X is the prototype-to-model scale ratio of the parameter X. For example, the length scale is usually denoted as N_L and the velocity scale is N_V.

3.2.1 Hydraulic Similitude

Hydraulic similitude requirements for coastal hydrodynamic short-wave models can be derived (e.g., Hughes 1993) from the continuity and Navier-Stokes equations governing incompressible, free-surface flows. The resulting similitude conditions are listed here. In Eqns. 3.2 through 3.4 the expressions on the left side give the similitude criteria, which are also given in terms of scale ratios on the right side (Hughes 2003).

1) The model must be geometrically undistorted, i.e., horizontal and vertical length scales are the same.

2) The Froude number, which is the ratio of inertia to gravity forces, must be the same in the model as in the prototype, and this results in the Froude Criterion, i.e.,

$$\left(\frac{V}{\sqrt{gL}}\right)_p = \left(\frac{V}{\sqrt{gL}}\right)_m \qquad \text{or} \qquad \frac{N_V}{\sqrt{N_g N_L}} = 1 \tag{3.2}$$

3) The Strouhal number, which is the ratio of temporal to convective inertial forces, must be the same in the model as in the prototype, i.e.,

$$\left(\frac{L}{Vt}\right)_p = \left(\frac{L}{Vt}\right)_m \qquad \text{or} \qquad \frac{N_L}{N_V N_t} = 1 \tag{3.3}$$

4) The Reynolds number, which is the ratio of inertia to viscous forces, must be the same in the model as in the prototype, i.e.,

$$\left(\frac{\rho LV}{\mu}\right)_p = \left(\frac{\rho LV}{\mu}\right)_m \qquad \text{or} \qquad \frac{N_\rho N_L N_V}{N_\mu} = 1 \tag{3.4}$$

where

V = characteristic velocity
g = gravitational acceleration
L = characteristic length
t = time
ρ = fluid density

and the subscripts p and m represent prototype and model, respectively.

The geometric similarity criterion (condition 1) coupled with the Froude Criterion (condition 2) assure that all terms in the governing flow equations are in similitude with the exception of the viscous terms. Froude similarity includes the turbulent Reynolds shear stress terms; thus, macro features of turbulent dissipative processes are also in similitude.

Viscous effects can only be modeled if the Reynolds Criterion (condition 3) is met along with the Froude criterion in a geometrically similar model. In general this is practical only at prototype scale (full-size scale). Consequently, coastal short-wave models can be either non-dissipative where viscous and capillary effects are negligible, such as waves prior to breaking; or the model can have highly turbulent flow dissipation over a relatively short distance, such as during wave breaking on a structure or a beach (Le Méhauté 1976). In reality, there will always be a small amount of wave attenuation due to viscous frictional losses and surface tension effects, but these scale effects can be minimized to the point of insignificance.

The hydrodynamic time scale for Froude-scaled hydrodynamic models is obtained by solving Eqn. 3.2 for N_V and substituting into Eqn 3.3 to give:

$$N_t = \sqrt{\frac{N_L}{N_g}} \tag{3.5}$$

Because the gravitational force will be the same in the model as in the prototype, the prototype-to-model ratio given by the term N_g will be unity, and it is usually not included in the scaling criteria. Other scale ratios derived from Froude and Reynolds scaling are given in most similitude texts (e.g., Hughes 1993).

3.2.2 Physical Model Scale and Laboratory Effects

Small-scale physical models are essentially analog computers of all the physical processes being simulated with the model. Nonlinearities and complex physical interactions between fluid and solid boundaries are faithfully reproduced without compromise provided the model has been scaled correctly and laboratory effects are controlled. For this reason, small-scale physical models offer an opportunity to examine those processes that are beyond theoretical understanding or are too complicated to represent adequately with simplified analytical or numerical modeling tools.

Scale effects in coastal hydrodynamic models result primarily from the Froude scaling assumption that gravity is the dominant physical force balancing the inertial forces. The other physical forces of viscosity, elasticity, and surface tension are incorrectly scaled with the belief that these forces contribute little to the physical processes. In fixed-bed models the primary scale effect occurs wherever flows in the model become so slow that the flow regime might transition from turbulent to laminar flow conditions whereas such a transition would not occur in the prototype. In this case the viscous forces in the model would not be in similitude.

Surface friction is another potential scale effect. Surface roughness affects water flow, and it provides contact friction between adjacent solid objects. However, it is difficult to scale precisely the surface roughness of levee grass slopes or potential protective measured placed to prevent erosion. In this situation it is best to error on the conservative side by making the model levee slopes smooth. This will allow slightly higher flow velocities than what would occur in the real-world situation.

As noted in Hughes and Nadal (2009) the small-scale overtopping experiments produced only minor air entrainment, whereas significant air entrainment occurs during full-scale wave overtopping. Some insight into this possible scale effect can be found from studies for very steep spillways (Henderson 1966). Air entrainment reduced theoretical maximum spillway velocities by about 10 percent for a spillway height of 7.6 m and a spillway head of 0.8 m. This reduction percentage decreases for less head and smaller spillway heights. Based on this observation, it would seem logical that a high percentage of air entrainment in overtopping flow might reduce maximum velocities at full-scale, but there would be no similar reduction in small-scale physical models. At the same time, air entrainment at full scale will increase the flow thickness by some unknown amount. So when instantaneous discharge is considered, which is the product of velocity and flow thickness, any decrease in velocity at full-scale due to air entrainment is partially offset by a corresponding increase in flow thickness (Hughes and Shaw 2011). Until such time that studies can quantify the air entrainment scale effect, one might be cautiously optimistic in assuming that the small-scale results are reasonable predictors of the macro features of full-scale flow behavior.

Finally, it is not possible to scale the levee soils to model size and expect similar erosive behavior of the earthen levee under whatever emergency protection has been placed over the levee surface. Erosion of levee soils, particularly vegetated surfaces, can only be modeled at full scale, which is the only way to assure there are no scale effects.

Laboratory effects in coastal physical models are primarily related to the following:

a) Physical constraints on flow in the model are caused by the need of representing a portion of the prototype in a finite amount of space. Model boundaries may exist where there is no boundary in the prototype. Waves reflect off model boundaries and introduce reflected wave trains back into the simulated wave field. This problem is partially solved using energy dissipating beaches composed of gentle slopes and rubberized horsehair mats that can minimize reflection to less than 5 percent.

b) Mechanical means of wave and current generation may introduce unintentional nonlinear effects. The most common example is incorrect reproduction of bound long waves that sometimes cause problems for harbor basins. The model engineer must attempt to make the mechanical waves resemble reasonably well the waves observed in nature.

c) Prototype forcing conditions are simplified and only a subset of all possible conditions can be selected for testing. A common laboratory effect in wave flumes is

representing directional waves that occur in nature as long-crested, two-dimensional waves in the flume. This compromise is not considered significant, but the model engineer must assess the approximation to determine whether it is reasonable. Another example is simulating a storm using a constant water level as opposed to a time-varying surge hydrograph.

The potential scale and laboratory effects described above were assessed during design of the physical model used for the laboratory tests documented in this report.

3.3 Physical Model Design

The experiments were conducted in a 0.91-m-wide wave flume at the ERDC/CHL in Vicksburg, Mississippi. The model levee cross section in the wave flume was originally designed for a previous set of experiments. Full details of the flume, model design, and test setup are given in Hughes (2008) and Hughes and Nadal (2009). A brief summary of the model design is given below.

3.3.1 Scale Section

Dimensions of a typical levee cross section on the Mississippi River Gulf Outlet (MRGO) were established, and several testing flumes were considered for hosting the physical model. The selected wave flume had high-quality wave generation equipment, it was sufficiently large to avoid viscous scale effects, and it was easily modified to support a recirculation system for simulating steady overflow. After consideration of several factors including the proposed range of negative freeboard, the selected range of incident wave conditions, and laboratory measurement capabilities, a model length scale of N_L = 25 was determined to be a reasonable compromise for the geometrically undistorted model.

The required Froude prototype-to-model velocity scale and time scale corresponding to a model length scale of N_L = 25 were given by Eqns. 3.2 and 3.5, respectively, i.e.,

$$N_V = \sqrt{N_g N_L} = \sqrt{(1)(25)} = 5.0 \tag{3.6}$$

and

$$N_T = \sqrt{\frac{N_L}{N_g}} = \sqrt{\frac{(25)}{(1)}} = 5.0 \tag{3.7}$$

where the gravitational scale ratio, N_g, is unity.

The recirculation pump needed sufficient capacity to simulate steady overflow created by a negative freeboard of 1.5 m above the levee crest (prototype-scale units). Using the wide-crested weir formulation (Eqn. 2.1), the prototype-scale unit discharge was found to be

$$q_p = 0.5443\sqrt{g}\,(h_1)^{3/2} = 0.5443\sqrt{9.816\ \text{m/s}^2}\,(1.5\ \text{m})^{3/2} = 3.13\ \text{m}^3/\text{s per m} \quad (3.8)$$

The 0.91-m flume width corresponds to a prototype-scale levee reach length of 22.75 m, so the total prototype-scale volumetric surge overtopping discharge for this width was determined as

$$Q_p = 3.13\ \text{m}^2/\text{s}\,(22.75\ \text{m}) = 71.2\ \text{m}^3/\text{s} \quad (3.9)$$

The Froude scale ratio for volumetric discharge is simply the scale ratio for area times the scale ratio for velocity, or

$$N_Q = (N_L)^2\ N_V = (N_L)^{5/2} = (25)^{5/2} = 3{,}125 \quad (3.10)$$

Thus, the required maximum pumping capacity needed to maintain the model equivalent of a 1.5-m overtopping surge in the physical model was

$$Q_m = \frac{Q_p}{N_Q} = \frac{71.2\ \text{m}^3/\text{s}}{3{,}125} = 0.023\ \text{m}^3/\text{s} = 1{,}382\ \text{l/s (365 gal/min)} \quad (3.11)$$

The important model scale ratios (value in the prototype divided by the equivalent value in the model) are summarized in Table 3.1. The fundamental scaling parameter is the length scale, N_L = 25, which can be interpreted as 1 m in the model equals 25 m in the real world.

Table 3.1. Model Scale Ratios and Prototype Equivalence.

Scale	Scale Value	Model-to-Prototype Equivalence
Length scale	$N_L = 25$	1 m = 25 m
Time scale	$N_T = 5.0$	1 s = 5.0 s
Velocity scale	$N_V = 5.0$	1 m/s = 5.0 m/s
Discharge scale	$N_Q = 3{,}125$	1 gal/s = 11.8 m^3/s

3.3.2 Wave Flume and Model Levee Cross Section

Figure 3.1 shows the selected MRGO levee cross section scaled to model dimensions using the length scale of N_L = 25. The seaward side is on the left side of the figure. In order to assure correct wave transformation of incident waves, it was necessary to reproduce the entire seaward portion of the levee including the 1V-on-5H toe slope, the 1V-on-24H berm, and the 1V-on-4.25H flood-side levee slope. The levee crown, the landward-side 1V-on-3H slope, and most of the protected-side 1V-on-24H slope were also included in the physical model. The levee model was carved out of high-density foam using a programmable router, and the cross section was constructed in several sections to facilitate placement in the flume and to allow installation of pressure gauges.

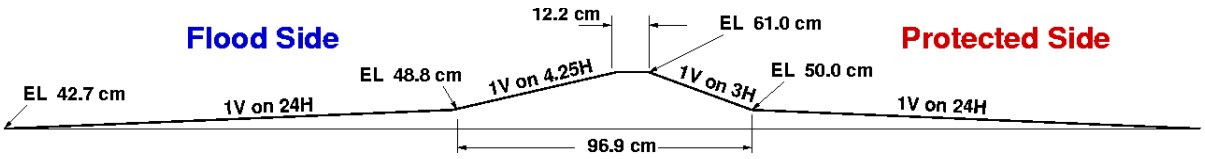

Figure 3.1. Model levee cross section (model-scale units).

The instrumentation plan included seven flush-mounted dynamic pressure gauges on the levee crest and down the levee protected-side slope. The router was programmed to rebate for the pressure gauge mounts, and provision was made for running the gauge cables under the levee model and out the rear side during installation. Figure 3.2 shows the pressure gauges mounting holes.

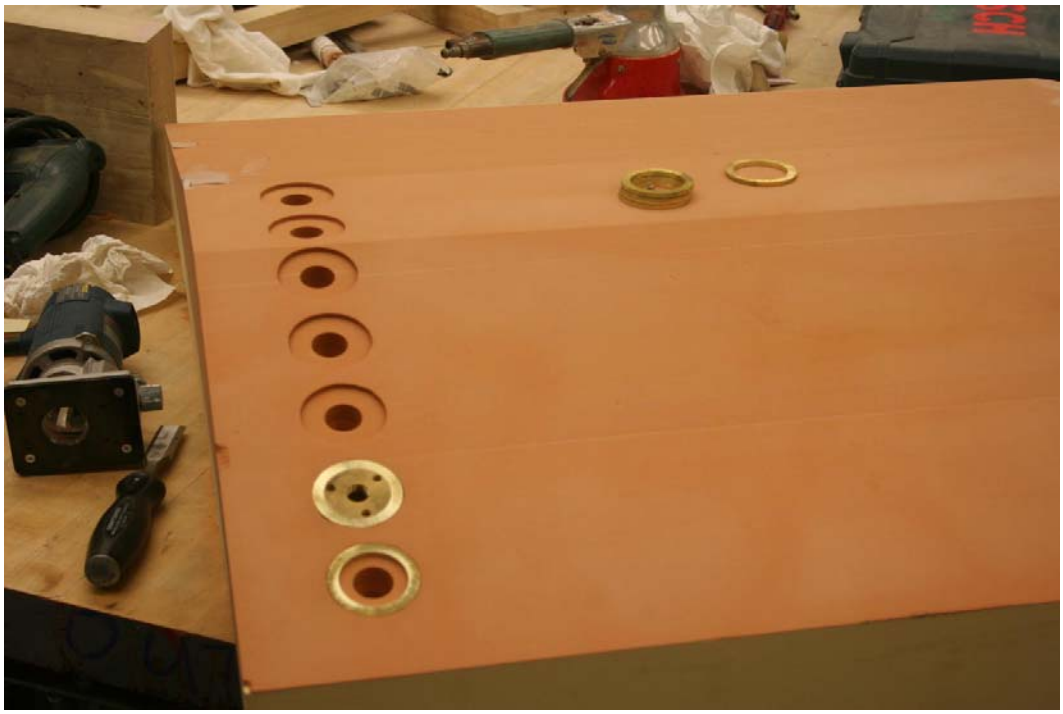

Figure 3.2. Mounting hardware for dynamic pressure gauges.

The scaled model levee cross section was placed in the 0.91-m-wide by 0.91-m-deep by 45.7-m-long flume as shown schematically in Figure 3.3. The model levee was located approximately 32 m from the piston-type wave board with the crest elevation 0.61 m above the wave flume bottom. Seaward of the levee model section was a long 1V:100H approach slope and a shorter 1V:20H slope transition to the bottom of the flume. Surge and waves that overtopped the levee flowed into the reservoir (right end of Figure 3.3), and a pump recirculated the water to the seaward end of the flume. A "horsehair" flow damper was placed above the pump intake downstream of the levee to prevent pump cavitation and to reduce disturbances in the receiving reservoir stilling basin so the water elevation could be monitored. Four wave gauges were mounted in the wave flume at the locations indicated on the sketch.

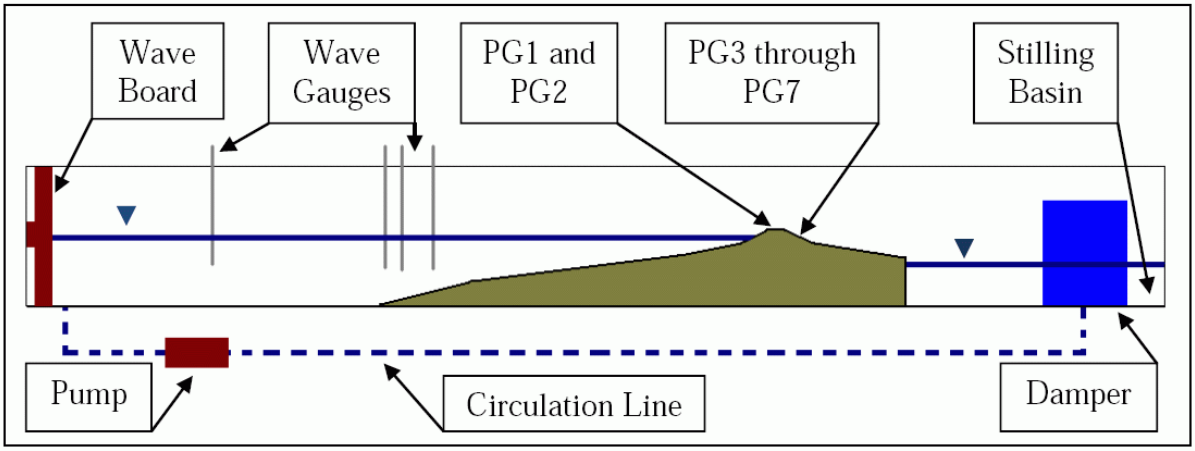

Figure 3.3. Wave flume layout.

3.4 Experiment Setup and Target Test Conditions

3.4.1 Instrumentation

Wave data (time series of instantaneous sea surface elevations) were collected using four capacitance-type wave gauges placed at the locations shown in Figure 3.3. Gauge 1 was located over the horizontal bottom of the wave flume closest to the wave board. Gauges 2-4 were placed as a three-gauge array near the toe of the levee model. The gauges work by sensing the change in capacitance in a thin insulated vertical wire as the water elevation varies on the wire. Each gauge captures a time series of information that can be converted into water surface elevations at that location. The time series can then be analyzed to obtain wave information.

All wave gauges were mounted on remotely-controlled stepping motors that permitted the gauges to be raised and lowered to precise vertical distances for calibration. Wave gauges were calibrated daily with the water motionless and at a depth equal to the model levee crest. Provided all gauges exhibited the expected calibration result, the calibration relationships were saved in a file for later application to the measured raw wave data collected the same day as the calibration. For all experiments wave data collection started at the same instant the wavemaker was activated, and continued until the wave board stopped. Time series sea surface elevation data were collected at a 100-Hz rate. Wave data were transmitted into the main control room and recorded on a computer for post-experiment processing.

Seven Druck PDCR-200 pressure cells were installed in the levee cross section with the surface of the pressure cells flush with the levee surface to minimize flow disturbance. The purpose of the pressure cells was to measure flow thickness variations over the levee as a function of time during combined wave and surge overtopping. Two of the instruments were

located on the levee crest, and the remaining five gauges were evenly spaced down the protected-side slope. Figure 3.4 shows the locations of the pressure cells with dimensions given in units of model cm. The pressure gauges were mounted approximately 8 cm from the flume wall to correspond with the position where velocity measurements would be acquired (see Figure 3.5).

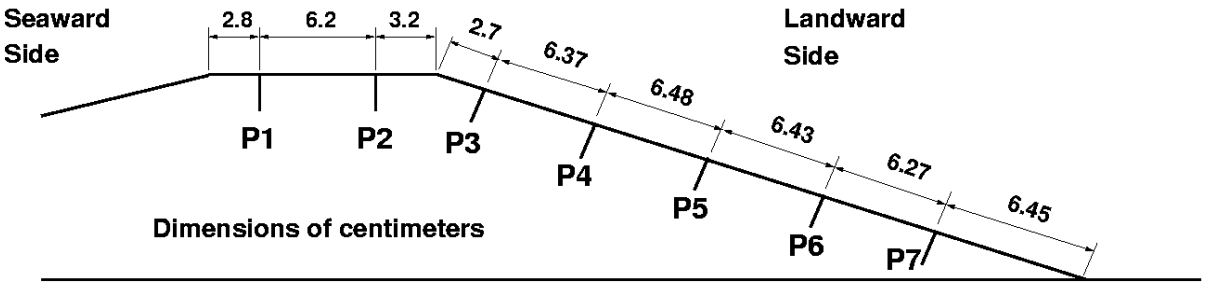

Figure 3.4. Pressure gauge locations.

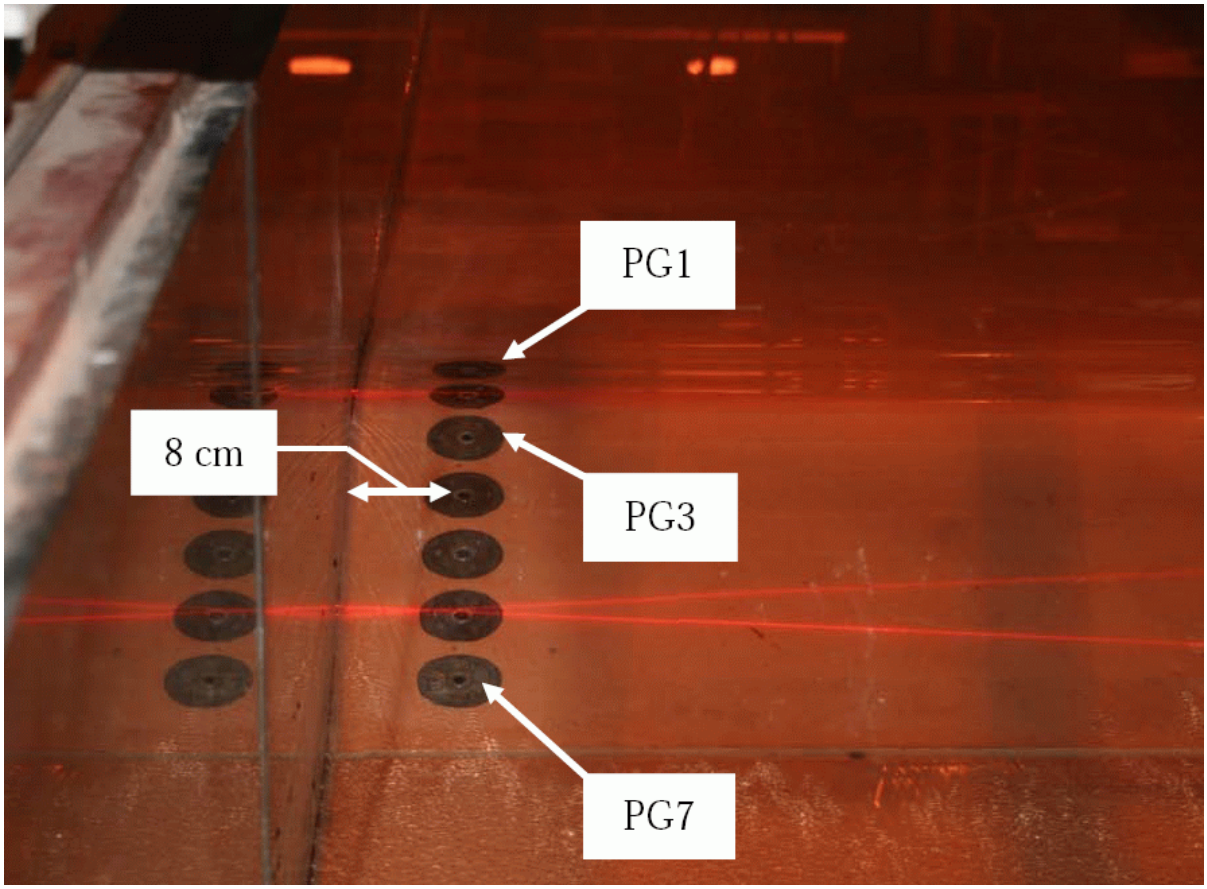

Figure 3.5. Pressure gauge positioning in the wave flume.

The pressure cells were initially calibrated before placement in the model, and the calibration was checked by flooding the levee model to known static levels and confirming the water depth over each gauge corresponded to the gauge output. Pressure data were collected at a 100-Hz rate concurrent with wave data. Data collection began when the wavemaker commenced operation, and collection ended when the wave generation ceased. Prior to each experiment, all the pressure cells were adjusted to read zero when no water was present over the instrument, i.e., when the crest and protected-side levee slope were dry.

Overtopping flow velocities were recorded using a Dantec laser Doppler velocimeter (LDV) system consisting of two lasers, a processor, and a laptop computer with Burst Spectrum Analyzer (BSA) Flow Software Version 4.50. The system was calibrated in the factory, and the included BSA F30 processor can record velocities up to a maximum of 68 m/s. The LDV system is a nonintrusive velocity measurement tool that mounts outside the wave flume, directs laser beams through the flume glass sidewall, and measures one component of velocity at a location inside the flume. Water velocities parallel to the levee surface were obtained at the laser beam crossing points located approximately 8 cm from the inside face of the glass flume wall as indicated on Figure 3.5. Figure 3.6 shows the two LDVs mounted outside the flume on a support system that allowed precise independent adjustment of each LDV spatial position.

Figure 3.6. Laser Doppler velocimeters positioned outside the wave flume.

The BSA software specifies the measurement capabilities of the lasers and has the option to record velocity measurements in ASCII text files. The software does not allow for user adjustment to laser calibration, but recording intervals and sensitivity can be changed. The non-coincident mode option records velocity independently at each laser, whereas the

coincident mode setting records both lasers in unison. The coincident setting requires each laser to be acquiring velocity data before recording can occur, so this mode would not record data until the overtopping wave front reached the downstream LDV. The LDV system gathers data in dead time mode or burst mode. Burst mode collects data anytime a noticeable change in velocity occurs and dead time collects the first data burst per specified time bin. Both methods collect velocity data at a non-uniform rate that is quite a bit faster (kHz range) than 100 Hz. As a result, velocity time series are not uniformly time spaced. Other system variables include sample size, sample rate, sample time, velocity range, and laser voltage.

The LDV system required that water in the wave flume be seeded with small particles of titanium dioxide (latex paint without hardening agent), and a series of systematic tests was conducted to determine an appropriate amount of seeding to assure consistent velocity readings. The seeding material stayed in suspension for extended time periods, but prior to each day's testing, energetic wave conditions were run in the flume to help agitate and suspend particles that had settled on the bottom of the tank.

3.4.2 Testing Program

The experimental program described in this section is an extension of previous levee overtopping work performed by Hughes and Nadal (2009), and the same range of hydrodynamics parameters were used in developing the test plan. The testing program was developed as two test series. The first test series consisted of 9 experiments using different combinations of incident wave conditions and negative freeboard. The purpose of the first test series was to verify continuity of the instantaneous overtopping discharge at different locations on the landward-side slope and to develop empirical relationships for discharge peaks. The second test series consisted of an expanded set of 27 unique hydrodynamic conditions with the purpose of estimating parameters associated with the shear stress on the landward-side slope induced by the unsteady overtopping flow. Test conditions associated with the two test series are given below.

3.4.2.1 Discharge Continuity Tests

For the discharge continuity tests 3 individual irregular wave conditions were selected to cover a broad range of potential hurricane conditions that could be expected to impact New Orleans. The 3 wave conditions were simulated in the model at 3 different surge elevations giving a total of 9 distinct hydrodynamic conditions. The prototype-scale target wave and freeboard parameters are shown in Table 3.2.

Table 3.2. Discharge Target Hydrodynamic Conditions (Prototype Scale).

Waves	SI Units			English Units		
	H_{m0}	T_p	R_c	H_{m0}	T_p	R_c
1	0.91 m	6 s	-0.3, -0.91, -1.52 m	3 ft	6 s	-1, -3, -5 ft
2	1.83 m	10 s	-0.3, -0.91, -1.52 m	6 ft	10 s	-1, -3, -5 ft
3	2.74 m	14 s	-0.3, -0.91, -1.52 m	9 ft	14 s	-1, -3, -5 ft

During these 9 tests, the LDVs were positioned at pressure gauge locations P2 and P6 as indicated by the dots in Figure 3.7. At location P2 the LDV beam crossing point was situated directly above the pressure sensor, and the LDV was oriented to measure horizontal velocity. The LDV vertical position was adjusted to an elevation that was approximately half the steady overflow depth for each experiment. This vertical position was thought to provide a reasonable value for depth-averaged horizontal velocity, but the drawback to this vertical positioning was the loss of velocity signal during wave troughs when the water level fell below the elevation of the laser beams.

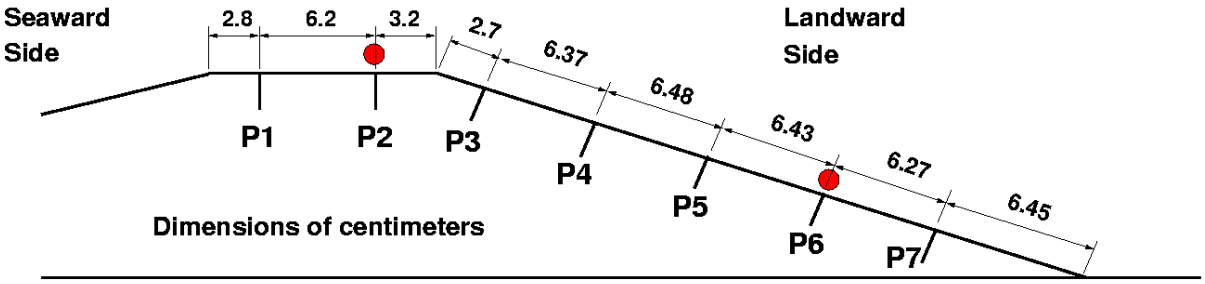

Figure 3.7. Laser Doppler velocimeter positions for the discharge continuity tests.

At location P6 the LDV beam crossing point was on a line perpendicular to the levee and centered on the pressure sensor. The LDV was oriented to measure slope-parallel velocity at a location that was generally half of the steady overflow thickness. The exceptions were tests with the lowest steady overflow. In these cases, the flow thickness for steady overflow was quite thin, so the LDV beams were moved closer to the upper limit of the flow thickness. The instantaneous discharge over the levee at each time step was estimated at locations P2 and P6 as the product of horizontal velocity and water depth.

3.4.2.2 Shear Stress Tests

For the shear stress tests 9 individual irregular wave conditions were selected. These target wave conditions were the same as those used in previous tests described by Hughes (2008) and Hughes and Nadal (2009). The 9 wave conditions were simulated in the model at 3 different surge elevations giving a total of 27 distinct hydrodynamic conditions. The prototype-scale target wave and freeboard parameters are shown in Table 3.3.

During these 27 tests, the LDVs were positioned at pressure gauge locations P4 and P7 on the landward-side slope as indicated by the dots in Figure 3.8. This was as close as the two instruments could be placed and still coincide with pressure gauges. At each location the LDV beam crossing points were on a line perpendicular to the levee and centered on the pressure sensor. The LDVs were oriented to measure slope-parallel velocity at a position that was generally half of the steady overflow thickness. As was the case with the discharge test series, the flow thickness for the lowest steady overflow was quite thin, so the LDV beams were moved closer to the upper limit of the flow thickness or even above the steady

flow free surface. This resulted in no data being acquired for some experiments during the initial steady overflow portion prior to wave arrival.

Table 3.3. Shear Stress Target Hydrodynamic Conditions (Prototype Scale).

Waves	SI Units			English Units		
	H_{m0}	T_p	R_c	H_{m0}	T_p	R_c
1	0.91 m	6 s	-0.3, -0.91, -1.52 m	3 ft	6 s	-1, -3, -5 ft
2	0.91 m	10 s	-0.3, -0.91, -1.52 m	3 ft	10 s	-1, -3, -5 ft
3	0.91 m	14 s	-0.3, -0.91, -1.52 m	3 ft	14 s	-1, -3, -5 ft
4	1.83 m	6 s	-0.3, -0.91, -1.52 m	6 ft	6 s	-1, -3, -5 ft
5	1.83 m	10 s	-0.3, -0.91, -1.52 m	6 ft	10 s	-1, -3, -5 ft
6	1.83 m	14 s	-0.3, -0.91, -1.52 m	6 ft	14 s	-1, -3, -5 ft
7	2.74 m	6 s	-0.3, -0.91, -1.52 m	9 ft	6 s	-1, -3, -5 ft
8	2.74 m	10 s	-0.3, -0.91, -1.52 m	9 ft	10 s	-1, -3, -5 ft
9	2.74 m	14 s	-0.3, -0.91, -1.52 m	9 ft	14 s	-1, -3, -5 ft

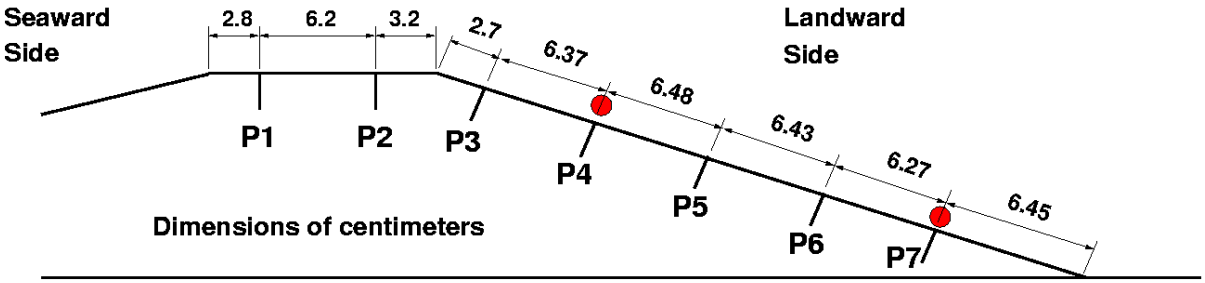

Figure 3.8. Laser Doppler velocimeter positions for the shear stress tests.

3.5 Testing Procedures and Data Collection

During the initial phase of the test program, time series of series realizations of sea elevations (i.e., irregular waves) at model scale fitting the target spectral wave parameters given in Tables 3.2 and 3.3 were synthesized and converted to corresponding irregular, cyclic motions of the piston-type wave board. The target conditions were run in the wave flume, and the measured results were analyzed. Depending on the result, the wave board amplitude gain was adjusted to produce the target wave parameters in the test facility. The calibrated wave board displacement time series were stored for use during subsequent testing.

Wave gauges were calibrated each morning of testing with the water level at the elevation of the levee crest. After calibration the wave gauges were moved vertically (via remote-controlled stepping motors) so the mid-point of the gauge would correspond with the target steady surge level for the experiment. Pressure gauges were set to zero (corresponding

to atmospheric pressure), and the LDV system was activated and configured for data collection.

Before data collection commenced for each experiment, the recirculation pump was activated and water from the reservoir was pumped into the seaward portion of the flume. The pipe valve was adjusted until the correct steady overflowing surge level was obtained at the nearby point gauge. The elevations of the laser beam crossings above the surface of the levee crown were set to approximately one-half of the steady flow thickness at each LDV location for the specific overtopping surge.

Once everything was ready, the flow discharge reading was noted, the computer operator was informed by handheld radio to begin running waves in the flume, and the wave board began generating the prescribed irregular wave time series realization conforming to the spectrum parameters. Data collection for the wave board (control and feedback), the four wave gauges, and the seven pressure gauges was begun at the same time as wave generation. The 13 channels of data were collected at 100-Hertz (Hz) as uniformly-spaced time series.

Velocity data collection using the two interconnected (synoptic) Dantec FlowExplorer LDVs was accomplished using a different computer system than used for the wave and pressure gauges, and the two systems were not synchronized. Therefore, it was necessary to synchronize the velocity data with the flow thickness measurements using the procedure described later in this chapter. Data collection with the LDVs was manually initiated to coincide approximately with the start of the wave and pressure data collection, and velocity measurements continued until the end of wave generation. Velocity data were saved to ASCII files for further processing.

The water level in the receiving reservoir remained at a constant level during steady flow overtopping. However, once waves started to push additional water over the levee, the level in the reservoir rose. This equated to a slight decrease in the surge level seaward of the levee. To minimize this effect, the water level in the reservoir was monitored at the stilling basin gauge (see Figure 3.3), and when the level increased, an observer signaled the pipe valve operator to slightly increase the flow rate. If the flow rate was increased too much, or overtopping decreased, the opposite signal was given. This process helped maintain a reasonably constant surge elevation throughout the experiment. The valve operator noted the changes in flow rate given by the flow meter, along with approximate duration at each rate. However, the data are not sufficient for estimating the wave-related component of overtopping during combined wave and surge overtopping tests.

Wave generation and data collection continued for a total of 10 min (600 s). This produced about 200 waves for experiments with the longest peak spectral periods, and about 280 waves for the shortest peak periods. The wave and pressure time series contained 60,000 points for each data channel, with the first 1,000 to 1,600 points recording only the steady overflow before the arrival of the first waves. At the completion of each experiment, the collected data were immediately converted into engineering units and stored in computer files containing the necessary identifying information. During the tests the engineer made observations of any unusual overtopping phenomena in a notebook.

At the end of wave generation, the pump was left running, and the water surface rapidly settled into steady-state surge overtopping. After a short time, the next wave condition at that surge level was run in the flume. If the surge level needed to be changed, the surge level was adjusted as described above. At the end of testing for the day, the pump was shut down, and the residual surge elevation was allowed to drain over the levee into the overtopping reservoir.

With the still water level above the levee crest elevation (negative freeboard), wave breaking on or seaward of the crest is not as common as it is for levees with emergent crests (positive freeboard) unless the wave heights are large and the negative freeboard is small. Figure 3.9 illustrates a common form for the overtopping wave with a submerged crest. With fewer waves breaking on the seaward-side slope, it might be expected that the Iribarren parameter (slope steepness divided by the square root of representative wave steepness) is not as important for parameterizing submerged-crest overtopping as it is for emergent crests.

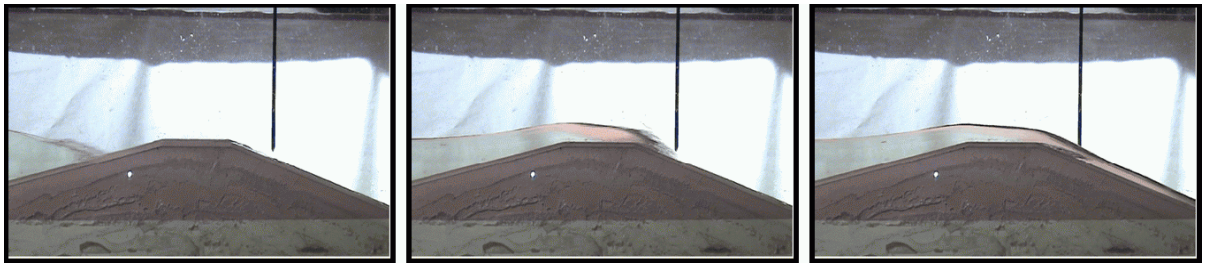

Figure 3.9. Wave overtopping sequence with negative freeboard.

3.6 Initial Data Preprocessing

Measured data time series underwent two preprocessing steps before the data were ready for analyses. Initial data preprocessing included conversion into engineering units, adjustments to compensate for laboratory conditions, and synchronization of the flow thickness and coincident velocity time series. The data were recorded in English standard units and converted to metric units during preprocessing.

3.6.1 Wave Data Preprocessing

Sea surface elevation time series from the three-gauge array closest to the model levee were analyzed for incident and reflected wave energy using the frequency-domain method of Goda and Suzuki (1976), and the results were expressed in terms of energy-based incident significant wave height, H_{m0}. Wave gauge spacing had been previously set to cover the entire frequency range of incident and reflected waves. Whereas the reflection analysis procedure was automated, the analysis frequency range was manually specified for each case. Analyzing beyond the range of appreciable spectral energy (region of reduced coherence) introduces significant error into the estimates of reflected wave energy. The other key parameters determined from frequency-domain analysis were the peak spectral wave period, T_p, and the mean energy-based wave period, $T_{m-1,0}$. No additional analyses of the wave data were performed.

3.6.2 Pressure Data Preprocessing

Additional post-processing of the pressure data was accomplished using MatLab® scripts. Pressures measured on the model levee crest (locations P1 and P2 on Figures 3.4, 3.7, and 3.8) were converted to flow thickness assuming hydrostatic pressure because the slope of the water surface was nearly horizontal. However, for the steep landward-side slope, the pressure measured by gauges P3 through P7 was not hydrostatic, and the slope-perpendicular flow thickness, h, was determined using the formula

$$h = \frac{p}{\gamma_w \cos\theta} \tag{3.12}$$

where p is the measured pressure, γ_w is the water specific weight, and θ is the angle of the landward-side slope (Henderson 1966). In addition, some of the pressure channels contained obvious spikes, and a spike removal MatLab® script called "func_despike_phasespace3d.m" developed by the Disaster Prevention Research Institute was implemented that removed some, but not all, of the more severe spikes. Parameters of the spike removal routine were adjusted by trial and error to assure that the spike filtering was not affecting the rest of the measured time series.

At the beginning of each day all of the pressure gauges were adjusted to a zero value, and this procedure was repeated at midday. The gauges needed to be wetted with a small amount of water to obtain readings, and setting an accurate zero was difficult. Examination of the pressure time series for tests when the levee crest and landward-side slope regularly went dry between waves revealed that some gauges registered a small amount above the zero whereas other gauges indicated unrealistic negative pressures when there was no water on the slope. In addition, the pressure gauges were thought to be the least reliable at very small water depths. Consequently, it was necessary to adjust each pressure time series by adding or subtracting a constant to shift the time series closer to the zero position during wave troughs when no water was on the slope. This was done visually by examining each time series for a particular gauge for all tests during the half-day period associated with pressure gauge adjustment, determining an appropriate shifting factor for each test, then selecting an average shift factor for each gauge during that half day period. An example would be determining the shift factor for gauge P2 during six tests that occurred during one afternoon, calculating the average shift factor, and then applying the same average shift factor for all six runs. Pressure gauge P5 recorded erratically, so results from this gauge were not analyzed further. Figure 3.10 illustrates a typical minor flow thickness adjustment that was applied during the initial pressure data preprocessing.

3.6.3 Flow Velocity Data Preprocessing

Post-processing of the velocity data was also accomplished using MatLab® scripts. The non-uniformly-spaced velocity time series from the two synchronized LDV instruments were first interpolated into time series with data uniformly spaced at the same 100-Hz

sampling rate as the flow thickness data. Overlays of the non-uniformly-spaced and uniformly-spaced times series showed almost perfect transformation of the velocity data.

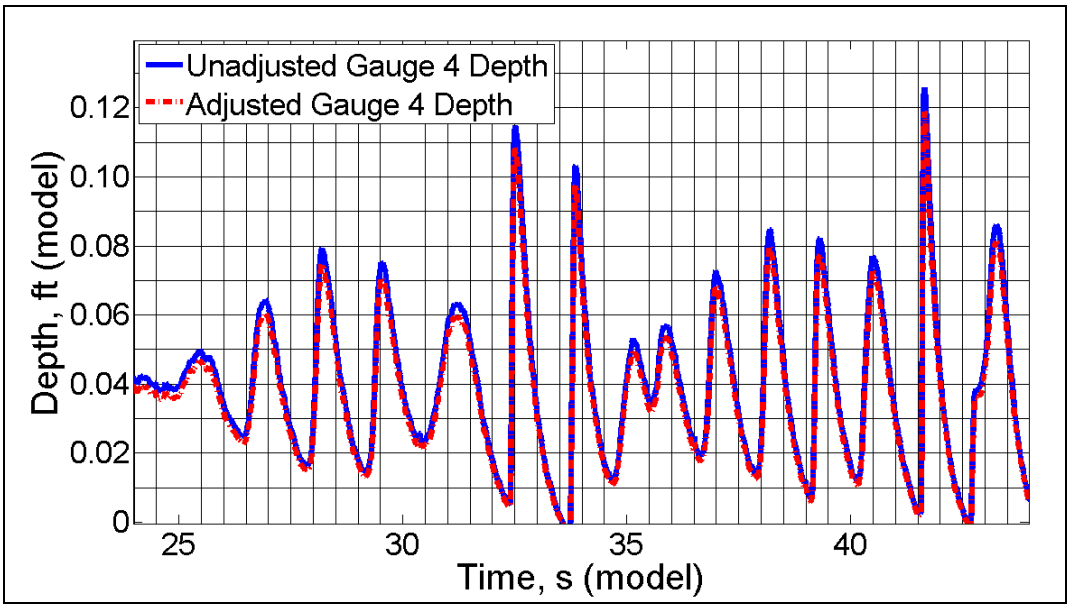

Figure 3.10. Typical flow thickness adjustment based on visual inspection.

Gaps existed in the velocity data because the laser beams had been positioned near the midpoint of the steady overflow water thickness. Thus, in experiments with lower surge elevations (negative freeboard) relative to the levee crest elevation, the flow thickness on the landward-side slope would often fall beneath the laser beams, and no legitimate velocities were recorded when this occurred. Hughes and Nadal (2009) analyzed the sensitivity related to not being able to determine discharge when the laser beams were emerged, and they found that the average error was around 4 percent when the instantaneous discharge time series were used to estimate the mean discharge. The error introduced by the lack of velocity measurement during wave troughs was considered manageable because low discharges have much less influence on levee erosion processes and design of protection to resist shear stress.

In the original velocity time series the software drew a straight line from the last good velocity reading to the next good velocity reading at the leading edge of the next wave, but this made it appear that the overtopping wave front had a gradual increase in velocity rather than the rapid rise known to occur. To correct this false interpolation between valid velocity data points, the velocity time series were automatically edited so whenever there were gaps of missing velocity data, the gaps were filled using the last valid velocity reading before the LDV beams emerged from the flow. This resulted in a rapid rise when the next wave front arrived that is not completely correct, but somewhat more realistic than before data editing. Figure 3.11 illustrates the velocity editing. The dashed lines show the original data gaps between valid measurements that interpolated onto straight lines between the valid points, and the solid line shows how the gaps were edited. The lower time series was recorded at

location P2 on the levee crest, and the upper time series was recorded at location P6 on the landward-side slope.

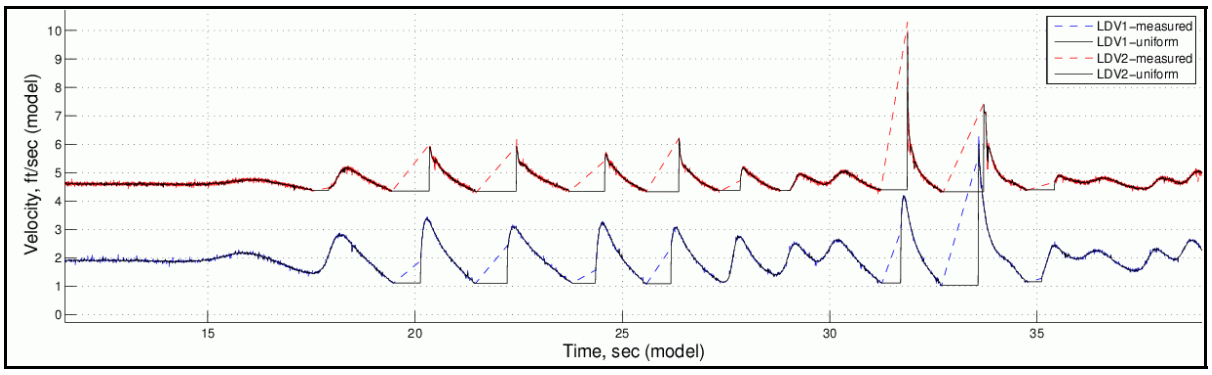

Figure 3.11. Example of velocity time series editing.

Occasional noise spikes were observed during velocity recordings in some runs. The outliers were typically two or three times larger than any other large velocity peaks, and the obvious noise peaks were removed by visual inspection. Figure 3.12 shows an example of the correction applied to velocity noise peaks.

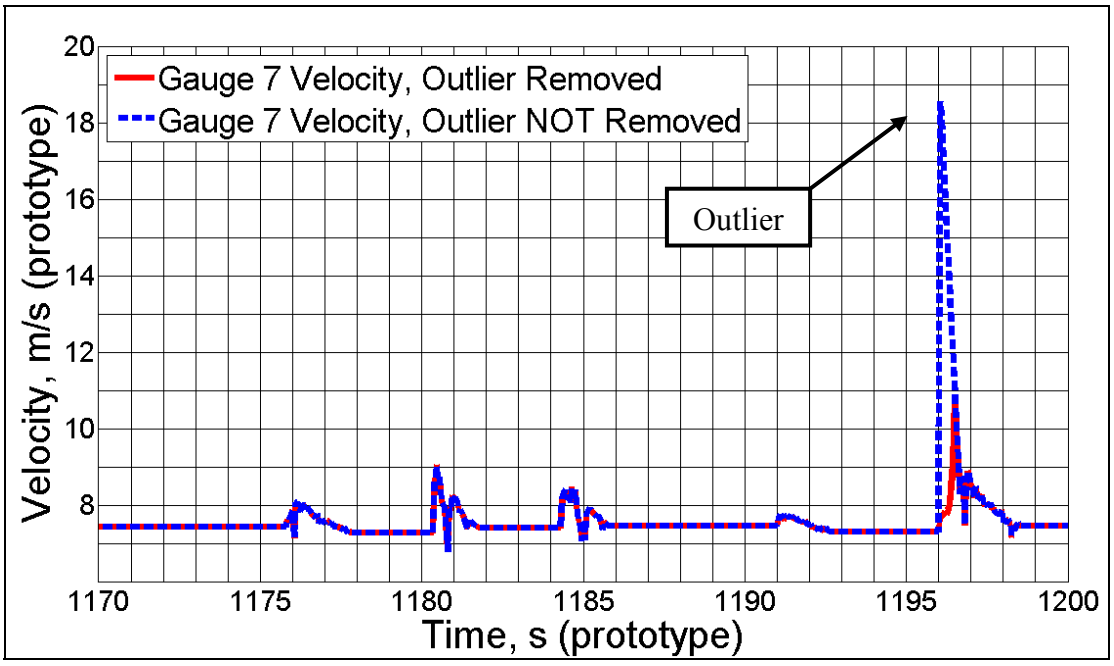

Figure 3.12. Example of manual velocity outlier removal.

3.7 Final Data Preprocessing

The final steps of data preprocessing were to synchronize the time series of flow thickness and velocity, and to make final adjustments to the flow thickness shift factors based on the total overtopping discharge that occurred during each experiment. These steps are described in the following subsections.

3.7.1 Synchronization of Flow Thickness and Velocity Time Series

As mentioned, velocity measurements were collected on a different computer system than the flow thickness data, and the two systems were not precisely synchronized using an external trigger. Synchronization of the flow depth and velocity time series for each run was accomplished by shifting the velocity time series at the upstream location relative to the flow thickness time series at that same location. For the discharge continuity test series, the upstream location was at pressure gauge P2 (see Figure 3.7), whereas pressure gauge location P4 was the upstream location for the shear stress test series (Figure 3.8). The velocity time series was incrementally shifted relative to the flow thickness time series until the sum of the squares of the differences between the two time series was minimized, which occurs when the flow thickness peaks align with the velocity peaks. Typically, the required time shift was on the order of 1 second or less, and visual inspection of the overlain time series confirmed the shift was correct.

The assumption that the velocity and flow thickness peaks should coincide was tested by performing the same shifting procedure on data acquired in previous experiments (Hughes and Nadal 2009) where velocity and flow depth measurements at location P2 were synchronized. It was found that the peaks in fact did align for the highest surge level (1.5 m above levee crest in prototype-scale units); but curiously, this was not the case at lower surge levels. At the 0.9 m (prototype scale) surge level the maximum velocity lagged the maximum flow thickness on average about 0.05 s (0.25 s at prototype scale). At the 0.3 m surge level the velocity lag was about 0.12 s (0.6 s prototype).

No simple physical explanation can be given for this observed lag between the peaks at lower surge levels. It may have something to do with runup on the seaward-side slope crossing the levee crest and transitioning into supercritical flow in the vicinity of location P2. At lower surge levels more forward momentum is lost (relatively speaking) in the runup phase than at higher surge levels, and this might also be a factor.

Based on the analysis of prior synchronized velocity and flow thickness data, these average velocity lags as a function of surge level were also applied when aligning the non-synchronized velocity and flow thickness time series. Table 3.4 presents the applied time shifts used to synchronize the measured flow thickness time series with the measured velocity time series. Runs numbered 13 though 21 correspond to the discharge continuity test series with the LDVs positioned at pressure gauges P2 and P6 (see Figure 3.7), and Runs 25 through 51 relate to the shear stress test series with the LDVs positioned at locations P4 and P7 as shown in Figure 3.8. Runs not included on Table 3.4 (i.e., Runs 1-12 and 22-24) were either configuration tests, aborted tests, or tests with poor data quality.

Table 3.4. Time Series Synchronization Shift Factors (Model Scale).

Run	Model Time Shift (*s*)	Run	Model Time Shift (*s*)	Run	Model Time Shift (*s*)
Discharge Continuity Test Series					
13	0.83	16	1.24	19	-0.03
14	1.23	17	0.50	20	0.58
15	0.26	18	0.37	21	0.24
Shear Stress Test Series					
25	0.59	34	0.29	43	0.19
26	-0.46	35	0.78	44	0.26
27	0.48	36	0.91	45	0.23
28	0.52	37	1.47	46	0.40
29	0.36	38	0.56	47	0.37
30	0.44	39	0.47	48	0.46
31	1.01	40	0.34	49	0.50
32	0.12	41	0.92	50	0.37
33	0.45	42	1.23	51	0.34

3.7.2 Final Flow Thickness Adjustment

The instantaneous discharge passing over the levee crest and down the landward-side slope at each time step was estimated at each location where velocity and flow thickness time series were measured. These discharge estimates assumed that velocity was parallel to the levee surface and constant throughout the water thickness at each location. This is a common assumption used in experimental hydraulics that greatly simplifies flow analysis. The turbulent boundary layer is quite thin, so approximating the majority of the flow thickness as having a uniform velocity is reasonable. If the velocity profile had a strong gradient, a fixed-point measurement with constantly varying flow depth would not be very useful.

An average of the discharge between data points 100 and 1,000 (1 s and 10 s model time) was taken as the steady overflow discharge for the experiment because the first waves generated in the flume had not yet reached the levee model. An estimate of the surge elevation above the levee crest (negative freeboard) was calculated seaward of the crest using the broad-crested weir formula given by Eqn. 2.1. Surge elevations determined from Eqn. 2.1 using the calculated steady overflow discharge at the upstream location where discharge was determined were assumed to be more accurate than the water elevations measured seaward in the flume. Steady inflow near the wave board that replaced overflowing water created a water surface slope between the wave board and the levee. Water elevations

measured at the seaward point gauges included an undetermined portion of this water surface slope.

Average overtopping discharge, q_{ws}, due to combined wave and surge overtopping was calculated at both discharge measurement locations using data points 3,000 to 59,400 (564 seconds at 100-Hz rate) for each time series. This data range did not include any measurements from the initial steady overflow portion at the start of the experiment before waves arrived at the levee. In theory, the calculated average overtopping discharges, whether it be for steady overflow or for combined wave and surge overtopping, should be the same at both measurement locations for each experiment because the overall mass of overtopping water is conserved. However, this was not the case, and appropriate corrections were made as described below.

3.7.2.1 Adjustment for Discharge Continuity Test Series

Figure 3.13 plots the calculated mean steady overflow and mean combined wave and surge overtopping discharges for all nine of the discharge continuity experiments (Runs 13 through 21). The values have been scaled to prototype size using the prototype-to-model model length of N_L = 25. The solid diagonal line is the line of equivalence, and the plotted points indicate that the mean estimates at location P6 on the levee slope are all greater than the corresponding estimates at levee crest location P2. Thus, the error is most likely systemic (pertaining to the system) rather than random.

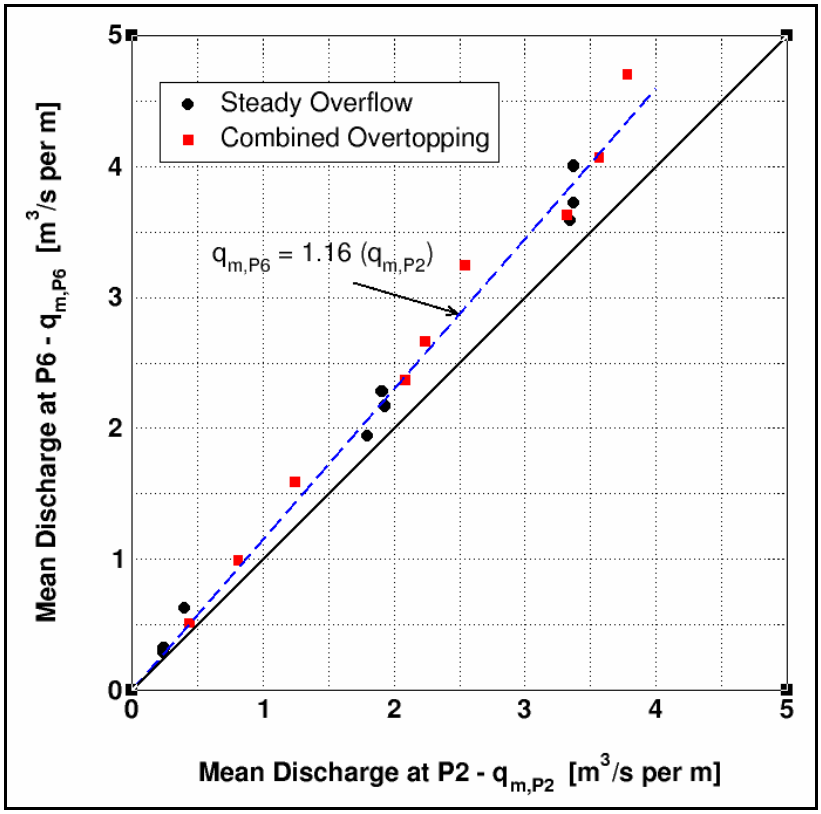

Figure 3.13. Mean overtopping discharge for discharge continuity test series.

The two main potential sources of systematic measurement error are errors in velocity and errors in flow thickness. The velocity measurements were considered to be more accurate than flow thickness pressure measurements because the LDVs are factory calibrated and verified well beyond the range of velocities encountered during the experiments. There are no user adjustments available that would alter the LDV calibration in any way. The pressure gauge calibration was the most likely source of difference in discharge means. Pressure gauges were calibrated hydrostatically prior to installation, and the calibration was checked by flooding the flume to submerge the gauges. However, the accuracy of the gauge at location P6 was harder to verify during the static checking because the surface of pressure transducer is mounted at an angle relative to the horizontal. Therefore, there is some uncertainty as to the elevation of the gauge relative to the horizontal water surface during static calibration tests.

The mean values plotted on Figure 3.13 exhibited a distinct linear trend, and a linear regression forced through the origin (dashed line) had a correlation coefficient of 0.994. An error in one or both of the pressure gauge calibration factors would explain the observed linear bias in the comparison. The pressure gauge located on the levee crest at location P2 was considered to be more accurate than the gauge at location P6. On the crest, the pressure is closer to being hydrostatic than on the landward-side slope, and estimates of the surge elevation above the crest using calculated values of q in Eqn. 2.1 were closer to the target values set using a point gauge in the flume. Similar estimates of surge level using the P6 estimates of steady overflow discharge did not match as closely.

Assuming the velocities are accurate and the P2 discharge estimates are nearly correct, the conclusion was that flow thicknesses at location P6 were overestimated by about 16 percent as indicated by the linear regression shown on Figure 3.13. As mentioned, pressures measured on the landward-side slope were not hydrostatic, and a theoretical correction given in Henderson (1966) was applied to the measurements.

To examine continuity of the instantaneous overtopping discharge, it was necessary that mean discharges at the two measurement locations be reasonably close for each experiment. This requires that mass flux integrated over time must be conserved, thus allowing analysis of the instantaneous discharge. To meet this overall mass conservation requirement, the measured and previously adjusted flow thicknesses at location P6 were decreased by a factor of 0.86, and the instantaneous overtopping discharge time series at location P6 were recalculated for all tests.

Table 3.5 presents the steady overflow and corrected combined wave and surge overtopping discharges per unit length at locations P2 and P6 for all discharge continuity experiments. Also included are the incident wave parameters and the surge elevation above the levee crest (negative freeboard) calculated from Eqn. 2.1 using the values of steady overflow q determined at location P2. The parameter $T_{m\text{-}1,0}$ is the mean spectral energy wave period. All parameter values in Table 3.5 have been converted to prototype scale units using the length scale of $N_L = 25$.

Table 3.5. Mean Overtopping Discharge for Runs 13 - 21 (Prototype Scale).

Run	Prototype-Scale Parameters				Position P2		Position P6	
	H_{mo} (m)	T_p (s)	$T_{m-1,0}$ (s)	R_c (m)	q (m^3/s/m)	q_{ws} (m^3/s/m)	q (m^3/s/m)	q_{ws} (m^3/s/m)
R13	0.88	6.02	5.47	-0.268	0.236	0.436	0.255	0.459
R14	1.76	10.44	8.75	-0.273	0.242	0.807	0.282	0.874
R15	2.59	13.85	9.79	-0.381	0.401	1.239	0.544	1.372
R16	0.69	5.88	5.63	-1.034	1.792	2.078	1.677	2.037
R17	1.63	10.04	8.57	-1.086	1.928	2.231	1.874	2.296
R18	2.51	13.85	10.47	-1.078	1.907	2.531	1.969	2.790
R19	0.68	6.02	5.62	-1.565	3.337	3.322	3.099	3.132
R20	1.63	10.04	8.58	-1.576	3.372	3.557	3.208	3.503
R21	2.45	13.85	10.28	-1.576	3.373	3.762	3.458	4.039

3.7.2.2 Adjustment for Shear Stress Test Series

The shear stress test series had co-located velocity and flow thickness measurements at locations designated as P4 and P7 in Figure 3.8. A similar adjustment as described above was applied to these measurements to assure that the average overtopping discharge were reasonably close in magnitude. It was assumed that the best estimate of mean discharge came from the gauges located at position P4, and that the flow thickness at location P7 should be adjusted as necessary to match the discharge at location P4. Because location P4 is on the landward-side slope, the estimate of mean discharge is probably not as reliable as estimates made on the levee crest at location P2 during the discharge continuity test series.

Figure 3.14 plots the average discharge for steady overflow and combined wave and surge overtopping estimated at locations P4 and P7. The discharge estimates at location P7 were consistently greater than at location P4 by about 7 percent, so the flow thickness shift factors were reduced by a factor of 0.94 to give a better match. Runs 25 and 27 were eliminated from further consideration because their discharge values were outside the region that could be explained by a systematic error (see Figure 3.14). This problem was likely due to the small flow thickness at locations P4 and P7 during the lowest surge overflow levels.

Table 3.6 presents the steady overflow and corrected combined wave and surge overtopping discharges per unit length at locations P4 and P7 for all shear stress experiments. Also included are the incident wave parameters and the surge elevation above the levee crest (negative freeboard) calculated from Eqn. 2.1 using the values of steady overflow q determined at location P4. Note that Runs 25 and 27 are not included in the table. All

parameter values in Table 3.6 have been converted to prototype scale size using the length scale of $N_L = 25$.

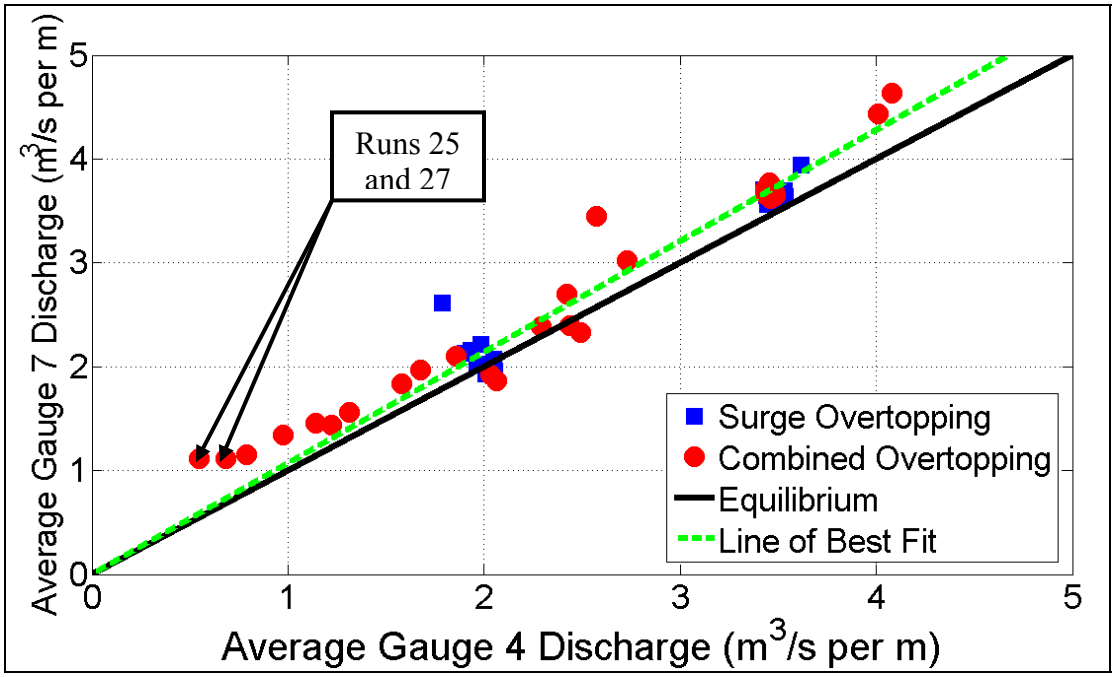

Figure 3.14. Mean overtopping discharge for shear stress test series.

Table 3.6. Mean Overtopping Discharge for Runs 26 - 51 (Prototype Scale).

Run #	Prototype-Scale Parameters				Position P4		Position P7	
	H_{mo} (m)	T_p (s)	$T_{m-1,0}$ (s)	R_c (m)	q (m^3/s/m)	q_{ws} (m^3/s/m)	q (m^3/s/m)	q_{ws} (m^3/s/m)
R26	0.92	10.40	8.70	—	—	0.68	—	1.04
R28	1.78	6.02	5.47	—	—	0.97	—	1.25
R29	1.77	10.44	8.72	—	—	1.14	—	1.36
R30	1.78	14.62	10.64	—	—	1.31	—	1.46
R31	2.56	6.02	5.70	—	—	1.22	—	1.34
R32	2.63	10.04	8.81	—	—	1.58	—	1.72
R33	2.58	14.62	9.96	—	—	1.67	—	1.84
R34	0.85	6.02	5.65	-1.12	2.03	2.04	1.83	1.80
R35	0.85	10.04	8.63	-1.12	2.01	2.06	1.80	1.74
R36	0.84	13.85	11.34	-1.08	1.90	1.86	1.99	1.97
R37	1.61	5.88	5.46	-1.10	1.96	2.29	1.89	2.23
R38	1.73	10.04	8.50	-1.13	2.05	2.44	1.93	2.24
R39	1.71	13.85	11.23	-1.13	2.06	2.49	1.83	2.18
R40	2.47	5.88	5.62	-1.09	1.93	2.42	2.02	2.53
R41	2.60	10.04	8.61	-1.11	1.98	2.73	2.07	2.82
R42	2.53	13.85	10.65	-1.03	1.79	2.57	2.45	3.22
R43	0.70	6.02	5.53	-1.59	3.43	3.43	3.46	3.47
R44	0.78	10.04	8.55	-1.60	3.44	3.44	3.41	3.42
R45	0.80	13.12	11.39	-1.60	3.45	3.46	3.33	3.39
R46	1.27	6.02	5.53	-1.61	3.49	3.48	3.38	3.41
R47	1.62	10.04	8.46	-1.62	3.50	3.48	3.36	3.45
R48	1.64	13.12	11.05	-1.62	3.52	3.48	3.38	3.43
R49	2.37	6.02	5.61	-1.63	3.53	3.46	3.40	3.52
R50	2.53	10.04	8.35	-1.62	3.53	4.01	3.46	4.14
R51	2.54	13.85	10.40	-1.65	3.62	4.08	3.69	4.33

*Runs 25 and 27 were excluded as previously noted.

CHAPTER 4 – EXPERIMENTAL TEST RESULTS

This chapter presents results and analyses from the physical model experiments. The first section contains analysis of results from the 9 experiments that comprised the discharge continuity test series. These results were previously summarized in Hughes and Shaw (2011). The second section contains analysis from the 25 valid tests conducted in the shear stress test series. Additional details on the shear stress test series are given in Shaw (2010).

4.1 Discharge Continuity Test Series Results

4.1.1 Continuity of Instantaneous Overtopping Discharge

The time series of instantaneous overtopping flow velocity and flow thickness resemble an irregular sequence of saw teeth characterized by a rapid increase up to the peak value with arrival of the wave leading edge, followed by a slower decrease in flow velocity and flow thickness values as the wave passes a position on the levee (see Figure 4.1 for an example). Time series measurements of overtopping flow parameters can be analyzed using standard time-domain procedures to produce representative parameters that are a convenient representation of the irregular waves and unsteady flow condition. For example, all data points contained in a measured velocity time series could be analyzed to produce representative parameters such as the mean velocity or the root-mean-squared velocity, or the time series could be represented as the distribution of measured velocities. Another approach is to apply the zero-upcrossing method to the time series to identify the peak velocities associated with individual waves. Then parameters could be determined that describe the distribution of the velocity peaks. Example peak velocity parameters might be the average of the highest 1/3 peaks, designated as $V_{p,1/3}$, and the velocity magnitude exceeded by just 2% of the velocity peaks, i.e., $V_{p,2\%}$.

Representative parameters describing overtopping flow thickness and flow velocity must be referenced to a specific location on the levee crest or landward-side slope because of changes that occur to the parameters between locations. For example, the mean flow thickness for unsteady overtopping on the levee crest is greater than the mean flow thickness on the landward-side slope. The opposite is true of velocity with higher mean velocities on the landward-side slope than on the crest. Therefore, the mean and other representative velocity and flow thickness time series parameters depend on specific location on the levee crest or landward-side slope.

The instantaneous overtopping discharge $q(t)$ per unit length of levee at a location across the levee crest or down the landward-side levee slope is the integration of the instantaneous slope-parallel velocity over the slope-perpendicular flow thickness at the location. The average (or mean) wave and surge overtopping discharge per unit length of levee crest, q_{ws}, is simply the mean value of the calculated instantaneous overtopping discharge time series over a specified duration.

It is known from mass continuity that mean wave overtopping discharge will be the same at each location on the levee crest and landward-side slope provided there are no along-

crest variations in forcing conditions or levee geometry. Still unanswered is the question of whether or not other parameters of the instantaneous overtopping discharge are the same at all locations. It is conceivable that the details of instantaneous discharge time series on the levee crest will be different from the time series farther down the landward-side slope while still producing the same mean value. If this is the case, then it would be necessary to associate discharge parameters (other than the mean) with a specific location on the levee. On the other hand, if the instantaneous discharge time series remains unchanged from one location to the next as the waves and surge overtop the levee, the task of characterizing overtopping parameters on a trapezoidal levee becomes independent of location.

The tentative hypothesis that the time series of instantaneous overtopping discharge due to combined wave overtopping and steady surge overflow was preserved during the overtopping process was previously offered by Nadal and Hughes (2009). Synoptic measurements of flow velocity and flow thickness acquired at the same position on a small-scale physical model levee crest were used to calculate time series of instantaneous discharge. By assuming the same discharge time series would occur at other locations on the landward-side levee slope after a very short time lag, it was possible to calculate an estimate of the velocity time series at other locations based on the measured flow thickness at those locations. In other words, each value of the time-shifted discharge time series was divided by the corresponding value of the flow thickness time series to derive an estimate of velocity time series at that location.

The discharge continuity test series in this study was conceived and conducted to test the hypothesis that the instantaneous discharge time series arising from combined wave overtopping and storm surge overflow is preserved during unsteady overtopping of a trapezoidal level cross section. If the continuity of instantaneous discharge is shown to be true, the task of developing empirical formulations for representative overtopping discharge parameters is simplified because there is no dependence on specific position on the levee crest or landward-side slope. An additional benefit is that measurements needed to calculate the instantaneous discharge time series can be made on the levee crest where flows are slower and have less air entrainment. Farther down the landward-side slope where velocity measurements are problematic, it may be feasible to estimate flow velocity using only flow depth measurements at that location along with the time-shifted discharge time series, as was done by Nadal and Hughes (2009).

Time series of flow thickness, velocity, and calculated overtopping discharge at levee crest location P2 and landward-side slope location P6 were plotted for all nine experiments. (See Figure 3.7 for P2 and P6 locations.) Example plot extracts are given in Figures 4.1, 4.2, and 4.3. All time series values have been scaled from model to prototype size using the length scale N_L = 25 to give a better sense of magnitudes relative to an actual levee.

Figure 4.1 was extracted from Test R14 that had a steady surge level 0.27 m above the crest elevation and irregular wave parameters of H_{mo} = 1.76 m and T_p = 10.4 s (prototype-scale parameters). During this test the crest would occasionally go dry between waves, and the landward-side slope went dry more often as seen in the upper plot of Figure 4.1. Velocities at location P6 on the slope exhibit a good bit of noise during periods when the

LDV beams were submerged. This was likely caused by the relatively thin flow thickness causing turbulence in the water column. On the crest, velocity measurements appear smooth, but the water level fell below the LDV beams between many of the waves as evidenced by the horizontal lines between waves. The calculated discharge time series at both locations are very similar as seen in the lower plot of Figure 4.1. If not for the short time lag between the two measurement locations, the discharge time series would nearly coincide.

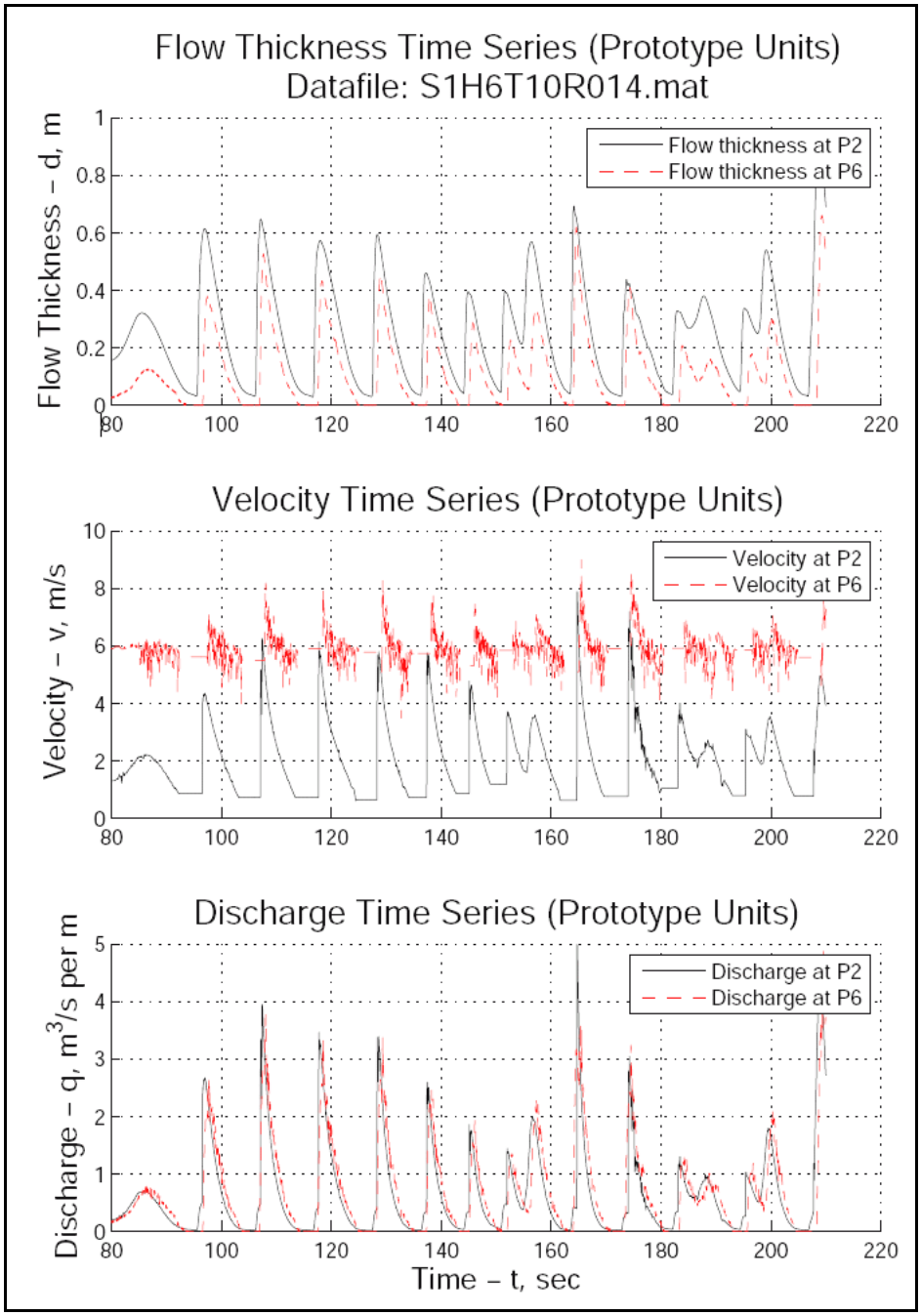

Figure 4.1. Time series extract of flow thickness, velocity, and discharge from Run 14.

The time series shown on Figure 4.2 were extracted from Test R18 that had a steady surge level of 1.08 m (prototype scale) above the crest elevation and prototype-scale irregular wave parameters of H_{mo} = 2.5 m and T_p = 13.9 s. During this test the landward-side slope went dry occasionally, and the LDV beams (set at steady overflow mid-depth) regularly were out of the flow. The comparison of discharge time series is once again very good. Note the spikes in the discharge time series at location P6. These spikes originated in the pressure record, and they were not eliminated by the non-aggressive spike removal routine.

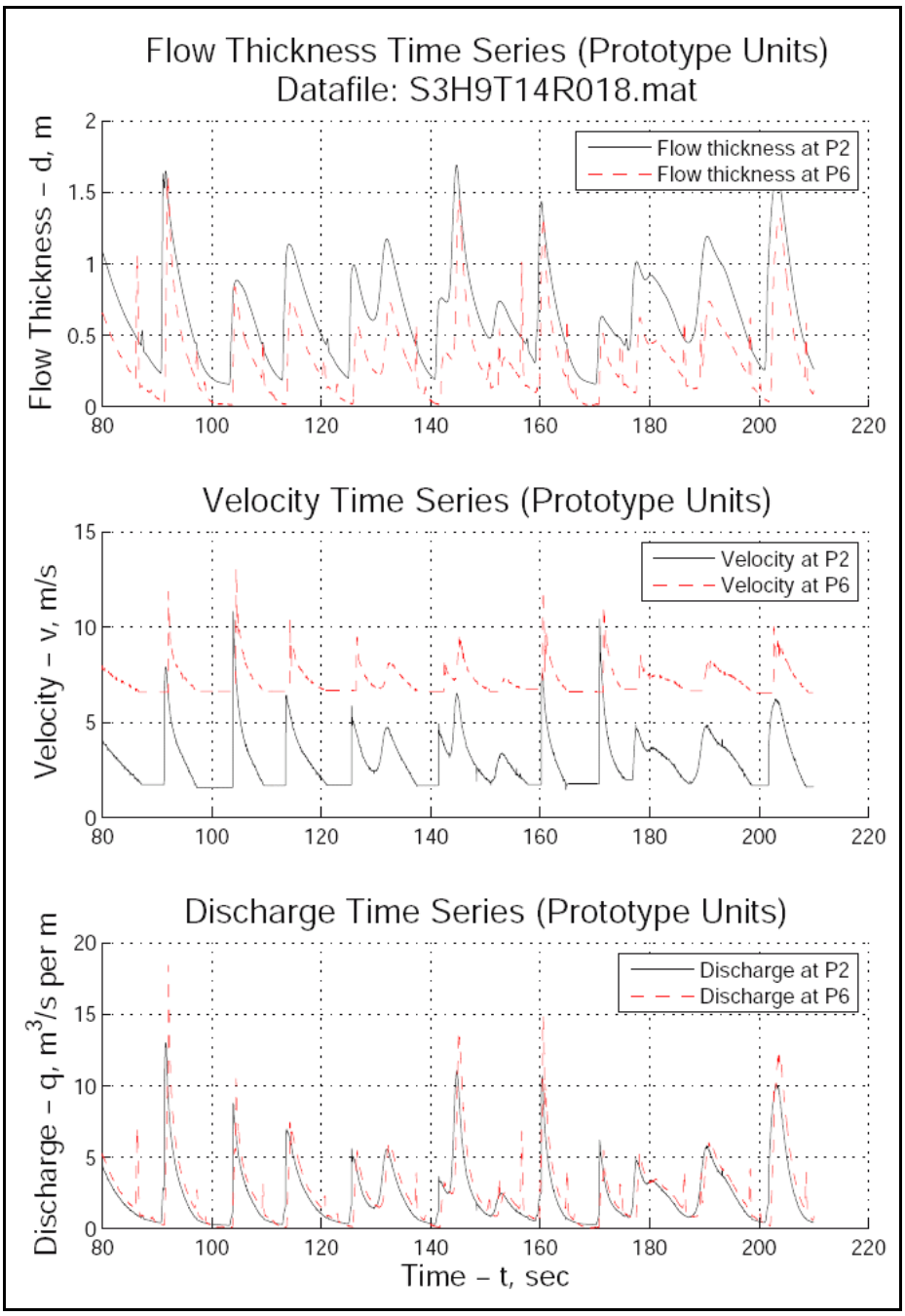

Figure 4.2. Time series extract of flow thickness, velocity, and discharge from Run 18.

The Test R20 time series extract shown on Figure 4.3 had a steady surge level 1.58 m above the crest elevation and irregular wave parameters of H_{mo} = 1.63 m and T_p = 10.0 s. At this surge level the levee never went dry between waves, and the LDV beams were almost always immersed in the flow. Comparison of instantaneous discharge was for the most part very good.

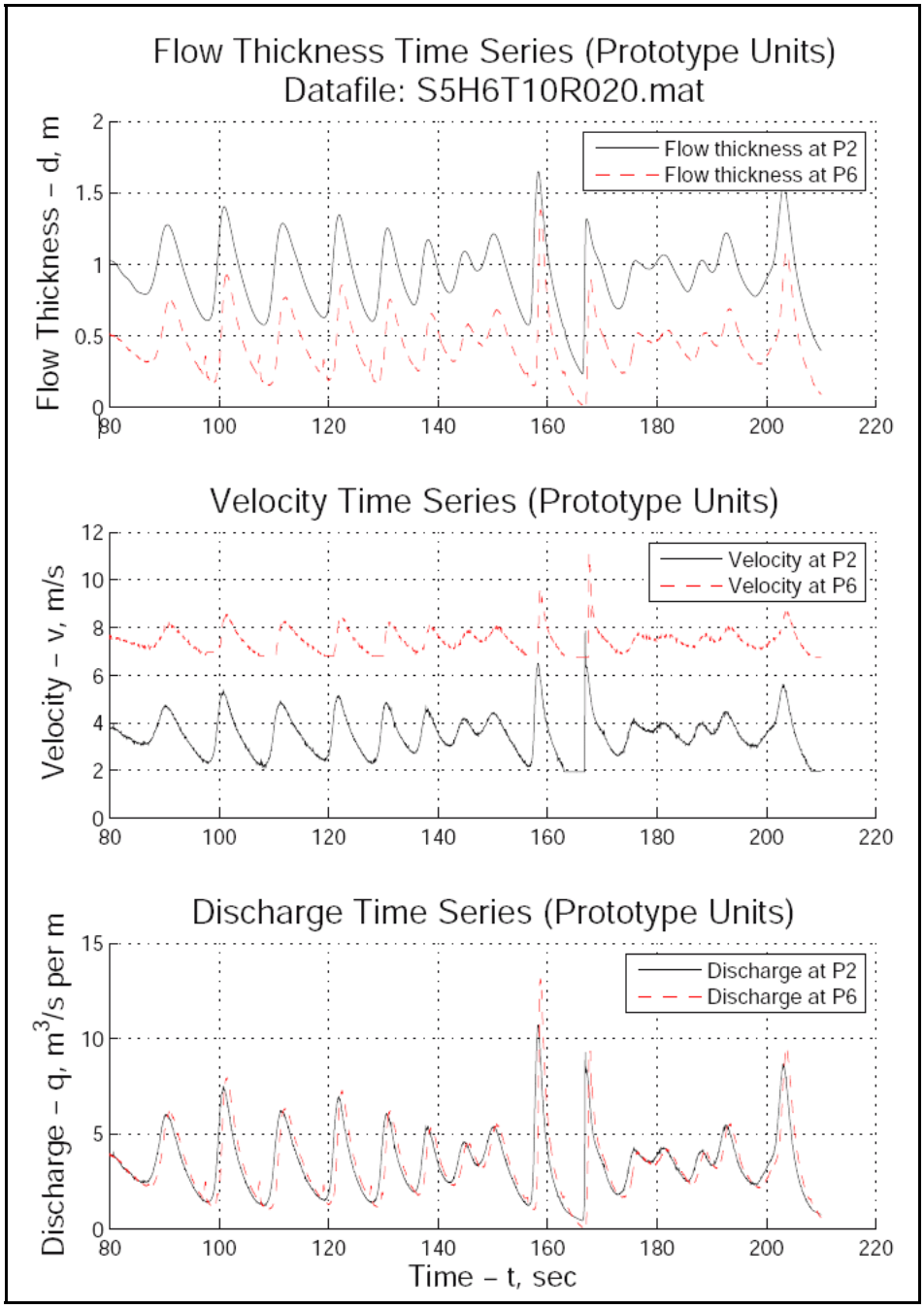

Figure 4.3. Time series extract of flow thickness, velocity, and discharge from Run 20.

Other portions of the time series from these three tests (and the other six tests) exhibited similar characteristics as illustrated by Figures 4.1 through 4.3 giving at least visual support for the hypothesis that instantaneous discharge for combined wave and surge overtopping is conserved between the levee crest and the landward-side slope.

An attempt was made to quantify the similarity between the overtopping discharge time series calculated at locations P2 and P6. The discharge time series at P6, $q_6(t)$, was shifted by time increments of $\tau = 0.01$ s (model scale) relative to the time series at P2, $q_2(t)$. After each time shift, the root-mean-squared (RMS) difference between the two discharge time series was calculated for the range of data points between 3,000 and 59,350 according to the formula

$$\Delta q_{rms} = \frac{1}{n}\sqrt{\sum^{n}\left[q_{6_n}(t+\tau) - q_{2_n}(t)\right]^2} \tag{4.1}$$

where n = 56,350 is the number of data points in the range and τ is the time shift. The minimum value of Δq_{rms} was found where the two time series most closely aligned. Table 4.1 lists the RMS difference between the discharge time series for all nine tests in prototype-scale units of discharge per unit length of levee. The absolute values of RMS difference are quite small and fairly consistent, with the maximum approaching 4 l/s/m (prototype scale). Table 4.1 also has columns that express the RMS difference as a percentage of the mean wave and surge overtopping discharge for each test. The percentages are all less than 0.3 percent, and the percentage decreases as the mean discharge increases.

Table 4.1. RMS Difference Between Discharge Time Series at Locations P2 and P6.

Run	Δq_{rms} (m^3/s/m)	% of q_{ws}	Run	Δq_{rms} (m^3/s/m)	% of q_{ws}	Run	Δq_{rms} (m^3/s/m)	% of q_{ws}
R13	0.0009	0.21	R16	0.0017	0.08	R19	0.0009	0.03
R14	0.0019	0.24	R17	0.0027	0.12	R20	0.0015	0.04
R15	0.0031	0.25	R18	0.0038	0.15	R21	0.0033	0.10

Thus, it is concluded that the laboratory measurements support the hypothesis that the unsteady time series of instantaneous overtopping at a trapezoidal levee by combined surge overflow and wave overtopping is conserved at all locations along the levee crest and down the landward-side slope. No measurements were made of wave-only overtopping with a positive freeboard, so it is not possible to state with certainty that similar continuity of instantaneous overtopping would also apply for wave-only overtopping. However, overtopping of individual waves for tests with the lowest surge levels (lowest negative freeboard) resembled the case of wave-only overtopping with low positive freeboard. As the wave troughs arrived at the levee, the levee crest and landward-side slope went dry the same way it does for intermittent wave-only overtopping with an emergent crest. Thus, there is reason to believe that continuity of instantaneous overtopping discharge would also apply to cases of wave-only overtopping that have relatively high mean discharge.

4.1.2 Estimation of Individual Overtopping Discharge Peaks

The peak instantaneous discharge for each individual wave in the overtopping discharge time series was determined for all the waves in all nine discharge continuity experiments. The peak discharge occurred near the leading front of the overtopping waves where the velocity and flow thickness are greatest. For each experiment the root-mean-squared (RMS) peak discharge, $Q_{p,rms}$, was determined from the rank-ordered peak discharges along with the representative peak parameters $Q_{p,1/3}$, $Q_{p,1/10}$, and $Q_{p,1/100}$ (average of the highest 1/3, 1/10, and 1/100 discharge peaks, respectively). These discharge peak parameters are listed in Table 4.2.

Table 4.2. Discharge Peak Parameters at Location P2.

Run	$Q_{p,mean}$ (m^3/s per m)	$Q_{p,rms}$ (m^3/s per m)	$Q_{p,1/3}$ (m^3/s per m)	$Q_{p,1/10}$ (m^3/s per m)	$Q_{p,1/100}$ (m^3/s per m)
13	1.23	1.36	1.92	2.47	3.31
14	2.97	3.31	4.64	5.66	7.59
15	4.77	5.65	8.26	10.57	15.89
16	2.86	2.95	3.69	4.26	5.07
17	4.95	5.45	7.66	9.41	11.30
18	7.32	8.09	11.25	13.41	16.29
19	4.02	4.08	4.82	5.44	6.62
20	6.02	6.38	8.45	10.17	12.13
21	8.67	9.49	13.18	16.28	19.74

Figure 4.4 presents a plot of the dimensionless peak RMS discharge, $Q_{p,rms}/q_{ws}$, as a function of relative freeboard, R_c/H_{m0}, where R_c is freeboard (negative) and H_{m0} is the energy-based significant wave height.

At low values of negative relative freeboard, the root-mean-square peak discharge is between 3 and 5 times the average overtopping discharge. As the overflow surge level increases (or incident wave height decreases) the RMS peak discharge decreases relative to the mean combined wave and surge overtopping discharge. The solid line shown on Figure 4.4 is the best-fit given by the equation

$$\frac{Q_{p,rms}}{q_{ws}} = 1 + 4.18 \exp\left[-1.56\left(\frac{-R_c}{H_{m0}}\right)^{0.88}\right] \qquad \text{for } (R_c < 0) \qquad (4.2)$$

The best-fit curve given by Eqn. 4.2 had a correlation coefficient of 0.986 and an RMS percent error of 0.058. Estimates of the mean overtopping discharge, q_{ws}, can be made using Eqn. 2.37.

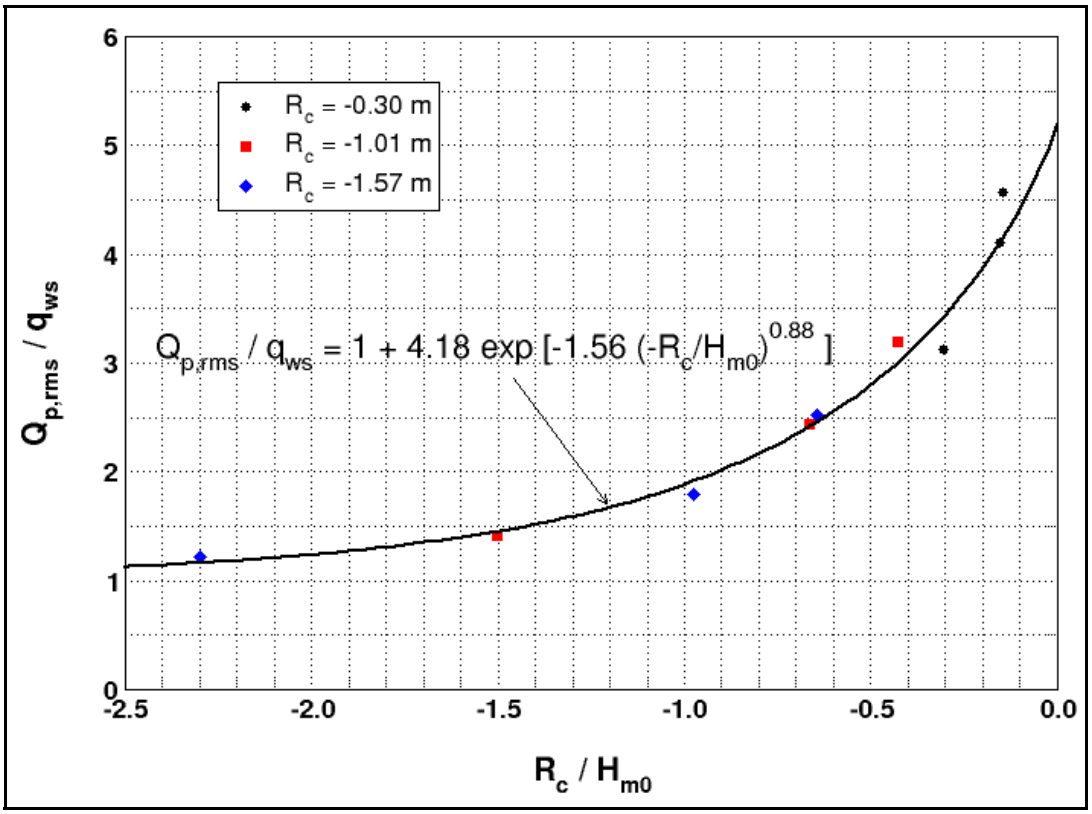

Figure 4.4. Estimation of the root-mean-squared peak discharge, $Q_{p,rms}$.

Irregular wave heights are commonly represented by the Rayleigh distribution expressed in terms of the RMS wave height. To test whether the peak discharges of individual overtopping waves could also be represented by the familiar Rayleigh distribution, the cumulative percent exceedance probability distributions of the discharge peaks, normalized by $Q_{p,rms}$, were plotted and compared to the corresponding Rayleigh cumulative exceedance probability distribution given by the formula

$$P_{\%}(Q_p > Q_{p*}) = 100 \cdot \exp\left[-\left(\frac{Q_{p*}}{Q_{p,rms}}\right)^2\right] \tag{4.3}$$

where $P_{\%}$ is the percent probability of the peak discharge being greater than the reference discharge, Q_{p*}.

Generally, the Rayleigh distribution using measured values of $Q_{p,rms}$ provided a good approximation of the discharge peaks distribution at the lowest steady overflow level for all but the highest peaks in the distribution. The highest peaks were overestimated by the Rayleigh distribution. At the two higher steady overflow levels, the Rayleigh distribution was reasonable for cases with large overtopping waves; but when wave heights were smaller, the large steady overflow velocity severely distorted the discharge peaks distribution.

Figures 4.5 and 4.6 present two examples of the cumulative percent exceedance distributions. These figures illustrate the effect of wave height on the distribution of overtopping discharge peaks at the higher surge levels. The logarithmic ordinate in Figures 4.5 and 4.6 helps to distinguish the differences in the range of largest discharge peaks. The distributions given in Figures 4.5 and 4.6 came from experiments with the steady overflow level at about 1.0 m above the levee crest (R_c = –1.01 m scaled to prototype).

For the low wave height of H_{m0} = 0.69 m (prototype scale) the Rayleigh distribution (dashed line) shown on Figure 4.5 greatly over-predicts the peak discharges for the highest 30 percent of the peaks, and the distribution clearly is not a good representation of the data. However, when the wave heights were larger with H_{m0} = 2.51 m (prototype scale), only the highest 10 percent of the peaks are underestimated by the Rayleigh distribution as shown on Figure 4.6. Examination of the cumulative distribution from all nine experiments indicated that the Rayleigh distribution is reasonably successful for all but the highest 10 percent of discharge peaks in the relative freeboard range of $-0.7 < R_c/H_{m0} < 0$.

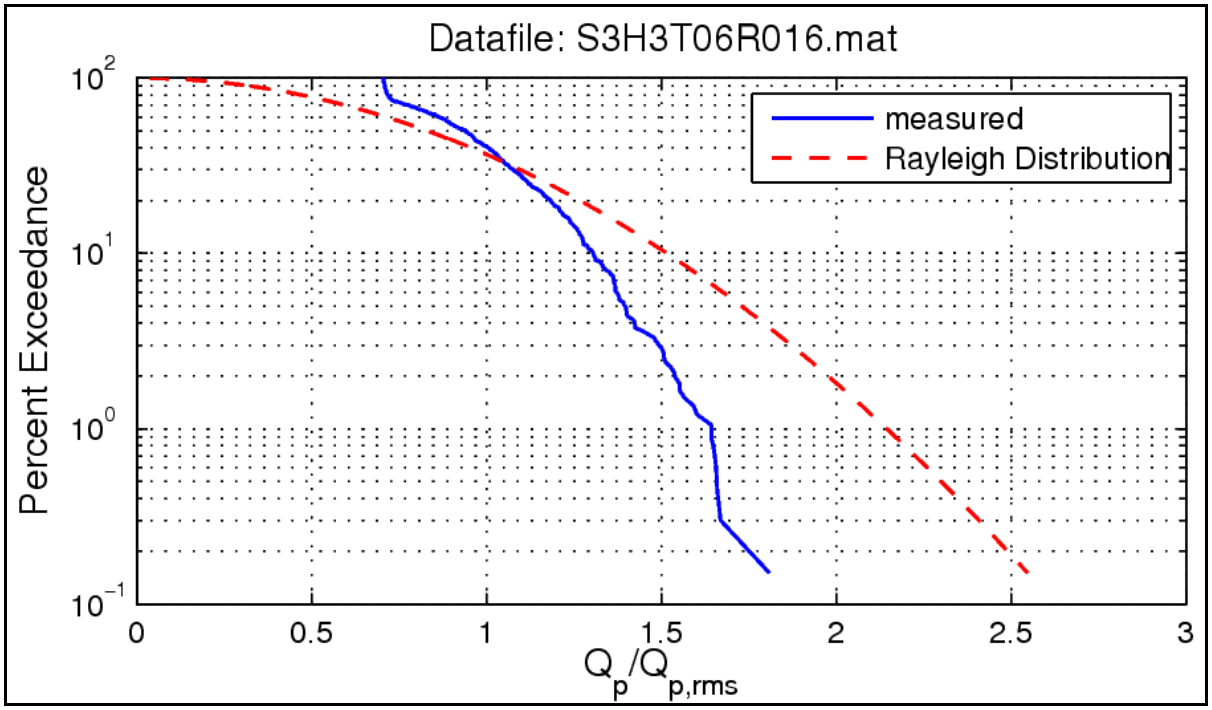

Figure 4.5. Cumulative percent exceedance probability distribution for R_c/H_{m0} = –1.50.

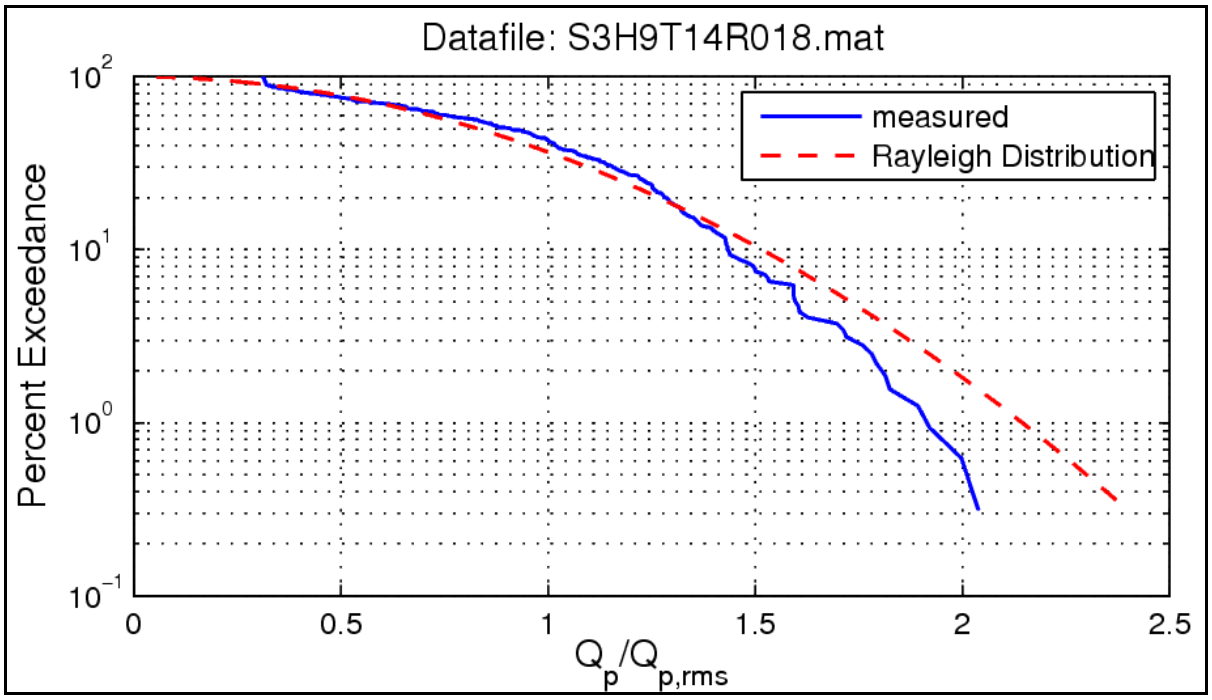

Figure 4.6. Cumulative percent exceedance probability distribution for R_c/H_{m0} = –0.43.

Estimates of the larger characteristic peak discharge parameters were made by substituting values of $Q_{p,rms}$ determined from measurements into the standard Rayleigh distribution formulas in Eqn. 4.4.

$$Q_{p,1/3} = 1.416 \cdot Q_{p,rms} \quad ; \quad Q_{p,1/10} = 1.80 \cdot Q_{p,rms} \quad ; \quad Q_{p,1/100} = 2.36 \cdot Q_{p,rms} \tag{4.4}$$

Comparisons between the actual peak representative parameters at location P2 (see Table 4.2) and those estimated from the Rayleigh distribution are shown on Figures 4.7, 4.8, and 4.9. The average of the highest 1/3 peaks are well predicted by the Rayleigh distribution (Figure 4.7). However, the Rayleigh distribution shows an increasing over-prediction of the higher parameters, $Q_{p,1/10}$, and $Q_{p,1/100}$, as seen in Figures 4.8 and 4.9 except at the lowest surge level. Nevertheless, Eqns. 4.2 through 4.4 provide reasonable first estimates of parameters related to the peak discharges of individual overtopping waves for the case of combined steady overflow and wave overtopping.

A predictive capability check of Eqns. 4.2 and 4.4 was conducted using representative peak discharge results obtained from time series measured during the shear stress test series (Section 4.2). Values of $Q_{p,1/3}$, $Q_{p,1/10}$, and $Q_{p,1/100}$ listed on Table 4.6 (discussed later) for locations P4 and P7 were compared to estimates of these peak parameters based on the Rayleigh distribution. Required values of $Q_{p,rms}$ were estimated using the measured mean overtopping discharge, q_{ws}, significant wave height, H_{m0}, and negative freeboard, R_c. The estimated value of $Q_{p,rms}$ was used in Eqn. 4.4. The comparison is shown on Figure 4.10. Generally, the comparison is not quite as good as seen for the discharge continuity test series.

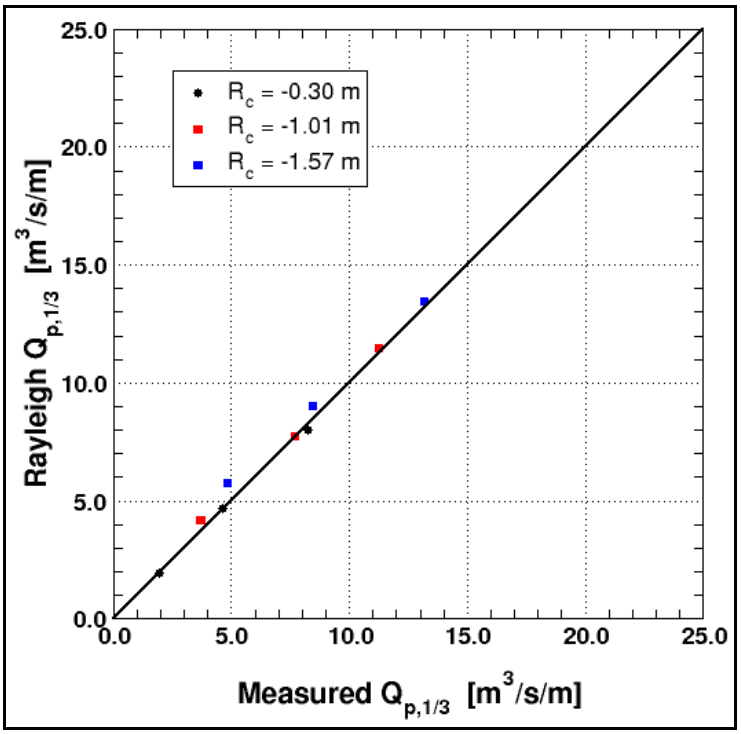

Figure 4.7. Prediction of $Q_{p,1/3}$ using measured $Q_{p,rms}$ (prototype scale).

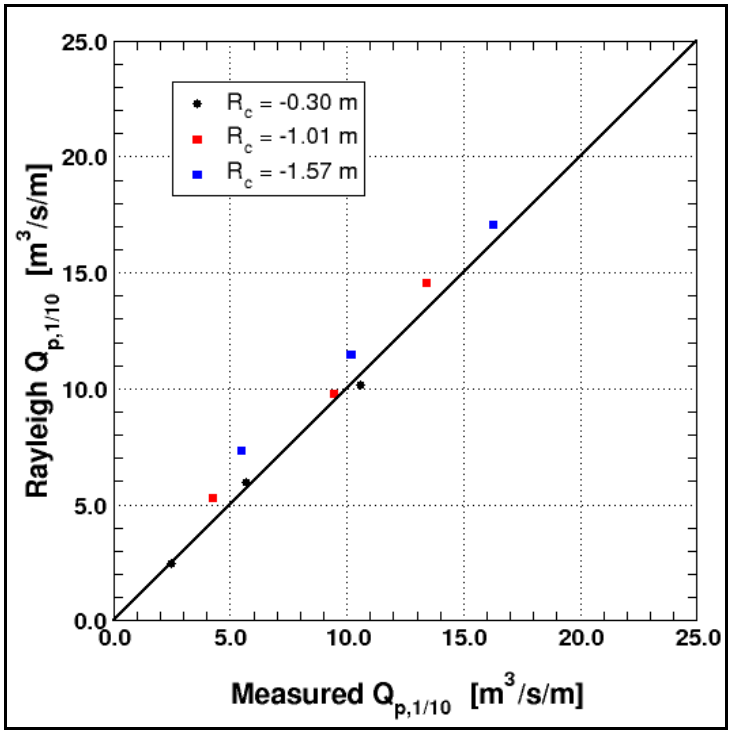

Figure 4.8. Prediction of $Q_{p,1/10}$ using measured $Q_{p,rms}$ (prototype scale).

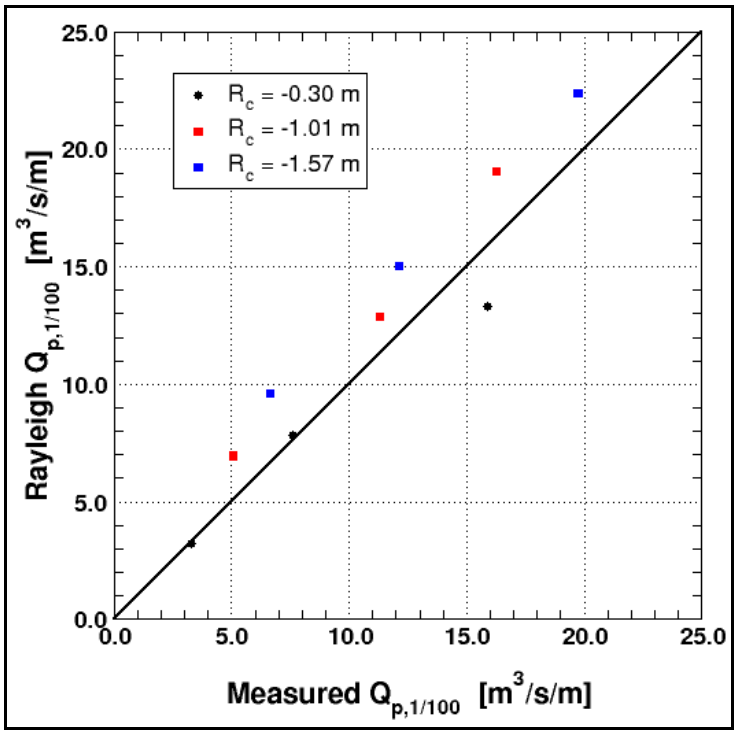

Figure 4.9. Prediction of $Q_{p,1/100}$ using measured $Q_{p,rms}$ (prototype scale).

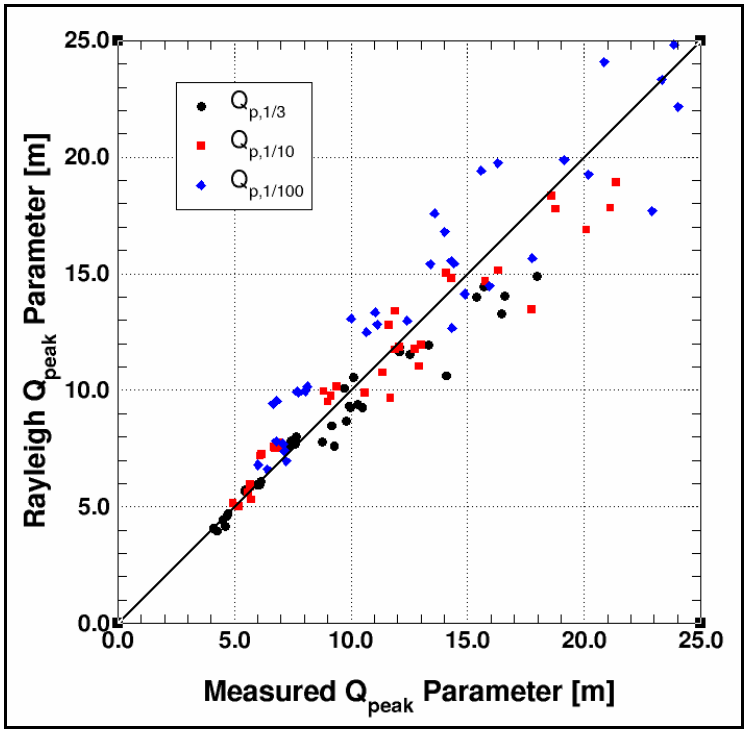

Figure 4.10. Prediction of discharge peak parameters using estimated $Q_{p,rms}$ (prototype scale).

4.1.3 Stream Power and Overtopping Discharge

The concept of stream power was introduced by Bagnold (1960, 1966). Bagnold considered the relationship between the rate of energy available and the rate of work being done in transporting sediments. Bagnold defined stream power (P_s) as power per unit area of stream bed, which could be expressed as shear stress (τ_0) times the free-stream flow velocity (v), as shown in Eqn. 4.5.

$$P_s = \tau_0 \cdot v \tag{4.5}$$

Stream power is defined as the rate of doing work, or as a measure of the energy available for moving rock, sediment particles, or woody or other debris in the stream channel. Thus, stream power has been directly related to sediment transport rates (USDA 2001). Given the wide-spread use of stream power as an estimator of sediment transport and erosion in rivers and stream, this same concept may prove valuable as an indicator of levee slope erosion due to wave overtopping combined with surge overflow.

Stream power at a location on the landward-side levee slope can be expressed in terms of instantaneous overtopping discharge by substituting Eqn. 2.42 into Eqn. 4.5 and noting that $v(t) \cdot h(t) = q(t)$, as shown in Eqn. 4.6.

$$P_s(t) = \tau_0(t) \cdot v(t) = \gamma_w \left[h(t)\, v(t)\right] S_f(t) = \gamma_w\, q(t)\, S_f(t) \tag{4.6}$$

In Eqn. 4.6 the instantaneous discharge is the same everywhere on the levee crest and landward-side slope as shown in section 4.1.1, but stream power will vary because the friction slope varies with location. However, farther down the landward-side slope the flow may reach a quasi-equilibrium balance between the forcing and slope resistance; and the friction slope will reduce to $S_f = \sin\theta = S_0$. For this special case, stream power will be the same at all locations where $S_f = \sin\theta$.

The cumulative probability distribution of stream power on the landward-side slope arising from combined wave overtopping and storm surge overflow can be derived using an empirical probability distribution for instantaneous discharge presented by Hughes and Nadal (2009). The overtopping discharge cumulative distribution of percent exceedance was given by Hughes and Nadal as

$$P_{\%}(q > q_*) = 100 \cdot \exp\left[-\left(\frac{q_*}{c}\right)^b\right] \tag{4.7}$$

where q_* is a specified threshold, and the shape factor b and the scale factor c are given by the following expressions

$$b = 8.10\left(\frac{q}{g\,H_{m0}\,T_p}\right)^{0.34} \tag{4.8}$$

and

$$c = \frac{q_{ws}}{\Gamma\left(1+\frac{1}{b}\right)} \tag{4.9}$$

In Eqns. 4.8 and 4.9, q is the steady overflow discharge from Eqn. 2.1, g is gravitational acceleration, H_{m0} is the energy-based significant wave height, T_p is peak spectral wave period, q_{ws} is the combined wave and surge average overtopping discharge from Eqn. 2.37, and Γ is the mathematical gamma function. The corresponding probability density function for instantaneous overtopping discharge is given by $\partial P/\partial q$, as shown in Eqn. 4.10.

$$p_d(q) = \frac{b}{c}\left(\frac{q}{c}\right)^{(b-1)} \exp\left[-\left(\frac{q}{c}\right)^{b}\right] \tag{4.10}$$

For locations on the slope where the friction slope is the same as the levee landward-side slope (i.e., $S_f = S_0 = \sin\theta$), the probability density function for instantaneous, unsteady overtopping stream power acting on the landward-side slope can be estimated as follows

$$p_d(P_s) = \gamma_w \sin\theta \cdot p_d(q) = \gamma_w \sin\theta \cdot \left\{\frac{b}{c}\left(\frac{q}{c}\right)^{(b-1)} \exp\left[-\left(\frac{q}{c}\right)^{b}\right]\right\} \tag{4.11}$$

The probability density function for stream power given by Eqn. 4.11 could be used in models presently being developed for estimating erosion potential as a function of unsteady overtopping duration.

4.2 Shear Stress Test Series Results

4.2.1 Representative Overtopping Flow Parameters

Measured time series of flow thickness and velocity at locations P4 and P7 (see Figure 3.8) were analyzed in the time domain to obtain representative parameters for each test. The raw time series had already been corrected and adjusted as described in Chapter 3 of this report. Table 4.3 presents the steady overflow mean flow thickness and the mean flow velocity (prototype scale units) for all valid tests in the test series. These values were calculated as the average of 600 data points acquired over a model time of 6 s during the first part of each experiment when only steady overflow occurred. Velocity was not acquired for steady overflow for runs 26 through 33 that had the lowest surge level. The flow at locations

P4 and P7 was too thin to acquire reliable velocity readings. Steady overflow discharge was listed with the experimental summary parameters shown in Table 3.6.

Table 4.3. Steady Overflow Mean Parameters at Locations P4 and P7 (Prototype Scale).

Run	Location P4		Location P7	
	Flow Thickness (m)	Velocity (m)	Flow Thickness (m)	Velocity (m)
26	0.07	—	0.10	—
28	0.07	—	0.09	—
29	0.07	—	0.07	—
30	0.07	—	0.08	—
31	0.07	—	0.03	—
32	0.10	—	0.06	—
33	0.10	—	0.07	—
34	0.39	5.27	0.24	7.68
35	0.38	5.24	0.23	7.67
36	0.36	5.24	0.26	7.67
37	0.37	5.24	0.25	7.67
38	0.39	5.26	0.25	7.67
39	0.39	5.25	0.24	7.67
40	0.37	5.26	0.26	7.68
41	0.38	5.26	0.27	7.67
42	0.34	5.28	0.32	7.69
43	0.59	5.76	0.43	8.11
44	0.60	5.75	0.42	8.11
45	0.60	5.76	0.41	8.10
46	0.61	5.76	0.42	8.11
47	0.61	5.75	0.41	8.11
48	0.61	5.75	0.42	8.10
49	0.62	5.75	0.42	8.11
50	0.62	5.74	0.43	8.10
51	0.63	5.75	0.45	8.11

For all tests the steady flow thickness at location P4 was larger than the flow thickness at location P7 and the opposite was true for velocity with faster velocities at P7. This indicated the steady overflow was accelerating between locations P4 and P7 on the landward-side slope. Figure 4.11 illustrates the measured depths for the steady overflow portion of the nine tests conducted at the highest surge level. The time series portion between prototype-scale times of 20 s and 50 s was analyzed for steady overflow mean values.

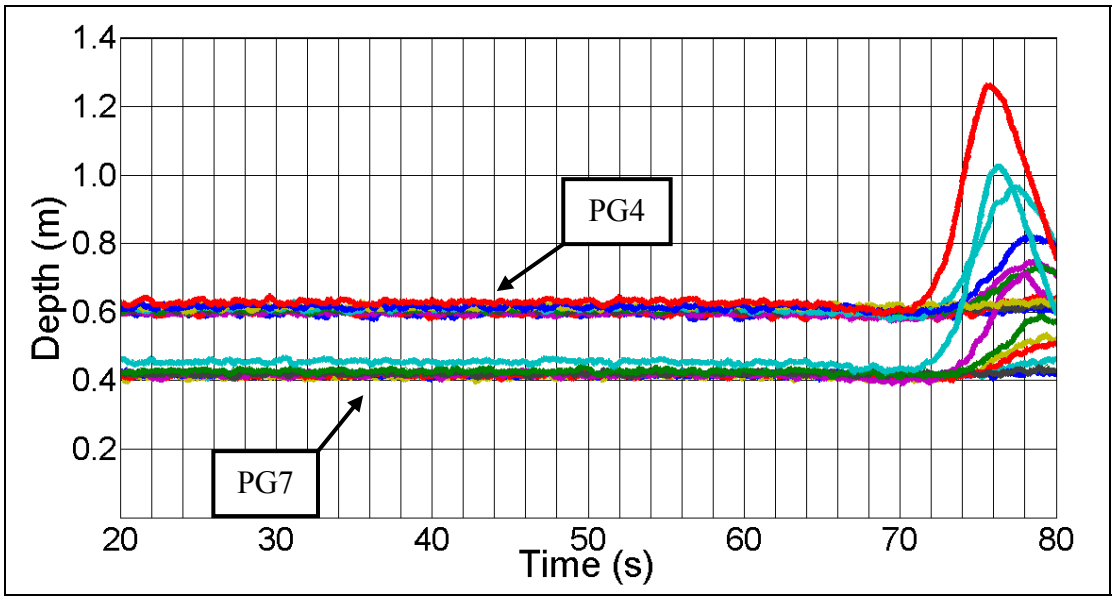

Figure 4.11. Surge overtopping flow thickness at P4 and P7 during Runs 43-51 (proto. scale).

Average flow thickness, velocity, and discharge are accurate and acceptable measures of storm surge steady overflow, but they are not fully descriptive of flow conditions on a levee's landward slope during combined wave and surge overtopping. Time series representative flow parameters on the landward-side slope for combined wave overtopping and steady overflow are given in Table 4.4 (flow thickness), Table 4.5 (velocity), and Table 4.6 (discharge). Parameters are listed for measurement locations P4 and P7. These flow parameters were determined by analyzing the 56,600 data points between the starting data point 3,400 and the end of the test at data point 60,000. This 566-s portion of the time series represented a prototype-scale time of 47 min 10 s.

The mean values listed in Tables 4.4 through 4.6 (i.e., h_{mean}, v_{mean}, and q_{ws}) are the averages of all data points in the analyzed portion of the time series. All other parameters pertain to the peak (or maximum) values associated with individual overtopping waves. For example, $h_{p,1/3}$ is the average of the highest 1/3 of the flow thickness peaks in the time series. Similarly, $h_{p,1/10}$ is the average of the highest 1/10 flow thickness peaks and $h_{p,1/100}$ is the average of the highest 1/100 flow thickness peaks. The individual peak parameters have been denoted using uppercase letters, but uppercase H is already used for wave height, so flow thickness peak parameters remain in lowercase.

Table 4.4. Combined Overtopping Flow Thickness Parameters (Prototype Scale).

Run	Prototype Flow Thickness (m)							
	Location P4				Location P7			
	h_{mean}	$h_{p,1/3}$	$h_{p,1/10}$	$h_{p,1/100}$	h_{mean}	$h_{p,1/3}$	$h_{p,1/10}$	$h_{p,1/100}$
26	0.13	0.48	0.56	0.71	0.14	0.39	0.45	0.52
28	0.18	0.61	0.72	0.93	0.16	0.47	0.54	0.63
29	0.21	0.81	0.98	1.28	0.17	0.61	0.73	0.82
30	0.24	1.02	1.26	1.57	0.18	0.75	0.86	0.94
31	0.23	0.78	0.93	1.15	0.17	0.57	0.66	0.79
32	0.28	1.07	1.32	1.52	0.21	0.84	1.01	1.13
33	0.29	1.33	1.62	1.89	0.22	1.05	1.23	1.35
34	0.38	0.75	0.85	1.02	0.23	0.46	0.53	0.61
35	0.38	0.76	0.87	1.01	0.22	0.49	0.57	0.66
36	0.34	0.74	0.87	1.04	0.25	0.52	0.63	0.76
37	0.41	1.05	1.20	1.37	0.28	0.72	0.83	0.93
38	0.42	1.19	1.40	1.72	0.27	0.84	0.99	1.11
39	0.43	1.28	1.57	1.83	0.27	0.94	1.14	1.25
40	0.42	1.25	1.41	1.64	0.31	0.92	1.04	1.15
41	0.45	1.53	1.84	2.09	0.34	1.20	1.42	1.55
42	0.42	1.65	1.98	2.43	0.38	1.47	1.68	1.82
43	0.59	0.86	0.94	1.01	0.43	0.63	0.70	0.76
44	0.59	0.92	1.01	1.12	0.42	0.87	0.95	1.05
45	0.60	0.95	1.04	1.17	0.42	0.69	0.78	0.89
46	0.59	1.11	1.30	1.45	0.42	0.82	0.96	1.06
47	0.58	1.33	1.52	1.74	0.42	1.06	1.22	1.34
48	0.58	1.39	1.64	1.96	0.41	1.13	1.34	1.49
49	0.58	1.53	1.72	1.86	0.42	1.22	1.37	1.48
50	0.64	1.82	2.10	2.39	0.49	1.57	1.82	1.93
51	0.65	1.95	2.30	2.72	0.51	1.80	2.08	2.27

Table 4.5. Combined Overtopping Velocity Parameters (Prototype Scale).

Run	Prototype Velocity (m/s)							
	Location P4				Location P7			
	v_{mean}	$V_{p,1/3}$	$V_{p,1/10}$	$V_{p,1/100}$	v_{mean}	$V_{p,1/3}$	$V_{p,1/10}$	$V_{p,1/100}$
26	4.87	7.06	7.71	8.52	7.44	9.21	9.76	10.49
28	5.10	7.91	8.37	8.97	7.61	10.42	11.15	12.17
29	5.04	8.48	9.13	10.11	7.58	11.15	12.04	13.12
30	5.04	8.86	9.74	10.97	7.57	11.59	12.81	14.36
31	5.12	8.30	8.79	9.99	7.64	11.01	11.75	13.06
32	5.18	9.24	10.09	11.35	7.67	11.90	12.91	14.46
33	5.16	9.72	10.76	11.78	7.68	12.64	13.96	16.49
34	5.27	6.36	6.96	8.21	7.68	9.02	9.84	11.10
35	5.27	6.34	6.84	7.71	7.68	8.91	9.64	10.66
36	5.24	6.36	6.85	7.92	7.68	8.78	9.36	10.33
37	5.36	7.78	8.69	9.45	7.78	10.95	12.15	13.21
38	5.40	8.53	9.35	10.82	7.82	11.51	12.75	14.47
39	5.39	8.23	9.09	10.68	7.80	10.93	12.29	14.61
40	5.44	8.78	9.65	11.07	7.85	12.05	13.21	14.66
41	5.52	9.50	10.39	11.68	7.93	12.72	14.14	15.90
42	5.53	9.48	10.41	11.55	7.90	12.70	14.29	16.42
43	5.75	6.38	6.54	6.69	8.10	8.74	8.92	9.11
44	5.73	6.50	6.68	6.88	8.08	8.81	8.98	9.22
45	5.72	6.51	6.69	6.98	8.08	8.80	8.99	9.24
46	5.71	6.88	7.29	7.82	8.06	9.47	10.18	11.89
47	5.68	7.57	8.34	9.46	8.03	10.46	11.89	13.09
48	5.67	7.55	8.32	9.81	8.02	10.07	11.12	13.05
49	5.65	8.32	9.05	10.30	8.01	11.88	13.39	14.98
50	5.77	9.14	10.15	11.70	8.10	12.63	14.05	15.54
51	5.77	8.94	9.92	11.11	8.08	11.85	13.38	15.69

Table 4.6. Combined Overtopping Discharge Parameters (Prototype Scale).

Run	Discharge (m^3/s per m)							
	Location P4				Location P7			
	q_{ws}	$Q_{p,1/3}$	$Q_{p,1/10}$	$Q_{p,1/100}$	q_{ws}	$Q_{p,1/3}$	$Q_{p,1/10}$	$Q_{p,1/100}$
26	0.68	2.99	3.71	5.13	1.04	3.31	3.97	5.06
28	0.97	3.81	4.52	5.42	1.25	4.27	5.03	6.52
29	1.14	5.57	7.10	9.11	1.36	6.06	7.64	9.25
30	1.31	7.43	9.35	12.76	1.46	7.67	9.31	11.02
31	1.22	5.08	6.11	7.51	1.34	5.45	6.67	8.79
32	1.58	7.75	9.68	12.70	1.72	8.40	10.82	14.46
33	1.67	10.20	13.10	16.10	1.84	11.32	14.02	16.59
34	2.04	4.68	5.67	7.09	1.80	4.10	4.92	6.01
35	2.06	4.72	5.66	6.79	1.74	4.24	5.17	6.41
36	1.86	4.61	5.70	7.22	1.97	4.50	5.57	7.16
37	2.29	7.59	9.12	11.12	2.23	7.31	8.99	10.66
38	2.44	9.16	11.34	14.87	2.24	8.75	10.58	12.41
39	2.49	9.79	12.89	15.94	2.18	9.28	11.68	14.32
40	2.42	9.71	11.60	14.01	2.53	10.11	11.86	13.58
41	2.73	12.52	15.74	20.17	2.82	13.32	16.31	19.14
42	2.57	14.10	17.74	22.90	3.22	16.45	20.08	24.03
43	3.43	5.45	6.08	6.66	3.47	5.46	6.14	6.81
44	3.44	5.96	6.69	7.69	3.42	5.94	6.74	7.74
45	3.46	6.12	6.91	8.12	3.39	6.07	6.96	8.04
46	3.48	7.65	9.38	11.04	3.41	7.41	8.82	10.01
47	3.48	9.91	12.06	14.30	3.45	9.98	11.88	13.40
48	3.48	10.30	12.98	17.76	3.43	10.49	12.71	14.41
49	3.46	12.06	14.30	15.58	3.52	12.06	14.06	16.28
50	4.01	15.37	18.77	23.32	4.14	15.71	18.58	20.85
51	4.08	16.60	21.11	26.41	4.33	17.96	21.36	23.85

Hughes and Nadal (2009) suggested a tentative equation relating the mean flow thickness on the landward-side levee slope to the combined wave and surge overtopping discharge. This expression, given by Eqn. 4.12, was determined empirically using a mean flow thickness consisting of the average of measured flow thickness means acquired at locations P4 though P7 (see Figure 3.4).

$$h_m = 0.4 \left[\frac{1}{g \sin\theta} \right]^{1/3} \left(q_{ws} \right)^{2/3} \tag{4.12}$$

Hughes and Nadal also presented a tentative equation for mean flow velocity that was simply derived by replacing h_m with Eqn. 4.12 in the definition $q_{ws} = v_m \cdot h_m$. The resulting mean velocity expression was given by Eqn. 4.13.

$$v_m = 2.5 \left(q_{ws} \cdot g \cdot \sin\theta \right)^{1/3} \tag{4.13}$$

In Eqns. 4.12 and 4.13, θ is slope of the landward-side levee slope, and the numeric constants are implicitly a function of the slope roughness. The equations are strictly only applicable for landward-side slopes of 1-on-3 having roughness similar to that of the laboratory experiments.

Measured mean flow thickness values from Table 4.4 for combined wave and surge overtopping were plotted versus the combined average overtopping discharge on Figure 4.12. The solid line is Eqn. 4.12. Mean flow thicknesses at location P4 are uniformly slightly less than predicted by Eqn. 4.12, and flow thicknesses at location P7 are considerably less than predicted. This comparison indicates that Hughes and Nadal (2009) were incorrect in assuming that small differences in flow thickness between locations P4 and P7 could be effectively represented by the average. The clear distinction between measured flow thicknesses at the two locations indicates flow acceleration was still occurring, whereas the formulation of Hughes and Nadal assumed that terminal conditions had been reached. The fact that the measurements for this test series are all less than predicted can probably be ascribed to the adjustments that were made to the flow thickness time series to compensate for inaccurate zeroing of the pressure gauges. A similar adjustment was not performed by Hughes and Nadal (2009).

Figure 4.13 presents the mean flow velocities on the landward-side levee slope from Table 4.5 as a function of combined overtopping discharge. The solid line represents Hughes and Nadal's (2009) tentative prediction equation given by Eqn. 4.13. Measured mean velocities at location P4 are only slightly under-predicted by Eqn. 4.13, but the mean velocities at location P7 are severely under-predicted. The difference between the measured velocities at the two locations is due to the fact that the flow was still accelerating down the slope. One factor that may be contributing to the difference is the loss of lower-speed velocity data when the LDV beams are not submerged in the flow at thin flow thicknesses. Thus, the velocity average does not include some of the lower velocity data points that would decrease the mean by some unknown amount. This would be more problematic at location P7 that experienced relatively thinner flows.

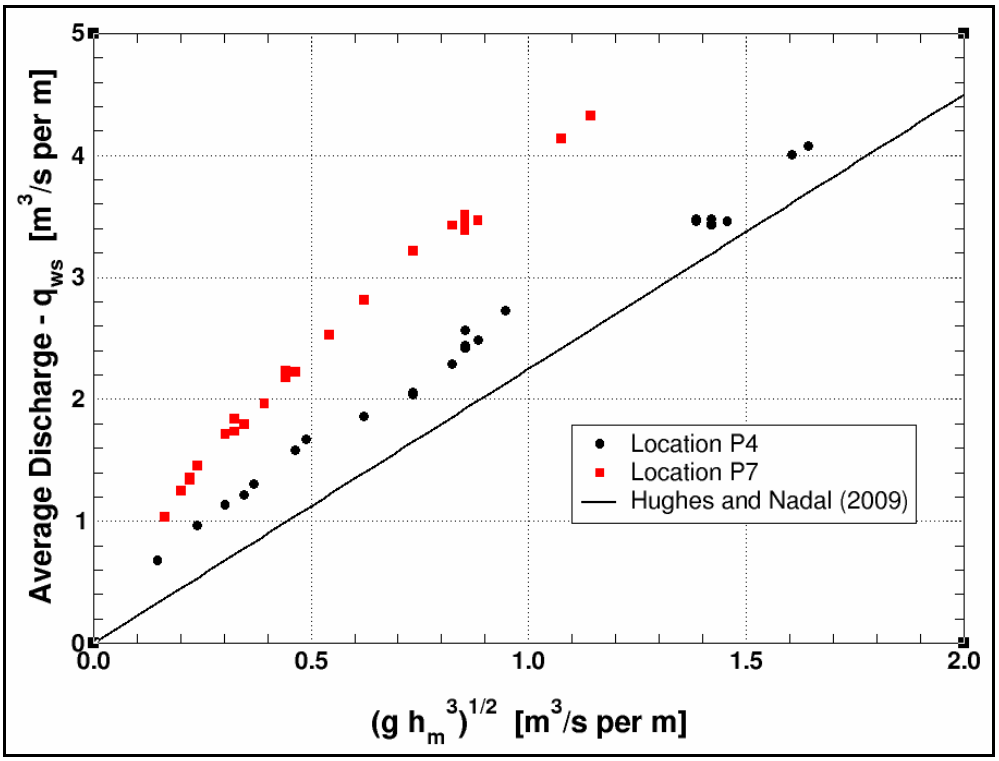

Figure 4.12. Mean combined overtopping flow thickness (prototype scale).

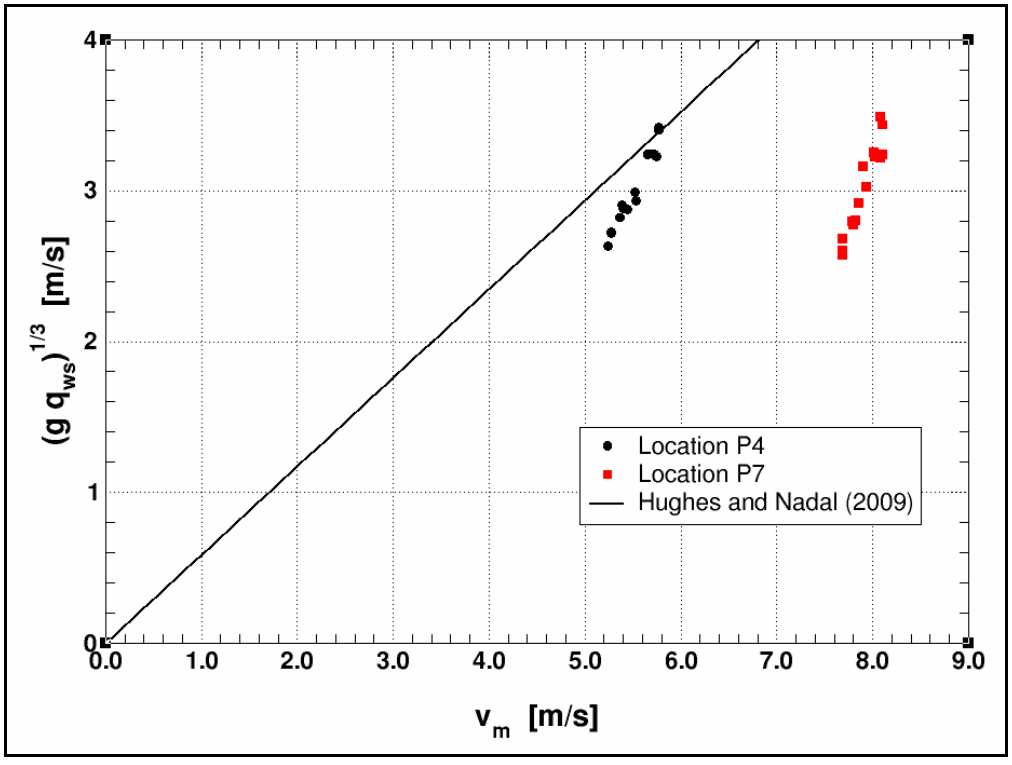

Figure 4.13. Mean combined overtopping flow velocity (prototype scale).

Flow thickness and flow velocity are a function of distance down the landward-side slope. At some distance down the slope, terminal flow conditions are reached. For this reason it is difficult to develop reliable empirical estimators of flow thickness and velocity parameters because the down-slope spatial variability will depend on levee slope and levee surface resistance. Therefore, the representative values for means and overtopping peaks shown in Tables 4.4 and 4.5 can serve as flow thickness and velocity guideline until such time that predictive equations are developed. Fortunately, mean discharge and parameters of the discharge peaks do not depend on down-slope location as proven in section 4.1.1.

In Figures 4.12 and 4.13 the mean flow thicknesses at location P4 are larger than the thicknesses at location P7, while the corresponding P4 velocities are smaller than measured at P7. Thus, the average overtopping discharge, determined as the product of mean flow thickness and mean velocity is expected to be nearly the same at both locations. Figure 4.14 compares the average combined overtopping discharge at locations P4 and P7. Generally, the comparison is good, but recall that equalizing average discharge at both locations was a partial consideration when adjusting the flow thickness zero offsets as described previously in Chapter 3.

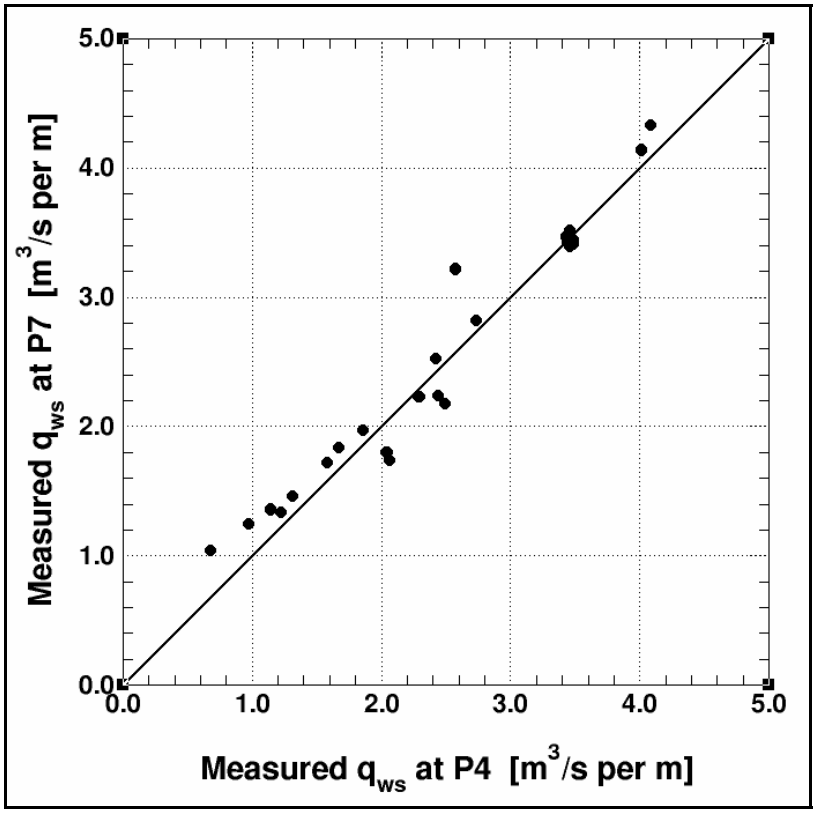

Figure 4.14. Comparison of average overtopping discharge at locations P4 and P7.

Hughes and Nadal (2009) presented an empirically-determined expression for estimating the average discharge associated with combined wave overtopping and surge overflow (see Eqn. 2.37) as a function of negative freeboard (R_c) and significant wave height (H_{m0}). The validity of this empirical equation was tested using the average discharges (q_{ws}) from Table 4.6. Figure 4.15 plots dimensionless average overtopping discharge as a function of relative negative freeboard (R_c / H_{m0}). Only average discharges for Runs 34 through 51 in Table 4.6 were plotted because reliable values of R_c could not be determined for Runs 26 through 33 at the lowest surge level (see Table 3.6). The solid line is the Hughes and Nadal (2009) expression given by Eqn. 2.37. As seen in Figure 4.15, the measured average discharge values from the shear stress test series provide good validation of Hughes and Nadal's equation for estimating combined wave and surge average overtopping discharge.

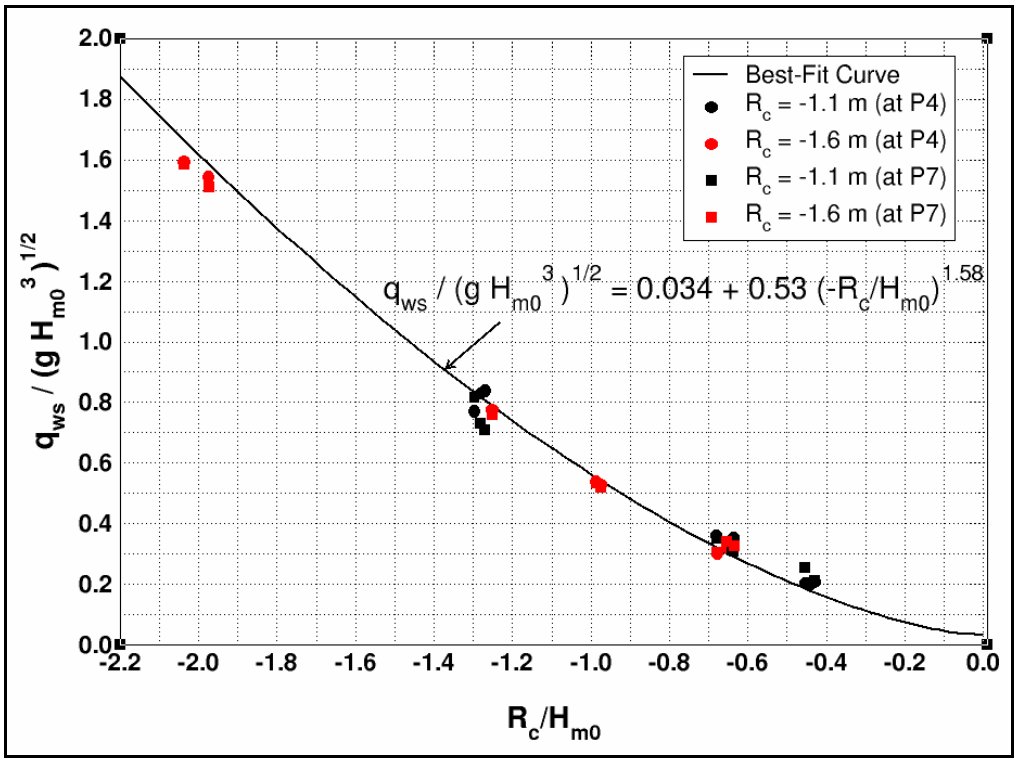

Figure 4.15. Dimensionless combined overtopping discharge versus relative freeboard.

During combined wave and surge overtopping, the net contribution to the total discharge due to wave overtopping decreases as the negative freeboard increases and/or the significant wave height decreases. This is illustrated by Figure 4.16 that shows the ratio of total overtopping discharge to steady overflow discharge (q_{wx} / q) as a function of relative negative freeboard (R_c / H_{m0}). The solid markers are values from the shear stress test series at the two higher surge levels, and the hollow markers are data from Hughes and Nadal (2009). In the range of $-2.5 < q_{wx} / q < -1.0$, the net wave contribution is negligible. However, once the significant wave height becomes greater than the negative freeboard, the waves have a net positive contribution to the average overtopping discharge.

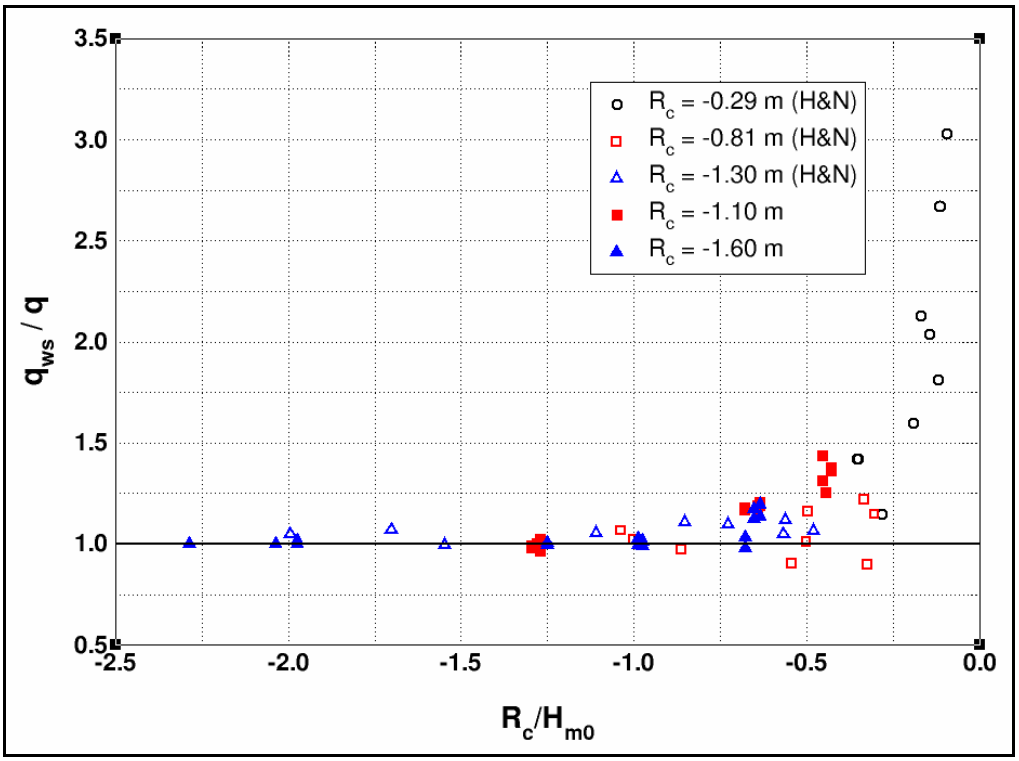

Figure 4.16. Relative contribution of wave overtopping to total discharge.

4.2.2 Estimation of Manning's *n* Values for Steady Overflow

Estimates of Manning's *n* values are given in the literature for different characteristic bottom roughness. These estimates assume steady, fully-developed flow on a constant slope that can be well described by the Manning equation, given as Eqn. 2.12 (SI units) or 2.13 (English units). In the Manning equation the friction slope has been replaced with $\sin\theta$, implying that terminal flow velocity has been reached. Inverting Eqn. 2.12 yields an equation in SI units for Manning's *n* in terms of steady overflow discharge, the local mean velocity, and the landward-side slope angle as seen in Eqn. 4.14.

$$n = \frac{\sqrt{\sin\theta}}{v_m^{5/3}} q^{2/3} \tag{4.14}$$

As noted previously, the steady overflow measured at the start of each experiment in the shear stress test series was accelerating between locations P4 and P7. Therefore, the flow at the most down-slope measurement location (P7) on the landward side of the levee most likely did not reach terminal flow velocity, particularly for those experiments at the higher surge elevations. Nevertheless, estimates of Manning's *n* were calculated by applying Eqn. 4.14 at location P7 for the 18 tests in which steady overflow velocity was measured. Table 4.7 lists the estimates of Manning's *n* along with the mean velocity in prototype-scale units. Runs 34 through 42 had a nominal freeboard of R_c = -1.10 m, and Runs 43 through 51 had a

nominal freeboard of R_c = -1.60 m. Figure 4.17 illustrates the fact that Manning's *n* is not actually constant, but instead varies with mean flow thickness, h_m. As noted, these estimates were made at a location where terminal velocity had not yet been reached. An increase in velocity up to terminal velocity will result in lower values of Manning's *n* because velocity is in the denominator of Eqn. 4.14.

Table 4.7. Manning's *n* Estimates for Steady Overflow at P7 (Prototype Scale).

Run	v_{mean} (m/s)	Manning's *n*	Run	v_{mean} (m/s)	Manning's *n*
34	7.68	0.028	43	8.11	0.039
35	7.67	0.028	44	8.11	0.039
36	7.67	0.030	45	8.10	0.038
37	7.67	0.029	46	8.11	0.039
38	7.67	0.029	47	8.11	0.039
39	7.67	0.028	48	8.10	0.039
40	7.68	0.030	49	8.11	0.039
41	7.67	0.031	50	8.10	0.039
42	7.69	0.034	51	8.11	0.041

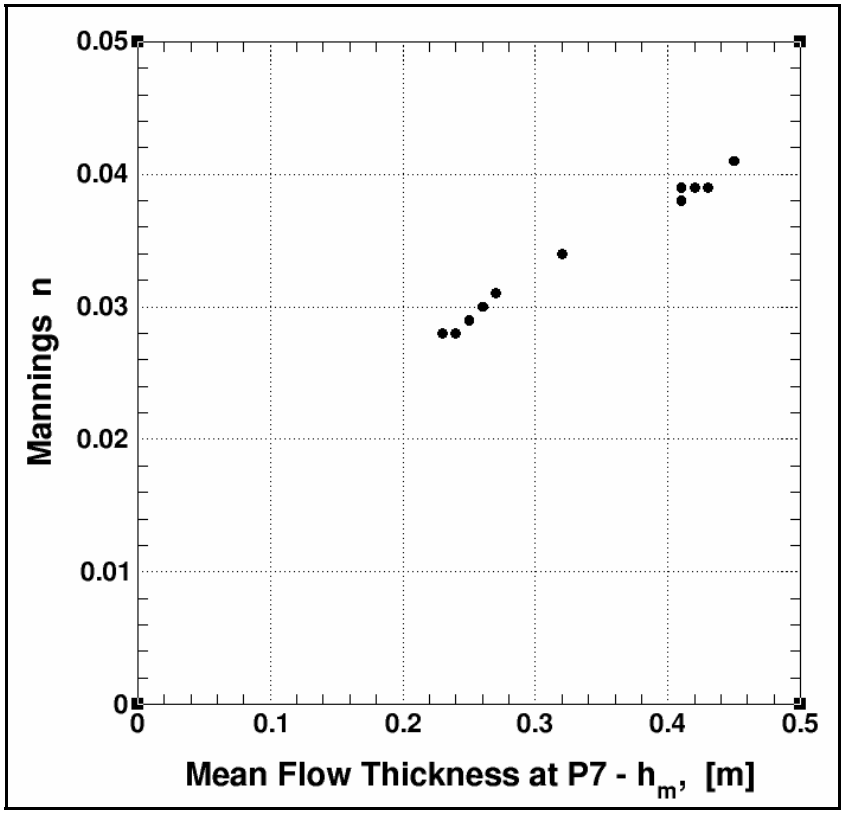

Figure 4.17. Estimated values of Manning's *n* at location P7 (prototype scale).

4.2.3 Estimation of Shear Stress

The most general expression for hydrodynamic shear stress on a slope is given by Eqn. 2.41 that is repeated below as Eqn. 4.15. This equation is appropriate for unsteady, non-uniform flows on a plane slope that have both convective and temporal accelerations. Shear stresses resulting from combined wave overtopping and steady overflow must be evaluated using Eqn. 4.15.

$$\tau_0 = \gamma_w \, h \left[\sin\theta - \frac{\partial h}{\partial s} - \frac{\partial}{\partial s}\left(\frac{v^2}{2g} \right) - \frac{1}{g}\frac{\partial v}{\partial t} \right] \qquad \text{(Unsteady, non-uniform flow)} \qquad (4.15)$$

Steady overflow without waves does not change with time (ignoring turbulent fluctuations), so the temporal acceleration term can be discarded leaving Eqn. 4.16 for steady, non-uniform flow. This equation accounts for convective accelerations on the landward-side slope in the region that is up-slope from the location where terminal velocity is reached. Note that Nadal and Hughes (2009) mistakenly did not include the down-slope variation of velocity in this equation, so their estimates for steady, non-uniform flow were incorrect.

$$\tau_0 = \gamma_w \, h \left[\sin\theta - \frac{\partial h}{\partial s} - \frac{\partial}{\partial s}\left(\frac{v^2}{2g} \right) \right] \qquad \text{(Steady, non-uniform flow)} \qquad (4.16)$$

Farther down the slope where the steady overflow has reached terminal velocity, there is no acceleration, and the expression for shear stress simplifies to Eqn. 4.17 for steady, uniform flow.

$$\tau_0 = \gamma_w \, h \sin\theta \qquad \text{(Steady, uniform flow)} \qquad (4.17)$$

Estimation of hydrodynamic shear stress requires synoptic time series measurements of instantaneous flow thickness and flow velocity at two locations on the landward-side slope. Denoting the up-steam location as position 1 and the down-stream location as position 2, Eqns. 4.15, 4.16, and 4.17 can be represented by discrete versions given by Eqns. 4.18, 4.19, and 4.20, respectively.

$$\tau_0 = \gamma_w \left(\frac{h_2 + h_1}{2} \right) \left[\sin\theta - \frac{h_2 - h_1}{s_{2,1}} - \left(\frac{v_2^2 - v_1^2}{2g\left(s_{2,1}\right)} \right) - \left(\frac{\left[v_2(i) - v_2(i+1)\right] + \left[v_1(i) - v_1(i+1)\right]}{2g\left[t(i) - t(i+1)\right]} \right) \right] \qquad (4.18)$$

$$\tau_0 = \gamma_w \left(\frac{h_2 + h_1}{2} \right) \left[\sin\theta - \frac{h_2 - h_1}{s_{2,1}} - \left(\frac{v_2^2 - v_1^2}{2g\left(s_{2,1}\right)} \right) \right] \qquad (4.19)$$

$$\tau_0 = \gamma_w \left(\frac{h_2 + h_1}{2} \right) \left[\sin\theta \right] \qquad (4.20)$$

where:

h_1 = Flow thickness at up-stream location
h_2 = Flow thickness at down-stream location
$s_{2,1}$ = Distance along slope between up-stream and down-stream locations
$v_1(i)$ = Velocity at up-stream location
$v_2(i)$ = Velocity at down-stream location
$v_1(i+1)$ = Velocity at up-stream location, one time increment later
$v_2(i+1)$ = Velocity at down-stream location, one time increment later
$t(i)$ = Time at increment i
$t(i+1)$ = Time at increment i +1

4.2.3.1 Steady Overflow Shear Stress Estimates

Steady, non-uniform overflow shear stresses were estimated using measured time series of flow thickness and velocity acquired at the initial portion of each test when only steady overflow occurred. Shear stress estimates were calculated using Eqn. 4.19. The calculated time series of steady overflow shear stress was averaged to determine the mean shear stress for each experiment, and this mean represented the average shear stress occurring over the spatial distance separating the up-stream and down-stream measurement locations.

Table 4.8 lists the steady overflow mean shear stresses for the nine experiments that comprised the discharge continuity test series. Measurements acquired at locations P2 and P6 were used, so the mean value represents the average shear stress between these two locations (see Figure 3.7).

Table 4.8. Steady Overflow Mean Shear Stress Between P2 and P6 (Prototype Scale).

Run	Average Discharge (m^3/s per m)	Average Shear Stress P2 to P6	
		Eqn. (4.19) (N/m^2)	Eqn. (4.20) (N/m^2)
13	0.25	1,155 [a]	329
14	0.26	263	357
15	0.47	353	529
16	1.73	923	1,352
17	1.90	1,013	1,448
18	1.94	939	1,477
19	3.22	1,133	2,100
20	3.29	1,185	2,146
21	3.42	1,119	2,197

[a] Estimate is most likely incorrect

As seen in Figure 3.7, location P2 is still on the levee crest, so the estimates for Runs 13 through 21 have decreased validity. By assuming the measurements at P2 are reasonably similar to what existed at the landward edge of the levee crest; the calculated shear stresses might be a satisfactory estimate of average shear stress between the crest and location P6, but this assumption is still suspect. The prototype-scale value of the distance from the edge of the levee crest to location P6 is 5.5 m.

Estimates of mean shear stress were also calculated for the discharge continuity test series experiments using Eqn. 4.20, and these estimates are listed in the rightmost column of Table 4.8. Equation 4.20 is only appropriate at slope locations where terminal velocity has been reached. Thus, estimates shown in Table 4.8 for Eqn. 4.20 are actually larger than the expected maximum shear stress on the slope for the given flow because the flow thickness at terminal velocity will be less than the average flow thickness measured over the 5.5-m length of the landward-side slope. Values of mean shear stress estimated by Eqn. 4.20 should always be larger than the more accurate values obtained from Eqn. 4.19; and clearly, the mean shear stress estimated by Eqn. 4.19 for Run 13 is incorrect.

More confidence was given to the mean shear stresses determined for the experiments in the shear stress test series. For these experiments the measurements were acquired at locations P4 and P7 on the landward-side slope as illustrated on Figure 3.8. The shear stress time series was calculated according to Eqn. 4.19, and the average shear stress was determined. Results are listed in Table 4.9. Estimates were not available for the tests having the lowest surge level because velocity was not measured during the steady overflow portion of the tests. The calculated mean shear stresses strictly represent the average shear stress over the 4.8-m section (prototype scale) of the landward-side slope starting at a distance 2.3 m down from the levee crest and ending at a location 7.1 m down from the levee crest. Mean shear stress estimates were also calculated using Eqn. 4.20 which provides conservative maximum shear stress estimates that are greater than what would be expected under the same overflow conditions farther down the slope where terminal velocity occurs.

Empirical correlations were sought that linked the calculated mean shear stresses to the overflow discharge for both experimental test series. The best correlation is shown in Figure 4.17 for the discharge continuity test series (black circles) and the shear stress test series (red squares). The best-fit equation determined for the discharge continuity test series for the mean shear stress between locations P2 and P6 is given by Eqn. 4.21. This equation, shown by the solid black line on Figure 4.17, had a correlation coefficient of 0.968 and an RMS-percent error of 0.107.

$$\tau_{0,mean} = 0.121\,\gamma_w \left(\frac{q^2}{g}\right)^{1/3} \qquad \text{(Between P2 and P6)} \qquad (4.21)$$

Equation 4.21 is dimensionally consistent, and it can be used with either SI or English units.

Table 4.9. Steady Overflow Mean Shear Stress Between P4 and P7 (Prototype Scale).

Run	Average Discharge (m^3/s per m)	Average Shear Stress P4 to P7	
		Eqn. (4.19) (N/m^2)	Eqn. (4.20) (N/m^2)
26	—	—	270
28	—	—	256
29	—	—	224
30	—	—	260
31	—	—	166
32	—	—	252
33	—	—	270
34	1.93	817	986
35	1.91	685	977
36	1.95	718	988
37	1.93	694	982
38	1.99	832	1,015
39	1.94	925	1,000
40	1.98	662	996
41	2.03	796	1,021
42	2.12	705	1,039
43	3.44	1,121	1,605
44	3.42	1,086	1,602
45	3.39	1,121	1,588
46	3.44	1,120	1,606
47	3.43	968	1,609
48	3.45	1,103	1,621
49	3.47	1,153	1,622
50	3.49	1,075	1,636
51	3.65	1,236	1,698

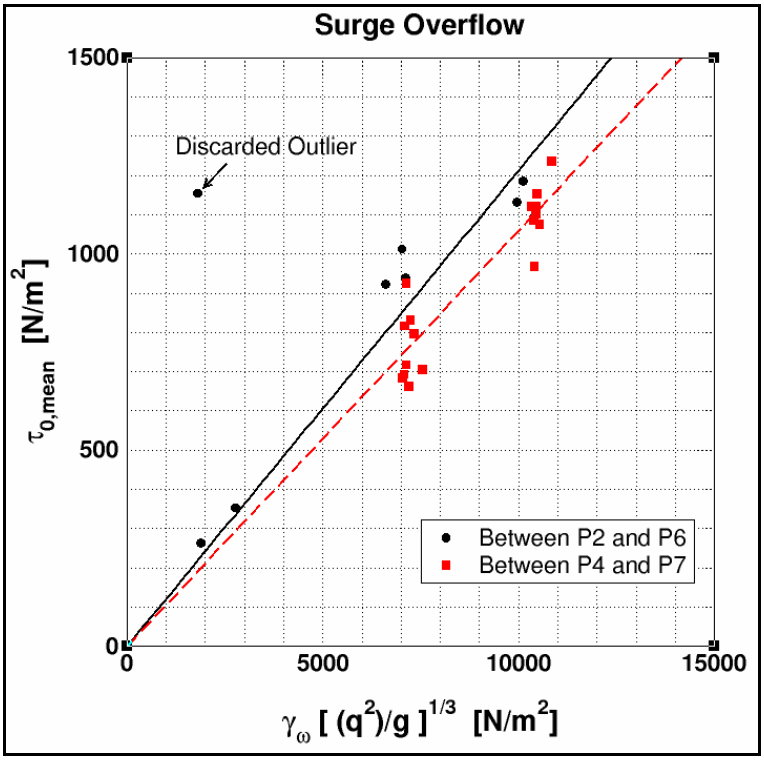

Figure 4.18. Surge overflow mean shear stress as a function of discharge (prototype scale).

The best-fit equation determined for the shear stress test series for the mean shear stress between locations P4 and P7 is given by Eqn. 4.22. This equation, shown by the dashed red line on Figure 4.17 had a correlation coefficient of 0.924 and an RMS-percent error of 0.086.

$$\tau_{0,mean} = 0.106\,\gamma_w \left(\frac{q^2}{g}\right)^{1/3} \qquad \text{(Between P4 and P7)} \qquad (4.22)$$

Strictly, the empirical correlations given in Eqns. 4.21 and 4.22 are only applicable to landward-side slopes having slopes of 1V:3H and similar roughness as the laboratory model, and these equations provide mean shear stress estimates for sections of the landward-side slope where the steady overflow has not yet reached terminal velocity.

Equation 4.21 gives mean shear stress estimates that are about 14% greater than the estimates of Eqn. 4.22. This is contrary to expectation because mean shear stress should be increasing down the landward-side slope until reaching maximum shear stress at terminal velocity. It is concluded that Eqn. 4.22 is closer to reality because the measurements more closely depict the discrete version of the governing equation 4.16 for steady, non-uniform overflow.

For a given steady overflow condition, the maximum $\tau_{0,mean}$ will occur at all locations farther down-slope from where terminal velocity is reached. This assumes the plane landward-side slope has sufficient length for terminal velocity to develop, and there is no backwater. Figure 4.19 plots the actual mean shear stress as determined from Eqn. 4.19 (abscissa) versus the conservative estimate of the maximum mean shear stress calculated using Eqn. 4.20 (ordinate). The black circles are from the discharge continuity test series experiments, and the red squares are from the shear stress test series experiments. The solid black line in Figure 4.19 is the line of equivalence.

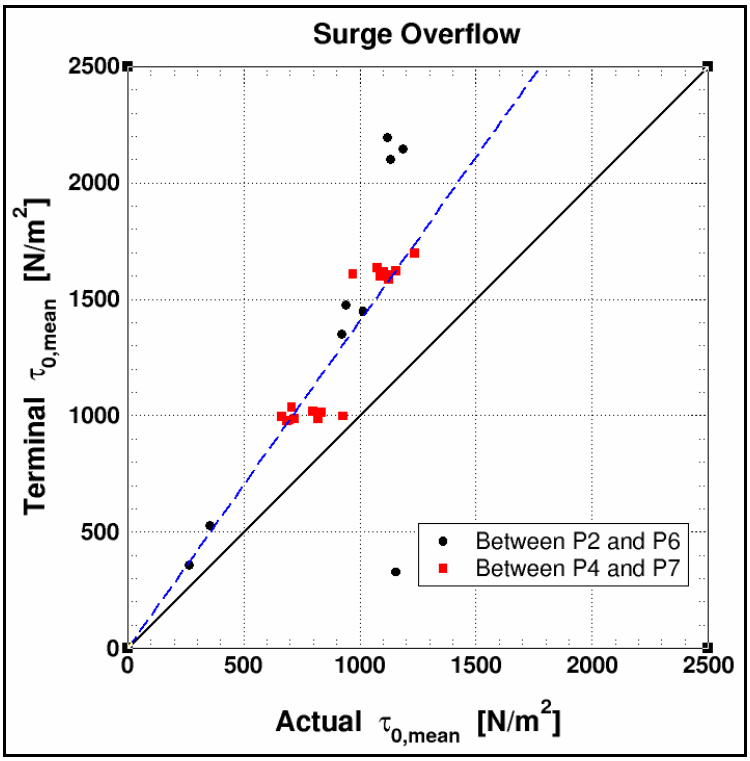

Figure 4.19. Overflow terminal mean shear stress versus actual shear stress (prototype scale).

A linear equation passing through the origin was fit to only the points from the shear stress test series (red squares) under the assumption these measurements have more veracity than those from the discharge continuity experiments. The best-fit, shown by the dashed blue line in Figure 4.19, is given by Eqn. 4.23.

$$\left(\tau_{0,mean}\right)_{\max} = 1.41\,\tau_{0,mean} \tag{4.23}$$

with $\tau_{0,mean}$ calculated using Eqn. 4.22. As mentioned, the estimate of maximum shear stress is conservative because values of mean flow thickness used in Eqn. 4.20 were larger than the flow thickness that would occur at terminal flow. Nevertheless, Eqn. 4.22 should provide reasonable first estimates of actual mean shear stresses that occur over the portion landward-

side slope between 2.3 and 7.1 m down from the crest, and Eqn. 4.23 should give a conservative estimate of the maximum mean shear stress farther down the slope where terminal velocity is reached. It is important to remember that these equations do not apply for landward-side slopes different than 1V:3H or where Manning's *n* is significantly different than the values listed in Table 4.7 above.

4.2.3.2 Combined Overtopping Shear Stress Estimates

Wave overtopping combined with steady overflow is unsteady in time and non-uniform over distance. The time series of instantaneous shear stresses for combined overtopping were calculated using measured time series of flow thickness and velocity acquired from when waves first arrived at the levee until the end of the experiment. Shear stress estimates were calculated using Eqn. 4.18, which is the discrete version of Eqn. 4.15. It was necessary to employ a filter to remove unrealistically large shear stress spikes due to errant velocity measurements. The filter removed the temporal acceleration term if velocity at the up-stream location was larger than the downstream location and/or shear stress increased more than 2,000 N/m^2 over a 0.05 second span (prototype scale). The calculated time series of unsteady shear stress was averaged to determine the mean shear stress for each experiment, and this mean represented the average shear stress occurring over the spatial distance between the up-stream and down-stream measurement locations.

Table 4.10 lists the combined overtopping mean shear stresses for the nine experiments that comprised the discharge continuity test series. Measurements acquired at locations P2 and P6 were used, so the mean value represents the average shear stress between these two locations (see Figure 3.7).

Table 4.10. Combined Overtopping Mean Shear Stress Between P2 and P6 (Prototype Scale).

Run	$Q_{p,rms}$ Peak Discharge (m^3/s per m)	Average Shear Stress P2 to P6	
		Eqn. (4.18) (N/m^2)	Eqn. (4.20) (N/m^2)
13	1.53	1,424	782
14	3.44	1,974	1,497
15	5.39	2,531	2,183
16	2.99	1,102	1,873
17	5.44	1,972	2,494
18	7.96	2,219	3,143
19	3.75	1,210	2,445
20	6.78	1,804	3,245
21	9.56	2,291	3,916

Estimates of mean shear stress were also calculated for the discharge continuity test series experiments using Eqn. 4.20, and these estimates are listed in the rightmost column of Table 4.10. Values of mean shear stress estimated by Eqn. 4.20 should always be larger than the more accurate values obtained from Eqn. 4.18.

As discussed for steady overflow, shear stress estimates determined for the discharge continuity experiments (Runs 13 through 21) are not considered as reliable as the estimates derived from the shear stress test series. Table 4.10 is included in this report for completeness, but the emphasis for combined wave and surge overtopping will be on the shear stresses determined from the experiments in the shear stress test series (Runs 26 through 51).

Measurements during the shear stress test series were acquired at locations P4 and P7 on the landward-side slope as illustrated on Figure 3.8. The shear stress time series was calculated according to Eqn. 4.18, and the average shear stress was determined. Results are listed in Table 4.11. Estimates were not available for the tests having the lowest surge level because velocity was not measured during the steady overflow portion of the tests. Just as for the steady overflow results, the calculated mean shear stresses strictly represent the average shear stress over the 4.8-m length (prototype scale) of the landward-side slope starting at a distance 2.3 m down from the levee crest and ending at a location 7.1 m down from the levee crest. Mean shear stress estimates were also calculated using Eqn. 4.20 which provides conservative maximum shear stress estimates that are greater than what would be expected under the same overflow conditions farther down the slope where terminal velocity occurs. The conservatism results from average flow thicknesses between the two measurement locations that are larger than what would occur farther down the slope where terminal velocity is reached.

Empirical correlations were sought that linked the calculated mean shear stresses to the combined overtopping discharge-related parameters. The best correlation is shown in Figure 4.20 for the shear stress test series (red squares). The best-fit equation determined from the shear stress test series for the mean shear stress between locations P4 and P7 is given by Eqn. 4.24. This equation, shown by the solid red line on Figure 4.20, had a correlation coefficient of 0.914 and an RMS-percent error of 0.095.

$$\tau_{0,mean} = 0.104\,\gamma_w \left(\frac{Q_{p,rms}{}^2}{g} \right)^{1/3} \qquad \text{(Between P4 and P7)} \qquad (4.24)$$

Equation 4.24 is dimensionally consistent, and it can be used with either SI or English units. Note that Eqn. 4.24 is nearly identical to Eqn. 4.22 for steady overflow with the exception that the discharge parameter is the root-mean-squared value of the shear stress peaks instead of the steady overflow discharge. The parameter $Q_{p,rms}$ can be estimated in terms of negative freeboard, significant wave height, and combined overtopping discharge using the empirical Eqn. 4.2. Because the value of $Q_{p,rms}$ is the same everywhere on the landward-side slope, the numeric coefficient must be a function of spatial position on the slope. Thus, Eqn. 4.24 is strictly the average shear stress over the 4.8-m length of levee slope between measurements.

Table 4.11. Combined Overtopping Mean Shear Stress Between P4 and P7 (Prototype Scale).

Run	$Q_{p,rms}$ Peak Discharge (m^3/s per m)	Average Shear Stress P4 to P7	
		Eqn. (4.18) (N/m^2)	Eqn. (4.20) (N/m^2)
26	—	838	919
28	—	1,238	1,135
29	—	1,333	1,437
30	—	1,394	1,651
31	—	1,523	1,412
32	—	1,765	1,931
33	—	1,588	2,178
34	3.02	1,129	1,414
35	2.99	1,084	1,474
36	3.06	964	1,464
37	5.36	1,764	1,889
38	5.69	1,641	2,177
39	5.64	1,627	2,209
40	7.32	2,033	2,319
41	8.32	2,140	2,816
42	8.86	1,884	2,977
43	4.03	1,130	1,990
44	4.19	1,142	2,088
45	4.24	1,135	2,084
46	5.55	1,452	2,317
47	6.51	1,614	2,715
48	6.54	1,506	2,725
49	8.24	2,040	2,927
50	10.01	1,994	3,637
51	10.25	1,947	3,763

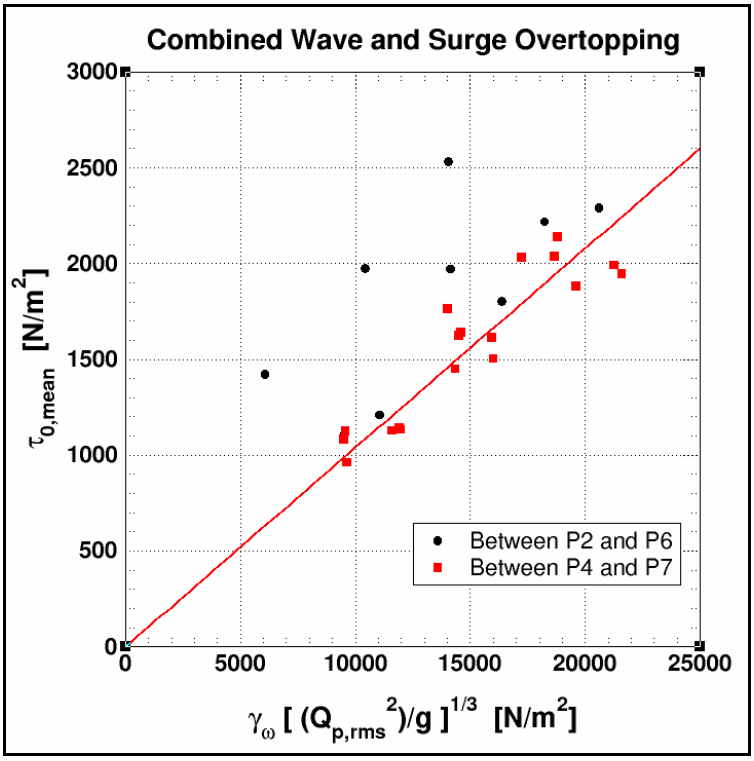

Figure 4.20. Combined overtopping mean shear stress as a function of $Q_{p,rms}$ (prototype scale).

Also, the empirical correlation given by Eqn. 4.24 is only applicable to landward-side slopes having slopes of 1V:3H and similar roughness as the laboratory model, and the equation provides mean shear stress estimates for sections of the landward-side slope where the instantaneous overtopping flow has not yet reached terminal velocity.

The maximum mean shear stress will occur at all locations farther down-slope from where terminal velocity is reached. This assumes the plane landward-side slope has sufficient length for terminal velocity to develop, and there is no backwater. A further assumption is that terminal velocity exists at each instant of time during the unsteady flow variations between maximum and minimum shear stress. Figure 4.21 plots the actual mean shear stress as determined from Eqn. 4.18 (abscissa) versus the conservative estimate of the maximum mean shear stress calculated using Eqn. 4.20 (ordinate). The black circles are from the discharge continuity test series experiments, and the red squares are from the shear stress test series experiments. The solid black line in Figure 4.21 is the line of equivalence.

A linear equation passing through the origin was fit to only the points from the shear stress test series (red squares) under the assumption these measurements have more veracity than those from the discharge continuity experiments. The best-fit, shown by the dashed blue line in Figure 4.21, is given by Eqn. 4.25.

$$\left(\tau_{0,mean}\right)_{\max} = 1.42\ \tau_{0,mean} \tag{4.25}$$

with $\tau_{0,mean}$ calculated using Eqn. 4.24. The correlation coefficient for the best-fit was 0.758 and the RMS-percent error was 0.24. As mentioned, the estimate of maximum shear stress is conservative because values of mean flow thickness used in Eqn. 4.20 were larger than the flow thickness that would occur at terminal flow. Nevertheless, Eqn. 4.24 should provide reasonable first estimates of actual mean shear stresses that occur over the portion of the landward-side slope between 2.3 and 7.1 m down from the crest, and Eqn. 4.25 should give a conservative estimate of the maximum $\tau_{0,mean}$ farther down the slope where terminal velocity is assumed at each instant in time. It is important to remember that these equations do not apply for landward-side slopes different than 1V:3H or where Manning's *n* is significantly different than the values listed in Table 4.7 above.

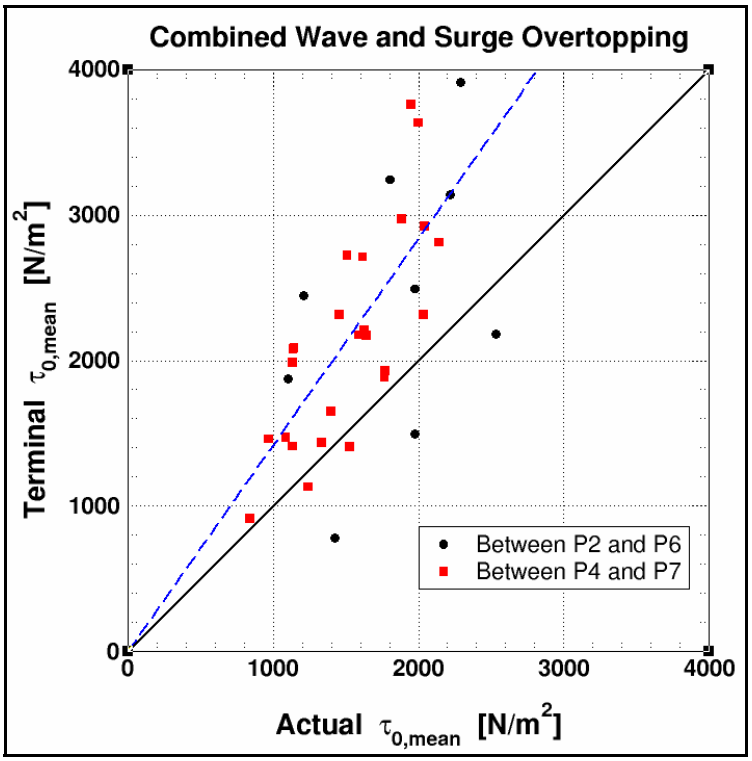

Figure 4.21. Combined terminal mean shear stress versus actual shear stress (prototype scale).

Nadal and Hughes (2009) observed that the mean shear stress values estimated for combined wave and surge overtopping provide an overall average that occurs during a combined overtopping event. However, in the time series of instantaneous shear stress acting on the landward-side slope, the peak stresses associated with the overtopping wave crests can be several times the magnitude of the mean shear stress. The peak shear stress acts for a short duration as the wave passes down the slope, but the peak shear stress may be the defining parameter with respect to stability of rapidly-placed protection alternatives or for determining rates of soil erosion.

The calculated time series of instantaneous shear stress from all experiments in the two test series were analyzed in the time domain using standard up-crossing analysis. The maximum shear stress values for each identified wave were rank-ordered, and representative values were determined for the average of the highest 1/3, highest 1/10, and highest 1/100 of the peak shear stresses. These values were denoted as $\tau_{p,1/3}$, $\tau_{p,1/10}$, and $\tau_{p,1/100}$, respectively. Results are tabulated for the discharge continuity test series experiments in Table 4.12 and for the shear stress test series experiments in Table 4.13.

Good correlations were found between the representative peak shear stresses and the mean shear stress estimated by Eqn. 4.24. Thus, the peak shear stress parameters are related to the product of specific weight of water, γ_w, and a representative measure of flow discharge given by the root-mean-square peak discharge on the landward-side levee slope, $Q_{p,rms}$. The resulting best-fit correlations are shown on Figure 4.22 for $\tau_{p,1/3}$, Figure 4.23 for $\tau_{p,1/10}$, and Figure 4.24 for $\tau_{p,1/100}$. Notice the high magnitudes of peak shear stress on the ordinate axis compared to the mean values given on the abscissa, and also note that scatter about the central trend increases for the larger representative shear stress parameters.

Table 4.12. Peak Shear Stress Parameters Between P2 and P6 (Prototype Scale).

Run	$\tau_{p,1/3}$ (N/m^2)	$\tau_{p,1/10}$ (N/m^2)	$\tau_{p,1/100}$ (N/m^2)
13	1,891	2,258	2,927
14	2,825	3,625	5,745
15	4,095	5,918	10,892
16	1,408	1,767	2,338
17	3,543	4,815	6,191
18	4,114	5,671	7,424
19	1,392	1,542	1,784
20	3,021	4,763	6,210
21	4,332	6,045	7,867

Table 4.13. Peak Shear Stress Parameters Between P4 and P7 (Prototype Scale).

Run	$\tau_{p,1/3}$ (N/m^2)	$\tau_{p,1/10}$ (N/m^2)	$\tau_{p,1/100}$ (N/m^2)
26	1,573	2,029	2,859
28	1,965	2,477	3,305
29	2,109	2,701	3,435
30	2,393	3,313	4,237
31	2,283	2,948	4,451
32	2,836	3,962	5,489
33	2,877	4,352	7,236
34	1,679	2,333	3,360
35	1,554	2,197	3,193
36	1,402	1,992	3,311
37	2,862	3,629	4,281
38	2,675	3,703	5,218
39	2,806	4,020	5,782
40	3,315	4,309	5,675
41	3,686	5,326	8,139
42	3,439	5,322	8,547
43	1,331	1,493	1,851
44	1,346	1,479	1,816
45	1,345	1,522	1,810
46	2,115	3,238	4,333
47	2,589	3,751	4,548
48	2,348	3,817	5,662
49	3,435	4,520	6,133
50	3,449	5,372	9,656
51	3,425	5,727	10,088

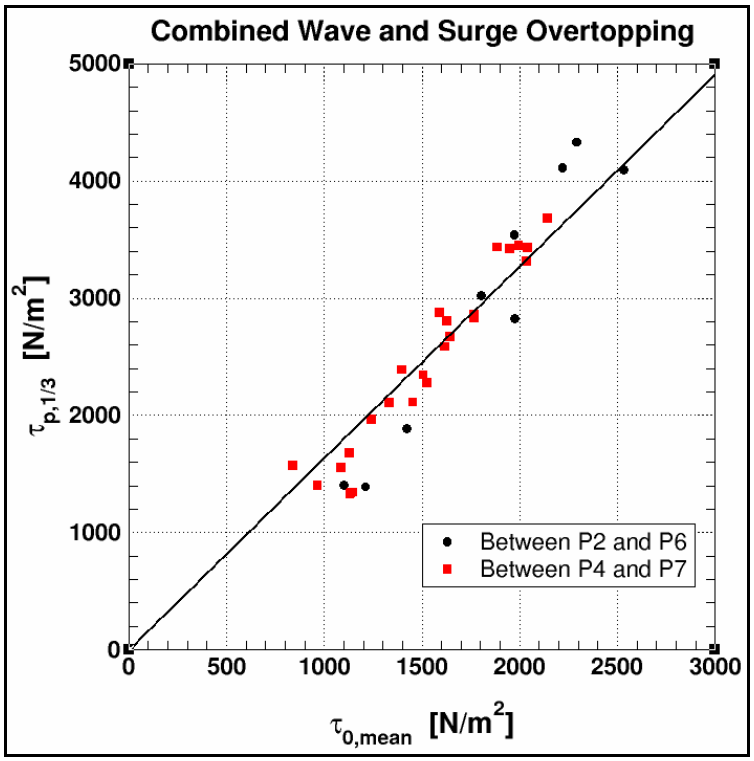

Figure 4.22. Average of highest 1/3 shear stress peaks (prototype scale).

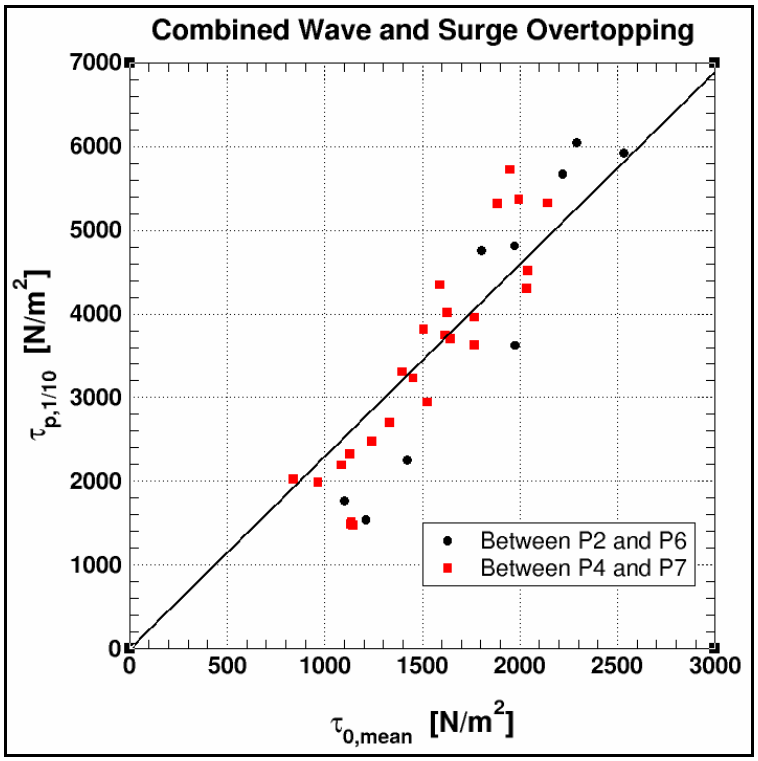

Figure 4.23. Average of highest 1/10 shear stress peaks (prototype scale).

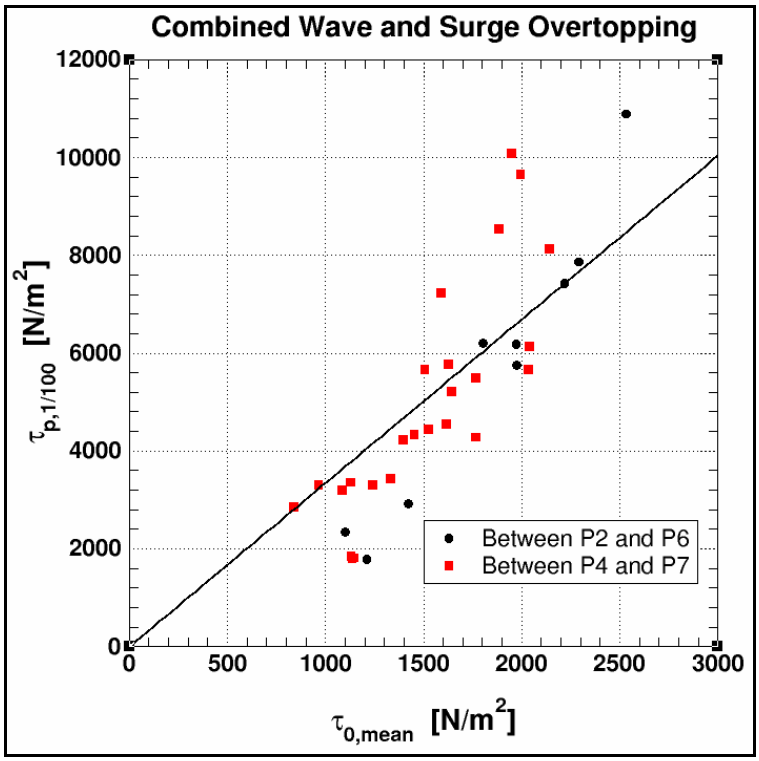

Figure 4.24. Average of highest 1/100 shear stress peaks (prototype scale).

The solid lines on Figures 4.22 through 4.24 are the best-fit linear equations forced through the origin which are provided by Eqns. 4.26 through 4.28 below. The best-fit equations are based only on the values obtained from the shear stress test series (red squares), but note that the relationships also work well for the data from the discharge continuity test series.

$$\tau_{p,1/3} = 1.64\ \tau_{0,mean} \tag{4.26}$$

$$\tau_{p,1/10} = 2.30\ \tau_{0,mean} \tag{4.27}$$

$$\tau_{p,1/100} = 3.35\ \tau_{0,mean} \tag{4.28}$$

The correlation coefficients for Eqns. 4.26 through 4.28 were 0.964, 0.925, and 0.865, respectively.

Estimation of the peak shear stress parameters ($\tau_{p,1/3}$, $\tau_{p,1/10}$, and $\tau_{p,1/100}$) requires an estimation of the mean shear stress, $\tau_{0,mean}$, using an estimated value of $Q_{p,rms}$. Each of these empirical equations represents a central trend with data scatter about the trend. Therefore, the combination of multiple empirical equations to estimate the peak shear stress parameters could introduce a cumulative error that might degrade the resulting estimates. This possibility was tested by comparing calculated peak shear stress values based on

measurements to shear stress values estimated using the empirical equations. The comparison is shown on Figure 4.25 for all experiments. The solid black line in Figure 4.25 is the line of equivalence.

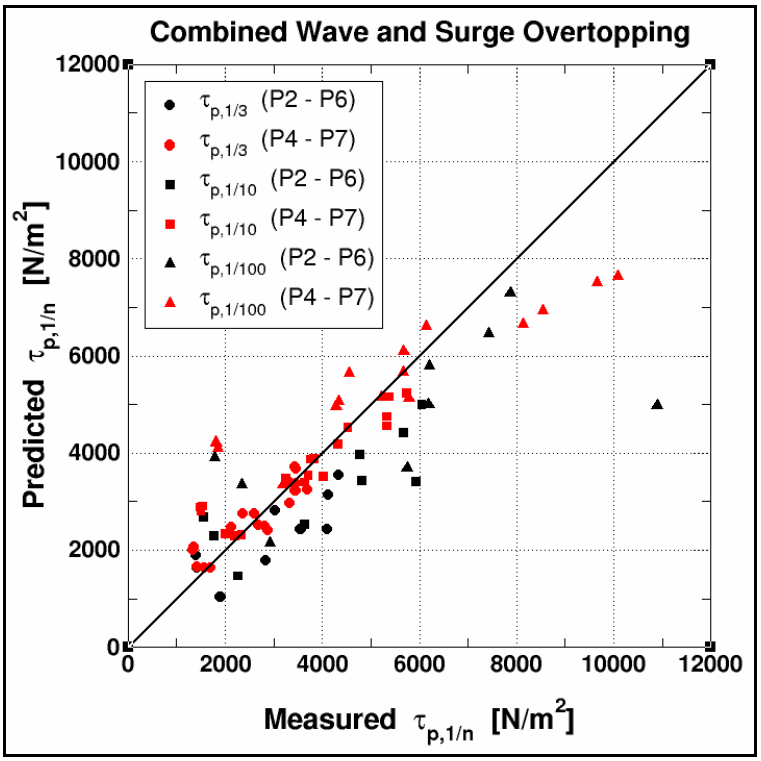

Figure 4.25. Prediction of representative shear stress peaks (prototype scale).

Generally, the empirical equations provided reasonably good predictions for the shear stress test series data with the poorest comparison (understandably) for $\tau_{p,1/100}$. The comparison for the discharge continuity test series data exhibits a distinct bias with predictions systematically overestimating the actual measured peak parameters. This can be attributed to the fact that mean shear stresses used in the comparison were estimated using the equation determined from the shear stress test series data. The measured mean shear stresses determined from the discharge continuity test series were all consistently greater, but less veracity was given to those estimates. The conclusion is that cumulative error from the empirical equations does not have a significant effect on the quality of the peak shear stress estimates.

4.2.4 Example Shear Stress Calculations

Measurements acquired during the small-scale laboratory experiments documented in this report led to empirical formulations for estimating the magnitude of several hydrodynamic shear stress parameters on the landward-side slope of trapezoidal-shaped earthen levees. This section provides worked examples that illustrate application of the empirical equations. These examples are restricted to levees with landward-side slopes of 1V:3H having relatively smooth surfaces with Manning's n values in the range of $n = 0.02$ to 0.04.

4.2.4.1 Steady Overflow Shear Stress Calculation

This example is for steady overflow of an earthen levee without any wave action contributing to the overtopping. River overflowing of a levee would be a typical example.

Given:	$\gamma_w = 10{,}050$ N/m^3	Specific weight of salt water
	$h_1 = 0.5$ m	Surge height above levee crest
	$R_c = -0.5$ m	Levee freeboard ($= -h_1$)
Estimate:	q	Average overflow discharge
	$\tau_{0,mean}$	Mean shear stress on landward-side slope
	$(\tau_{0,mean})_{max}$	Maximum mean shear stress at terminal velocity

Procedure:

The broad-crested weir formula given by Eqn. 2.1 is used to estimate steady overflow discharge, i.e.,

$$q = 0.5443 \sqrt{g}\ h_1^{3/2} = 0.5443 \sqrt{9.816 \text{ m/s}^2}\ (0.5 \text{ m})^{3/2} = 0.603 \text{ m}^3\text{/s per m}$$

The mean shear stress is found using Eqn. 4.22.

$$\tau_{0,mean} = 0.106\, \gamma_w \left(\frac{q^2}{g} \right)^{1/3} = 0.106\, (10{,}050 \text{ N/m}^3) \left(\frac{(0.603 \text{ m}^3\text{/s/m})^2}{9.816 \text{ m/s}^2} \right)^{1/3} = 355 \text{ N/m}^2$$

This mean shear stress represents the average over the 4.8-m-long portion of the landward-side slope beginning a distance of 2.3 m from the landward side of the levee crest and ending at a distance of 7.1 m from the levee crest.

Farther down the plane slope where the flow reaches terminal velocity, a conservative estimate of the maximum steady overflow shear stress can be calculated using Eqn. 4.23.

$$(\tau_{0,mean})_{\max} = 1.41\, \tau_{0,mean} = 1.41\, (355 \text{ N/m}^2) = 500 \text{ N/m}^2$$

4.2.4.2 Combined Wave and Surge Shear Stress Calculations

This example is for wave overtopping combined with the same steady overflow given in the first example. This situation occurs at coastal levees or river levees with sufficient fetch for local wave generation.

Given:	$\gamma_w = 10{,}050$ N/m^3	Specific weight of salt water
	$h_1 = 0.5$ m	Surge height above levee crest
	$R_c = -0.5$ m	Levee freeboard ($= -h_1$)
	$H_{m0} = 1.5$ m	Significant wave height
Estimate:	q_{ws}	Average combined wave and surge discharge
	$\tau_{0,mean}$	Mean shear stress on landward-side slope
	$(\tau_{0,mean})_{max}$	Maximum mean shear stress at terminal velocity
	$\tau_{p,1/3}$, $\tau_{p,1/10}$, $\tau_{p,1/100}$	Peak shear stress parameters

Procedure:

The average overtopping discharge associated with combined wave and surge overtopping is calculated using Eqn. 2.37 after a slight rearrangement, i.e.,

$$q_{ws} = \sqrt{g\ H_{m0}^3}\left[0.034 + 0.53\left(\frac{-R_c}{H_{m0}}\right)^{1.58}\right]$$

$$= \sqrt{\left(9.816\ \text{m/s}^2\right)\left(1.5\ \text{m}\right)^3}\left[0.034 + 0.53\left(\frac{-\left(-0.5\ \text{m}\right)}{1.5\ \text{m}}\right)^{1.58}\right] = 0.733\ \text{m}^3\text{/s per m}$$

Note that the freeboard was entered as a negative number. Waves added an additional 22 percent to the average overtopping discharge when compared to the same steady overflow without waves.

The representative discharge parameter needed for estimating mean shear stress is the root-mean-squared peak discharge given by Eqn. 4.2. Solving for $Q_{p,rms}$ results in the following.

$$Q_{p,rms} = q_{ws}\left\{1 + 4.18\exp\left[-1.56\left(\frac{-R_c}{H_{m0}}\right)^{0.88}\right]\right\}$$

$$= \left(0.733\ \text{m}^3\text{/s/m}\right)\left\{1 + 4.18\exp\left[-1.56\left(\frac{-\left(-0.5\ \text{m}\right)}{1.5\ \text{m}}\right)^{0.88}\right]\right\} = 2.43\ \text{m}^3\text{/s per m}$$

Thus, the RMS-peak discharge is about 3.3 times greater than the average discharge, and this illustrates the periodic loading that occurs on the landward-side levee slope during combined wave and surge overtopping. Other representative discharge parameters can be estimated using Eqn. 4.4.

The mean shear stress representing the average over the 4.8-m-long portion of the landward-side slope beginning a distance of 2.3 m from the landward side of the levee crest and ending at a distance of 7.1 m from the levee crest is estimated using Eqn. 4.24 as follows:

$$\tau_{0,mean} = 0.104\,\gamma_w \left(\frac{Q_{p,rms}{}^2}{g} \right)^{1/3} = 0.104\,(10{,}050\ \text{N/m}^3) \left(\frac{(2.43\ \text{m}^3/\text{s/m})^2}{9.816\ \text{m/s}^2} \right)^{1/3} = 882\ \text{N/m}^2$$

The mean shear stress due to combined waves and surge overtopping is about 250 percent larger than the mean shear stress due to steady overflow alone. This is a significant increase in mean hydrodynamic shear stress.

Farther down the plane slope where the flow reaches terminal velocity, a conservative estimate of the maximum mean shear stress can be calculated using Eqn. 4.25.

$$(\tau_{0,mean})_{\max} = 1.42\,\tau_{0,mean} = 1.42\,(882\ \text{N/m}^2) = 1{,}252\ \text{N/m}^2$$

Finally, parameters of the shear stress peaks are estimated using Eqns. 4.26 through 4.28, i.e.,

$$\tau_{p,1/3} = 1.64\,\tau_{0,mean} = 1.64\,(882\ \text{N/m}^2) = 1{,}446\ \text{N/m}^2$$

$$\tau_{p,1/10} = 2.30\,\tau_{0,mean} = 2.30\,(882\ \text{N/m}^2) = 2{,}029\ \text{N/m}^2$$

$$\tau_{p,1/100} = 3.35\,\tau_{0,mean} = 3.35\,(882\ \text{N/m}^2) = 2{,}955\ \text{N/m}^2$$

These momentary peak shear stresses are extremely large with values several times larger than the mean shear stress. However, the peak loading is quite brief, so designing resiliency into any temporary protective levee covering is feasible, provided the covering is not brittle.

CHAPTER 5 – NUMERICAL MODELING

Numerical modeling is a means through which researchers/engineers can quickly evaluate specific levee section geometries to determine the potential shear stress due to an overtopping event. The USACE Adaptive Hydraulics Model (AdH) is implemented in this chapter. The purpose of the numerical model is to provide an alternate way of analyzing levee overtopping events. Controlling parameters (e.g. negative freeboard, skin friction, and levee geometry) can easily be changed such that multiple levee conditions can be evaluated. Legitimacy of the AdH model is provided by validating it to the physical model previously discussed.

AdH is used to calculate velocity and depth during an overtopping event. Using these values, the work explores the application of AdH for the estimation of associated shear stresses, so that appropriate measures are applied for protection to ultimately reduce the probability of levee failure during an overtopping event. Four different depths and three Manning's *n* values were used for a total of twelve different test cases. Results show mean shear stress increases with increased surge depth and roughness. Additionally, the area of greatest shear stress is shown to be at the slope transition from levee to berm. Values calculated in this effort should be considered in the design and implementation of levee protection.

5.1 Numerical Modeling Approach

Physical modeling results of the overtopping process are critical in the validation of the numerical models. Likewise, validated numerical models can fill gaps in physical model studies due to limitations of instruments, and they also provide a means of applying a large set of varying domain conditions. However, in numerical modeling the physics are limited to the equations implemented; therefore, it is important to have data that accurately represents the true behavior to the best extent possible. The issues/concerns associated with previous experiments by Reeve, et al. (2008) need addressing, and the flexibility of AdH modeling allows exploration of key issues. The objective of this work is twofold:

- Validate numerical model with respect to the physical modeling of surge overtopping done by Hughes and Nadal (2009).
- Explore changes in landward-side levee face shear stresses due to levee berm effects and variations in slope roughness.

Use of the 2-dimensional model will result in the raw output of depth and velocity magnitudes for surge overtopping at multiple locations on the landward side levee face. This overcomes issues with pressure cell and velocity meter limitations in the physical model study. Shear stresses are estimated from the results of AdH using the same equations implemented by Nadal and Hughes (2009).

5.2 Adaptive Hydraulics Levee Grid

The grid is a 15.24 m wide and 609.6 m long numerical flume with a slope of 0.0005 m/m. The transition zone from the berm to the flume slope, or steep to mild slope, imposes a hydraulic jump which prevents the transfer of backwater effects into the domain. A flat flume slope would perform likewise, but would not provide an efficient means of removing excess water from the transition zone. Additionally, the grid has a 152.4 m radius bulb at the end of the flume. The bulb is used to reduce reflection and upstream flow effects. At the upstream end, the boundary condition is specified as a water surface elevation. The levee section is in the first third of the flume and has a 1:4 flood-side slope and a 1:3 protected-side slope. Berms are on both sides of the levee and are sloped at 1:20. Shown in Figure 5.1 are the plan and oblique views of the model's mesh.

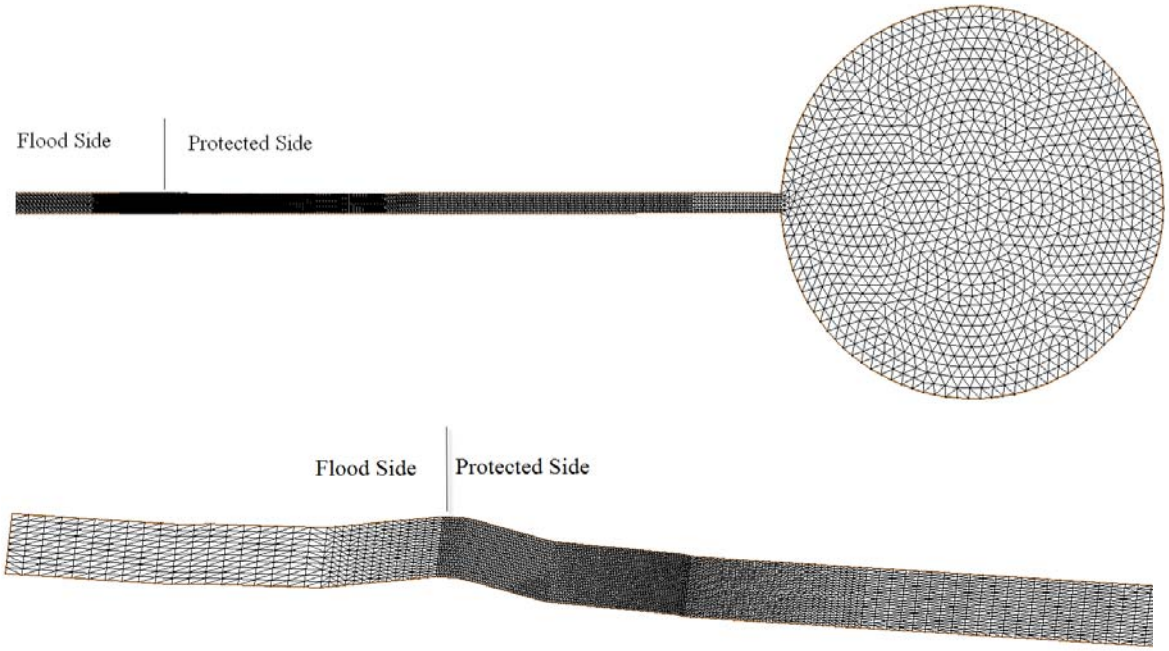

Figure 5.1. Plan (top) and oblique (bottom) views of AdH mesh.

Simulations are varied by changing the surface roughness coefficient and varying the total surge depth. In all, twelve different combinations are evaluated using a Manning's n of 0.0125, 0.02, and 0.035, and a surge depth of 0.61, 0.91, 1.22, and 1.52 m. In the work conducted by Nadal and Hughes (2009), Manning's n ranged from 0.012 to 0.04. The following is a list of the possible variation in material based on the selected Manning's n values:

- 0.0125 = Steel Surface, Cement, Wood (Sturm 2001)
- 0.02 = Stone in Mortar, Excavated Earth (Sturm 2001), Gravel (Julien 2002)
- 0.035 = High Grass, Smooth Rocks (Sturm 2001)

The selection of a Manning's n is based on experience (Sturm 2001), and the above values are only a few possible examples that might be appropriate for simulating skin friction on a levee slope. Prior to the implementation of these results it is recommended that the

roughness ratio or hydraulic radius divided by roughness height, be estimated and be less than 276 and greater than 4.32. If it falls outside this range then the Manning's roughness approximation is not valid for the levee cover (Sturm 2001).

5.3 Adaptive Hydraulics Model

As mentioned, the equations solved for in the 2-dimensional shallow water module of AdH are the 2-dimensional non-linear shallow water equations. Although not applicable for turbulent flow, these equations have proven successful in describing non-breaking conditions (Reeve, et al. 2008). Fundamentally, the equations are derived on the assumption that the vertical velocity component is negligible. For this study, the primary application is to simulate a steady state, surge-only flow; therefore, it is assumed that the equations are applicable for the given conditions.

Neglecting shear stress and fluid pressure at the free surface, the 2D shallow water equations as implemented within AdH are written as:

$$\frac{\partial Q}{\partial t} + \frac{\partial F_x}{\partial x} + \frac{\partial F_y}{\partial y} + H = 0 \tag{5.1}$$

where

$$Q = \begin{Bmatrix} h \\ uh \\ vh \end{Bmatrix} \tag{5.2}$$

$$F_x = \begin{Bmatrix} uh \\ u^2 h + \frac{1}{2} g h^2 - h\frac{\sigma_{xx}}{\rho} \\ uvh - h\frac{\sigma_{yx}}{\rho} \end{Bmatrix} \tag{5.3}$$

$$F_y = \begin{Bmatrix} vh \\ uvh - h\frac{\sigma_{yx}}{\rho} \\ v^2 h + \frac{1}{2} g h^2 - h\frac{\sigma_{yy}}{\rho} \end{Bmatrix} \tag{5.4}$$

and

$$H = \begin{Bmatrix} 0 \\ gh\dfrac{\partial z_b}{\partial x} + n^2 g \dfrac{u\sqrt{u^2+v^2}}{h^{1/3}} \\ gh\dfrac{\partial z_b}{\partial y} + n^2 g \dfrac{v\sqrt{u^2+v^2}}{h^{1/3}} \end{Bmatrix} \tag{5.5}$$

Here, ρ = fluid density
u = flow velocity in the x-direction
v = flow velocity in the y-direction
h = flow depth
g = gravitational acceleration
z_b = bed elevation
n = Manning's roughness coefficient
σ = Reynolds stress

The Reynolds stresses (σ), where the first subscript indicates the direction, and the second subscript indicates the face on which the stress acts, are due to turbulence. The Reynolds stresses are determined using the Boussinesq approach to the gradient in the mean currents:

$$\sigma_{xx} = 2\rho\, v_t \frac{\partial u}{\partial x} \tag{5.6}$$

$$\sigma_{yy} = 2\rho\, v_t \frac{\partial v}{\partial y} \tag{5.7}$$

and

$$\sigma_{xy} = \sigma_{yx} = 2\rho\, v_t \left(\frac{\partial u}{\partial y} + \frac{\partial v}{\partial x} \right) \tag{5.8}$$

Here v_t = kinematic eddy viscosity, which varies spatially where turbulence closure is achieved through the algebraic eddy viscosity formulation described by Rodi (1993).

The equations are discretized using the finite element method in which u, v, and h are represented as linear polynomials on each element. The system of partial differential equations represented in Eqn. 5.1 is solved with the finite element method using the approach of Petrov-Galerkin that incorporates a combination of a Galerkin test function and a non Galerkin component to control oscillations due to convection (Berger, 1997).

AdH utilizes a Pseudo-Transient Continuation and Switched Evolution Relaxation inspired time step size selection algorithm (Savant, et al. 2010). This technique computes the optimal time step size dependent on the L2 norm of the system of equations. This selection algorithm provides an efficient technique for temporally accurate solutions of rapidly varying hydrodynamic and sediment flows. Additional information about the AdH model can be accessed at www.adh.usace.army.mil.

In most numerical model studies a grid convergence test is typically conducted prior to model validation. AdH enables the user to forgo the cumbersome task of grid convergence with the use of an adaptive mesh. "As its name implies, AdH applies mesh adaption techniques, which are based on the normal of the continuity equation residual integrated over the element and computed for each time step, to refine and coarsen a mesh based on flow complexity" (Hammack, et al. 2008, page 5). "If the residual is larger than the refinement tolerance, the element will be refined (split in half); otherwise, no adaption occurs" (Hammack, et al. 2008, page 8). Adaption eliminates the need for the construction of multiple grids with varying resolution that are then compared to determine the most appropriate mesh based on both resolution and run time. AdH adaption details can be found in the AdH Manual (Berger, et al. 2010).

Although not necessary for most applications, five different levels of adaption were used to ensure the model was properly simulating the hydromechanics of the surge event. Adaption 0, the base mesh, consists of 6300 nodes. The number denoted in the name of each mesh indicates the number of times the mesh can adapt in the area of interest, which is the area of the protected side slope, (e.g. Adaption 0 adapts zero times). Using Adaption 0 as a reference, Adaption 1, Adaption 2, Adaption 3, and Adaption 4 were used with a 0.6096 m surge event to determine the best convergent and time efficient mesh. Outside the area of interest, the unprotected side and downstream in the flume, the model was allowed to adapt one time for Adaption 1-3. However, in order to determine the impacts of the surrounding mesh on the area of interest, in Adaption 4 the surrounding mesh was set to an adaption of two. It is shown that this increased resolution does decrease the amount of residual error used for setting the refinement parameters (see Figure 5.2). However, Adaption 4 doubled the runtime and, when compared to the other levels of adaption, the velocity and depth profile did not produce a significant enough difference to justify the less computationally efficient model. Figure A.1 in Appendix A provides additional information related to error and the number of adaptations.

With complex flow conditions in levee overtopping events the need for validation is imperative to ensure the model represents the true behavior of the process. Model validation is achieved using results from empirical equations and physical model measurements. For the most part discharges calculated with AdH were shown to be at or near that of the weir equation for the 0.61 m and 0.91 m surge events. The 1.22 m and 1.52 m surge event discharges are greater than the weir equation. Conversely, the Hughes (2008) results showed a greater discharge than that of AdH for the 0.61 m and 0.91 m surges and the 1.22 m and 1.52 m surge events agreed more closely to the AdH results (see Figure 5.3). Table 5.1 provides unit discharge results for varying surge levels and Manning's n.

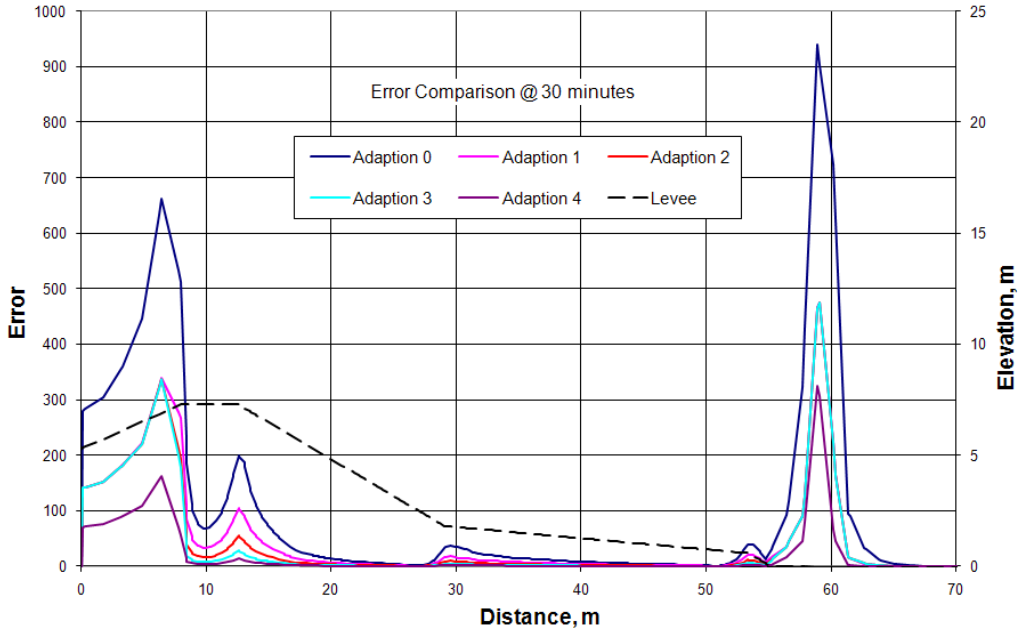

Figure 5.2. Comparison of error for different levees of adaption.

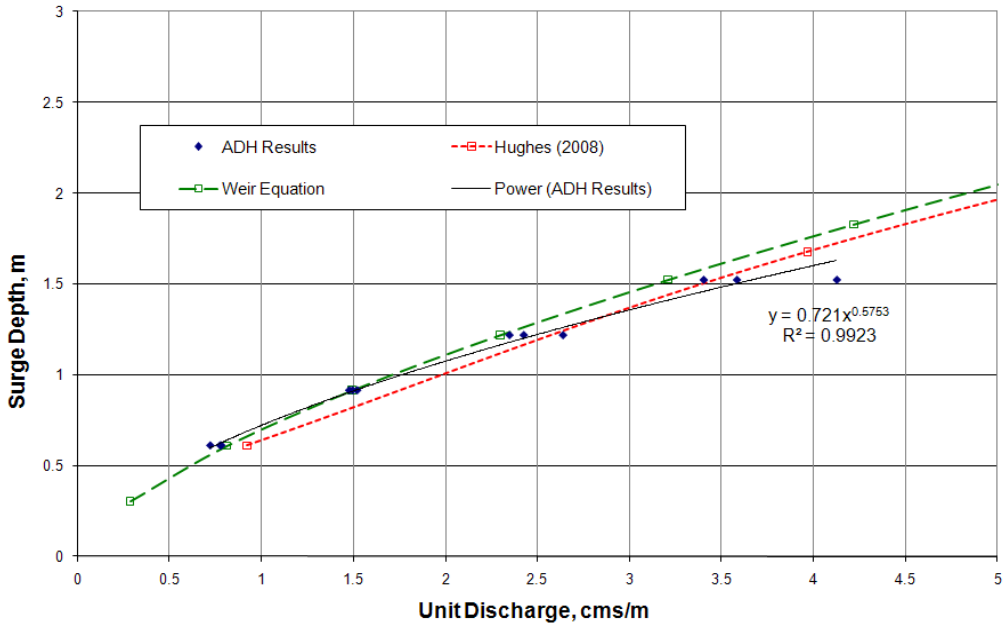

Figure 5.3. Comparison of unit discharge.

Table 5.1. Unit Discharge for Varying Manning's n and Surge.

AdH Steady State Surge Overtopping			
Surge, m	Manning's *n*	Discharge, (m^3/s)	Unit Discharge, (m^3/s per m)
0.61	0.0125	11.90	0.78
0.61	0.02	11.79	0.77
0.61	0.035	10.99	0.72
0.91	0.0125	22.49	1.48
0.91	0.02	22.77	1.49
0.91	0.035	23.16	1.52
1.22	0.0125	35.77	2.35
1.22	0.02	36.95	2.42
1.22	0.035	40.20	2.64
1.52	0.0125	51.85	3.40
1.52	0.02	54.61	3.58
1.52	0.035	62.88	4.13

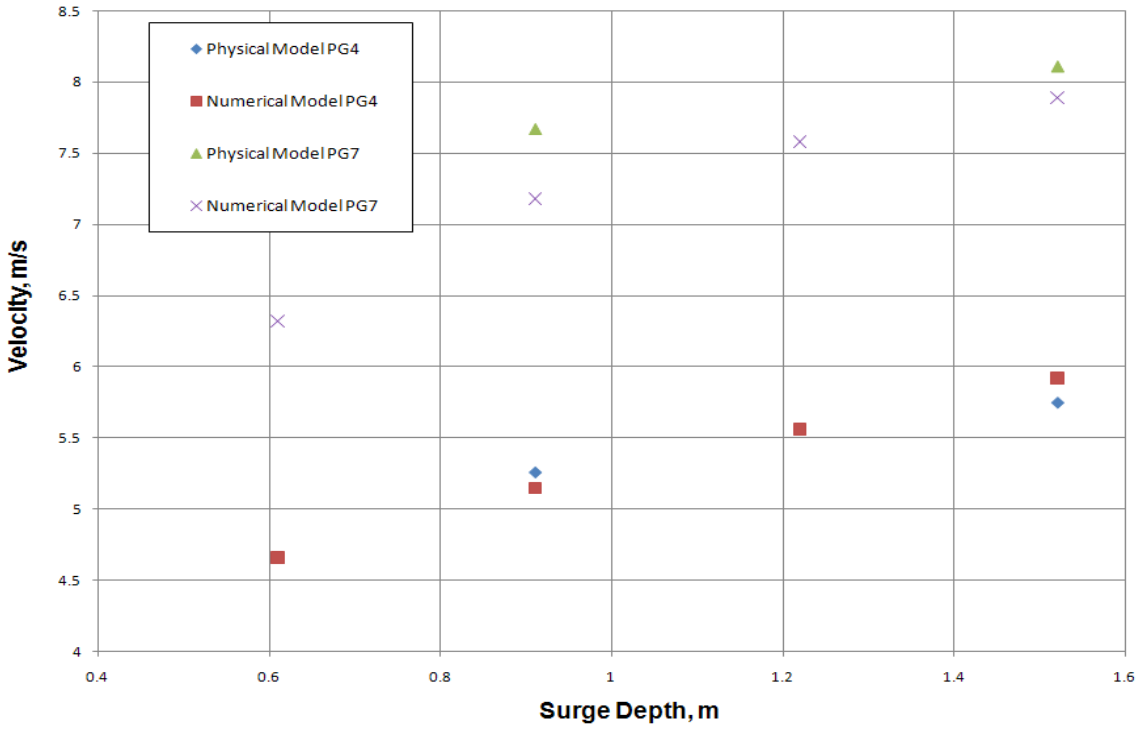

Figure 5.4. Comparison of velocity at locations of physical model gages.

The velocity comparison between the numerical and physical model showed close agreement. Unfortunately, at the lower surge depth of 0.61 m the velocity meters were suspect of measuring erroneous and inconsistent velocity data and could not be used for comparison (Shaw 2010). The available velocity data, shown at Hughes (2008) and Shaw (2010) pressure gages PG 4 and PG 7 (Figure 3.4), was captured at two different surge depths

0.91 and 1.52 m. For the case of the 0.91 m surge both gages in the physical model measured a velocity that is higher than that of the numerical model (see Figure 5.4). Variation between the two models at PG4 and PG7 is 2 and 6%, respectively. Similarly, at a 1.52 m surge depth variation at PG4 and PG7 is -2% and 2%, respectively. This indicates a closer agreement for the two models at the higher surge depth. Agreement of 10% or less was deemed sufficient for validation.

5.4 Numerical Model Calculations

For estimating shear stress experienced on the protected side levee face due to the non-uniform and unsteady overtopping flow the 1-D momentum equations applicable to steep slopes was implemented. From (Nadal and Hughes 2009):

$$S_f = \frac{\tau_0}{\gamma_w h} = \sin\theta - \frac{\partial h}{\partial s} - \frac{\partial}{\partial s}\left(\frac{v^2}{2g}\right) - \frac{1}{g}\frac{\partial v}{\partial t} \tag{5.9}$$

where

τ_o = shear stress

γ_w = specific weight of water

h = flow thickness perpendicular to the slope

S_f = friction slope

θ = angle of levee slope to horizontal

s = down - slope coordinate

v = flow velocity parallel to the slope

g = acceleration of gravity

t = time

The unknown variables are depth and velocity. This work took a three step approach to the shear stress analysis. First, an approximation assuming steady-state flow reduces the momentum equation to the weight of the water offset by the bottom shear stress as shown in Eqn. 5.10.

$$\tau_{0,mean} = \gamma_w\, h \sin\theta \qquad \text{(Steady, uniform flow)} \tag{5.10}$$

Next, the momentum equation, with the acceleration term between two points was implemented to produce Eqn. 5.11. Note that Nadal and Hughes (2009) mistakenly omitted the velocity term that is part of the convective acceleration in Eqn. 5.11. Therefore, the Nadal and Hughes shear stress estimates based on the incorrect version of Eqn. 5.11 are invalid.

$$\tau_0 = \gamma_w \, h \left[\sin\theta - \frac{\partial h}{\partial s} - \frac{\partial}{\partial s}\left(\frac{v^2}{2g} \right) \right] \qquad \text{(Steady, non-uniform flow)} \qquad (5.11)$$

Including the acceleration terms in the equation results in the following form (Nadal and Hughes 2009):

$$\tau_0 = \gamma_w \, h \left[\sin\theta - \frac{\partial h}{\partial s} - \frac{\partial}{\partial s}\left(\frac{v^2}{2g} \right) - \frac{1}{g}\frac{\partial v}{\partial t} \right] \qquad \text{(Unsteady, non-uniform flow)} \qquad (5.12)$$

As the final approach the full 1-D version of the momentum equation is used as shown in Eqn. 5.12, and the temporal acceleration term has no effect since the model is at steady state. As noted, "estimating the time series of shear stress using the momentum equation is difficult for these experiments because no direct measurements of flow velocity were acquired on the landward-side slope" (Hughes and Nadal 2009, page 248). The numerical model overcomes this issue since AdH can solve for velocity.

Equation 5.12 is invalid in areas that include zero slope, such as on the crest, and locations of rapid spatial variation, i.e., the hydraulic jumps, and slope transitions. At locations of rapid spatial variations, Eqn. 5.12 will often exhibit a negative shear stress indicating a flow reversal, which obviously is not the case in a 2-dimensional depth-averaged model. Eqn. 5.13 is implemented where Eqn. 5.12 is invalid.

$$\tau_0 = \frac{\rho}{2} C_f \, v^2 \qquad (5.13)$$

with

$$C_f = \frac{2g\,n^2}{(R)^{1/3}} \qquad (5.14)$$

where

R = hydraulic radius
n = Manning's number

Using Eqn. 5.12, estimated average shear stresses on the protected face of the levee are shown in Figure 5.5; which, show less agreement to Hughes (2008) estimated results than the estimates of unit discharges. Note: Hughes (2008) estimated that the Manning's n for the prototype surge cases of 0.31 m, 0.91 m, and 1.52 m were 0.0115, 0.0262, and 0.0381 respectively. Since the shear stresses are estimated based on calculations from AdH, velocity results are dependent on surface friction, error is amplified. However, the shear stresses do appear to have some similarity to Hughes (2008) results as shown in Figure 5.5. Here it is shown that the physical model results fall between those of the numerical model and are most similar to the AdH results using a Manning's n of 0.035. This is possibly the result of both an over-prediction in the discharge at lower flows and under-prediction of discharge at higher

flows as shown in the difference between unit discharge of the physical model and numerical model (see Figure 5.3).

Rather than presenting a mean shear stress for the protected side slope, this numerical study presents a shear stress profile such that critical failure points on the levee are identified. Areas of transition present the greatest degree of equation limitation and a case by case base evaluation (application of the equations is dependent on the geometry so a different levee section might require a slight variation in the application of shear equations) is required to implement the correct equation for the specific location. The equations implemented are Eqns. 5.12 and 5.13. Eqn. 5.12 is applied for gradually varying flow, and is applicable for the majority of the protected side of the levee cross-section. Equation 5.13 is ideal for steady uniform flow and can be used if the velocity and depth are changing (see Figure 5.6). Where Eqn. 5.12 fails, Eqn. 5.13 is used.

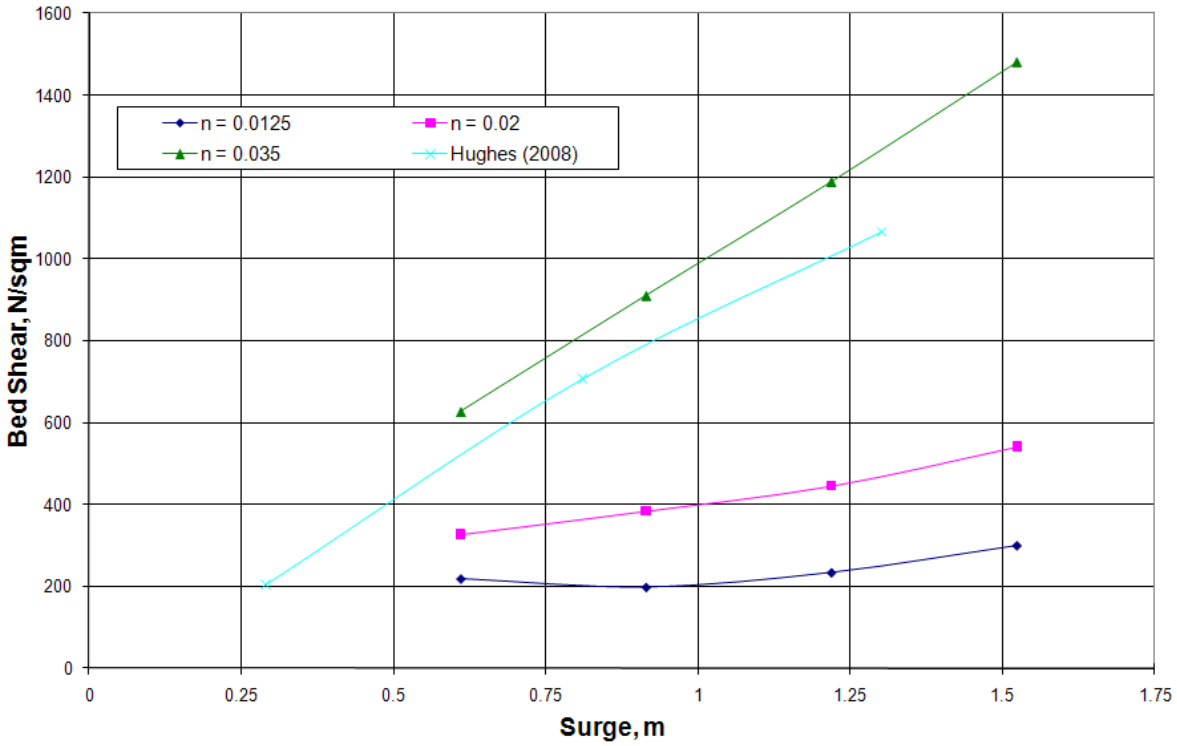

Figure 5.5. AdH bed shear compared to Hughes (2008) results.

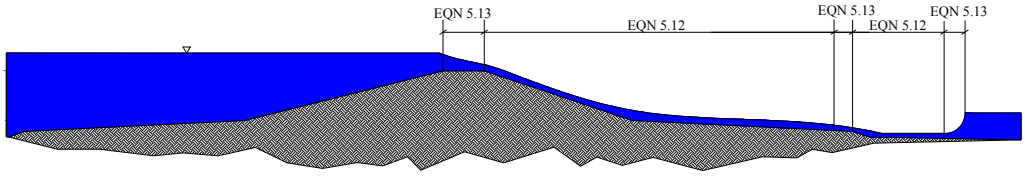

Figure 5.6. Location of applied shear stress equations.

5.5 Numerical Modeling Results

Physical and numerical model results show that velocity profiles vary with respect to location on the levee cross-section. A single point velocity or mean velocity is misleading in an overtopping analysis because of the rapid spatial variations in velocity. Since the evaluation is analyzing a steady state flow condition, the model is allowed to reach steady state converging in approximately three minutes, and the velocity profiles fifteen minutes into the simulation are used (see Figures A.2, A.5, A.11, A.17, and A.23 flow convergence plots). This time was selected to avoid both initial unsteady and later downstream backwater conditions that could affect the velocity profile. From the levee crest to the protected side levee toe, the velocity profile increased. Velocity profiles indicated a velocity maximum at or near the landward side levee slope toe. A secondary local maximum of lower magnitude occurred at or near the toe of the berm, so velocity inflection points occur at abrupt changes in slope. These maximums are unlikely since a real world levee would have smoother transitions. As expected for uniform flow, a greater roughness results in greater flow depth and lower velocity, as expected from the energy equation and illustrated in Figures A.15 and A.16. As surge depth on the unprotected side increased so did the corresponding velocities. Numerical results are provided in Figures A.3, A.4, A.9, A.10, A.15, A.16, A.21, and A.22. All functions of the velocities should be carefully considered when evaluating a protective measure.

The water surface profile (Figures A.3, A.9, A.15, and A.21) is more intuitive since it follows basic hydraulic logic. At the crest the water surface behaves as a broad crested weir. Moving down the levee slope the depth gradually decreases as the potential energy is transformed to kinetic energy and attempts to reach a terminal velocity. At the levee and berm slope transition, the flow deepens and continues to deepen until it runs off the berm where a hydraulic jump forms directly after or slightly downstream. At a Manning's n of 0.035 the jump will form above the end of the berm with a Manning's n of 0.02 the jump occurs slightly inland of the berm. With a Manning's n of 0.0125 the jump is much further

inland. Therefore, the higher the surge the deeper the flow depth; likewise, the rougher the levee section the deeper the flow depth.

As shown in Figure 5.7 shear stress evaluation requires appropriate equation selection. In Figure 5.7 each equation yields vastly different results and appropriate application is imperative for the correct calculation of bed shear in its corresponding location. Some, such as the one on the crest, are wildly incorrect; therefore, ultimately in this work, the bed shear is estimated using a combination of Eqns. 5.12 and 5.13, both shown in Figure 5.9, at different locations along the levee as shown in Figure 5.6.

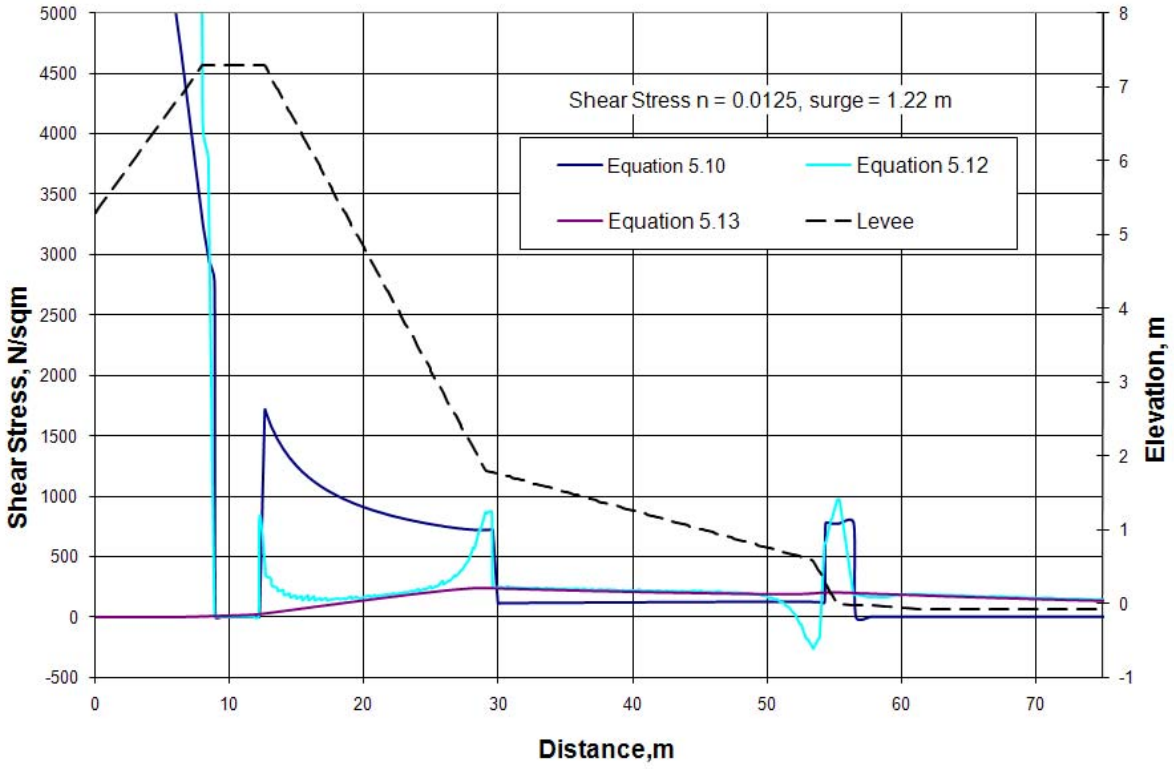

Figure 5.7. Shear stress of three equations with respect to location on the levee.

The resulting bed shear stress profile calculated with Eqns. 5.12 and 5.13 combined spatially as illustrated in Figure 5.6 is the best estimate for the shear stress profile. Shear stress profiles developed in this manner are provided in Figures A.6 to A.8, A.12 to A.14, A.18 to A.20, and A.24 to A.26. Lower Manning's n should more closely represent the surface friction of a geo-fabric used for levee armoring.

Table 5.2 shows the mean shear stress behavior with respect to surge depth and Manning's n, and Figure 5.8 shows mean bed shear stresses on the protected slope. The mean shear stress represents an average for the entire protected side levee slope. Shear stress increases with both surge and increasing Manning's n. For a comprehensive understanding of the erosive nature during the initial stages of levee failure peak shear stress values are

essential. It is evident from the stress profiles that the greatest areas of shear stress are at the transitions from the levee-berm and then from the berm to flume bed. The highest magnitude at the levee and berm transition occurred in the most extreme case of a 1.52 m overtopping event as seen in Figure 5.9. However, at the berm to flume transition, with increasing depth the flow overcame the skin drag decreasing the shear peak for the higher surge events, as shown in the reversed downward trend of the highest surge in Figure 5.10.

Table 5.2. Mean Bed Shear for the Levee Landward-Side Slope.

	Bed Shear, N/m^2		
Surge, m	n = 0.0125	n = 0.02	n = 0.035
0.61	218	328	627
0.91	197	385	911
1.22	234	446	1189
1.52	300	541	1481

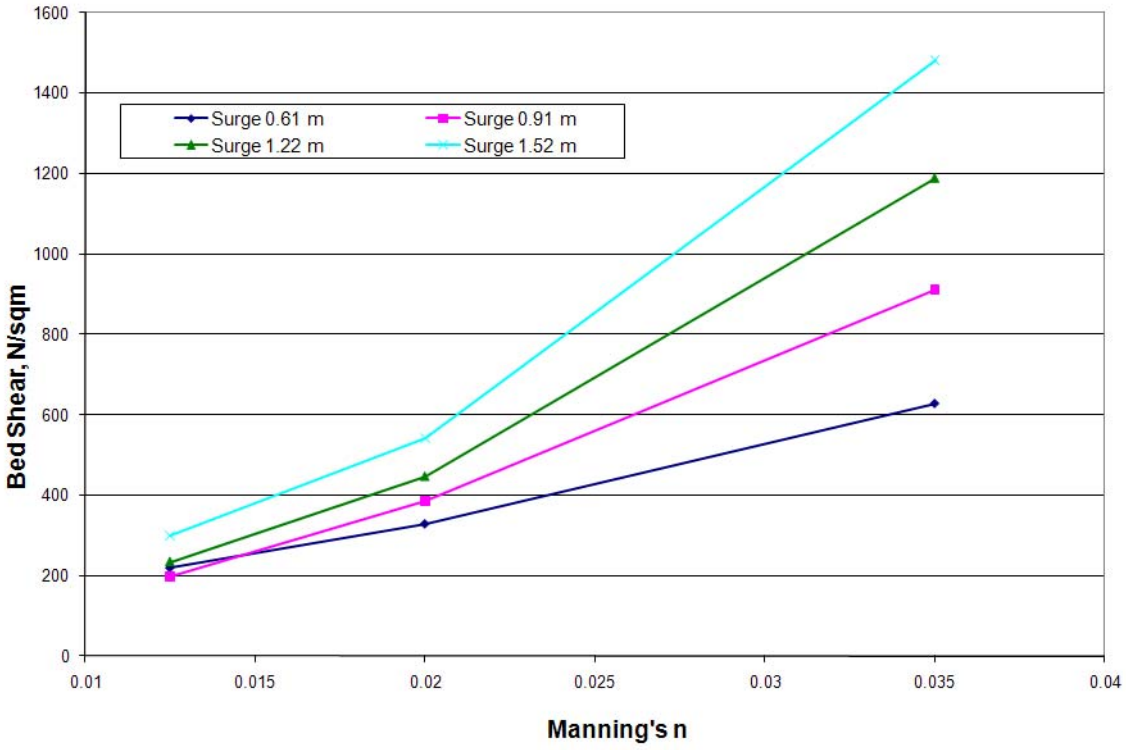

Figure 5.8. Mean bed shear for the levee landward-side slope.

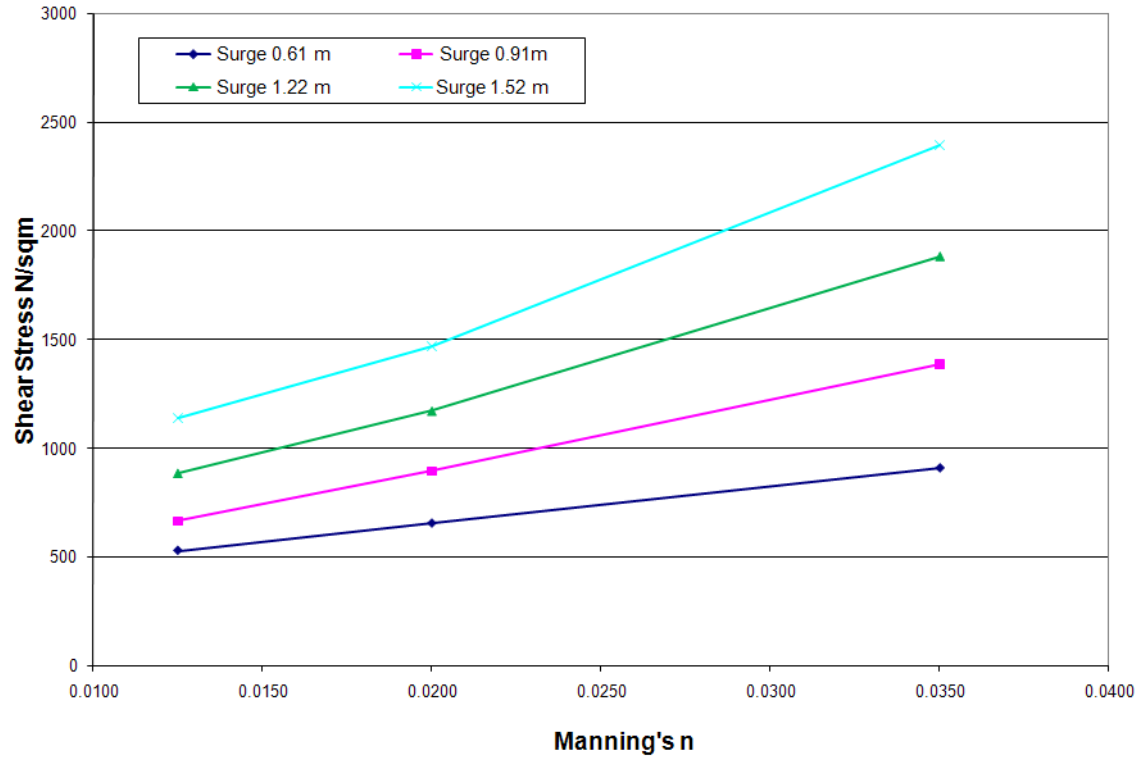

Figure 5.9. Peak shear at levee berm transition 21.04 m from crest.

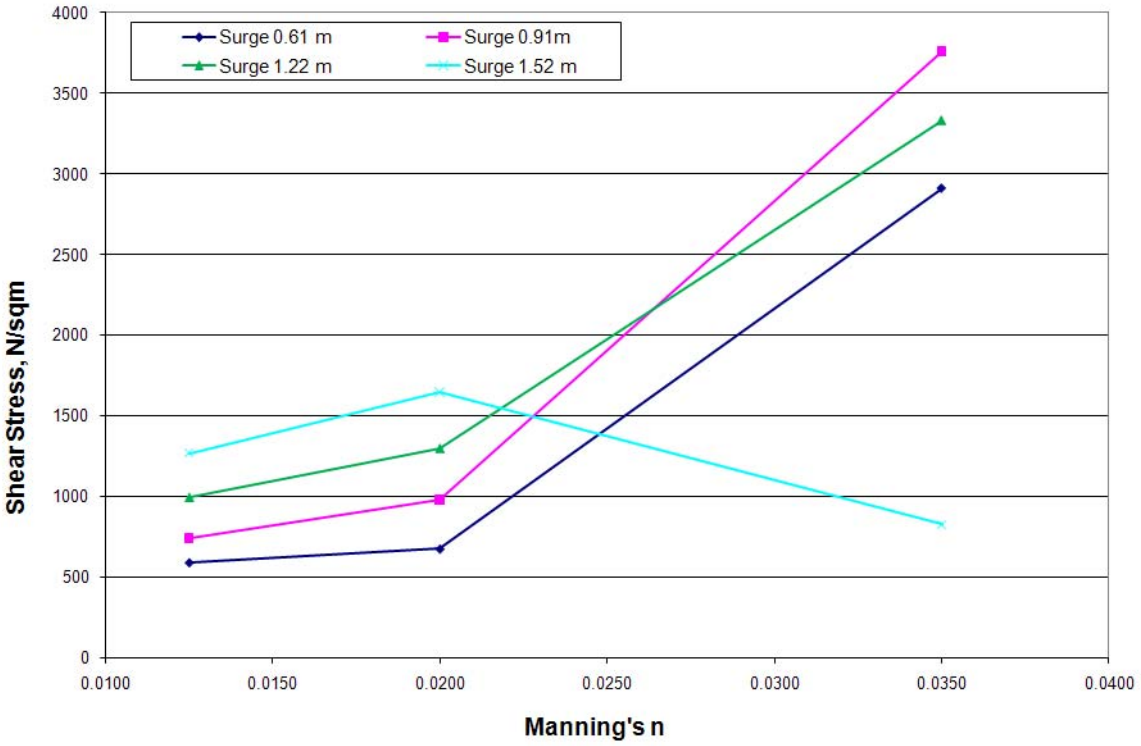

Figure 5.10. Peak shear at berm flume transition 46.92 m from crest.

5.6 Summary of Numerical Modeling

The work was sufficiently validated with average shear stress, velocity, and discharge comparisons to Hughes (2008) and Shaw (2010) physical models. Validation provides a level of confidence in that the results are shown to be reasonable illuminating a few key points. First, the 2-dimensional form of AdH appears adequate to produce reasonable results. The 2-D AdH model provides an option for other levee geometries; however, it is recommended to only evaluate shallower slopes, those less than 1:3, on the protected side of the levee. Additionally, a numerical model is more easily applied for different geometries than that of a physical model. Secondly, lower surge events were shown at the berm to flume transition on the levee to produce greater shear stresses than that of higher surge events when the surface friction coefficient (Manning) was equal to 0.035. That effect is caused by a hydraulic jump forming at the base of the berm, which was permitted in the numerical experiments but not in the physical experiments. For events that are less than 0.91 m, it appears that protective measures, if only based on shear, can be designed based on the lower surge event being considered, since concurrent increases in surges which are less than 0.91 m, results in proportionate increase in shear. However, for events greater than 0.91 m both the "higher" event and a range of lower events should be considered for the proper design and assessment of defensive measures for protected-side levee slopes, in particular at slope transitions.

Velocity and shear stresses seem to be greatest at locations of transitions. The transitions were modeled conservatively in this report, in that they were abrupt changes in slope resulting in the maximum local shear stress. Understanding the maximums ensures that forces on the levee during overtopping events are not underestimated. Therefore, abrupt changes are the most ideal in investigating protective measures to counteract shear forces exerted on a levee during an overtopping event. If levee protection measures are designed to the maximum occurring shear stresses across the entire protected side then levee failure probability is reduced.

CHAPTER 6 – SUMMARY AND CONCLUSIONS

6.1 Summary

Earthen levees are used throughout the world to protect communities and resources from elevated water levels in coastal and inland areas. Ideally, all levees would have a crest elevation with ample freeboard to prevent wave and/or surge overtopping for any conceivable storm scenario. However, economics dictate more practical levee designs having lower crest elevations, but with the risk that some wave/surge overtopping will occur during extreme events. Rapid erosion of levee soil can occur during overtopping flood events; and if unchecked, there is a risk of a catastrophic levee breach with massive flooding of the protected region. Earthen levees constructed without slope protection or armoring must rely on the erosion resistance of the outer soil layer during episodes of wave and/or storm surge overtopping.

The work presented in this report was developed in partial fulfillment of the requirements of Task Order 4000064719 sponsored by the *Department of Homeland Security (DHS)* through its *Southeast Region Research Initiative (SERRI)* program administered by *UT-Battelle* at the *Oak Ridge National Laboratory (ORNL)* in Oak Ridge, Tennessee. The primary objective of the research was to perform physical model testing and numerical simulations of combined wave overtopping and surge overflow of earthen levees to characterize shear stresses experienced by the landward side of the levee. These shear stresses are intended for use in investigating means of rapidly armoring the landward side of the levee to protect against sustained overtopping from events such as a hurricane. A secondary objective was to improve numerical simulation techniques related to levee overtopping and to provide unique physical model test results for use by future researchers.

A 1-to-25 small-scale physical model of a typical levee cross section adjacent to the Mississippi River Gulf Outlet (MRGO) was previously constructed and installed in a 0.9-m-wide wave flume at the U.S. Army Engineer Research and Development Center (ERDC), Coastal and Hydraulics Laboratory (CHL) in Vicksburg, MS. This model was activated and utilized for the studies described in this report. The physical model featured fixed-bed bathymetry seaward of the levee, and the levee cross-section was fabricated out of high-density foam. Because of scaling effects, no attempt was made to construct the levee using erodible soil. Thus, aspects related to erodibility of the underlying soil were not simulated in these tests. In addition to the wave generation capacity, a recirculation system was installed to simulate steady surge overflow of the levee combined with wave propagation and overtopping. The physical model was capable of simulating steady storm surge overflow, wave overtopping when the surge level was lower than the levee crest elevation, and wave overtopping when the surge elevation exceeded the levee crest elevation.

Model instrumentation consisted of three components. Seaward of the model levee, mean water level and instantaneous sea surface elevations (i.e., waves) were measured with four capacitance-type wave gauges. Three of the gauges were placed in an array near the levee structure so the incident wave conditions could be resolved using standard reflection

analysis. Seven pressure gauges were flush-mounted on the model levee cross section to measure instantaneous flow thickness during combined wave and surge overtopping. Two of the pressure gauges measured flow depth on the levee crest, and the remaining five gauges were evenly spaced down the landward-side levee slope to measure flow thickness. Velocities were measured using two laser Doppler velocimeters (LDVs). The LDVs were situated at locations coincident with pressure gauges so that instantaneous discharge at those locations could be calculated as the product of flow thickness and velocity.

Physical model simulations were conducted using combinations of three different levee crest elevations (negative freeboard), three different significant wave heights, and three different peak spectral wave periods. This gave a total of 27 unique conditions used to simulate the hydrodynamic forcing. Nominal negative freeboards scaled to prototype values were -0.3 m, -0.91 m, and -1.52 m. Prototype-scale wave heights were 0.91 m, 1.83 m, and 2.74 m. Peak spectral wave periods were 6 s, 9 s, and 14 s at prototype scale.

Testing in the physical model was divided into two phases. Nine tests were conducted with one LDV positioned over a pressure gauge located toward the rear of the levee crest and the other LDV situated over a pressure gauge located midway down the landward-side levee slope. Time series measurements were made of instantaneous flow thickness perpendicular to the levee surface and flow velocity parallel to the levee surface. The product of the flow thickness and velocity time series at each location provided an estimate of the instantaneous discharge due to combined wave and surge overtopping. These estimates assumed the velocity was constant over the flow thickness. The nine tests were referred to as the *discharge continuity test series*, and the main purpose of this test series was to validate the hypothesis that instantaneous overtopping discharge is conserved at all locations on the landward-side levee slope during combined wave and surge overtopping.

The second set of 27 tests was conducted with the LDVs relocated coincident to pressure gauges on the landward-side. The LDVs were separated by a distance of about 4.8 m in prototype-scale units. This test series was referred to as *the shear stress test series* because the primary purpose was to develop estimates of average and peak shear stresses acting on the landward-side levee slope during combined wave and surge overtopping events associated with a broad range of overtopping parameters. Shear stress estimates were based on the measured time series of flow thickness and velocity at the two locations on the landward-side slope. For steady overflow that occurred at the model levee before arrival of the first waves, shear stress was calculated using the formulation for steady, non-uniform flow on a slope that included the convective acceleration terms. Once waves also begin to overtop the levee, it was necessary to include the temporal acceleration term in the shear stress calculation.

A parallel numerical modeling effort was conducted using the Adaptive Hydraulics Numerical Model (AdH). This model is an unstructured finite element code developed by ERDC. The two-dimensional form of the AdH model was applied to a typical levee section in a numerical flume. The numerical flume was a 12,600-node mesh with the first third of the flume domain containing the levee section and seaward side. The remainder of the flume was designed to prevent back water effects so that a steady-state flow over the levee cross

section could be maintained. The model was run in fixed-bed mode because no attempt was made to evaluate levee erosion with the model. The numerical model simulated a series of steady-state surge-only events to estimate the shear stress on the landward side slope. The objective of the numerical modeling simulations was to validate the numerical surge-only overflow simulations by comparing results to physical model measurements for similar conditions. The model was also used to explore the effects of levee berms and slope roughness variation on the hydrodynamic shear stresses exerted on the landward-side levee slope.

6.2 Conclusions

6.2.1 Discharge Continuity Test Series

The magnitudes of the velocities and flow thickness were quite different between the levee crest and farther down on the landward-side slope because the supercritical flow was accelerating over this distance. However, comparisons of the calculated overtopping discharge time series at the two locations revealed that the time series of instantaneous discharge was the same at both locations with the only difference being a short phase lag. Previously, continuity of instantaneous discharge was suspected, but never confirmed. With the assumption of instantaneous discharge continuity it is possible to measure the discharge time series on the crest where measurements are less difficult, and then apply the discharge time series anywhere else on the levee landward-side slope. An obvious application would be dividing the discharge time series (after applying an appropriate time lag) by the time series of flow thickness measured on the slope to derive the associated velocity time series at that location. This helps alleviate the problem of how to acquire velocity measurements on levee slopes.

The individual peaks of the discharge time series were examined, and an empirical expression was determined for the root-mean-squared discharge peak as a function of average wave-surge overtopping discharge, significant wave height, and negative freeboard. Higher discharge peak statistics were compared to Rayleigh distributions estimates, and it was found that the Rayleigh distribution overestimates the largest discharge peaks. Nevertheless, reasonable estimates of extreme discharge peaks can be made using the Rayleigh distribution equations presented in this report.

The concept of stream power is used in river mechanics as a predictor of sediment transport. Time-varying stream power can also be expressed in terms of the instantaneous overtopping discharge. For locations on the landward-side slope where the friction slope is approximately the same as the levee slope, it is possible to derive a stream power probability density function based on the overtopping discharge cumulative exceedance probability given in Hughes and Nadal (2009) for combined wave and storm surge overtopping. The stream power probability density function may be a useful tool for assessing erosion potential of overtopped levees.

6.2.2 Shear Stress Test Series

Time series measurements of instantaneous flow thickness and velocity at two locations on the landward-side levee slope revealed that average velocities increased between the two locations whereas average flow thickness decreased. The change in average flow thickness and velocity was due to the fact that flow was continuing to accelerate between measurement locations. Estimates of average overtopping discharge at the two measurement locations were well predicted by a previous empirical formulation given by Hughes and Nadal (2009). Estimates of Manning's *n* for the smooth physical model slope ranged between 0.03 and 0.04 for the two highest overflowing surge levels.

The time series measurements of instantaneous flow parameters were used to develop estimates of the shear stress time series. These values of instantaneous shear stress represented the average shear stress over the 4.8-m length (prototype scale) of levee slope between the two measurement locations. A simple empirical equation was developed for steady overflow that related the mean shear stress to the specific weight of water and the steady discharge. The equation was based on estimates from the shear stress test series because these measurements appeared to be more accurate compared to the discharge continuity test series. The predictive equations are strictly only applicable for levees having landward-side slopes of 1V:3H with similar values of Manning's *n*. Also the mean shear stress estimates are for the region of the landward-side slope beginning a distance of 2.3 m from the levee crest and ending a distance of 7.1 m from the crest. At some location farther down the levee slope, the flow will reach terminal velocity for even the highest discharge. A conservative estimate for the maximum mean shear stress was found to be about 40% greater than the estimated mean shear stress.

Similar empirical correlations were developed for the mean shear stress caused by combined wave overtopping and surge overflow. Mean shear stress was found to be a function of the root-mean-squared overtopping discharge peak, and an equation was given for calculating the mean shear stress estimates. Maximum mean shear stresses associated with terminal flow conditions for even the largest discharge peaks were found to be about 40% larger, the same as for steady overflow. The more extreme shear stress peaks representing the average of the highest 1/3, 1/10, and 1/100 of the peaks were found to be linearly related to the estimated mean shear stress. The average of the highest 1/100 peaks is about 3.3 times the mean shear stress.

6.2.3 Numerical Model Simulations

The USACE 2-dimensional Adaptive Hydraulics Model (AdH) was used to calculate velocity and depth during a levee overtopping event in a numerical flume. The objective of the numerical model was twofold: (1) Validation of the numerical model to that of the physical model was imperative to demonstrate the effectiveness of the AdH numerical model; and (2) Evaluation of the changes of levee shear stress due to levee berm effects and variations in slope roughness was crucial for discerning impacts due to slope transitions and levee cover. The numerical model levee section was positioned in the upstream third of the flume with a catch basin at the tailwater end to eliminate back water affects. The model was

run to steady state in fixed bed mode. Twelve different test cases were simulated, varying surge depth and Manning's *n*, to determine the corresponding shear stresses.

The work was sufficiently validated with average shear stress, velocity, and discharge comparisons to Hughes (2008) and Shaw (2010) physical models. The 2-dimensional form of AdH appears adequate to produce reasonable results. Lower surge events were shown at the berm-to-flume transition on the levee to produce greater shear stresses than that of higher surge events when the surface friction coefficient (Manning) was equal to 0.035. That effect is caused by a hydraulic jump forming at the base of the berm, which was permitted in the numerical experiments but not in the physical experiments. Here velocity and shear stresses seem to be greatest. Understanding the maximums ensures that forces on the levee during overtopping events are not underestimated. Therefore, abrupt changes, which produce the greatest shear, are the most ideal in investigating protective measures to counteract shear forces exerted on a levee during an overtopping event. If levee protection measures are designed to the maximum occurring shear stresses across the entire protected side then levee failure probability is reduced.

6.3 Recommendations

Recommendations for future investigation related to overtopping of earthen levees are listed below. These recommendations are areas where additional investigation could prove useful in the design and protection of earthen levees against wave and surge overtopping.

- Test the resistance properties of geosynthetics when impacted with waves. The response of a geotextile resting on soil and impacted by high shear stress and short period overtopping waves is not fully understood. Design of a geotextiles-based temporary levee armoring system could be optimized if this interaction were captured in a test program.
- Perform small-scale overtopping experiments similar to those described in this report with a rigid levee covered with different geotextiles to evaluate the effect their roughness has on discharge and shear stress.
- Perform small-scale overtopping experiments similar to those documented in this report at different landward-side levee slopes (e.g. 1V:4H and 1V:5H) with different slope roughness. A test sequence of this nature would allow the empirical formulations in this report to be extended to a more general set of conditions that would be applicable to the majority of earthen levees currently in service.

REFERENCES

ASCE Katrina External Review Panel. 2007. *The New Orleans Hurricane Protection System: What Went Wrong and Why*, American Society of Civil Engineers, Reston, Virginia.

Bagnold, R. A. 1960. "Sediment discharge and stream power", *Preliminary Announcement*, U.S. Geological Survey Circular 421, Menlo Park, CA.

Bagnold, R.A. 1966. "An approach to the sediment transport problem from general physics", U.S. Geological Survey, Professional Paper 422-J.

Berger, R. C. 1997. "HIVEL 2D v2.0 Users Manual," Hydraulics Laboratory, Waterways Experiment Station, US Army Corps of Engineers, Vicksburg, MS.

Berger, R. C., Tate, J. N., Brown, G. L., and Savant, G. 2010. "Adaptive Hydraulics User Manual; A Two-Dimensional Modeling System," Waterways Experiment Station, US Army Corps of Engineers, Vicksburg, MS.

Briaud, J.-L., Chen, H.-C., Govindasamy, A. V., and Storesund, R. 2008. "Levee erosion by overtopping in New Orleans during the Hurricane Katrina. *Journal of Geotechnical and Geoenvironmental Engineering,* American Society of Civil Engineers, Vol 134, No. 5, pp 618-632.

Budhu, M. 2008. *Foundations and Earth Retaining Structures*, John Wiley & Sons, Inc., Danvers, MA.

Chaudhry, H. 1993. *Open-Channel Flow,* Prentice Hall, Inc., Englewood Cliffs, New Jersey.

Causon, D., Ingram, D., Mingham, C., Zang, J., Hu, K., Zhou, J.G. 2000. "Numerical simulation seawall overtopping," *Proceedings of the 27th International Conference on Coastal Engineering*, American Society of Civil Engineers, New York, pp. 2086-2099.

Cornett, A. M., and Mansard, E. 1994. "Wave stresses on rubble mound armour," *Proceedings of the 24th International Coastal Engineering Conference,* American Society of Civil Engineers, Vol 1, pp 986-1000.

de Waal, J. P., and van der Meer, J. W. 1992. "Wave run-up and overtopping on coastal structures," *Proceedings of the 23rd International Coastal Engineering Conference*, American Society of Civil Engineers, Vol 2, pp 1758-1771.

FHWA. 2005. "Design of roadside channels with flexible linings." Hydraulics Engineering Circular No. 15, 3rd Ed., Federal Highway Administration, Publication No. FHWA-NHI-05-114.

Goda, Y., and Y. Suzuki. 1976. "Estimation of incident and reflected waves in random wave experiments," *Proceedings 15th International Coastal Engineering Conference*, American Society of Civil Engineers, Vol 1, pp 828-845.

Hammack, E. A., Smith, D. S., Stockstill, R. L. 2008. "Modeling vessel-generated currents and bed shear stress" Technical Report TR-08-7, Coastal and Hydraulics Laboratory, US Army Engineer Research and Development Center, Vicksburg, MS.

Henderson, F. M. 1966. *Open channel flow*, MacMillian Publishing Co., New York.

Hu, K., Mingham, C. G., Causon, D. M. 2000. "Numerical simulation of wave overtopping of coastal structure using the non-linear shallow water equation," *Coastal Engineering*, Elsevier, Vol 41, pp 433-465.

Hubbard, M. E., Dodd, N. 2002. "A 2D numerical model of wave run-up and overtopping," *Coastal Engineering*, Elsevier, Vol 47, pp 1-26.

Hudson , R. Y., F. A. Herrmann, R. A. Sager, R. W. Whalin, G. H. Keulegan, C. E. Chatham, and L. Z. Hales. 1979. "Coastal hydraulic models," Special Report No. 5, U.S. Army Engineer Waterways Experiment Station, Vicksburg, MS.

Hughes, S. A. 1993. *Physical models and laboratory techniques in coastal engineering*, World Scientific, Singapore.

Hughes, S. A. 2003. "Physical modeling considerations for coastal structures," In *Advances in coastal structure design*, R. Mohan, ed., American Society of Civil Engineers, pp 97-115.

Hughes, S. A. 2008. "Combined wave and surge overtopping of levees: flow hydrodynamics and articulated concrete mat stability," ERDC/CHL TR-08-10, U.S. Army Engineer Research and Development Center, Vicksburg, Mississippi.

Hughes, S. A., and Nadal, N. C. 2009. "Laboratory study of combined wave overtopping and storm surge overflow of a levee," *Coastal Engineering*, Vol 56. No. 3, Elsevier, pp 244-259.

Hughes, S. A., and Nadal, N. C. 2010. "Flow parameters of combined wave overtopping and storm surge overflow of a trapezoidal levee," *Proceedings of Coasts, Marine Structures and Breakwaters: 9th International Breakwaters Conference 2009*, Institution of Civil Engineers, London, Vol 2, pp 562-573.

Hughes, S. A., and Shaw, J. M. 2011. Continuity of instantaneous overtopping discharge with application to stream power concepts. *Journal of Waterway, Port, Coastal, and Ocean Engineering*. Vol 137, No. 1, pp 12-25.

Irish, J., Resio, D., and Ratcliff, J. 2003. "The influence of storm size on hurricane surge," *Journal of Physical Oceanography*, American Meteorological Society, Vol 38, No. 9, pp 2003-2013.

Julien, P. Y. 2002. *River Mechanics.* Cambridge University Press. Cambridge, UK.

Le Méhauté, B. 1976. "Similitude in coastal engineering," *Journal of the Waterways, Harbors and Coastal Engineering Division*, American Society of Civil Engineers, Vol 102 No. WW3, pp 317-335.

Lin, P., Liu, P. L.-F. 1998. "A numerical study of breaking waves in the surf zone," *Journal of Fluid Mechanics*, Vol 359, pp 239-264.

Lin, P., Xu, W. 2006. "NEWFLUME: a numerical water flume for the tow dimensional turbulent free surface flows," Journal of Hydraulic Research, Vol 44, No. 1, pp 79-93.

Mansard, E., and Funke, E. 1980. "The measurement of incident and reflected spectra using a least square method," *Proceedings of the 17th International Coastal Engineering Conference*, World Scientific, Vol 1, pp 154-172.

Munson, B. R., Young, D. F., and Okiishi, T. H. 2002. *Fundamentals of fluid mechanics*. 4th Ed., John Wiley & Sons, Inc., New York, NY.

Nadal, N. C., and Hughes, S. A. 2009. "Shear stress estimates for combined wave and surge overtopping at earthen levees." Coastal and Hydraulics Engineering Technical Note ERDC/CHL CHETN-III-79, U.S. Army Engineer Research and Development Center, Vicksburg, MS.

NRF. 2008. *National Response Framework,* US Department of Homeland Security, Washington, DC, 82pp.

Okayasu, A, Suzuki, T., and Matsubayashi, Y. 2005. "Laboratory experiment and three-dimensional large eddy simulation of wave overtopping on gentle slope seawalls," *Coastal Engineering Journal*. World Scientific, Vol 47, Nos. 2 and 3, pp 71-89. World Scientific.

Pullen T., Allsop, N.W.H., Bruce, T., Kortenhaus A., Schüttrumpf H., van der Meer, J. W. 2007. "EurOtop: Wave overtopping of sea defences and related structures: Assessment Manual," www.overtopping-manual.com.

Reeve, D. E., Soliman, A., and Lin, P. Z. 2008. "Numerical study of combined overflow and wave overtopping over a smooth impermeable seawall," *Coastal Engineering*, Elsevier, Vol 55, pp 155-166.

Rodi, W. 1993. *Turbulence models and their application in hydraulics – a state of the art review*, Balkema.

Savant, G., Berger, C., McAlpin, T., and Tate, J. 2010. "Application of Adaptive Hydraulics (ADH) to Rapidly Evolving Hydrodynamic Flows", System Wide Water Resource Program, US Army Corp of Engineers, Vicksburg, MS.

Schüttrumpf, H. 2001. Wellenüberlaufströmung bei Seedeichen – Experimentelle und Theoretische Untersuchungen. PhD-Thesis.

Schüttrumpf, H. 2006. Personal communication via email, April 5, 2006.

Schüttrumpf, H., Möller, J., and Oumeraci, H., Grüne, J., and Weissmann, R. 2001. "Effects of natural sea states on wave overtopping of seadikes," *Proceedings of the 4th International Symposium Waves 2001, Ocean Wave Measurement and Analysis*, American Society of Civil Engineers, Vol 2, pp 1565-1574.

Schüttrumpf, H., Möller, J., and Oumeraci, H. 2002. "Overtopping flow parameters on the inner slope of seadikes," *Proceedings of the 28th International Coastal Engineering Conference*, World Scientific, Vol 2, pp 2116-2127.

Schüttrumpf, H., and van Gent, M. R. 2003. "Wave overtopping at seadikes," *Proceedings of Coastal Structures, '03*, American Society of Civil Engineers, pp 431-443.

Schüttrumpf, H., and Oumeraci, H. 2005. "Layer thicknesses and velocities of wave overtopping flow at seadikes," *Coastal Engineering*, Elsevier, Vol 52, pp 473-495.

Shaw, J. M. 2010. "Shear stress analysis of levees subjected to combined surge and wave overtopping," Masters thesis, Mississippi State University.

Shiach, J. B., Mingham, C. G., Ingram, D. M., and Bruce, T. 2004. "The applicability of the shallow water equations for modeling violent wave overtopping," *Coastal Engineering*, Vol 51, No. 1, pp 1 -15.

Soliman, A. 2003. "Numerical study of irregular wave overtopping and overflow," Ph.D. Dissertation, University of Nottingham, United Kingdom.

Soliman, A., and Reeve, D. E. 2004. "Numerical study for small negative freeboard wave overtopping and overflow of sloping sea wall," *Proceedings of 3rd International Conference of Coastal Structures 2003*, Portland, Oregon. American Society of Civil Engineers, New York, pp 643-655.

Sturm, T.W. 2001. *Open channel hydraulics*. McGraw-Hill, New York, NY.

TAW. 2002. "Technical Report - Wave run-up and wave overtopping at dikes," Technical Advisory Committee for Flood Defence in the Netherlands (TAW), Delft, The Netherlands.

USDA 2001. "Stream corridor restoration: principles, processes, and practices", The Federal Interagency Stream Restoration Working Group, United States Department of Agriculture (USDA) - Natural Resources Conservation Service, Part 653 of the National Engineering Handbook.

van der Meer, J. W., and Janssen, W. 1995. "Wave run-up and wave overtopping at dikes," In: Kabayashi and Demirbilek (Eds.), *Wave Forces on Inclined and Vertical Wall Structures*, American Society of Civil Engineers, pp 1-27.

van der Meer, J. W., Bernardini, P., Snijders, W., and Regeling, E. 2006. "The wave overtopping simulator," *Proceedings of the 30th International Conference on Coastal Engineering*, World Scientific, Vol 5, pp 4654-4666.

van Gent, M. R. 2001. "Wave run-up on dikes with shallow foreshores," *Journal of Waterway, Port, Coastal and Ocean Engineering*, American Society of Civil Engineers, Vol 127, No. 5, pp 254-262.

van Gent, M. R. 2002. "Wave overtopping events at dikes," *Proceedings of the 28th International Coastal Engineering Conference*, World Scientific, Vol 2, pp 2203-2215.

Warnock, J. E. 1950. "Hydraulic similitude," In *Engineering hydraulics*, H. Rouse, ed., John Wiley & Sons, New York, pp 136-176.

APPENDIX A
SUPPLEMENTARY NUMERIAL MODELING RESULTS

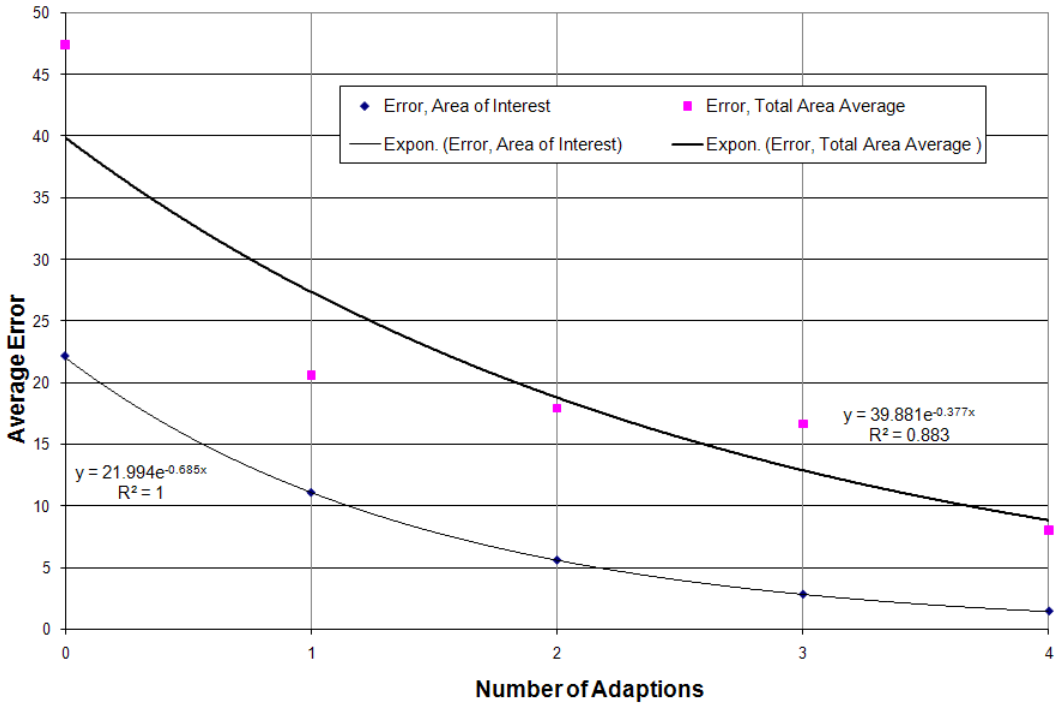

Figure A.1. Average residual error vs. number of adaptations.

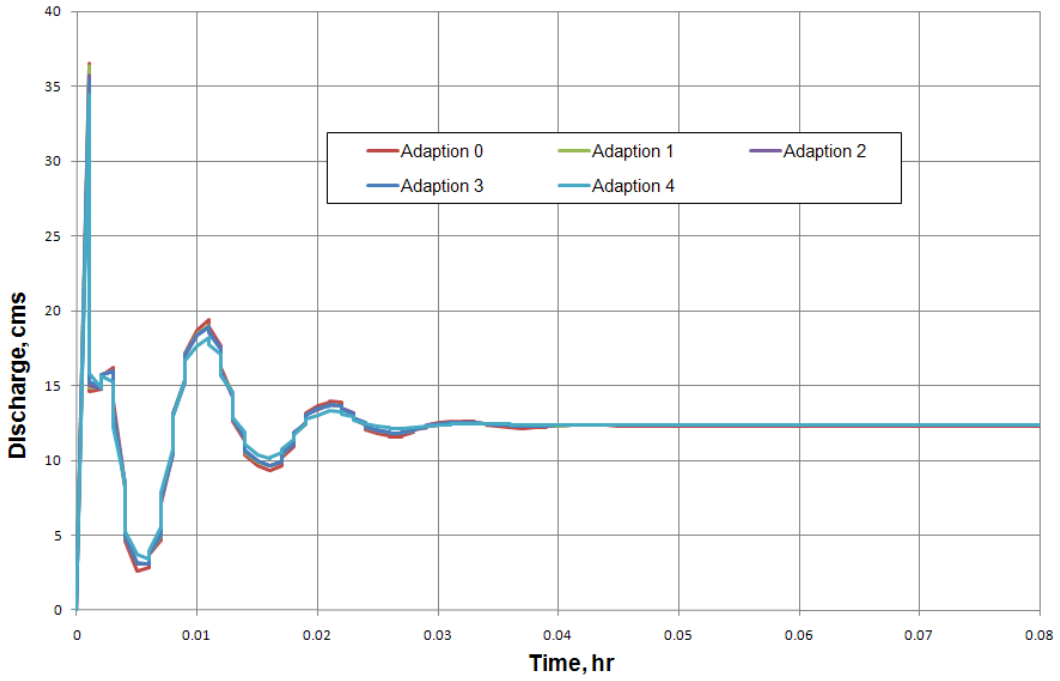

Figure A.2. Flow convergence for determination of time required to reach steady state.

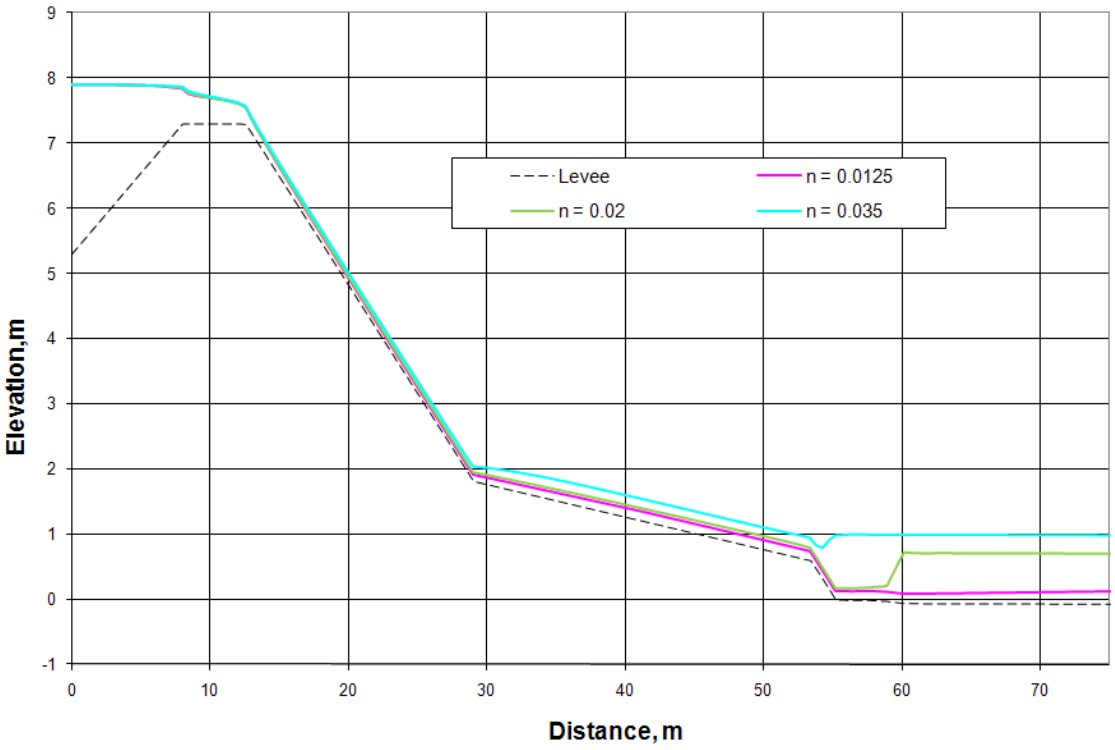

Figure A.3. Water surface profile for 0.61 m surge event.

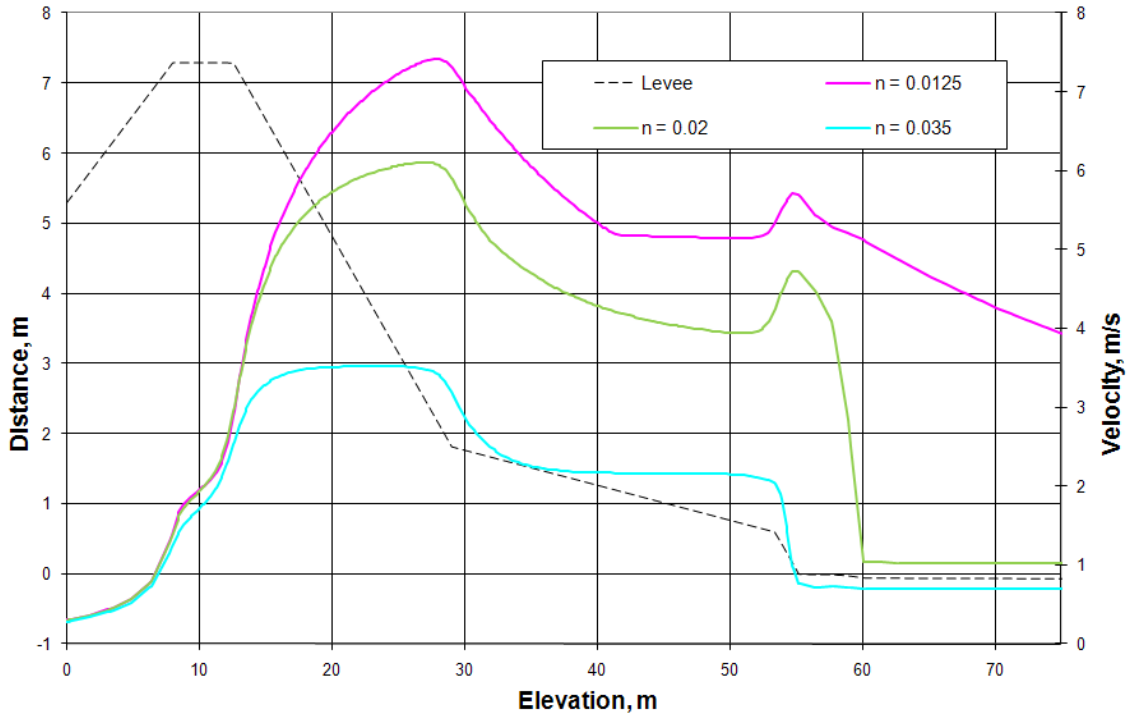

Figure A.4. Velocity profile for 0.61 m surge event.

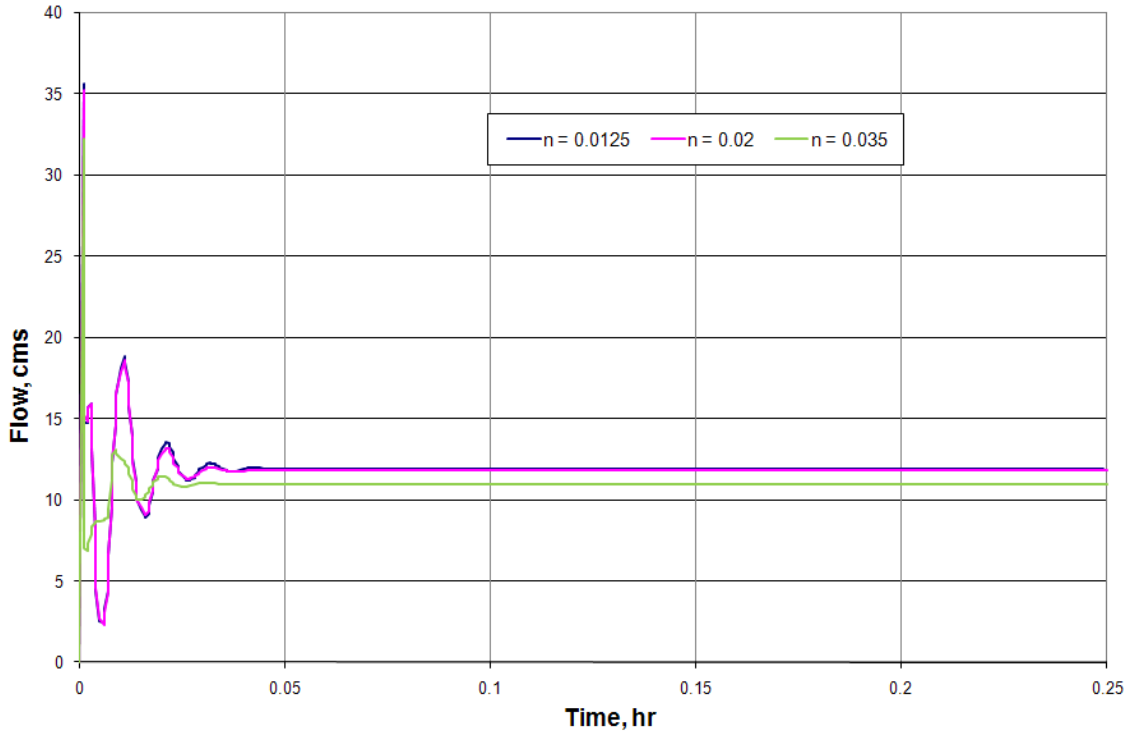

Figure A.5. Flow convergence for 0.61 m surge event.

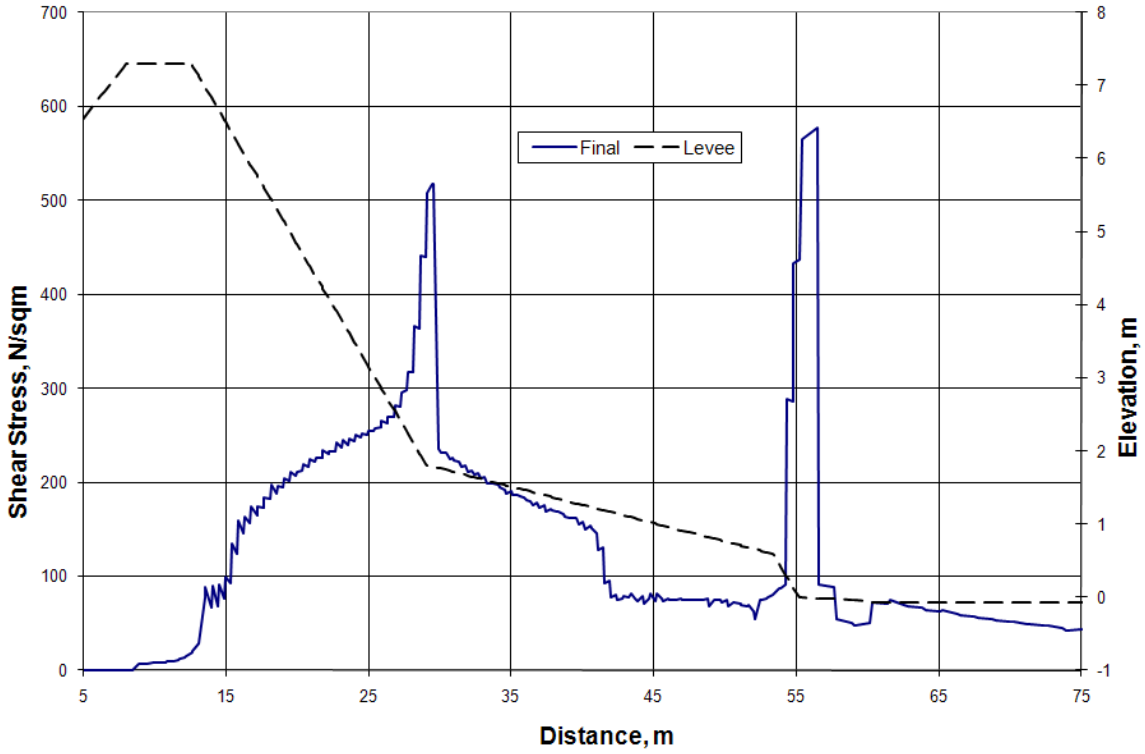

Figure A.6. Shear Stress Profile for 0.61 m surge event with n = 0.0125.

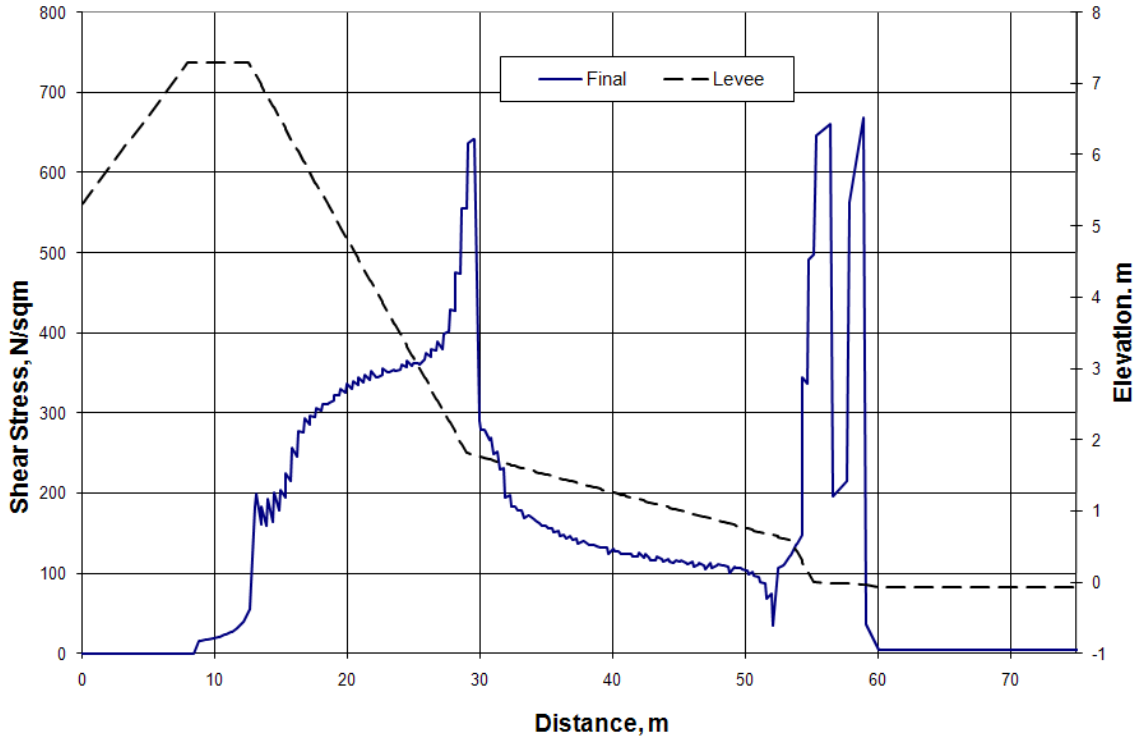

Figure A.7. Shear stress profile for 0.61 m surge event and n = 0.02.

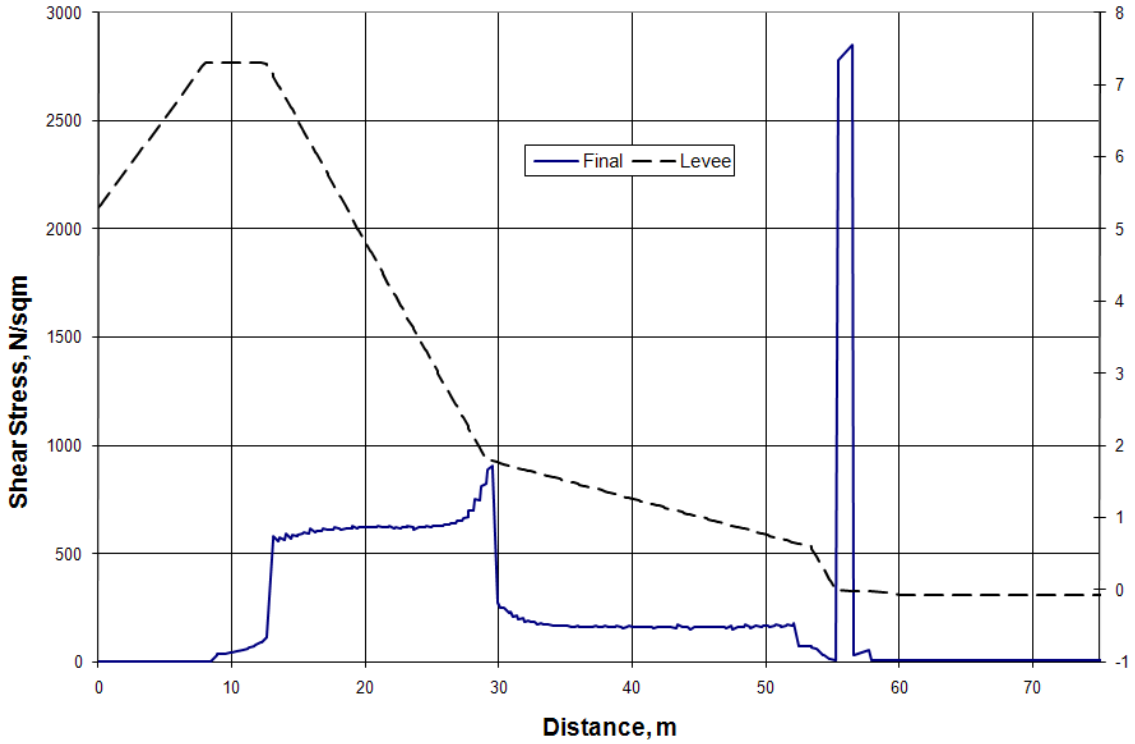

Figure A.8. Shear stress profile for 0.61 m surge event and n = 0.035.

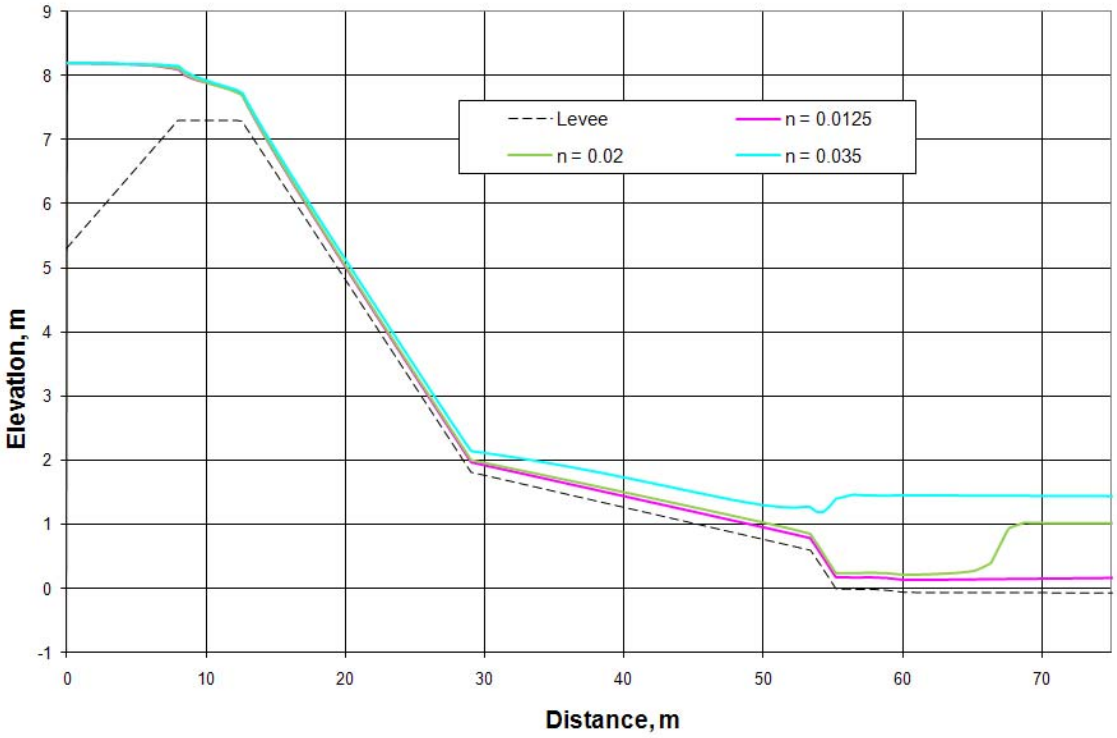

Figure A.9. Water surface profile for 0.91 m surge event.

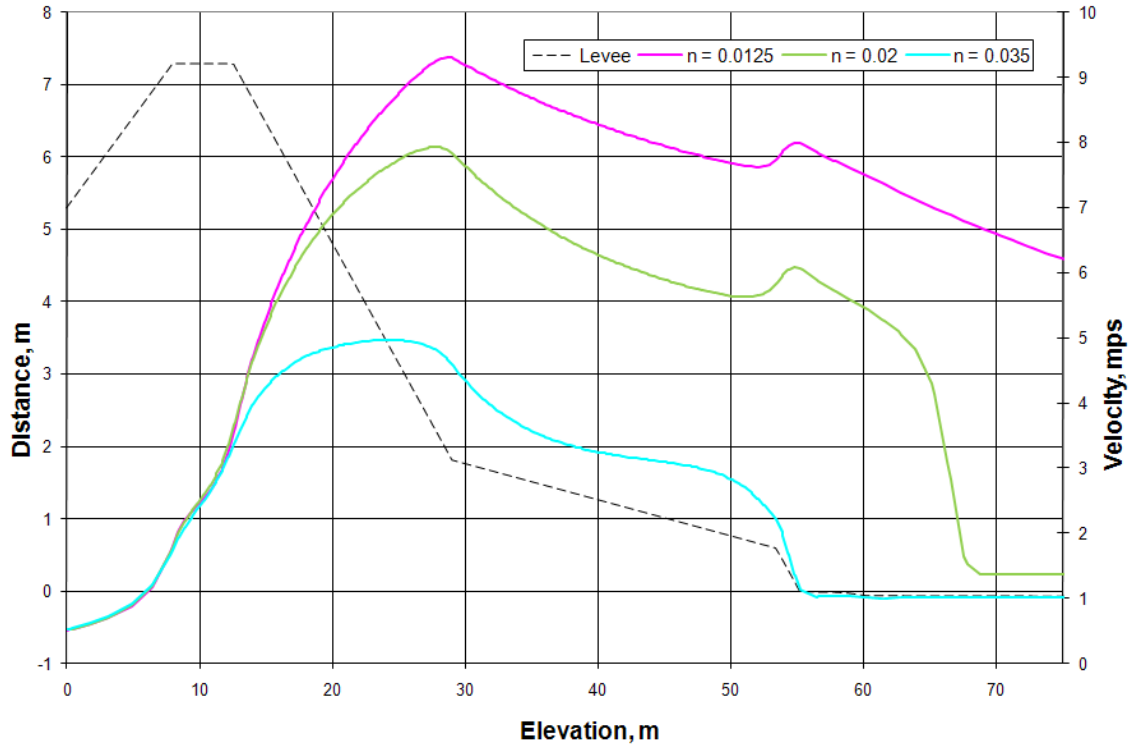

Figure A.10. Velocity profile for 0.91 m surge event.

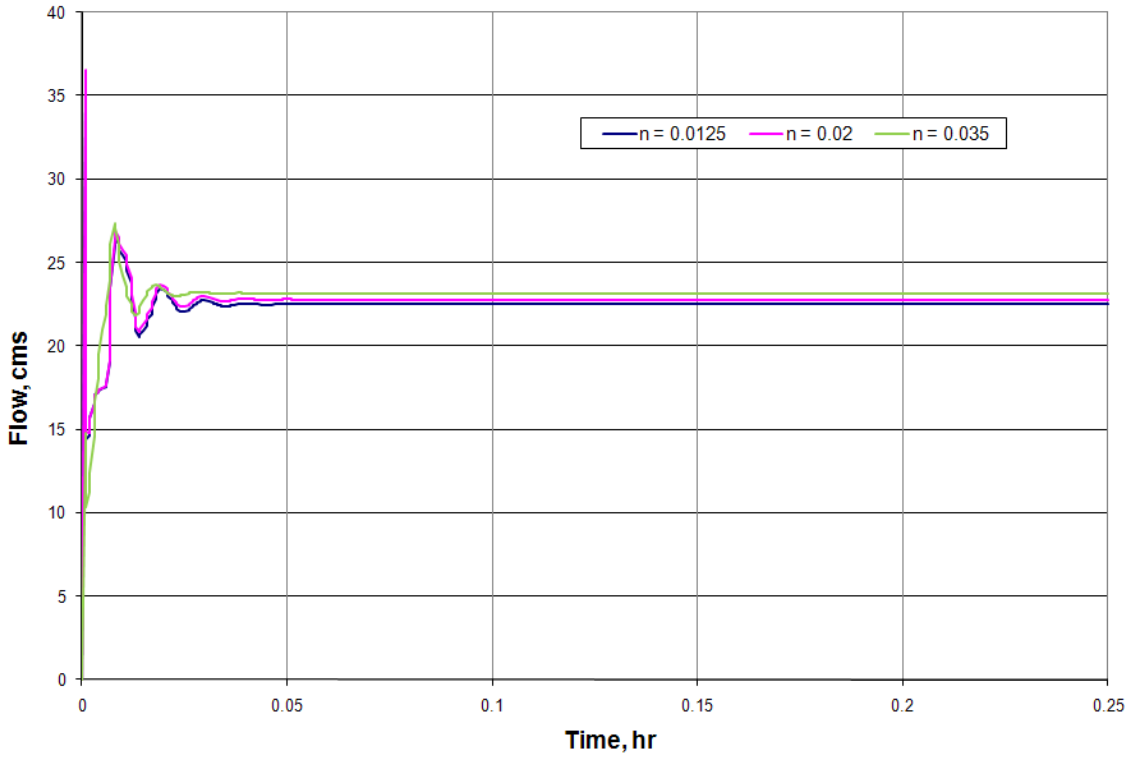

Figure A.11. Flow convergence for 0.91 m surge event.

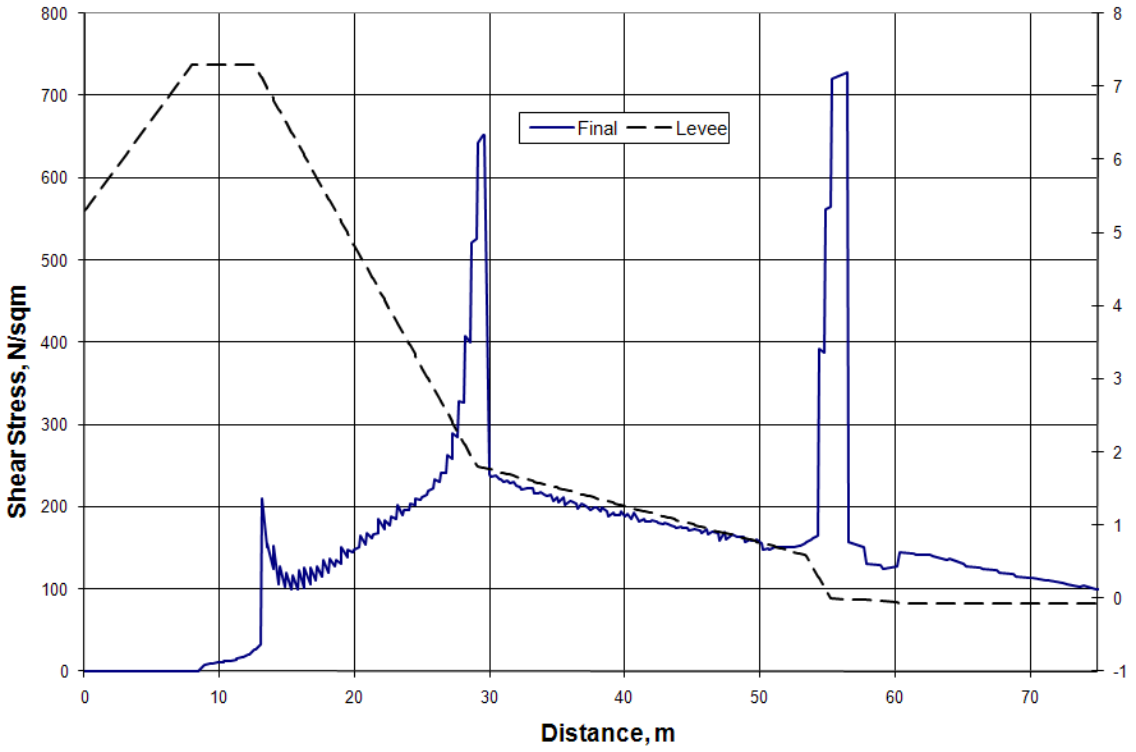

Figure A.12. Shear stress profile for 0.91 m surge event and n = 0.0125.

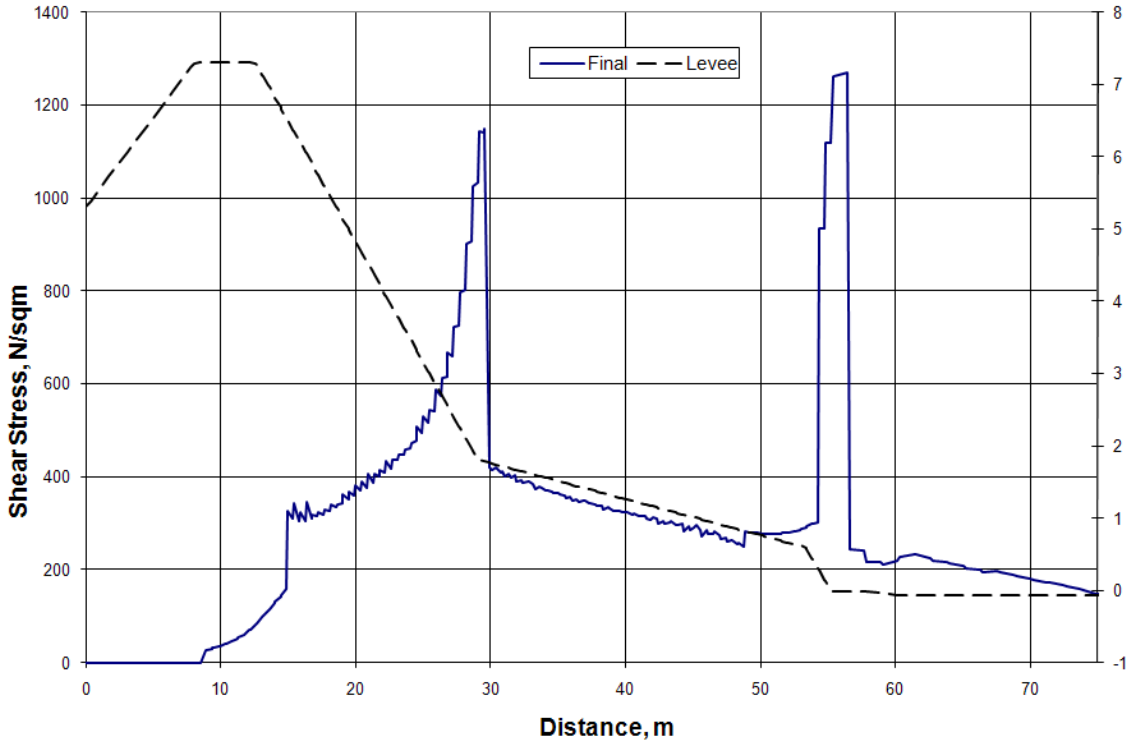

Figure A.13. Shear stress profile for 0.91 m surge event and n = 0.02.

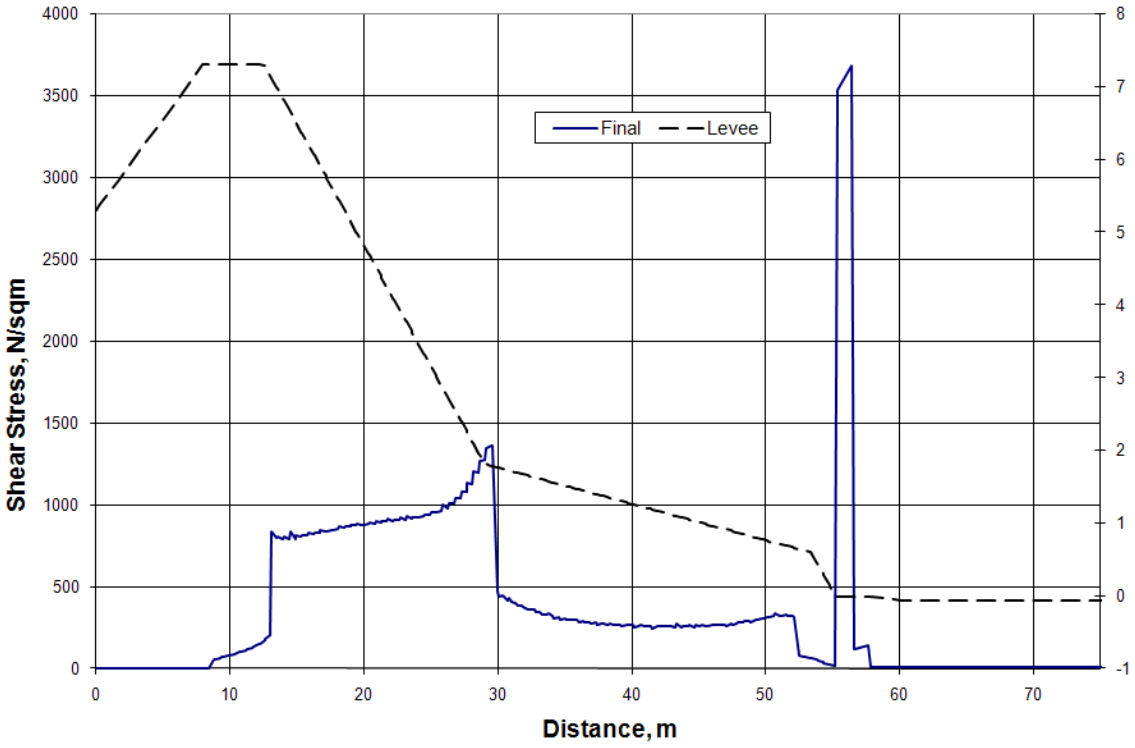

Figure A.14. Shear stress profile for 0.91 m surge event and n = 0.035.

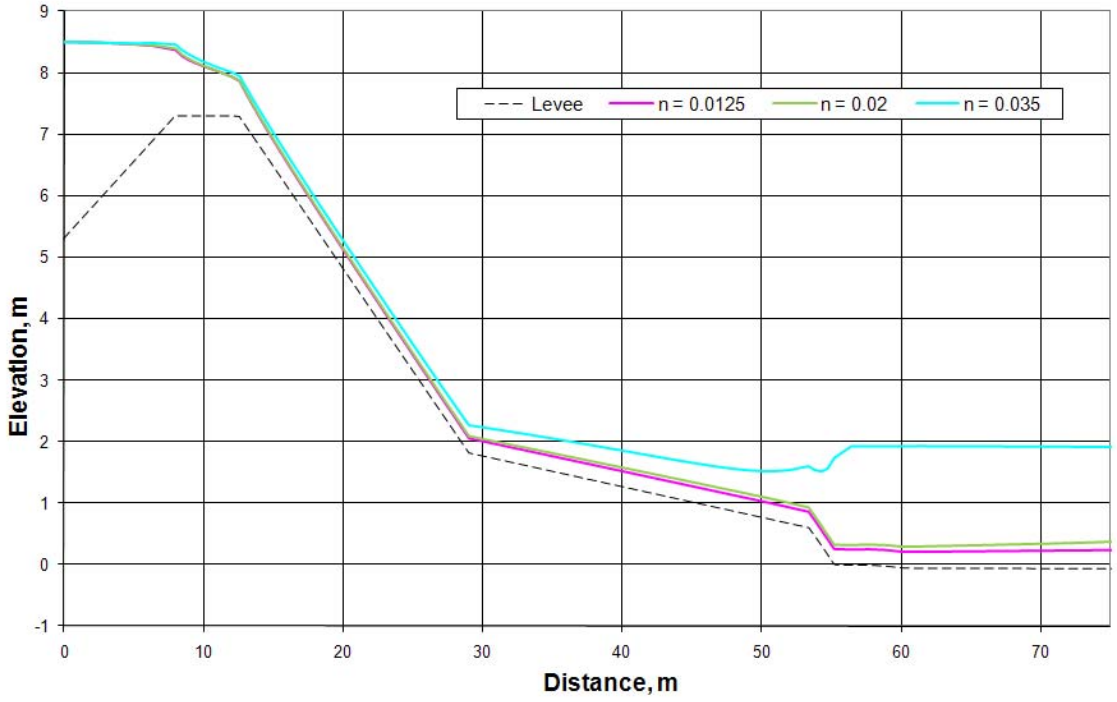

Figure A.15. Water surface profile for 1.22 m surge event.

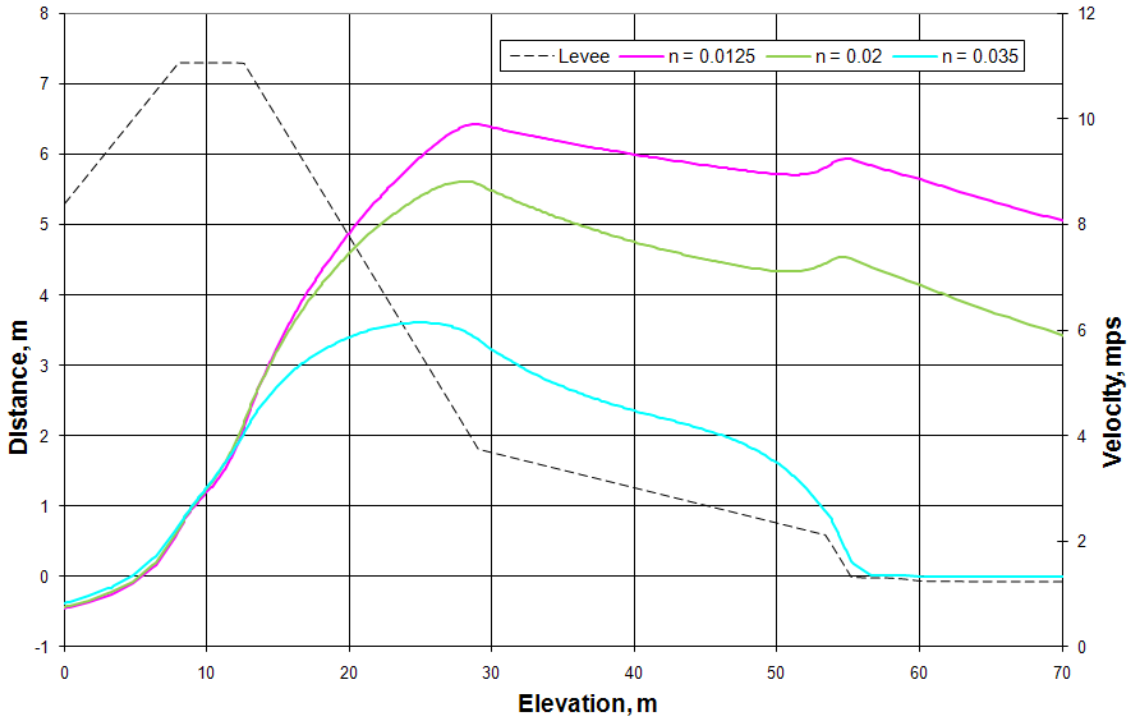

Figure A.16. Velocity profile for 1.22 m surge event.

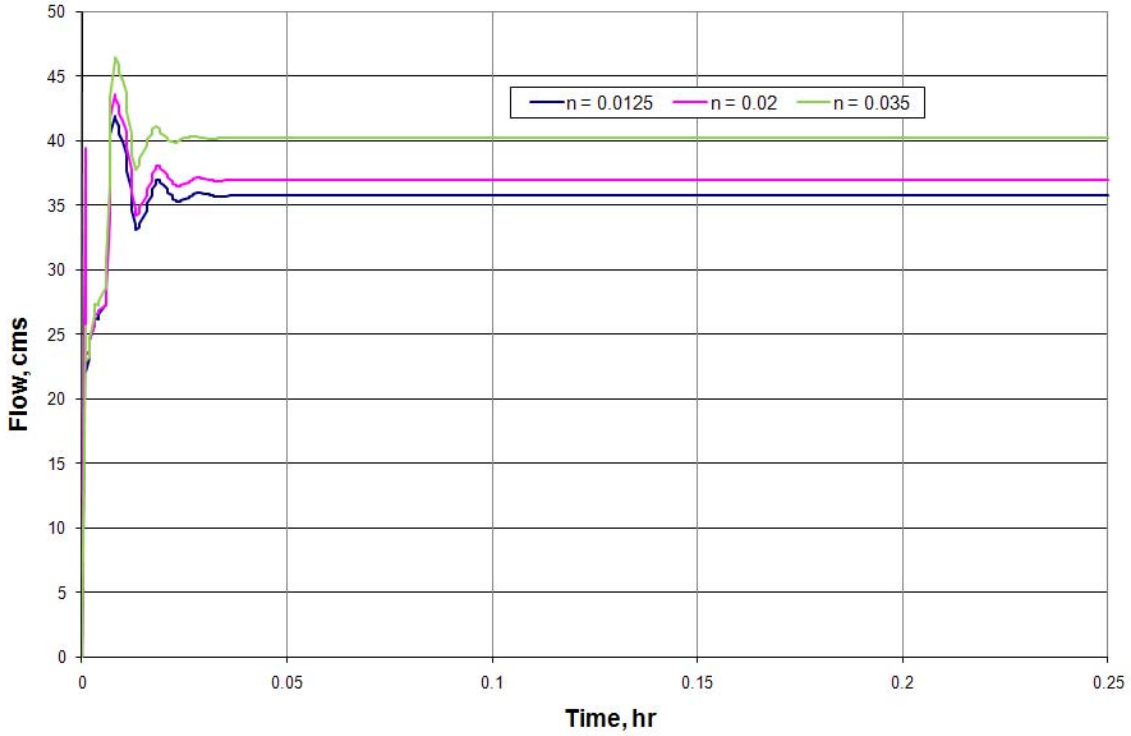

Figure A.17. Flow convergence for 1.22 m surge event.

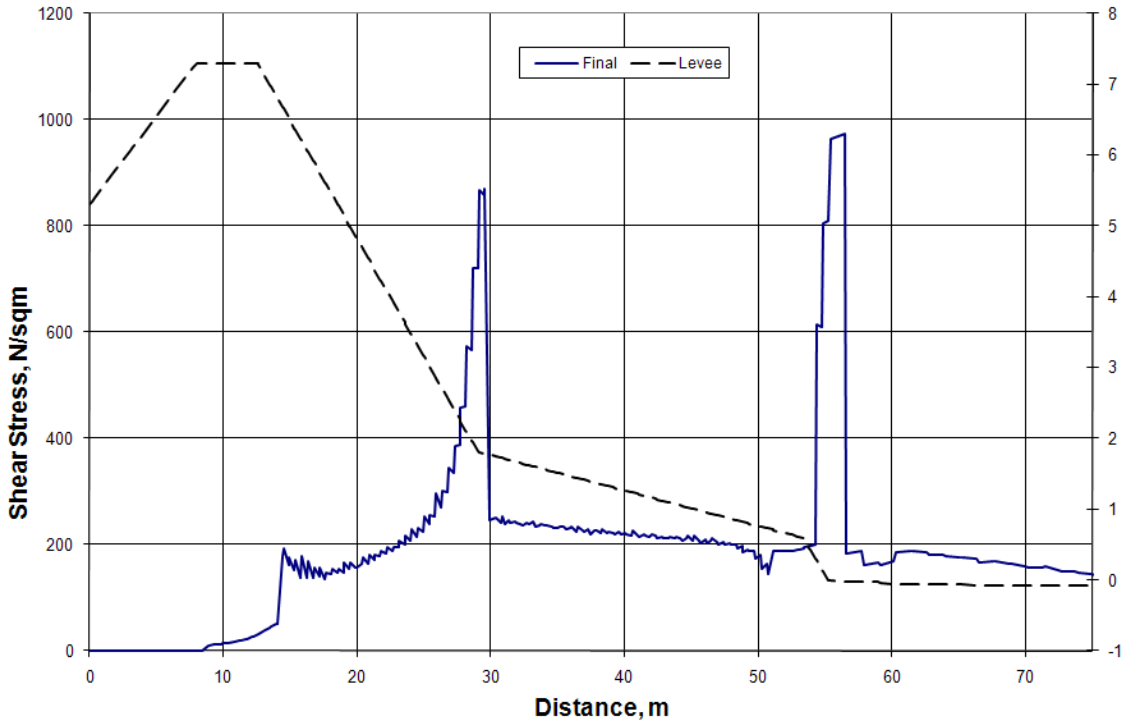

Figure A.18. Shear stress profile for 1.22 m surge event and n = 0.0125.

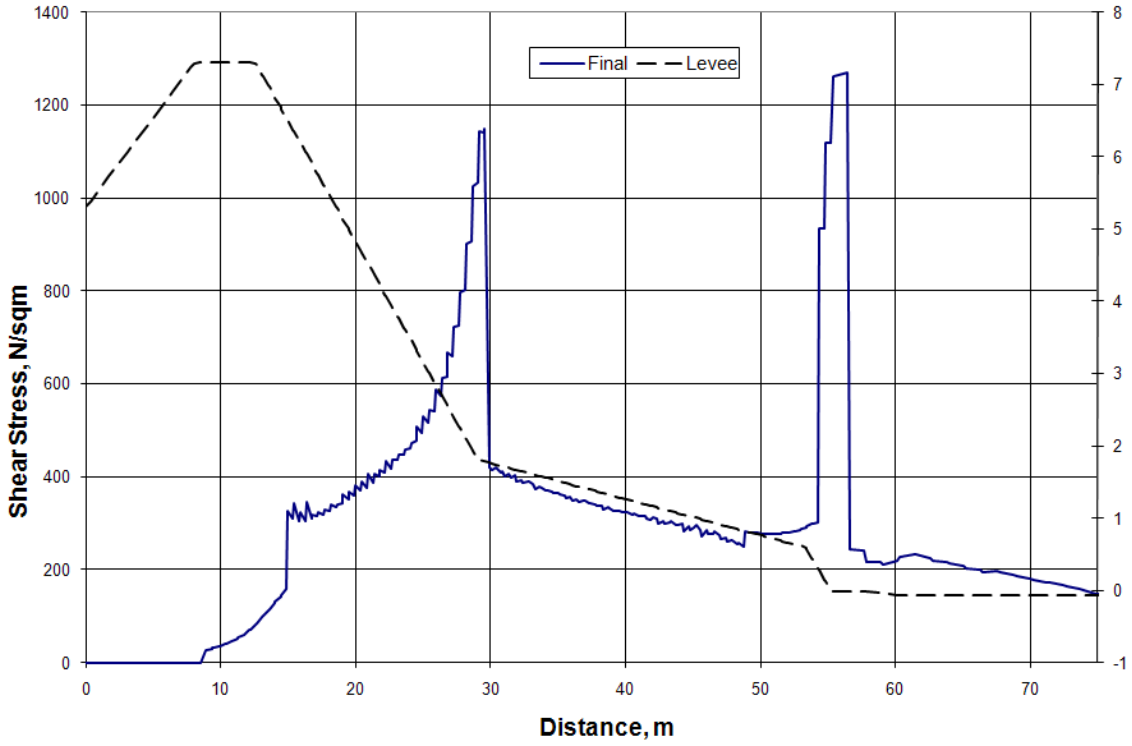

Figure A.19. Shear stress profile for 1.22 m surge event and n = 0.02.

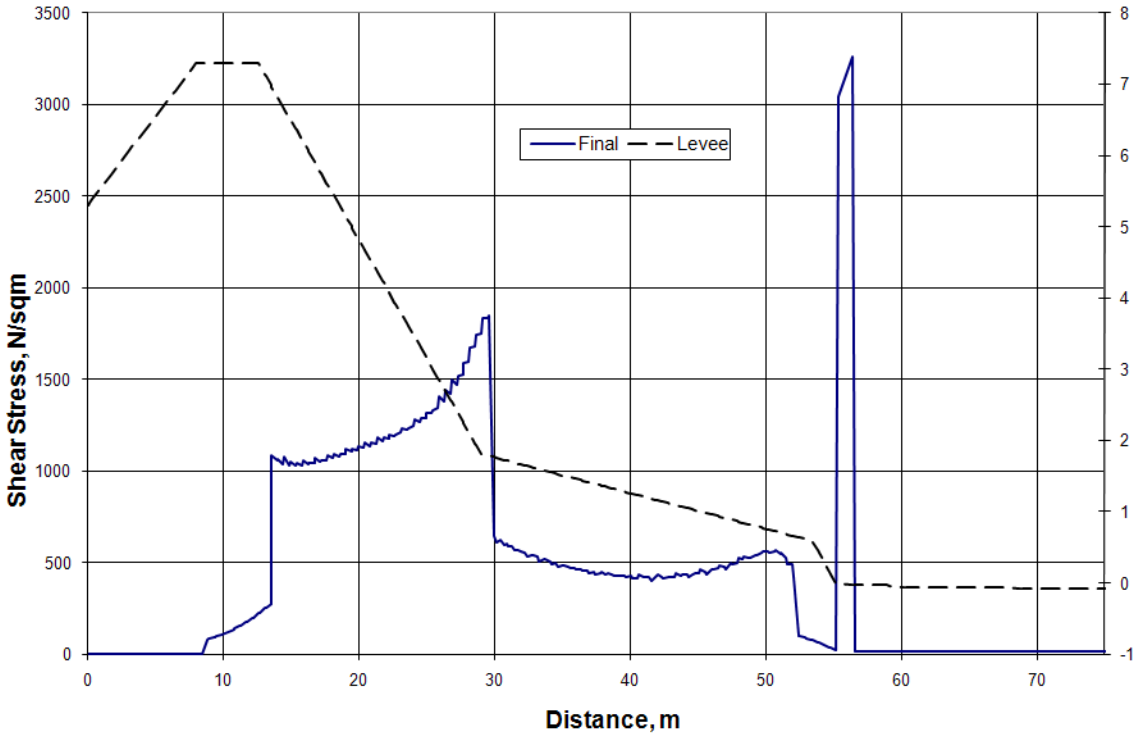

Figure A.20. Shear stress profile for 1.22 m surge event and n = 0.035.

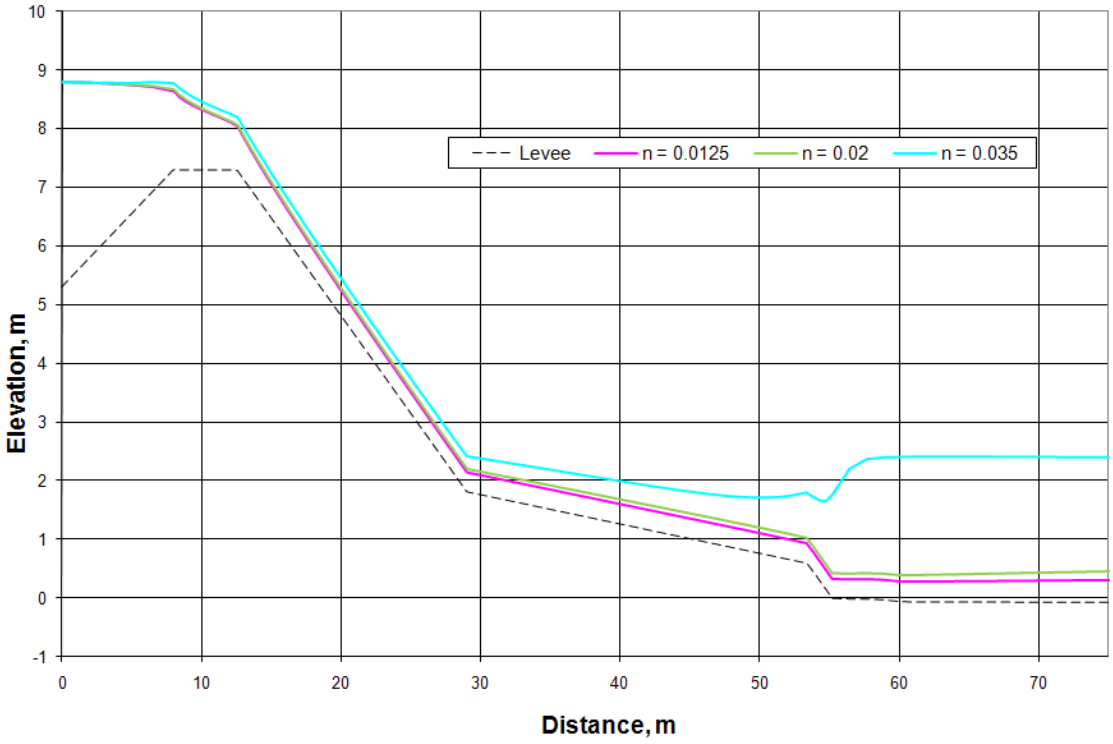

Figure A.21. Water surface profile for 1.52 m surge event.

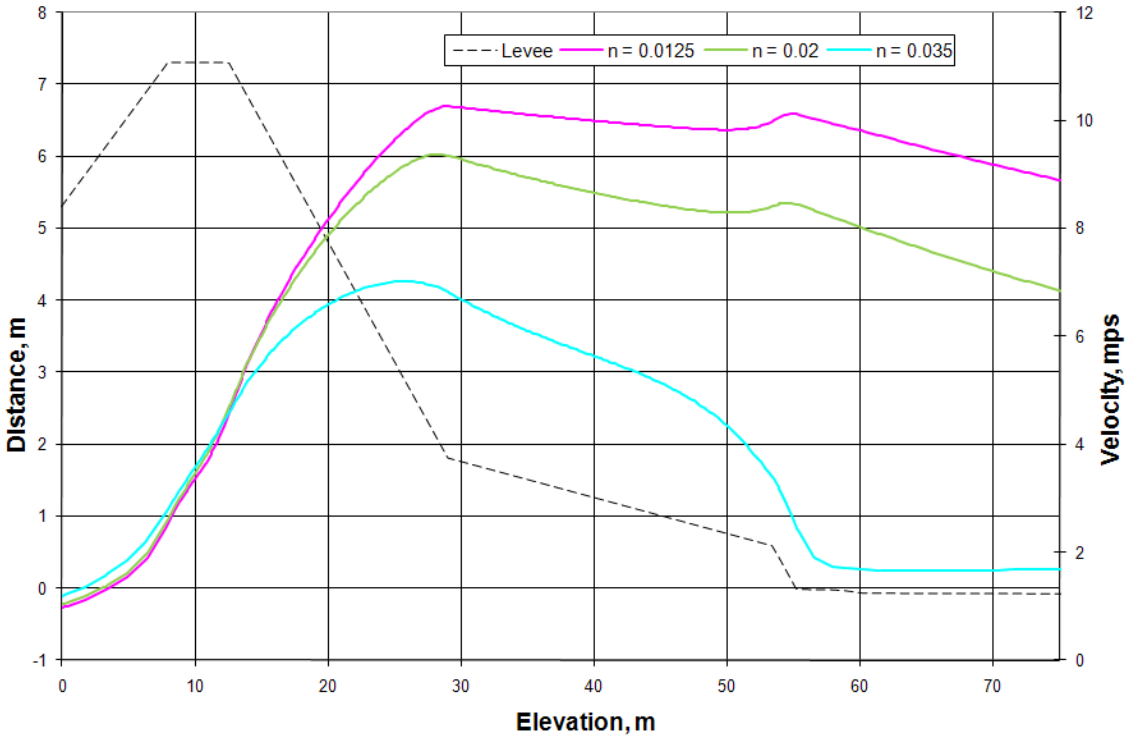

Figure A.22. Velocity profile for 1.52 m surge event.

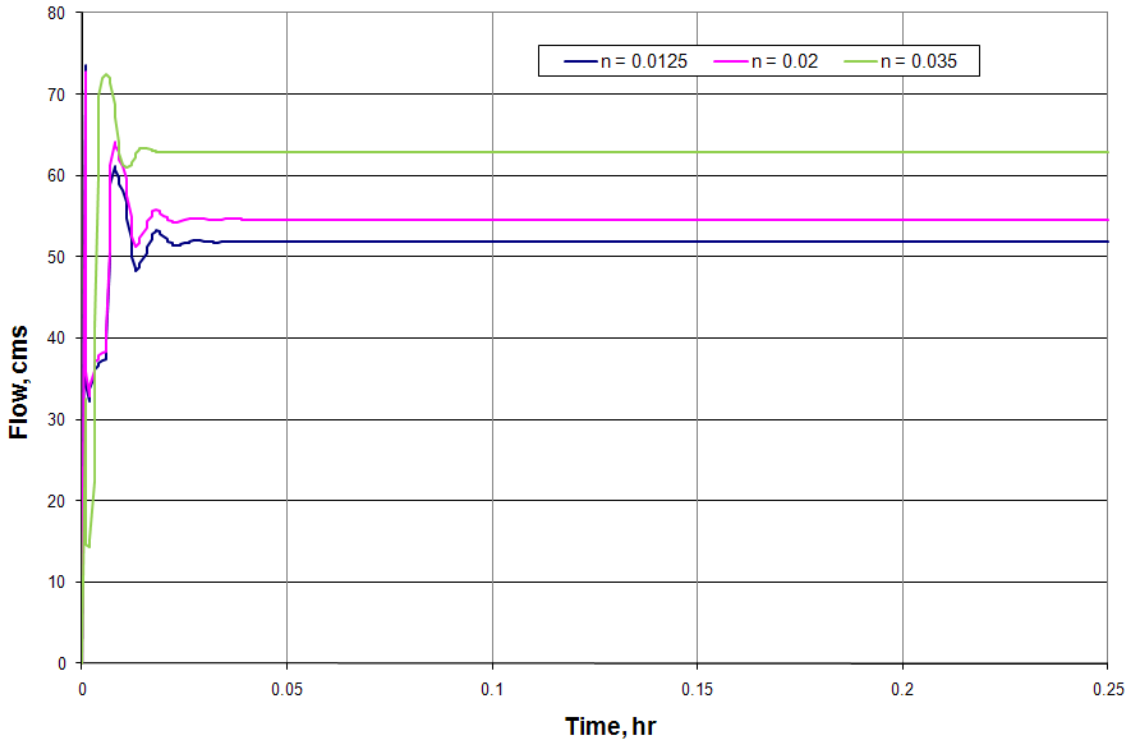

Figure A.23. Flow convergence for 1.52 m surge event.

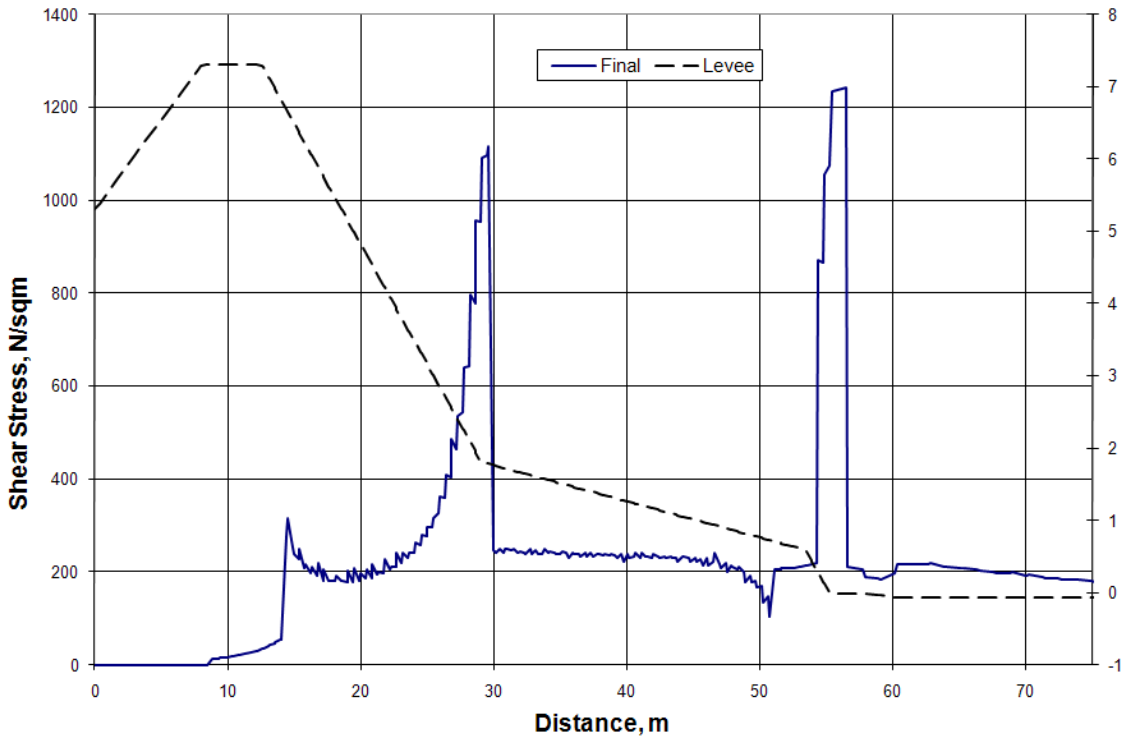

Figure A.24. Shear stress profile for 1.52 m surge event and n = 0.0125.

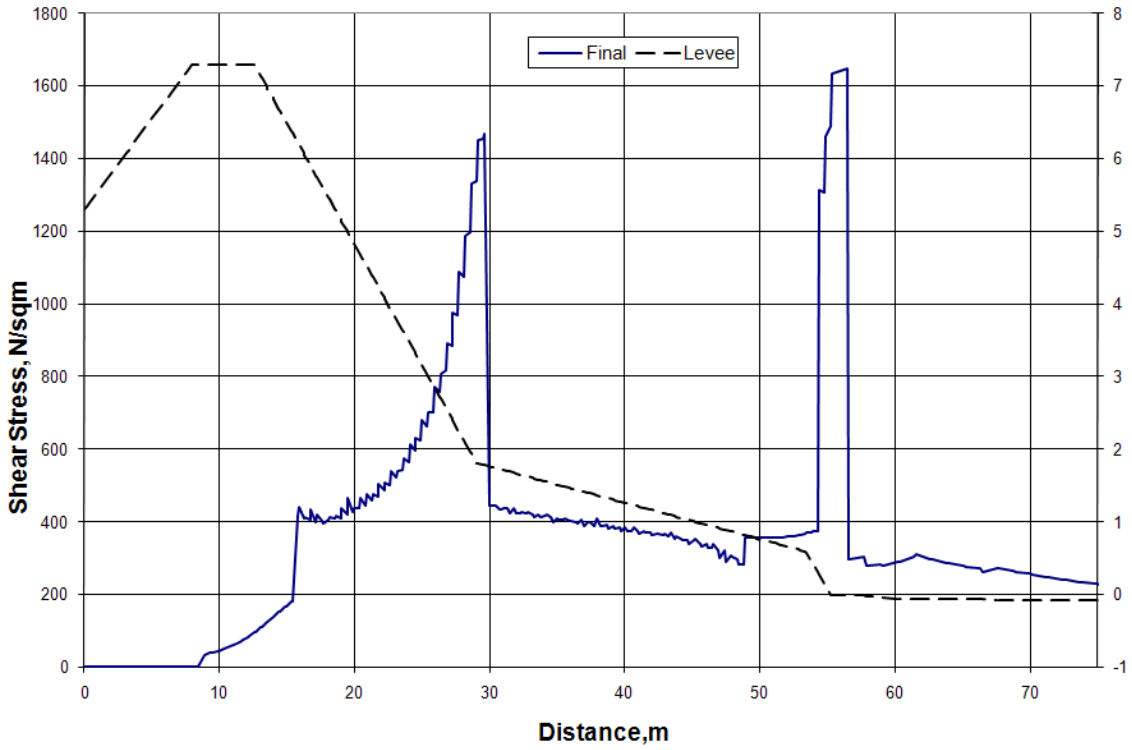

Figure A.25. Shear stress profile for 1.52 m surge event and n = 0.02.

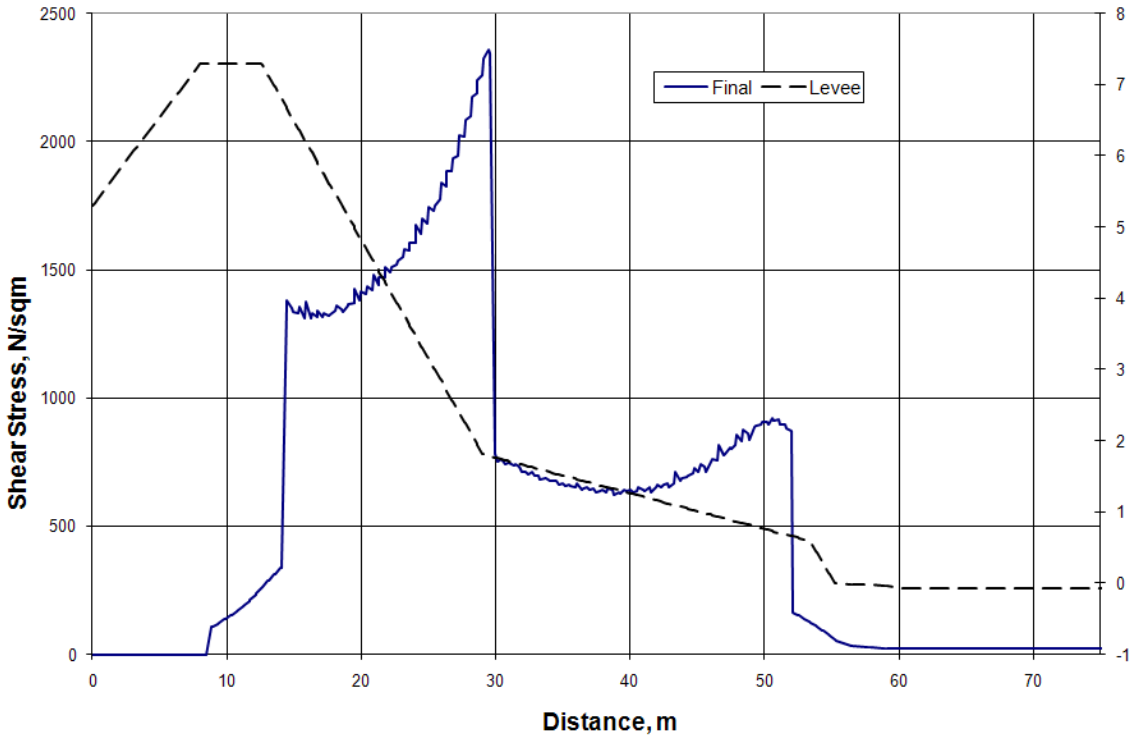

Figure A.26. Shear stress profile for 1.52 m surge event and n = 0.035.

OAK RIDGE
National Laboratory

Mississippi State University
CMRC
Construction Materials
Research Center
"An Industry, Agency & University Partnership"

JAMES WORTH
BAGLEY
COLLEGE OF ENGINEERING
MISSISSIPPI STATE UNIVERSITY
CIVIL & ENVIRONMENTAL
ENGINEERING